Conception and development of a novel grade of high resistance High Entropy Alloy from the CrFeMnNi family

Julia Olszewska

▶ **To cite this version:**

Julia Olszewska. Conception and development of a novel grade of high resistance High Entropy Alloy from the CrFeMnNi family. Other. Université de Lyon, 2019. English. NNT : 2019LYSEM007 . tel-03534289

HAL Id: tel-03534289
https://theses.hal.science/tel-03534289

Submitted on 19 Jan 2022

HAL is a multi-disciplinary open access archive for the deposit and dissemination of scientific research documents, whether they are published or not. The documents may come from teaching and research institutions in France or abroad, or from public or private research centers.

L'archive ouverte pluridisciplinaire **HAL**, est destinée au dépôt et à la diffusion de documents scientifiques de niveau recherche, publiés ou non, émanant des établissements d'enseignement et de recherche français ou étrangers, des laboratoires publics ou privés.

N° d'ordre NNT : 2019LYSEM007

THÈSE DE DOCTORAT DE L'UNIVERSITÉ DE LYON

opérée au sein de

l'École des Mines de Saint-Étienne

École Doctorale N°488
Sciences, Ingénierie, Santé

Spécialité : Science et Génie des Matériaux

présentée par

Julia OLSZEWSKA

Conception et développement d'une nuance d'alliage de type HEA (High Entropy Alloys) de la famille CrFeMnNi à résistance mécanique élevée

---

Soutenue publiquement à Saint-Etienne, le 26 Février 2019

Devant le jury composé de :

Pascal Jacques	Professeur, Université Catholique de Louvain	Rapporteur
Xavier Sauvage	Directeur de recherche CNRS, GPM Université de Rouen Normandie	Rapporteur
Jean Dhers	Responsable de l'innovation, Framatome Lyon	Examinateur
Patricia Donnadieu	Directrice de recherche CNRS, SIMaP Université Grenoble Alpes	Examinatrice
Franck Tancret	Professeur, IMN Université de Nantes	Examinateur
Jean-Denis Mithieux	Directeur scientifique, APERAM R&D Isbergues	Co-encadrant de thèse
David Piot	Chargé de recherche, Mines Saint-Étienne	Co-encadrant de thèse
Anna Fraczkiewicz	Directrice de recherche, Mines Saint-Étienne	Directrice de thèse
Gilles Adjanor	Ingénieur-chercheur, EDF R&D Les Renadière	Invité

Spécialités doctorales	Responsables :	Spécialités doctorales	Responsables
SCIENCES ET GENIE DES MATERIAUX	K. Wolski Directeur de recherche	MATHEMATIQUES APPLIQUEES	O. Roustant, Maître-assistant
MECANIQUE ET INGENIERIE	S. Drapier, professeur	INFORMATIQUE	O. Boissier, Professeur
GENIE DES PROCEDES	F. Gruy, Maître de recherche	SCIENCES DES IMAGES ET DES FORMES	JC. Pinoli, Professeur
SCIENCES DE LA TERRE	B. Guy, Directeur de recherche	GENIE INDUSTRIEL	N. Absi, Maitre de recherche
SCIENCES ET GENIE DE L'ENVIRONNEMENT	D. Graillot, Directeur de recherche	MICROELECTRONIQUE	Ph. Lalevée, Professeur

EMSE : Enseignants-chercheurs et chercheurs autorisés à diriger des thèses de doctorat (titulaires d'un doctorat d'État ou d'une HDR)

ABSI	Nabil	MR	Génie industriel	CMP
AUGUSTO	Vincent	CR	Image, Vision, Signal	CIS
AVRIL	Stéphane	PR2	Mécanique et ingénierie	CIS
BADEL	Pierre	MA(MDC)	Mécanique et ingénierie	CIS
BALBO	Flavien	PR2	Informatique	FAYOL
BASSEREAU	Jean-François	PR	Sciences et génie des matériaux	SMS
BATTON-HUBERT	Mireille	PR2	Sciences et génie de l'environnement	FAYOL
BEIGBEDER	Michel	MA(MDC)	Informatique	FAYOL
BLAYAC	Sylvain	MA(MDC)	Microélectronique	CMP
BOISSIER	Olivier	PR1	Informatique	FAYOL
BONNEFOY	Olivier	PR	Génie des Procédés	SPIN
BORBELY	Andras	MR(DR2)	Sciences et génie des matériaux	SMS
BOUCHER	Xavier	PR2	Génie Industriel	FAYOL
BRODHAG	Christian	DR	Sciences et génie de l'environnement	FAYOL
BRUCHON	Julien	MA(MDC)	Mécanique et ingénierie	SMS
CAMEIRAO	Ana	MA(MDC)	Génie des Procédés	SPIN
CHRISTIEN	Frédéric	PR	Science et génie des matériaux	SMS
DAUZERE-PERES	Stéphane	PR1	Génie Industriel	CMP
DEBAYLE	Johan	MR	Sciences des Images et des Formes	SPIN
DEGEORGE	Jean-Michel	MA(MDC)	Génie industriel	Fayol
DELAFOSSE	David	PR0	Sciences et génie des matériaux	SMS
DELORME	Xavier	MA(MDC)	Génie industriel	FAYOL
DESRAYAUD	Christophe	PR1	Mécanique et ingénierie	SMS
DJENIZIAN	Thierry	PR	Science et génie des matériaux	CMP
BERGER-DOUCE	Sandrine	PR1	Sciences de gestion	FAYOL
DRAPIER	Sylvain	PR1	Mécanique et ingénierie	SMS
DUTERTRE	Jean-Max	MA(MDC)		CMP
EL MRABET	Nadia	MA(MDC)		CMP
FAUCHEU	Jenny	MA(MDC)	Sciences et génie des matériaux	SMS
FAVERGEON	Loïc	CR	Génie des Procédés	SPIN
FEILLET	Dominique	PR1	Génie Industriel	CMP
FOREST	Valérie	MA(MDC)	Génie des Procédés	CIS
FRACZKIEWICZ	Anna	DR	Sciences et génie des matériaux	SMS
GARCIA	Daniel	MR(DR2)	Sciences de la Terre	SPIN
GAVET	Yann	MA(MDC)	Sciences des Images et des Formes	SPIN
GERINGER	Jean	MA(MDC)	Sciences et génie des matériaux	CIS
GOEURIOT	Dominique	DR	Sciences et génie des matériaux	SMS
GONDRAN	Natacha	MA(MDC)	Sciences et génie de l'environnement	FAYOL
GONZALEZ FELIU	Jesus	MA(MDC)	Sciences économiques	FAYOL
GRAILLOT	Didier	DR	Sciences et génie de l'environnement	SPIN
GROSSEAU	Philippe	DR	Génie des Procédés	SPIN
GRUY	Frédéric	PR1	Génie des Procédés	SPIN
HAN	Woo-Suck	MR	Mécanique et ingénierie	SMS
HERRI	Jean Michel	PR1	Génie des Procédés	SPIN
KERMOUCHE	Guillaume	PR2	Mécanique et Ingénierie	SMS
KLOCKER	Helmut	DR	Sciences et génie des matériaux	SMS
LAFOREST	Valérie	MR(DR2)	Sciences et génie de l'environnement	FAYOL
LERICHE	Rodolphe	CR	Mécanique et ingénierie	FAYOL
MALLIARAS	Georges	PR1	Microélectronique	CMP
MOLIMARD	Jérôme	PR2	Mécanique et ingénierie	CIS
MOUTTE	Jacques	CR	Génie des Procédés	SPIN
NAVARRO	Laurent	CR		CIS
NEUBERT	Gilles			FAYOL
NIKOLOVSKI	Jean-Pierre	Ingénieur de recherche	Mécanique et ingénierie	CMP
NORTIER	Patrice	PR1	Génie des Procédés	SPIN
O CONNOR	Rodney Philip	MA(MDC)	Microélectronique	CMP
PICARD	Gauthier	MA(MDC)	Informatique	FAYOL
PINOLI	Jean Charles	PR0	Sciences des Images et des Formes	SPIN
POURCHEZ	Jérémy	MR	Génie des Procédés	CIS
ROUSSY	Agnès	MA(MDC)	Microélectronique	CMP
ROUSTANT	Olivier	MA(MDC)	Mathématiques appliquées	FAYOL
SANAUR	Sébastien	MA(MDC)	Microélectronique	CMP
SERRIS	Eric	IRD		FAYOL
STOLARZ	Jacques	CR	Sciences et génie des matériaux	SMS
TRIA	Assia	Ingénieur de recherche	Microélectronique	CMP
VALDIVIESO	François	PR2	Sciences et génie des matériaux	SMS
VIRICELLE	Jean Paul	DR	Génie des Procédés	SPIN
WOLSKI	Krzystof	DR	Sciences et génie des matériaux	SMS
XIE	Xiaolan	PR0	Génie industriel	CIS
YUGMA	Gallian	CR	Génie industriel	CMP

Mise à jour : 30/08/2018

Remercîments

Je présente mes sincères remercîments aux membres du jury qui ont accepté d'évaluer mon travail de thèse : Franck Tancret, Pascal Jacques, Xavier Sauvage, Jean Dhers, Patricia Donnadieu et Gilles Adjanor.

Tout d'abord, je tiens à exprimer ma gratitude à ma directrice de thèse Anna Fraczkiewicz. Dès notre première rencontre à Varsovie une certaine complicité est née entre nous, et a rendu ce travail passionnant. Tu as toujours fait de ton mieux pour me donner les moyens d'apprendre et de me former. Merci pour ton temps et pour les conversations scientifique (et pas que) dans ton bureau (et pas que). C'est grâce à toi que j'ai pu participer à de multiples conférences et devenir un membre de la société métallurgique. Tout ton apport ressort à travers la qualité de ce travail de thèse. Merci !

Je remercie également Jean-Denis Mithieux, qui m'a encadré du côté de APERAM. Sans ton ouverture d'esprit et ta passion pour la science cette thèse n'aurait pas pu se dérouler aussi bien. Ce fut un énorme plaisir de pouvoir travailler avec toi en tant que chercheur mais surtout en tant qu'humain.

Merci également aux co-encadrants, David Piot et Mathieu Lenci qui ont toujours été là pour m'aider. Je remercie aussi Frank Motheillet qui a suivi ce projet de près et a été de très bon conseil. Une pensée particulière pour Julien Favre qui est intervenu tard dans ma thèse mais qui a eu un impact majeur sur le rendu final. Merci pour tes idées, tes conseils et ton soutien jusqu'au bout !

Je souhaite remercier toutes les personnes qui ont participé à ces travaux et qui ont partagé leur savoir-faire avec moi. Pour commencer Claude et Simon, responsables de la préparation de la matière. Tout le personnel de l'atelier, Édith, Marc, Bernard et Gilles, pour l'usinage rapide et efficace (Marc, mon tourneur préféré, merci aussi pour ton aide sur d'autres projets !). Merci à Gilles Blanc, le maître de la métallographie ! Merci Yoan pour l'introduction à l'apiculture et Max pour les quelques leçons de laser ;) Merci à Marilyne et Sergio, qui ont a passé beaucoup de temps à travailler sur les MEB et le MET, mais aussi à les réparer, ce qui a également été extrêmement intéressant ! Merci aux filles des essais mécaniques Claire, Séverine et Pauline, même si mon premier contact avec la machine de compression s'est fait avec Nathalie, avec qui nous avons ensuite passé de bons moments dans le nouveau

labo XRD (qui sent bon ;)). J'ai beaucoup appris grâce à vous tous! Un énorme merci également au duo Sophie et Sophie, qui ont presque réussi à rendre mes tâches administratives agréables (un véritable exploit !).

Je dois aussi de grands remercîments à Marc Legros du CEMES Toulouse, qui grâce à ses observations MET in situ a apporté une réponse concrète à certaines questions à cette thèse, et en a soulevé beaucoup plus !

Ce fut également un énorme plaisir de découvrir le laboratoire d'APERAM à Isbergues. Merci à Virginie qui s'est occupé de moi pendant le stage et ensuite pendant la thèse. Merci aussi à Christine qui participait vivement aux expériences sur mes matériaux bizarres. Enfin, je souhaite remercier Nadège pour son amour de la Gleeble mais principalement pour les super moments passés ensemble et pour son accueil. Merci à tous les autres que j'ai pu rencontrer au nord !

La thèse ce n'est pas que les mois d'apprentissage et de travail, mais surtout les gens que nous rencontrons et les amitiés qui se créent. Pour commencer je voudrais remercier tous les anciens doctorants qui m'ont accueilli au K4 en premier : Guillaume, Diego, Joris, Aladji, Romain, Quentin, Jean Gabriel, Ernesto. Une forte pensée à Michał qui m'a présenté le fonctionnement du laboratoire et la thématique commune à nos deux thèses. J'ai eu la chance de me retrouver dans le même bureau que Lisa et Clément, où je me suis sentie tout de suite à ma place, merci ;). Elia, Antonis, Arnaud, nos aventures ont démarré ensemble, malgré le petit décalage de ma part, je vous souhaite le meilleur pour la suite. Je n'oublie pas les passages d'Ada à l'école, nous étions devenues presque inséparables. Des remercîments tout particuliers à Justin, le clown, l'optimiste, et surtout un très bon ami. Je n'oublie pas tous les jeunes qui sont arrivé en cours de route, voir vers la fin de mon séjour : Ahmed, Cindy, Michella, Sebastien, Safa, Jihene, Zineb, Ayoub, Margaux, Antonin, Mariam. Je voudrais aussi remercier mes voisins favoris : Jeremy et Alex. Vous êtes les meilleurs organisateurs de soirées !

Mathieu et Matthieu, je ne vous ai pas oublié ;) On a passé tellement de soirées MAGnifiques à manger et créer notre petite fierté (vive Optimus Price). Merci pour tout ce qu'on a vécu ensemble et tout ce qui est toujours devant nous.

Il y a aussi ceux que j'ai rencontré avant commencer la thèse, pendant le Master, que j'ai le plaisir d'appeler mes amis proches : Vendulka et Yassine. Même si nous sommes dans des coins du Monde éloignés nous parvenons à garder un lien fort.

Claudine, nous nous sommes rencontré d'une manière originale, mais nos points communs et nos différences ont fait de nous de vraies amies. On a passé des soirées de mamies, on a fait des voyages et des randos magnifique. Merci pour ton amitié!

Ces remercîments vont aussi à Ania, sans laquelle je ne serais pas venue à Saint Etienne. C'est elle qui m'a inspiré pour faire l'Erasmus qui s'est ensuite transformé en thèse. Thank you for being there for me despite the enormous distance separating

us. You are and will be my very best friend!

Une chance particulière m'a été donnée en te rencontrant Jolan. Merci pour ta présence, ton soutien et ton aide si précieux. Tu es devenu une partie intégrale de ma vie et j'en suis ravie !

Je ne peux pas finir sans remercier ma maman. Tu es mon exemple et soutien ultime. Même si je ne te le dis pas tous les jours, sache que je t'aime et que je te remercie pour m'avoir donné autant de toi. Merci maman !

Contents

Introduction

The modern world, in full evolution, requires constantly enhanced performances. To do so materials with improved properties are continuously necessary, and consequently, research of metallic alloys fulfilling the high demands is needed. Due to ecological as well as economical reasons, we search for materials that are able to work both in more extreme conditions and for longer time. This way, already diminishing metallic resources, would be conserved. At the same time, from economical point of view, some strategic elements should be avoided. We seek to use less, better, wiser, longer: to do so, new materials are searched for through various concepts. Numerous possibilities came to life from the novel view on alloys, with multiple principal elements, called the *High Entropy Alloys*, *HEAs*.

This change of perspective on metallic alloys opened the view on central parts of phase diagrams, omitted up to now. Multitude of new compositions could be ultimately designed. Some of them have already been shown to possess improved properties, such as enhanced mechanical resistance. Other alloys with augmented resistance to creep, irradiation or others could be imagined to replace standard materials. Stainless steels are one of the biggest group of materials used where the targeted improvement can be sought in the future, in particular in the areas of applications, where the most enhanced properties are required. HEAs from the CoCrFeMnNi family, Cantor's family, show a high potential to do so upon optimisation of their single fcc phased structure and high mechanical resistance accompanied by excellent ductility even at cryogenic temperatures.

Design of new compositions from this family, their optimisation and comprehension of mechanisms and the origin of good mechanical properties are the aim of this PhD thesis. The demand to lower or completely eliminate cobalt from the Cantor's alloy was the driving force for this project, since this expensive and strategic element entails some technological (recycling) and utility (irradiation) difficulties. Thereby, original grades of alloys were proposed with decreased Co content or even Co-free. Their design was done by thermodynamic simulations followed by experimental verification leading to the understanding of strengthening mechanisms based on profound microstructural observations and mechanical tests.

Our research was focused on characterisation of the unusual microstructures

observed in these alloys, with special focus on recrystallisation process and consecutive dislocation structure evolution. Next, the influence of obtained microstructures on mechanical resistance was analysed. As a consequence, a study of active hardening mechanisms was done. The application of standard strengthening models, usual for existing and well analysed fcc materials, allowed to position the selected grades of HEAs among those classical alloys and verify the existence of any casualties typical for HEAs from the Cantor's family.

This thesis dissertation is divided into five chapters.

Chapter 1 presents the state of the art of the HEAs topic. It first focuses on contemporary definitions of HEAs, thermodynamics at the origin of those alloys as well as the phase formation criteria empirically established and currently in use. Next, presentation of recent results in the domain of development of HEAs from various families is addressed. Finally, an insight on the CoCrFeMnNi family is given, concentrating on the microstructure and mechanical properties of those alloys. A special focus is given to state of research on the Co-free compositions even if only few available alloys respect this criterion nowadays.

Chapter 2 shows the selected alloys, as well as the experimental methods applied during this thesis research.

Chapter 3 focuses on the design of new compositions, with detailed route of thermodynamic simulations performed within this work. Following, an empirical verification of those calculations is presented, focusing on phase formation and stability predicted by phase diagrams. The fulfilment of empirical phase formation criteria is also shown. Next, an initial evaluation of selected compositions is done, at the level of microstructure and basic mechanical properties, which allows to narrow down the selection of promising alloys to one single composition: the so-called Y3 Co-free alloy.

Chapter 4 is dedicated to thorough analysis of microstructure, with focus on dislocation structure evolution. Question about occurrence of recrystallisation upon annealing, arisen during those observations, is addressed.

Chapter 5 analyses the possible strengthening mechanisms present in the selected Y3 alloy at all possible structural scales, starting from dislocations through grain boundaries up to precipitation hardening. Classical hardening models, like dislocations forest hardening and Kocks-Mecking model are applied to verify the divergence of HEAs compared do standard fcc materials. Hall-Petch analysis is used to estimate the magnitude of strengthening of the Y3 alloy in various states by grain boundaries. To conclude, further strengthening of this single fcc material by secondary precipitation, is verified.

The dissertation is completed by general conclusions. Perspectives for further work are also suggested.

Chapter 1

New classes of metallic materials: High Entropy Alloys

Contents

1.1 Many names of HEAs

The concept of High Entropy Alloys (HEAs) has been introduced by Yeh in 2004 [1] where he proposed the increased entropy of mixing as a possible reason for solid solution stability in multi-principal element alloys. He argues that high number of constituent elements significantly increases the ΔS term in the Gibbs free energy equation thus lowering the total energy of mixing (more details in Chapter 1.2) and favouring the solid solution formation over intermetallic compounds.

$$\Delta G = \Delta H - T\Delta S \tag{1.1}$$

In the same publication Yeh gave the first definition of HEAs as follows: *"High entropy alloys are composed of five or more principal elements whose concentrations are contained between 5 and 35 at.%"* [1]. Second part of this definition focuses on the configurational entropy, where HEAs are defined as alloys with $\Delta S \geq 1.5$R, Medium Entropy Alloys (MEAs) are in the range $1.0\text{R} \leq \Delta S \leq 1.5\text{R}$ and Low Entropy Alloys (LEAs) $\Delta S \leq 1.0$R [2,3]. Both criteria cover a large range of alloys and for most cases they overlap, but it is enough for a single phased alloy to fulfil one of them to be called a HEA.

In parallel with Yeh's first definition of HEAs, independently another article was published, this time in the United Kingdom, by Cantor [4] where he presents microstructural results of many multicomponent alloys. It is him who first introduced the now most well known and largely studied composition, the single phased equimolar CoCrFeMnNi that is often referred to as the *Cantor's Alloy*.

Since 2004 the novel HEA group of alloys have been given many other names such as: multi principal elements alloys (MPEAs), equimolar alloys, substitutional alloys, multi component alloys or complex concentrated alloys (CCAs) depending on their chemical and phase composition [5,6]. It shows how vast is the area of interest, with an immense number of alloys *"to investigate in the unexplored central regions of multicomponent alloy phase space"* [4]. In the latest review on HEAs, Miracle and Senkov [6] proposed to use the High Entropy name for alloys where stabilisation of a single solid solution is the key feature. Whether on purpose or not, the first approach in the early days of HEAs was directly associated with single phased solid solutions controlled by configurational entropy. Alloys that do not necessarily fulfil the entropy definition, like ternary or quaternary compositions, are usually included in the MPEAs and multiphased alloys are often called the CCAs [6]. No matter the name we give them, those alloys are a whole new direction in the search for enhanced phase stability, mechanical properties or other special features.

1.2 Thermodynamics of High Entropy Alloys

Yeh proposed four core effects that differentiate HEAs from classical alloys [7]. Three out of those effects, in explicit high-entropy effect, sluggish diffusion and severe lattice distortion, were under the form of hypotheses that in the last years researchers tried to confirm or discard. In this chapter those four effects will be presented and confronted to recent results in each field.

High-entropy effect

The high entropy effect is said to be the signature concept of HEAs. It suggests that in near equiatomic compositions of 5 or more elements the formation of solid solution may be favoured over intermetallic phases due to increased configurational entropy. According to Gibbs free energy equation 1.2, the increase of entropy of mixing decreases the total free energy. However, it has been pointed out that addition of a new component may lead to formation of intermetallics more stable than solid solutions [5,8]. Up to now the enthalpy was considered as non-existent but obviously, it plays a role side by side with entropy in stabilisation of solid solutions. It has been shown by Takeuchi et al. [9] that ideal and regular solutions are uncommon. In fact out of 1176 binary metallic systems they analysed about 85% are non-regular with non-negligible H. In consequence enthalpies and entropies of mixing for both solid solution and intermetallics are in constant competition and it is the small differences between them that decide about phase stability.

$$\Delta G_{mix} = \Delta H_{mix} - T\Delta S_{mix} \tag{1.2}$$

If we consider an ideal solution, the effect of enthalpy of mixing can be neglected ($\Delta H_{mix} = 0$) compared to the entropy ΔS_{mix}. In such case, the change in Gibbs free energy due to mixing depends only on change in the configurational entropy [10]:

$$\Delta G_{mix} = -T\Delta S_{mix} = RT\sum x_i ln x_i \tag{1.3}$$

where R is the ideal gas constant and x_i is the concentration of component i in the alloy. For an equiatomic alloy, the configurational entropy of mixing reaches its maximum and can be written as follows [5]:

$$\Delta S_{mix} = RlnN \tag{1.4}$$

where N is the number of components. For quinary equiatomic alloy $\Delta S_{mix} = 1{,}61\mathrm{R}$, this value is to be compared to traditional metallic alloys where the entropy is of the order of 1R. Figure 1.1a shows the change of entropy for a hypothetical ideal

ternary system. The maximum is reached for the equimolar ratio [5]. Zhang et al. [8] showed on the example of theoretical binary A-B and ternary alloys A-B-C that addition of one more element in the system may be beneficial in suppressing the formation of compounds. It is represented by Figure 1.1b, where the red line a_3b_3, corresponding to the Gibbs energy for ternary alloy, is lower than blue line a_1b_1, equivalent to a binary alloy.

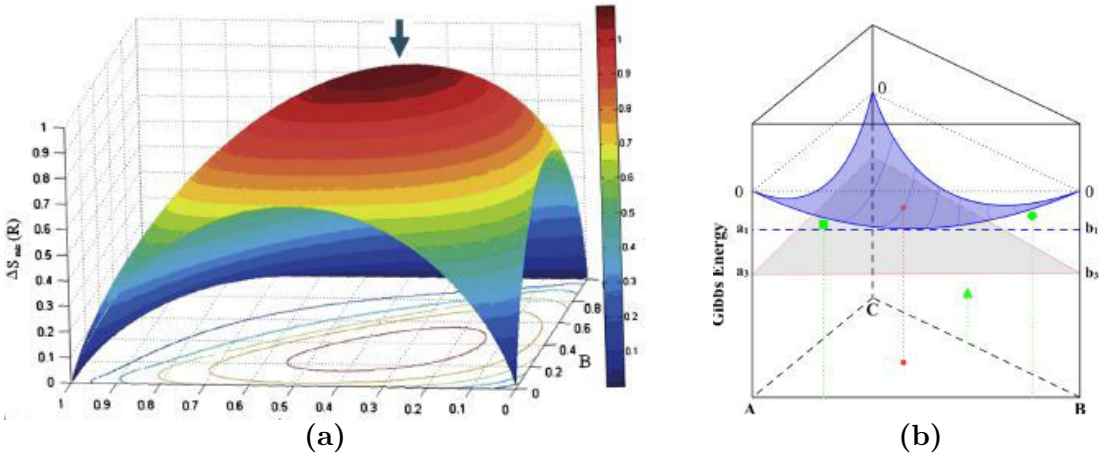

Figure 1.1: *a) Illustration of the ΔS_{mix} for ternary alloy system with the composition change [5]; b) Gibbs energies of phases in a hypothetical A-B-C system [8]*

The above analysis considers only a random configuration in solid solution which is often a poor estimation of total value of entropy. In real solutions the ΔS term can be more complex since other types of entropy must be considered, such as vibrational, electronic and magnetic. All those variables result in very different entropy curves, that can be highly asymmetric with respect to composition. At the same time, influence of temperature is not included in this reasoning. The importance of ΔS term is magnified by the temperature and at low temperatures its impact decreases. The values of entropy and enthalpy depend on each individual system and are not the sole parameter to take into account for phase formation prediction. It is also very important to bear in mind that all the thermodynamic approaches consider only solutions in equilibrium [6].

According to Gibbs phase rule, in equilibrium conditions, under constant pressure, the number of phases possible to form P, in an alloy of C components can be calculated from:

$$P = C + 1 - F \tag{1.5}$$

where F is the maximum number of thermodynamic degrees of freedom in the system. This means that for a 5-component system at a given pressure, a maximum of 6 equilibrium phases can be expected (for $F = 0$). Some researchers express surprise to frequently find fewer phases than allowed by the Gibbs phase rule [5, 11], others claim that HEAs violate the Gibbs phase rule [12]. The low number of

phases present in HEAs has been also used to support the presence of entropy effect in those alloys [13]. Despite the evidences confirming that high entropy of mixing truly extends the solubility limits of solid solutions [14], it can not be used as confirmation of "high entropy" hypothesis. The fact is that the phase rule gives only the allowed number of phases for each system but it in no case suggests the probabilities or expectations of phases that will actually exist in any given alloy [6]. It is very uncommon even in simple or complex solutions to observe the maximal number of allowed phases as it implies very specific conditions.

Sluggish diffusion effect

Atom diffusion plays an important role in almost all phenomena involving microstructure in materials. It influences among others solidification, any solid state phase transformation (except martensitic ones) or grain growth. The diffusion coefficient D depends on the temperature T and apparent activation energy Q and is defined as follows [15]:

$$D = D_0 e^{\frac{-Q}{kT}} \tag{1.6}$$

where D_0 is the maximum diffusion coefficient at infinite temperature and k is the Boltzmann constant. With increasing activation energy the movement of atoms becomes more difficult and so, the diffusion slows down. Q is highly influenced by nature of diffusing atoms and the environment of their motion. It is claimed that diffusion in HEAs might be slowed down due to larger fluctuation of lattice potential energy (LPE) between lattice sites [2]. Vacancy concentration plays an essential role for substitutional diffusion but due to increased complexity of HEA systems, the concentration of vacancies is limited. Their creation in those alloys is associated with positive enthalpy of formation and excessive mixing entropy [3].

The sluggish diffusion effect has been proposed based on secondary observations since direct measurements of diffusion coefficient are very difficult in such complex systems. It was presented as one of possible explanations for some of the noticed behaviours in HEAs, for example the formation of nanostructures upon solidification [16] or slow phase transformations upon annealing [17]. Unfortunately, those indirect observations are proof of slow kinetics but they do not show that the diffusion is slowed down in HEAs compared to conventional alloys.

Major results about diffusion coefficients in complex alloys available in literature come in fact from only one publication. Tsai et al. [15] studied the diffusion kinetics in HEA, by analysing quasi-binary systems in the ideal-solution-like FCC Co-Cr-Fe-Mn-Ni alloys. It was observed that elements, listed in the order of decreasing diffusion rate are Mn, Cr, Fe, Co and Ni (presented in Fig. 1.2a), which is similar to the sequence in conventional metals. The diffusion coefficients of elements in this

HEA system are clearly smaller than in the pure FCC metals, but also smaller than in alloys with lower number of constituents. Moreover, the normalised activation energies Q/T_m in the CoCrFeMnNi HEA are higher than in reference metals which is in accordance with sluggish diffusion theory. However Miracle and Senkov in their latest review of HEAs [6] suggest that the diffusion rate in analysed alloys can not be considered as significantly lower. The authors have analysed the data set of Tsai et al. and they have come to conclusion that for instance the $CoCrFeMn_{0.5}Ni$ alloy does not show any significant differences in diffusion coefficient if placed among many other FCC metals and alloys, for data normalised at T_m. This wide range is shown in Fig. 1.2b. The authors conclude that differences within one order of magnitude are negligible. The topic needs to be further explored to support the conviction that MPEAs/HEAs/CCAs show unusually slow diffusion.

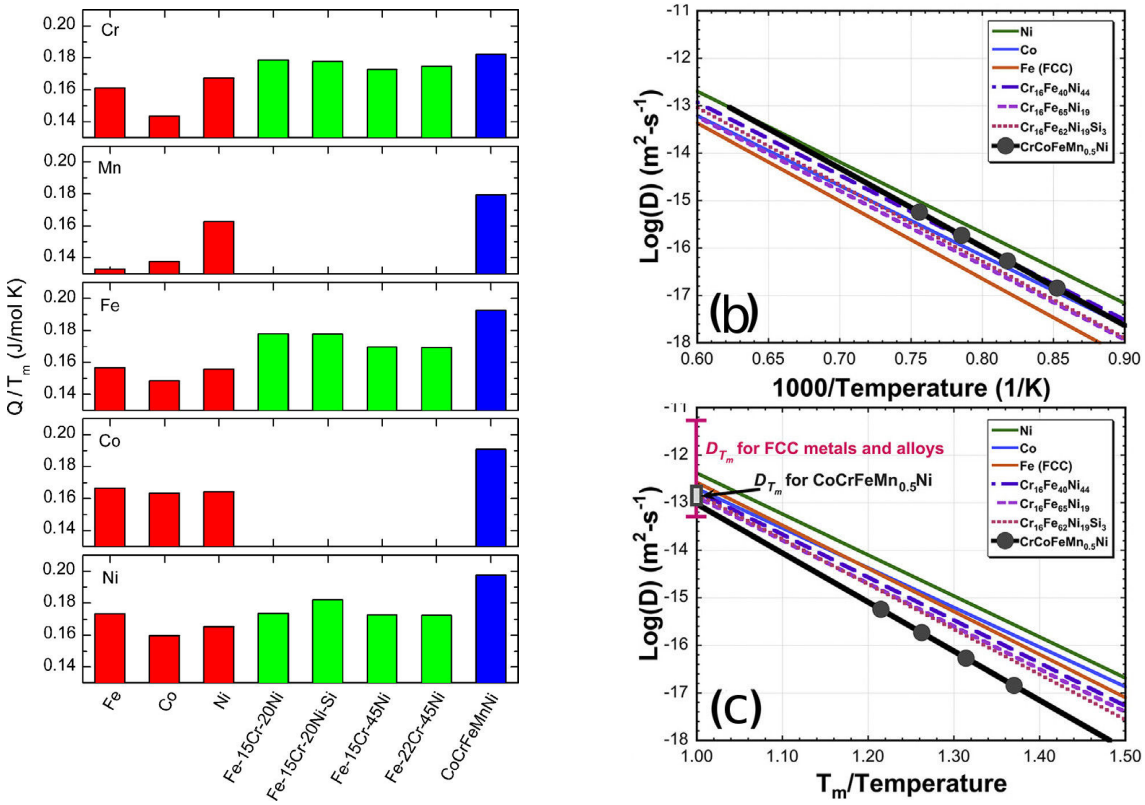

Figure 1.2: *a) Normalised activation energies of diffusion for Cr, Mn, Fe, Co and Ni in different matrices [15]; Diffusion coefficients of Ni (D_{Ni}) in FCC elements, stainless steel alloys (composition in at.%) and $CoCrFeMn_{0.5}Ni$ as a function of b) inverse absolute temperature and c) inverse absolute temperature normalised by the melting or solidus temperature of the host alloy, T_m [6]*

If it were to be confirmed, sluggish diffusion may be at the origin of enhanced phase stability and slowed down microstructural evolution with phenomena dependant from it like precipitation, recrystallisation or creep. Indirectly it can stabilise the microstructure resulting in slower coarsening of precipitates or grains, increased temperatures of recrystallisation and better creep resistance. Let us take the grain

growth as an example. This process does not include change in composition, but requires cooperative diffusion of all composing elements during the movement of grain boundary. Therefore, grain growth rate will be determined by the slowest diffusing element, which in the case of Cantor's alloy is Ni (Q = 318 kJ/mol) [15]. Comparative values of Q activation energy for grain growth reported in literature are as follow:

CoCrFeMnNi HEA	>	SS 304L
322 kJ/mol [18]		150 kJ/mol [18]

Of course those values depend strongly on the history of treatments of the material, but they can show the trend, where HEAs present a lower diffusion rate (assuming the values are defined correctly by Tsai et al. which is also argued by Aloke [19]). This in turn, strongly influences the evolution of microstructure during annealing. Small diffusion coefficient describes more limited mobility of atoms. Sluggish diffusion can for example be used to explain the fine microstructure and the formation of nano-sized precipitations [5], but as it was evoked before it is just one of possible explanations and it does not prove the actual slowed diffusion.

Severe lattice-distortion effect

Due to high number of components of different sizes, where each atom has the same probability to occupy a given place in the lattice, distortion of the lattice can be severe in HEAs (as presented in Figure 1.3). Furthermore the atomic displacement is enhanced by bonding differences and crystal structure disparities among multiple compounds [3]. Those changes in atoms positions can affect various properties like hardness, electrical and thermal conductivity and effect of temperature on properties [7, 13]. Unfortunately attempts to quantify the lattice-distortion effect are problematic, since it is difficult to separate it from other contributions like shear modulus mismatch between elements or electronic structures influencing the local bond states [20]. Just like sluggish diffusion effect, the lattice distortion has been guessed based on secondary observations, for example grain boundary hardening efficiency [18] or unexpected loss of x-ray diffraction peak intensities due to enhanced X-ray scattering on roughened atomic planes [21].

One of the predicted effects of severely distorted lattice should be large solution hardening. Several studies have tried to find explicit proof of this phenomenon [20, 22–26]. They all come to the same conclusion that strengthening does not depend directly on number of constituents, nor is it maximised by the equiatomic composition. It is influenced in greater extent by the nature of chemical elements in the multicomponent alloys. Toda-Caraballo has developed a model predicting the solid solution hardening in alloys that can be extended to HEAs [25]. Based on

some data available in literature the model has been proved to be in good agreement with experiment for both fcc and bcc alloys and could be used in design of new compositions.

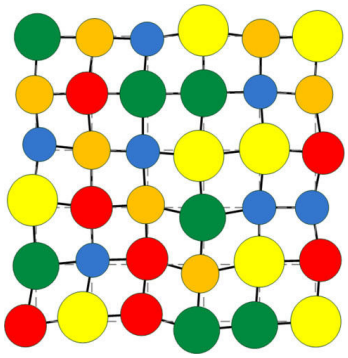

Figure 1.3: *Severe lattice distortion in a multicomponent crystal structure [2]*

Cocktail effect

Cocktail effect is the only one that is not a hypothesis needing a confirmation. It was first proposed by Ranganathan to illustrate the many possibilities and surprising effects of alloy design and development [27]. It reminds us as well that numerous exceptional properties are the result of unexpected synergies. This effect is found in many alloys, also the so called "conventional" ones, but in HEAs it is enhanced since the number of major elements is high. No matter how many phases are present in the HE alloy, each of them is a multi-principal solid solution that can be considered as an atomic-scale composite [3].

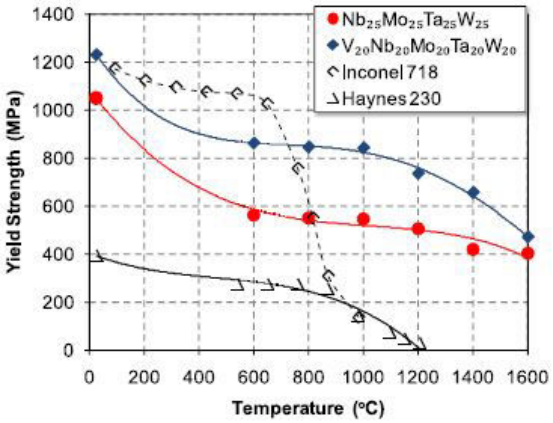

Figure 1.4: *Temperature dependance of yield stress of $Nb_{25}Mo_{25}Ta_{25}W_{25}$ and $V_{20}Nb_{20}Mo_{20}Ta_{20}W_{20}$ HEAs and two superalloys, Inconel 718 and Haynes 230 [29]*

While designing an alloy it is important to remember that there are many sources of its properties. Firstly coming from the constituent elements by the mixture rule. Secondly from the interactions between various atoms and lattice distortion at the atomic-scale and finally the multiphase composite effect at the micro-scale (if multiple phases are present). Those interactions may increase the effects predicted

by the mixture rule and result in unforeseen properties. An example frequently evoked in literature reviews is that of refractory HEAs. Senkov et al. managed to obtain single BCC phased alloys: $Nb_{25}Mo_{25}Ta_{25}W_{25}$ and $V_{20}Nb_{20}Mo_{20}Ta_{20}W_{20}$ that present high yield strength even at very high temperatures. Due to their high melting temperature they maintain satisfying properties up to 1600°C, increasing possible range of temperatures at which they could work (Fig. 1.4) whereas the superalloys currently used in turbine engines show significant drop in YS at about 750°C. It is also found for hardness measurements within the same family of alloys. It reaches the values of 4455 MPa and 5250 MPa respectively which are about 3 times higher than the mixture rule predicts [28].

1.3 Empirical criteria of solid solution formation

Initial definition of HEAs imposed the search for one single phase [1]. Now, this condition seams to be too restraining and more possibilities are accepted and considered as promising: dual-phased alloys with fcc and bcc phases or presence of intermetallics. In all cases, availability of tools allowing the prediction of phase formation is of big utility, regardless if the goal is single or multi phased alloy.

In classical metallurgical approach, alloys are composed of a solvent, that is the major element, and solutes added to form new solid solutions or secondary phases with better and more desirable properties. A basic set of rules have been defined by W. Hume-Rothery since 1936 for solid solution formation, for substitutional alloying. It describes the conditions under which an element can dissolve in a metal, forming a solid solution. Most important of them are the following [30]:

- Solid solution formation is more probable when atomic size mismatch between the solute and the solvent is of less than 15%. The mismatch factor is defined as:
$$\frac{r_{solute} - r_{solvent}}{r_{solvent}} \cdot 100 < 15\% \tag{1.7}$$
- The lower the difference in electronegativity (or electropositivity) between the solute and the host, the more likely is the formation of substitutional solid solution. Otherwise, formation of intermetallic compounds will be promoted due to limited solubility.
- A metal with a lower valency is more likely to dissolve in one which has a higher valency than vice versa. The maximum solubility is achieved when solute and solvent have the same valency.
- the crystal structures of the solute and the solvent should be similar for better solubility.

1.3 Empirical criteria of solid solution formation

Multiple elements present in HEAs do not allow to define the solvent and solutes in a straightforward way. It has been attempted by many researchers to define guidelines for phase formation in HEAs, but at the moment most of them are empirical observations of high number of compositions in attempt to find some general trends [30–40]. It should be noted that many phases have been defined based on as cast state, that is not necessarily the closest to equilibrium. According to equation 1.2 the influence of entropy of mixing is enhanced at high temperatures where disordered solid solution formation is favoured during solidification, but it does not mean that intermetallics are not thermodynamically more stable phases at lower temperatures. In addition, phase identification done currently by XRD measurements is burdened with the technique uncertainty and some minority phases might have not been detected.

Even though the Hume-Rothery rules can not be directly applied to this kind of alloys, some similarities can be found within the proposed phase formation rules for HEAs. The most apparent similarity is the atomic radii mismatch, δ:

$$\delta = \sqrt{\sum_{i=1}^{n} c_i \left(1 - \frac{r_i}{\sum_{j=1}^{n} c_j r_j}\right)^2} \tag{1.8}$$

where c_i, c_j are mole percentages of ith and jth components and r_i, r_j are their respective radii [30, 31, 35].

Correlation between atomic mismatch and phase formation for various alloys was done in several studies [30, 31, 35]. It was shown that δ should be below 6.6% to form a random solid solution, and just like the mismatch rule by Hume-Rothery, it imposes a maximum atomic size differences. Otherwise ordered structures are promoted or even the amorphous phase might be formed. The δ parameter is often used as a base to compare other criteria of formation proposed in literature and so, most diagrams to determine phase formation put it as the abscissa.

Naturally, phase formation is ruled by thermodynamics, and the phase with lowest free energy will be stabilised (following the Gibbs free energy equation 1.2). There is a constant competition between entropy and enthalpy of mixing and so the first parameter proposed to predict phase formation was the Ω, which can be defined as follows:

$$\Omega = \frac{T_m \Delta S_{mix}}{|\Delta H_{mix}|} \tag{1.9}$$

It is dependent on ΔH_{mix}, ΔS_{mix} and T_m which are described as presented below:

$$\Delta S_{mix} = -R \sum_{i=1}^{n} (c_i ln c_i) \tag{1.10}$$

where c_i is the mole percentages of ith component and $R = 8.314$ JK^{-1}mol^{-1} is the gas constant;

$$\Delta H_{mix} = \sum_{i=1}^{n} \sum_{i \neq j} 4 \Delta H_{AB}^{mix} c_i c_j \tag{1.11}$$

where c_i, c_j are mole percentages of ith and jth components and ΔH_{AB}^{mix} is the enthalpy of mixing of binary liquid alloys.
T_m is the predicted melting temperature based on the rule of mixing:

$$T_m = \sum_{i=1}^{n} c_i \left(T_m\right)_i \tag{1.12}$$

where T_m is the melting point of i^{th} component in the alloy.

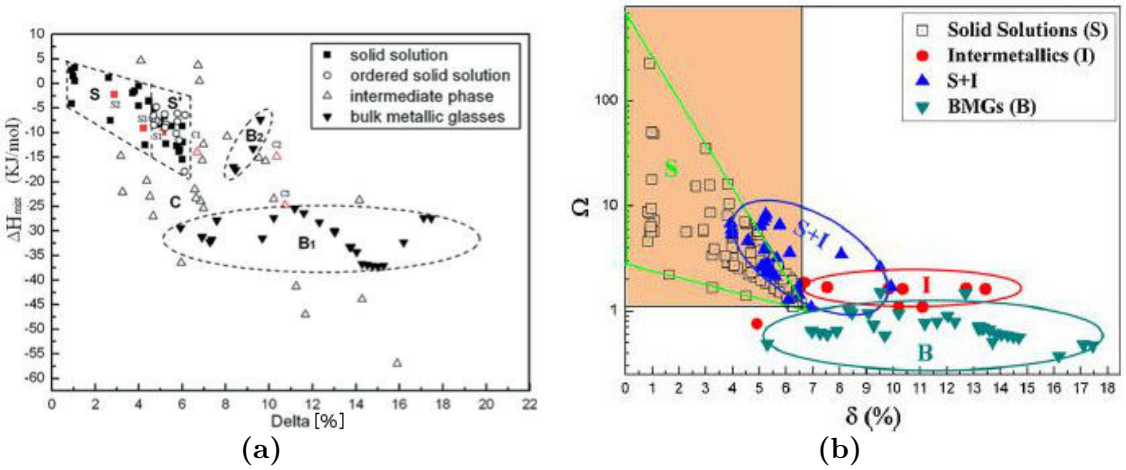

Figure 1.5: *Relatchionships between phase formation parameters for multi-component alloys a) ΔH_{mix} as a function of δ [31] b) Ω as a function of δ [35]*

The relationships between ΔH_{mix}, Ω, and δ have been plotted in Figure 1.5. They regroup typical HEAs reported in literature (a table assembling all the available data can be found in [3]). Some tendencies can be found, although the boundaries between various regions are vague. In the zones marked by S, disordered solid solution should typically be formed. The atomic size difference is relatively small, and the atoms can easily substitute each other, the lattice distortion is quite low. Entropy of mixing reflects the level of „confusion of the system" and the higher it is, the more difficult formation of ordered structures is, and creation of solid solution is favoured. Guo et al. [37] was the first to use the term of „confusion of the system" for HEAs in a way similar as it was used in reference to amorphous phases in metallic glasses, where it means that the more alloying elements are involved the lower the chance that the alloy can form a well defined crystal structure. For HEAs the confusion reflects the random distribution of elements, without any order of short or long range. With high confusion the system has the possibility to choose between solid solution and amorphous phase formation. At the same time, the contribution of enthalpy of mixing has to be taken under consideration. When it is only slightly negative, the

effect of entropy of mixing is dominant and compound formation can be avoided. On the other hand, when the ΔH_{mix} decreases significantly, the tendency to create ordered structures becomes higher and some intermetallics appear. If in addition the atomic mismatch increases it becomes difficult for atoms to create a crystalline structure and bulk metallic glasses are obtained (zone B) [31,35]. It is due to strain that is created by the size mismatch, which can lead to topological instability and finally formation of amorphous phase, which is in accordance with Hume-Rothery rules.

The parametric approaches evoked until now can help predict the solid solution formation but can not tell much about the achieved crystalline structure. It is widely known that crystalline structure significantly affects the mechanical behaviour of alloys. Most known HEAs form either bcc or fcc solid solutions and sometimes it depends merely on content of one element. An example can be given here citing Yeh's first publication in the topic [1], where change in Al content influences the obtained crystalline structure and as a consequence, the hardness of the alloy. With increasing Al content first a single fcc structure is obtained, then a dual-phased fcc + bcc alloy is reached to finally become a fully bcc one. It is well known that bcc structure increases materials strength (unfortunately usually followed by increased brittleness). Therefore, being able to predict the appearance and the fraction of bcc phase could lead to tailored properties (as shown in Figure 1.6a).

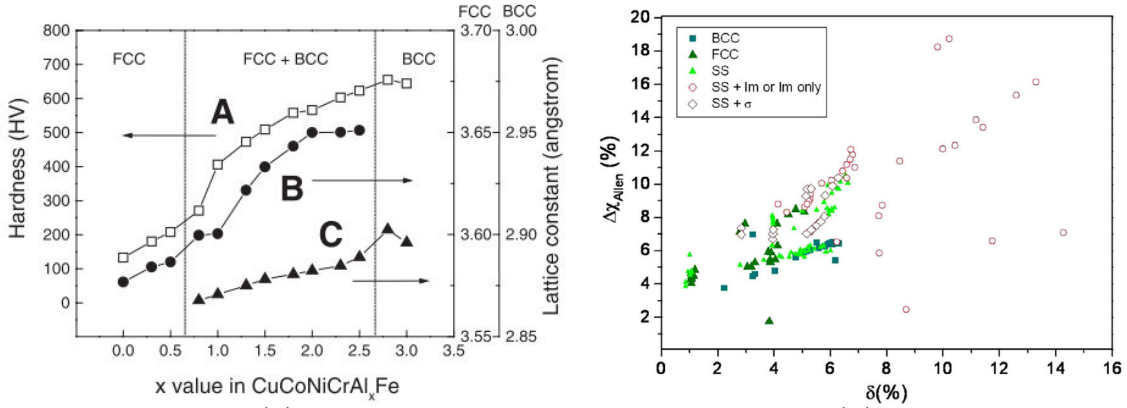

(a) **(b)**

Figure 1.6: *a) Hardness and lattice constants of $CuCoNiCrAl_xFe$ alloy system with different x values (A hardness, B lattice parameter of fcc phase and C lattice parameter of bcc phase) [1]; b)Radius vs. electronegativity mismatch for the multicomponent systems. BCC and FCC stands for formation of only one phase, SS stands for formation of more solid solutions, SS + IM for formation of solid solution and compounds or only compounds, SS + σ for systems where the formation of solid solution plus σ phase occurs [30]*

New parameters are needed to predict formation of a specific crystalline structure. Inspiration comes again from Hume-Rothery rules that evoke the equivalency and electronegativity of alloying elements stabilising fcc- or bcc-type solid solutions. In general, atoms with similar electronic structure will have a tendency to force the creation of specific crystalline structure. The concept could be in simplification

described as a way the atoms perceive each other and their surroundings. Let's focus first on the difference in electronegativity between constituent atoms. It is defined as follows:

$$\Delta\chi = \sqrt{\sum_{i=1}^{n} c_i \left(\chi_i - \sum_{j=1}^{n} c_j\chi_j\right)^2} \tag{1.13}$$

where χ_i is the electronegativity of ith element and $\sum_{j=1}^{n} c_j\chi_j$ represents the average electronegativity in the alloy. A comment about the way to determine the electronegativity is necessary. In fact, it was suggested by Poletti et al. [30] that instead of empirical Pauling scale, the values of Allen electronegativity should be used. Pauling assumed that the electronegativity represents the power of a molecule or atom to attract electrons to itself. On the other hand, Allens scale represents a more recent and physically based way to express electronegativity where it is considered as the average energy of valence electrons in a free atom [41]. Even though the values are comparable with Pauling for most elements, some differences can be found, especially for transition metals [42].

Just like previous parameters, $\Delta\chi$ was represented for numerous alloys in function of the atomic radii mismatch, Figure 1.6b [30]. Considered structures are single fcc or bcc, mix of two solid solutions SS, systems with intermetallic phase SS + IM and systems with σ phase SS + σ. A clear division was obtained between the area of solid solutions (FCC, BCC, SS) and the area where intermetallics or σ phase were observed. The radius mismatch is between 1% and 6%, like in previously analysed works. The electronegativity difference is of the order of 3-6 %. A tendency can be found: for higher δ and lower $\Delta\chi$, bcc solid solutions occur more frequently than fcc.

Next parameter, the effect of electron concentration, is a slightly more complex parameter to analyse. There are two possible ways to define it: firstly by the number of total electrons accommodated in the valence band, named the valence electron concentration or VEC and secondly the average number of itinerant electrons per atom, e/a [36]. One should be careful about the choice of parameter. Hume-Rothery rule uses e/a that has a clear influence on the crystalline structure for the so called *electron compounds*. Most HEAs are composed of transition metals for which this parameter has shown to be controversial and difficult to estimate since it varies in different environments; moreover, it has not been yet verified for all elements [43]. For convenience VEC is used more frequently as a concentration parameter for HEAs containing transition metals. VEC of an alloy can be defined as a weighted average from VEC of the constituent elements, as shown by equation 1.14:

$$VEC = \sum_{i=1}^{n} c_i(VEC)_i \tag{1.14}$$

1.3 Empirical criteria of solid solution formation

Guo et al. [36] have analysed numerous alloys from AlCoCrCuFeNi family forming solid solutions (where in particular no intermetallic or amorphous phases exist), where different elements vary in content. Some correlations between VEC and phase formation have been established and presented in a form of graph in Figure 1.7. For VEC $\geq$ 8.0 the only present phase is fcc; in the range of 6.9 $\leq$ VEC $<$ 8.0 the structure is a mix of both fcc and bcc structure and finally under VEC = 6.9, only bcc exists. Those experimental observations lead to some general conclusions that fcc phases are stabilised for higher VEC while bcc phases formation is preferential at lower VEC values. Some exceptions occur from this rule, mostly for alloys containing manganese, but essentially it is a convenient way to design crystalline structure of HEAs containing transition metals. Nevertheless it has to be remembered that the obtained results come from as cast samples and different ways of solidification or cooling rates may move the alloy away from its equilibrium crystalline structure [44]. It is understandable since as cast HEAs may be considered as frozen solid solution from high temperatures [3]. In Guo et al.'s work there has been no distinction between ordered or disordered phases and no indication of a number of created phases.

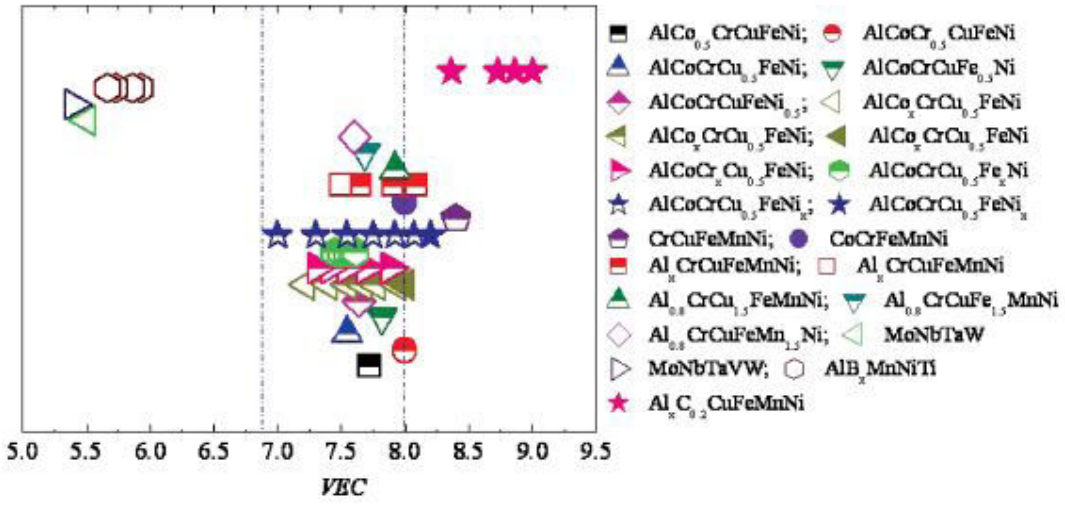

Figure 1.7: *Relationship between VEC and the fcc, bcc phase stability for more HEA systems. Note on the legend: fully closed symbols for sole fcc phases; fully open symbols for sole bcc phase; top-half closed symbols for mixes fcc and bcc phases [36]*

For ease, parameter used for phase formation prediction are presented in Table 1.1 along with their definitions and experimentally determined values for solid solution formation. In recap, critical thresholds for fcc and bcc phases formation have been confirmed for many alloys but must be used as a reference and not strict bounds. They are and empirical indication and not a general rule.

Table 1.1: *Summary of phase formation parameters and their empirically defined values in HEAs*

	Parameter	Definition	Values for solid solution formation	Ref.
1.	δ	$\sqrt{\sum_{i=1}^{n} c_i \left(1 - \frac{r_i}{\bar{r}}\right)^2}$	$\leq 6.6\%$	[30, 31, 35]
2.	ΔS_{mix}	-R$\sum_{i=1}^{n} c_i ln c_i$	$11 \leq \Delta S_{mix} \leq 19.5$ J/K·mol	[32]
3.	ΔH_{mix}	$\sum_{i=1\ i\neq j}^{n} 4\Delta H_{AB}^{mix} c_i c_j$	-11.6 $\leq \Delta H_{mix} \leq$ 3.2 kJ/mol	[31]
4.	Ω	$\frac{T_m \Delta S_{mix}}{\lvert\Delta H_{mix}\rvert}$	≥ 1.1	[35]
5.	$\Delta\chi$	$\sqrt{\sum_{i=1}^{n} c_i \left(\chi_i - \bar{\chi}\right)^2}$	3-6%	[30]
6.	VEC	$\sum_{i=1}^{n} c_i (VEC)_i$	fcc $\geq 8.0\%$ $6.9\% \leq$ fcc + bcc $< 8.0\%$ bcc $<6.9\%$	[36]

1.4 Design of HEAs

The empirical parameters presented in the previous section are not easy to establish and give only an approximate idea of possible phase formation. It is now known that the configurational entropy of mixing is not always the dominant factor, specially with decreasing temperature. Other factors like atomic size difference, enthalpy of mixing and electron configuration need to be taken into consideration in phase formation prediction. Unfortunately, it is still not intuitive as to what crystallographic structure will be obtained for a specific composition. The most instinctive way to represent the phase stability are phase diagrams and it might be the next step in designing new HEAs [8, 45, 46].

Empirical way to obtain phase diagrams are casting and phase identification in high number of alloys. It can be very costly and time consuming, especially if multicomponent systems are to be explored. Thermodynamic calculations used in CALPHAD (CALculation of PHAse Diagrams) method can be a good complementary tool to this empirical technique. It is based on the fundamental thermodynamic law saying that a system reaches its equilibrium when the lowest Gibbs energy at a given composition, temperature and pressure is obtained [47]. An important advantage of CALPHAD method is that it can predict phase diagrams of higher order by extrapolation from lower order systems, such as binary and ternary systems; although the accuracy of extrapolation is highly dependant on input databases. The CALPHAD method requires both a computational software, like Thermo-Calc [48, 49], and thermodynamic databases. The term "thermodynamic databases" refers to an assembly of Gibbs energy parameters for a large number of binary and ternary systems. The latest Thermo-Calc release, the High Entropy

Alloys database TCHEA3 2018, contains almost all binary systems in the 26-element framework, which are assessed to their full range of composition and temperature. In addition, more than 400 ternaries are assessed, and 136 of them to the full range of composition and temperature. Senkov et al. [50] carried out numerous CALPHAD calculations using various thermodynamic databases developed by Another company, CompuTherm. They found that, with increasing number of components the fraction of solid solution phases decreases, while content of solid solutions with intermetallic phases increases, as shown in Figure 1.8. It is an expected outcome due to increased complexity of the system.

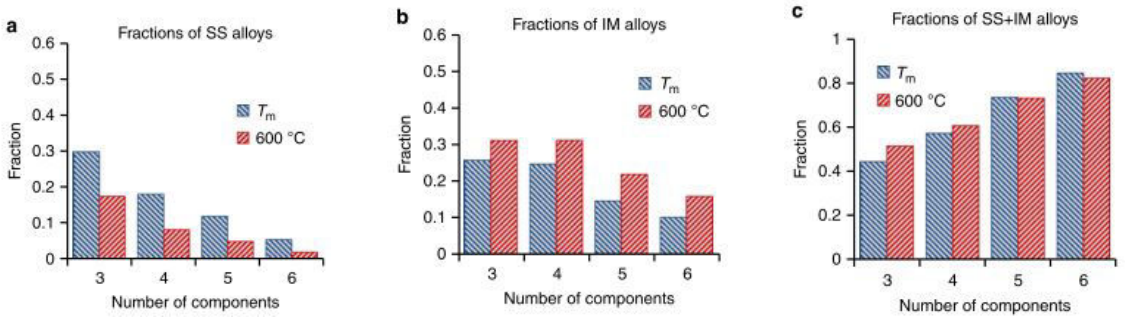

Figure 1.8: *Distribution of multi-principal element alloys by categories. Fractions of a) solid solution phases, b) intermetallic phases, and c) solid solution + intermetallic phases for equimolar alloys from 3 - 6 component systems at solidus temperature (T_m) and 600° C [50]*

It is also in accordance with experimental observations of empirical formation parameters, that despite the elevated entropy of mixing due to increased number of constituent elements, formation of intermetallics is allowed due to lowered enthalpy [3]. General conclusions seam to say that CALPHAD method calculations are capable of producing accurate and reliable phase diagrams as long as the used database is well adapted to the designed system. A credibility parameter is evoked which would consist of fractions of fully thermodynamically assessed systems of lower order. It is considered that calculations are fully credible when the thermodynamic data for all systems are available. Unfortunately for N-component alloys with N $>$ 3, it is impossible to possess all systems embedded in the database and so the CALPHAD predictions should not be overestimated and considered cautiously when extrapolating the compositions to the centre of a multicomponent phase diagram.

Another approach to design of alloys was proposed by Tancret et al. [51]. They combine all the previously proposed empirical parameters through a statistical analysis of existing highly concentrated multicomponent alloys using Gaussian processes. Several probability functions are defined based on the chance of a parameter value to result in a solid solution. The reliability of predictions is increased by integrating computational thermodynamics (Thermo-Calc) and its databases to the process. In this work only single phased alloys are considered as HEAs and so the method was verified on over 300 alloys from the literature. More than 60 equiatomic alloys were successfully proposed by the method to be single phased.

1.5 Various HEA families for various applications

There have been more than 400 complex, concentrated alloys reported in literature. They can be divided into seven families: 3d transition metal alloys, refractory metal alloys, light metal alloys, lanthanide (4f) transition metal alloys, brasses and bronzes, precious metal alloys and interstitial compound (boride, carbide and nitride) alloys [6].

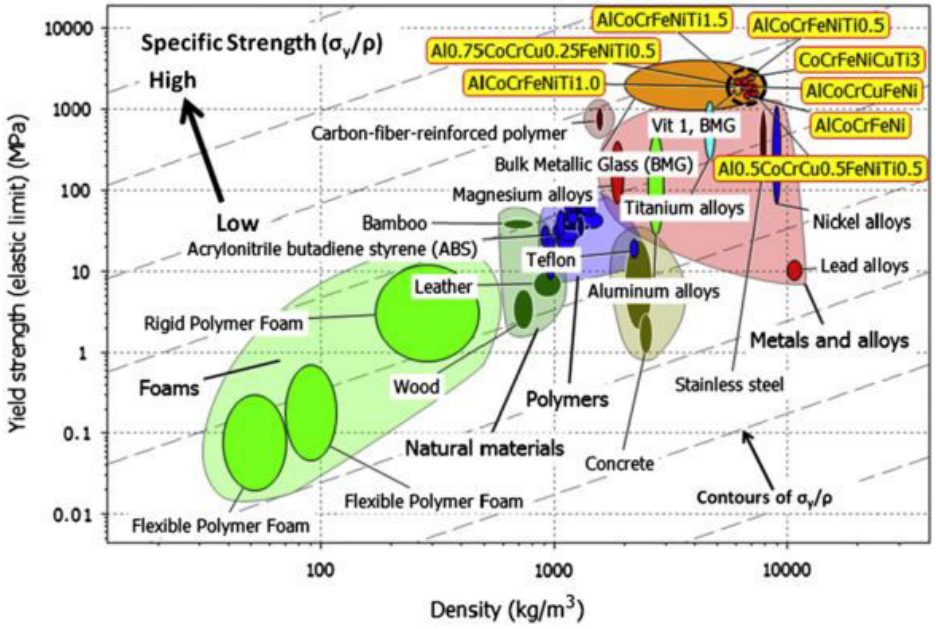

Figure 1.9: *Yield strength, σ_y, vs density, ρ. HEAs in dark dashed circle. Grey dashed contours (arrow indication) label the specific strength, σ_y/ρ , from low (right bottom) to high (left top) [8]*

Most widely studied family contains **3d transition metals** and more precisely at least four out of the following: Co, Cr, Cu, Fe, Mn, Ni, with occasional additions of Al. Among others, the "Cantor's alloy", the first reported HEA and a prototypical single phase disordered solid solution alloy, belongs in that family. This family of HEAs can be considered as an extension of stainless steels and superalloys who all have Fe-Cr-Ni as base and in which, cobalt is sometimes present. Austenitic stainless steels often have high amounts of Mn and smaller additions of Al, Ti, Nb for precipitation hardening or increased oxidation resistance. Nickel alloys have Mo as one of the principal elements and some additions of Co, Fe, Al or Ti. Finally nickel superalloys are already part of complex concentrated alloys with Ni-Co-Cr-Fe-Mo as base and additions of Al, Nb, Ti to form significant volume fraction of hardening intermetallic phases. This extension is clearly visible on the Ashby plot of yield strength as a function of density (Figure 1.9). Newly developed alloys position themselves slightly above stainless steels and nickel alloys. They are characterised by good mechanical resistance combined with good ductility if the alloy is single fcc phased and further increased strength if γ' phase is present which could lead

to substitution of some steels, especially working at extreme temperatures (from cryogenic to 0.5 - 0.7 T_m). Cantor's family and its variations will be described in more detail in section 1.6.

Second biggest group of HEAs are the **refractory metal alloys**. They contain at least four out of following elements: Cr, Hf, Mo, Nb, Ta, Ti, V, W, Zr and very often an addition of Al. These compositions were imagined to serve in the industry fields where high strength and phase stability at elevated temperatures are most valuable, for example the aerospace industry. Potential application may include thermal protection sheets or even turbine blades and disks if other problematic aspects, like corrosion or brittleness are solved. It might be the first HEA family with a specific purpose and particular requirements to compete with nickel superalloys. To be able to achieve this purpose, the alloys they need to be lighter and more oxidation resistant than what could have been reached until now. The refractory HEAs might increase the operating stress or the operating temperature, or both. Designed alloys are usually based on one of the following groups of elements: Mo-Nb-Ta-W, Hf-Nb-Ta-Zr, Cr-Mo-Nb-Ta or Cr-Nb-V-Zr. They can contain non-refractory elements, like Al or Si, to decrease the total density [6, 29, 52–60]. Mechanical properties in this family of alloys can vary significantly. Vickers hardness can be considered as an example, where for $NbTiV_2Zr$ it is of the order of 3 GPa [53] and for $AlMo_{0.5}NbTa_{0.5}TiZr$ it goes up to 5.8 GPa [55]. Looking at the compressive yield stress, σ_y, they are also some exceptional materials. It is usual for curently used materials, like $Haynes^{®}$ 230®, $INCONEL^{®}$ 718 and MAR-M 247®, to present a significant drop in σ_y around 1000 K, but some newly developed refractory HEAs can overcome this limitation. In Figure 1.10 compressive yield stresses in function of temperature for various compositions are presented.

Two alloys stand out: MoNbTaW and MoNbTaVW retain useful strength of nearly 400 MPa up to about 2000 K. If we consider the normalised yield stress, σ_y/ρ, those two alloys easily fulfill the conditions imposed to thermal protection sheets and could compete in this area with the $Haynes^{®}$ 230® alloy (Figure 1.10). Even though the result is impressive and highly promising, one has to bear in mind that these are compressive results and very little is known about the tensile behaviour of these materials. They have been shown to undergo brittle to ductile transition between room temperature (RT) and $600°C$ in addition to elevated densities, 13.75 and 12.36 g/cm^3 respectively. At the same time nearly no information is available about the oxidation resistance of those compositions and the little tests done show rather poor corrosion behaviour. These, nevertheless optimistic results, lead to design of refractory alloys with lower densities, by addition of elements like Al and/or Si (ρ between 5.59 g/cm^3 and 8.0 g/cm^3). Here again one of the compositions stands out among the others with highest RT σ_y and σ_y/ρ measured to

date, accompanied by 10% ductility in compressive RT, and density of 7.40 g/cm^3. Its composition is $AlMo_{0.5}NbTa_{0.5}TiZr$ [61] and appears as the fist HEA able to compete with $INCONEL^{®}$ 718 and MAR-M 247® as a material for turbine blades and disks (Figure 1.10).

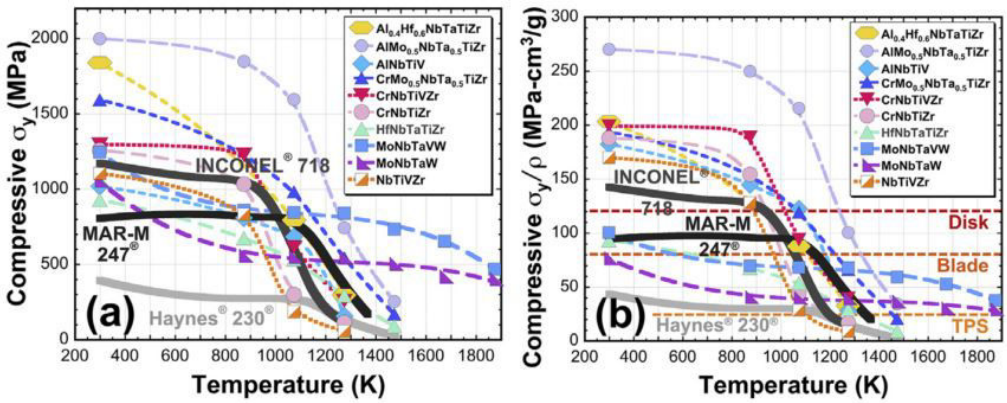

Figure 1.10: *Temperature dependence of a) compressive yield strength, σ_y, and b) σ_y normalized by alloy density, ρ, of refractory concentrated, complex alloys. Initial strain rates, $\dot{\epsilon}$, range from $2 \cdot 10^{-4}$ to 10^{-3} s^{-1}. Data are taken from Refs. [29, 52–57]. Tensile σ_y for commercial superalloys (Haynes® 230®, $INCONEL^{®}$ 718 and MAR-M 247®) are shown for reference. Typical σ_y/ρ requirements for thermal protection sheet (TPS), turbine blades and disks are shown in b) [6]*

The microstructure of $AlMo_{0.5}NbTa_{0.5}TiZr$ is composed of bcc cuboids roughly 50 nm on a side surrounded by B2 ordered nano-lamellae parallel to the cuboid faces (Figure 1.11) [61, 62]. Chemical analyses show that the ordered phase is enriched in Al, Ti and Zr, whereas the disordered bcc solid solution richer in Mo, Nb and Ta. This microstructure resembles visually the known and currently used Ni-based superalloys which have high fraction of $L1_2$ ordered γ' phase in form of cubes embedded in the fcc γ matrix. Unfortunately the reversed structural composition questions the possibility of tensile deformation in this alloy, since the matrix is the brittle phase.

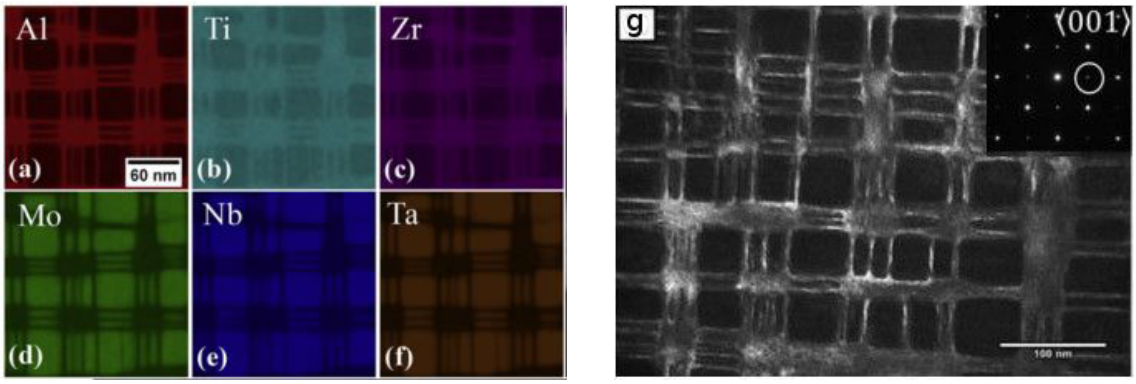

Figure 1.11: *(a–f) XEDS elemental-maps of Al, Ti, Zr, Mo, Nb, and Ta, respectively, recorded in STEMusing the Super-X™detector, g) Dark-field TEM micrograph of the nano-phase structure of $AlMo_{0.5}NbTa_{0.5}TiZr$; and respective selected area diffraction pattern. The dark field image was obtained with a (001) respective selected area diffraction pattern. The dark field image was obtained with a (001) superlattice reflection placed inside the objective aperture (indicated by the circle) [61]*

Unfortunately, for the time being direct comparison between newly developed HEAs and currently used alloys proves to be quite difficult. Principally, because all the HEA data presented in this graph come from compression tests and no information about tensile behaviour is provided contrarily to Haynes or Inconel alloys. Furthermore, superalloys have various other properties that have been optimised and adapted according to the application, for example fracture toughness, oxidation resistance, creep strength, fatigue strength and processibility. None of the above have been yet verified for refractory HEAs, pointing the future direction of development.

Other HEA families were imagined as possible solutions for various applications. The industry being in constant search for high strength light materials motivated the development of new structural alloys with low density, mostly for aerospace and transportation. They are composed of Al, Be, Li, Mg, Sc, Si, Sn, Ti and Zn [63–65]. Processing of those alloys proves to be complicated due to wide range of elements' melting and boiling point. Careful choice of master alloys and mechanical alloying via powder route are necessary in their primary processing.

Family containing **lanthanide (4f) elements** Dy, Gd, Lu, Tb, Tm and Y were motivated mainly by scientific curiosity. The aim is to obtain single phased, solid solution HEAs with hcp crystal structure [12]. Two alloys researched up to now are DyGdLuTbY and DyGdLuTbTm.

Purpose behind research on **HEA bronzes and brasses** is to expand their already broad range reaching for higher strength via concentrated solid solutions [66]. They are composed of: Cu, Sn, Zn with addition of Al, Mn, Ni. For now equiatomic substitution was made so the compositions present themselves as follows: $\mathrm{Al}_x\mathrm{Sn}_y\mathrm{Zn}_z[\mathrm{CuMnNi}]_{(1-x-y-z)}$.

Another recently developed family of HEAs is based on **precious metals** for catalysis applications [6]. They contain at least four of the following elements: Ag, Au, Co, Cr, Cu, Ni, Pd, Pt, Rh and Ru. An early analysis of phase diagrams allowed to identify a single-phased hcp MoPdRhRu alloy [6].

Last but not least come the **HEAs containing B, C or N**. They are mostly based on 3d transition metals; yet they were separated as a distinct group due to the dramatic effect of alloying interstitial elements on the phases and microstructures as well as properties, but also because this group of alloys is usually processed under the form of thin films. Largest number of publications refer to HEA nitrides [13, 67, 68], followed by limited reports on carbides [13, 69] and borides [70]. An example of notable properties comes from Tsai et al. [68] who developed a 70 nm thick film of $(\mathrm{AlMoNbSiTaTiVZr})_{50}\mathrm{N}_{50}$, which has an amorphous structure and is an efficient diffusion barrier. Its belonging to the HEAs is questionable due to amorphous phase; nevertheless, it successfully prevents copper and silicon to react during annealing at

850°C for 30 min. The amorphous structure remained stable even after exposure to temperature. Its stability is attributed to large lattice distortion and limited diffusion.

Numerous elements included in various HEA families give plenty of possibilities for future applications. There is always a high demand for materials with improved properties. First of all structural properties that will allow more efficient, economical and ecological design, say in transportation or aeronautical industries. Vast field of HEAs gives also possibilities for more functional applications regarding such properties like: thermal, electrical, magnetic, mechanical and structural response to irradiation, shape memory response, but also reduced thermal conductivity for diffusion barriers applications, as well as hydrogen storage or catalyst [6, 7]. The research on new compositions is far from being finished.

1.6 The CoCrFeMnNi family of HEAs

Research on multicomponent alloys begun in 1981 with work of Cantor and his undergraduate student Alain Vincent, where different equiatomic compositions formed by up to 20 elements were analysed [71]. In frame of this work the quinary, single fcc phased $Co_{20}Cr_{20}Fr_{20}Mn_{20}Ni_{20}$ was discovered. The work was followed by another student, Peter Knight, who performed similar studies with a wider range of compositions. He came to alike conclusions. Unfortunately none of these research was published apart from master theses at their respective Universities in Sussex and Oxford. The topic was put aside and later undertaken again by another student, Isaac Chang, who deepened it further by new tests. This time the results were published in *Materials Science and Engineering A* in July 2004 [4]. This publication is considered by many as the starting point of High Entropy Alloys. The paper focuses on two multielement compositions that lead to discovery of the single phased quinary alloy. The two compositions are an alloy containing 20 elements at 5 at.% concentration each (i.e. Mn, Cr, Fe, Co, Ni, Cu, Ag, W, Mo, Nb, Al, Cd, Sn, Pb, Bi, Zn, Ge, Si, Sb and Mg) and an alloy containing 16 elements at 6.25 at.% (i.e. Mn, Cr, Fe, Co, Ni, Cu, Ag, W, Mo, Nb, Al, Cd, Sn, Pb, Zn and Mg). The first conclusion was that both alloys are multiphase, crystalline and brittle no matter the casting conditions (induction melting or rapid solidification by melt spinning). The surprise was hidden in the distribution of present phases. The alloy consisted predominantly of a single fcc primary phase particularly rich in transition elements: Cr, Mn, Fe, Co and Ni. This led to casting of a quinary $Co_{20}Cr_{20}Fr_{20}Mn_{20}Ni_{20}$ which proved to be single fcc phased and presented a typical dendritic structure in as cast state as shown in Figure 1.12.

Based on this composition some six- to nine-element compositions were cast choos-

ing out of the following: Cu, Ti, Nb, V, W, Mo, Ta and Ge. In all the alloys dendritic zones were vastly fcc single phased with high concentration of other transition metals (Nb, Ti and V). On the other hand, elements with higher electronegativity (Cu and Ge) were mostly rejected to the interdendritic regions. Nevertheless the final conclusion was that the total number of phases is significantly lower than maximum number allowed by the Gibbs phase rule (Eq.1.5).

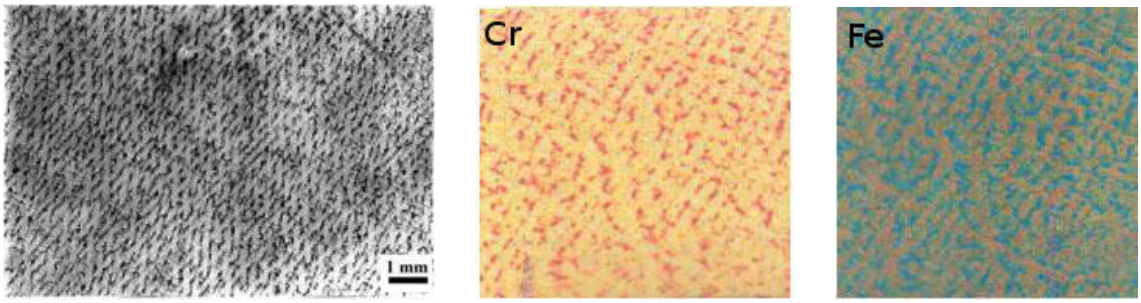

Figure 1.12: *Optical micrograph of etched $Co_{20}Cr_{20}Fe_{20}Mn_{20}Ni_{20}$ [4]; SEM X-ray maps showing Cr and Fe distribution in as-solidified cored dendritic structure in chill cast single phase fcc $Co_{20}Cr_{20}Fe_{20}Mn_{20}Ni_{20}$ [71]*

The quinary CoCrFeMnNi composition has been reported to be monophased by many other authors [18, 22, 23, 72–85], to cite a few. The microstructure presented by Cantor [71] and his students is a representative image of as cast alloy. In their publication, Gali and George [73] show microstructures for CoCrFeMnNi and CoCrFeNi after casting and homogenisation, as well as after hot rolling (Figure 1.13). It is easily seen that after homogenisation the grain approaches the equiaxed form. Hot deformation leads to appearance of a high number of deformation twins. Other studies reported the presence of annealing twins in case of material deformed and heat treated [20, 74]. These phenomena are observed by all authors researching this family of composition so the presented microstructures can be treated as representative for most studies on annealed massive materials.

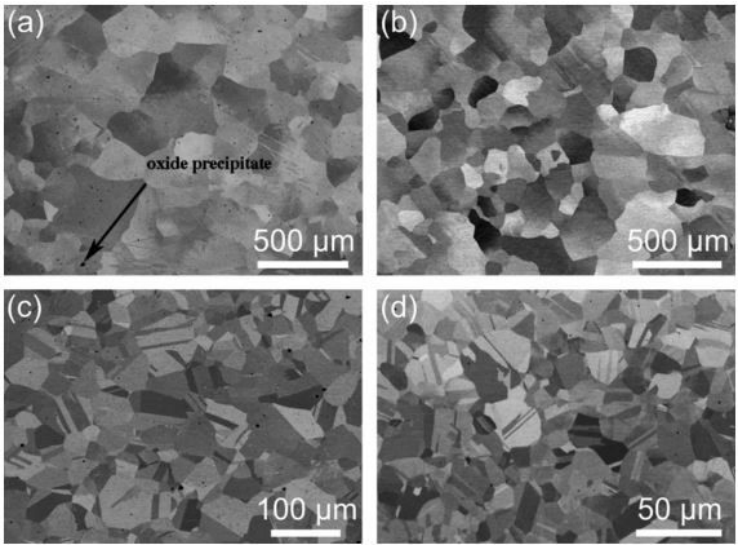

Figure 1.13: *Backscattered electron images of a) CoCrFeMnNi b) CoCrFeNi after casting and homogenization, and c) CoCrFeMnNi, d) CoCrFeNi after hot rolling. [73]*

1.6.1 Mechanical properties

First reports of mechanical behaviour of Cantor's alloy proved it to be an unusual material. First, unexpected tensile behaviour was observed in this alloy in a wide range of temperatures by Otto et al. [72]. Tensile tests were performed on dog bone shaped samples with fully recrystallised microstructure (various grain size). The stress-strain curves are presented in Figure 1.14a for two different grain sizes: 4,4 μm and 155 μm. The influence of temperature on alloy's strength is easy to notice in these graphs. With decreasing test temperature both the yield stress, σ_y, and the ultimate tensile stress, σ_u, increase, which is a typical behaviour for an austenitic material. The surprising part is the increasing elongation to fracture, ϵ_f, accompanying the elevated strength at low temperatures. There is no compromise between strength and ductility like currently observed in classical materials. In Figure 1.14d ϵ_f is depicted as a function of temperature. For medium (50 μm) and coarse (155 μm) grained alloy after a big drop between liquid nitrogen and room temperatures elongation stabilises forming a plateau up to 673 K, after which another significant drop is visible. On the contrary the $\epsilon_f(T)$ curve for fine grain material presents a minimum at intermediate temperatures. Authors have also observed yield point phenomenon between 77 K and 473 K for the fine grain material. Similar behaviour was observed by Jang et al. but this time in a coarse grain material at elevated temperatures (900°C - 1100°C) [75]. Authors suggest that the phenomenon is due to dynamic recrystallisation (local decrease of grain size) or to dislocation pinning and breakaway mechanism caused by short-range ordering or short-range clustering. Further study of yield point formation is needed to determine the influence of both grain size and temperature. Grain size influence is also visible on the $\sigma_y(T)$ curve, Figure 1.14c. For all the temperatures up to 873 K, yield stress is increased for samples with smaller grain size (at 873 K for fine grain material σ_y is nearly 3 times higher than for the coarse grain material). Above this temperature there is no significant change in σ_y for medium and coarse grain materials while a substantial drop of almost 50 % is observed for the fine grain material. Dynamic recrystallisation may play a major role in this case, but microstructural evolution will be addressed later on in this chapter.

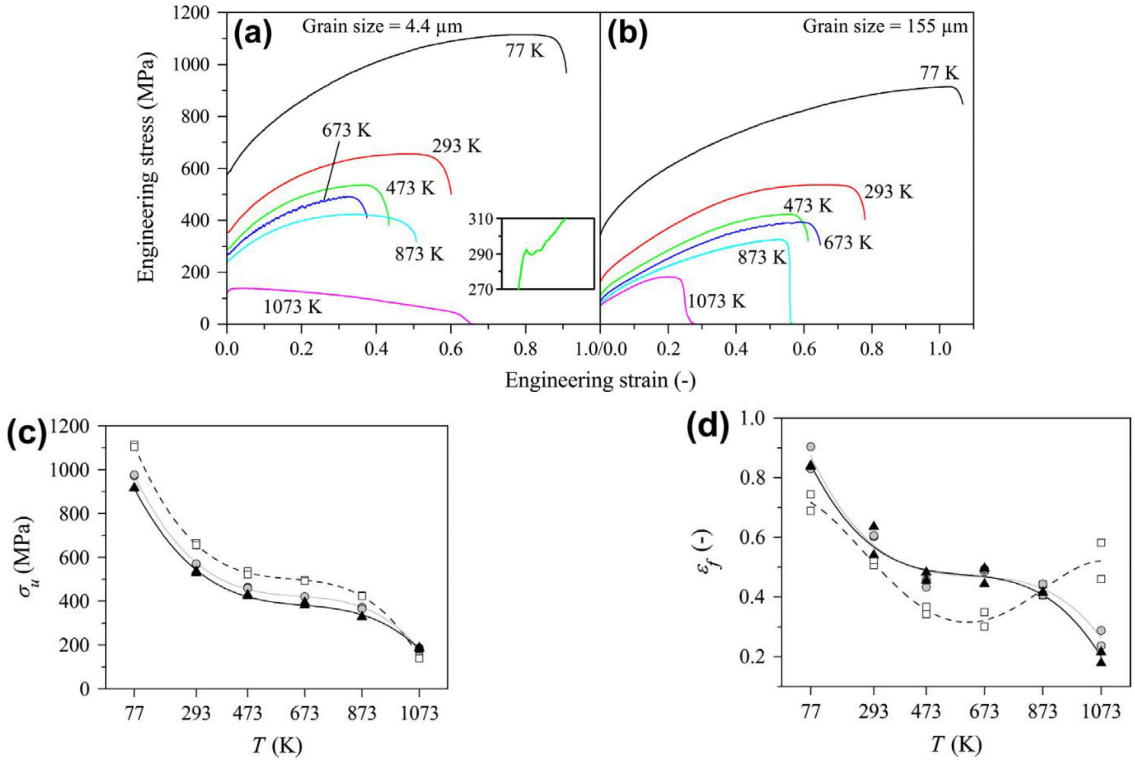

Figure 1.14: *Representative engineering stress–strain curves of the CoCrFeMnNi alloy at the six testing temperatures for the a) fine-grained (grain size 4.4 µm) and b) coarse-grained (grain size 155 µm) materials. The inset in a) shows a small load drop after yielding for a fine-grained sample that was tested at 473 K; Temperature and grain size dependence of c) 0.2 % offset yield stress (σ_y) and d) elongation to fracture (ϵ_f) for the CoCrFeMnNi alloy [72]*

It is typical for alloys to show grains size dependence, where with decreasing grain size the yield stress, σ_y, and ultimate stress, σ_u, increase. Classical Hall-Petch relation, $\sigma = \sigma_0 + \frac{k_{HP}}{\sqrt{d}}$, depicts this behaviour observed in most alloys. It can also be presented as a relation between grain size and hardness: $H = H_0 + \frac{k_{HP}}{\sqrt{d}}$. Under such a form it was verified for the Cantor's alloy. The results are presented in Figure 1.15.

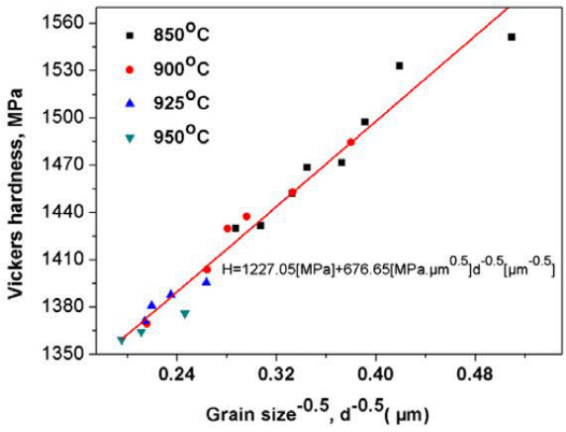

Figure 1.15: *Hall-Petch relation based on hardness measurements presented as a function of grain size in the CoCrFeMnNi alloy [18]. Indicated temperatures correspond to annealing temperatures.*

Diverse grain sizes (from 4.0 μm to 26 μm) were obtained upon annealings at different temperatures and for various times after cold rolling. Vickers hardness values vary roughly from 1360 MPa to 1550 MPa as a function of grain size. The authors have come to conclusion that the Hall-Petch coefficient k_{HP} = 677 MPa $\mu m^{-0.5}$ is above the upper bound for fcc metals (600 MPa $\mu m^{-0.5}$). It suggests that the hardening by grain boundary is more efficient in the CoCrFeMnNi, promoting the lattice distortion effect hypothesis [18].

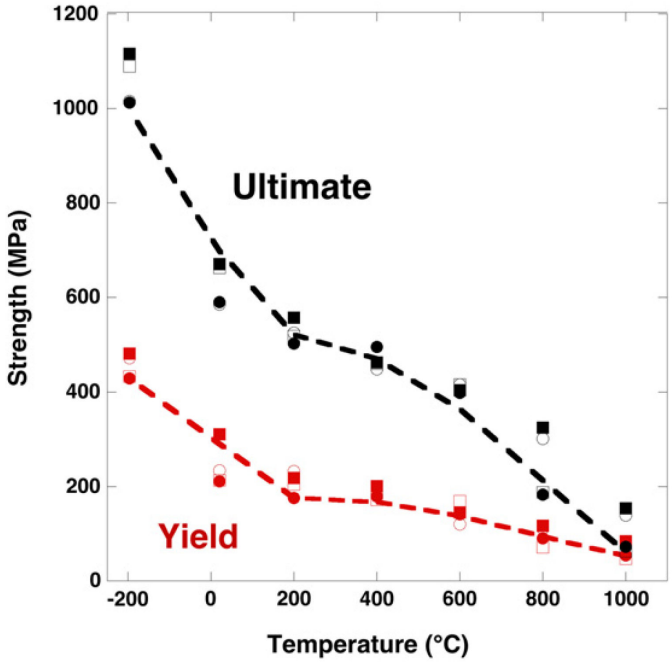

Figure 1.16: *Comparison of the temperature dependencies of the ultimate tensile strength and yield strength. The circles represent the CoCrFeMnNi alloy and the squares the CoCrFeNi; for each, the filled symbols are for 10^{-3} s^{-1} strain rate and the open symbols for 10^{-1} s^{-1}, one dashed curve is drawn (as a guide to the eye) through each data set [73]*

A different study of tensile properties of alloys from Cantor's family was done by Gali and George [73]. They have not only verified the temperature dependence of yield and ultimate stress but also the influence of the strain rate for two various compositions: the quinary CoCrFeMnNi and quaternary CoCrFeNi. Data summarising the paper are presented in Figure 1.16 where σ_y and σ_u values are presented for both alloys at two various strain rates as a function of temperature. The conclusions they have reached are strong temperature dependence and weak strain rate dependence. For higher strain rate both alloys exhibit somewhat higher strengths, specially at temperatures < 600°C. The temperature dependence of yield strength as presented is not usually observed in pure fcc alloys. The athermal part of the curve at medium temperatures is usually much larger, on the contrary to bcc metals. It is believed that barriers to dislocation motion are weak and easily overcome by thermal activation even at cryogenic temperatures. Such thermal behaviour was observed in binary fcc alloys (for example Cu-Zn binaries [86]). Extension of the

thermal region to relatively low temperatures (about 200°C) in the HEAs implies a presence of rather strong obstacles to dislocation motion.

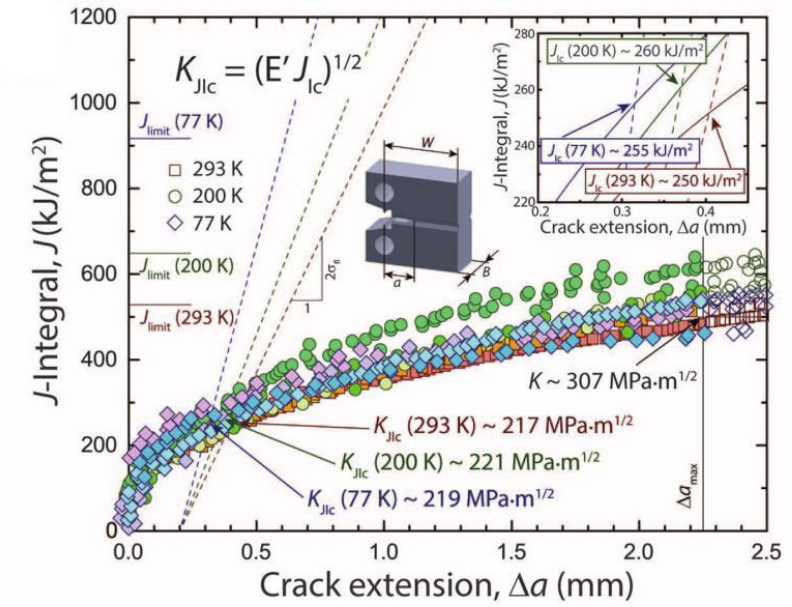

Figure 1.17: *Fracture toughness measurements show K_{JIc} values of 217 MPa·m$^{1/2}$, 221 MPa·m$^{1/2}$, and 219 MPa·m$^{1/2}$ at 293 K, 200 K, and 77 K, respectively, and an increasing fracture resistance in terms of the J integral as a function of crack extension Δa (i.e., resistance curve (R curve) behaviour) [74]*

Measurements of fracture toughness of CoCrFeMnNi were performed as well. Authors have performed crack-resistance curve (R curve) measurements in terms of J integral (Figure 1.17) on cold rolled and recrystallised material (equiatomic CoCrFeMnNi). The specificity of this kind of test is that J integral characterises the stress and displacement fields in the vicinity of the crack tip for a non-linear elastic solid (both plastic and elastic contributions are measured). K values can be back-calculated from J if the test conditions are respected. As indicated before, Cantor's alloy is characterised by significantly increased strength at low temperatures, however Gludovatz et al. came to conclusion that K_{JIc} remains relatively constant for all three temperatures 77 K, 200 K and 293 K, with values 219 MPa·m$^{1/2}$, 221 MPa·m$^{1/2}$ and 217 MPa·m$^{1/2}$ respectively. With a crack extension reaching 2 mm, crack growth toughness exceeds 300 MPa·m$^{1/2}$. Such values are more than satisfyingly comparable with fracture toughness values for austenitic steels (304L, 316L) and best cryogenic steels (5Ni, 9Ni) whose K varies between 100 and 400 MPa·m$^{1/2}$. The difference in favour of HEA is that with decreasing temperature the K value is constant, whereas for steels it decreases. Compared to numerous other materials there exist some that are stronger in respect to yield strength, but according to the authors, the toughness of this HEA exceeds all pure metals and metallic alloys. Also, such high levels of fracture toughness for Cantor's alloy suggests a mode of plastic deformation allowing a steady degree of strain rate hardening. Deformation mechanisms will be approached in the section 1.6.2.

Using Cantor's alloy as the model alloy though requires a deeper characterisation of basic properties: elastic constants, mechanisms of deformation or recrystallisation. At the beginning let's aboard the elastic constants as their temperature dependence might contribute to the observed temperature dependence of strength. First calculations on CoCrFeMnNi system were performed by Zaddach et al. [87] in 2013. The authors have combined some experimental results and first-principle electronic structure methods. Elastic constants were calculated using density functional theory (DFT) at 0 K by implementing the XRD measurements of lattice parameter, dislocation density, grain size, twin fault probability and stacking fault probability. The obtained values for Young modulus, shear modulus, bulk modulus and Poisson ratio are 207 GPa, 86 GPa, 117 GPa and 0,204 respectively. Those values were later compared to some experimental data obtained by Haglund et al. [88], by Laplanche et al. [89] in 2015 and Okamoto et al. [77] in 2016. The elastic moduli were measured by resonant ultrasound spectroscopy in the temperature range 50 - 300 K [88], 200 - 1000 K [89] an at room temperature [77]. Room temperature values for all three research groups were very similar, so just Laplanche's results are given here. For Young and shear modulus empirical temperature dependencies have been determined and the relationships have also been shown in Table 1.2.

Table 1.2: *Calculated [87] and empirical [89] elastic constants at room temperature and their empirical definitions as temperature dependencies [89].*

Elastic constant	RT value [GPa]		Empirical equation [GPa]
	[87]	[89]	[89]
Young's modulus, E	207	203	$E = 214 - 35/(e^{416/T} - 1)$
Shear modulus, μ	86	81	$\mu = 85 - 16/(e^{448/T} - 1)$
Bulk modulus, K	117	137	
Poisson's ratio, ν	0.204	0,25	

Compared to the DFT calculation those values are reasonably alike, although lower than experimental tendency predicts for 0 K. In Figure 1.18 temperature dependencies of Young's modulus E and shear modulus μ were plotted for two studies [88, 89] in a very wide range of temperatures (between 55 K and 1000 K). Good correspondence of both curves is to be noted. The observed trends are monotonic decrease with increasing temperature with a faster drop towards higher T. Similar behaviour is observed for paramagnetic materials where no phase transformation occurs. It can be concluded that evolution of Young's modulus as a function of temperature of the CoCrFeMnNi does not differ from other metals or alloys.

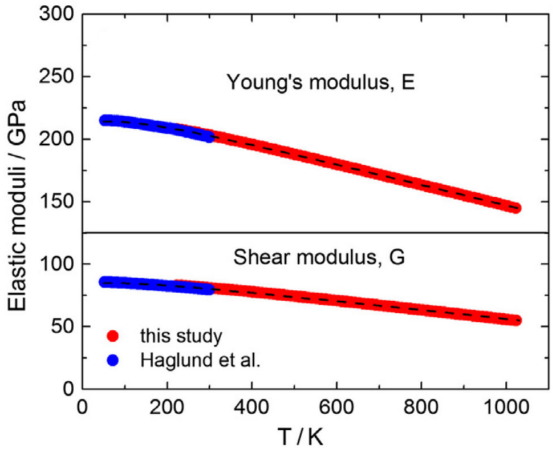

Figure 1.18: *Corrected E and G measured in the study of Laplanche et al [89] between 200 and 1000 K (red curve) together with measurements between 55 and 300 K (blue curve) reported by Haglund et al. [88]*

This overview of basic mechanical properties of quinary CoCrFeMnNi shows high potential of high entropy alloys and most importantly, is the source of motivation for understanding the mechanisms being the source of properties to be able to optimise them in hope of future applications. Cantor's alloy stays a single phased alloy whose characteristics can still be enhanced in many ways, some of which will be presented further in this chapter. Despite it being far from the optimised composition the equiatomic CoCrFeMnNi became the most studied alloy treated as a reference for 3d transition HEAs. Most of fundamental research for transition elements high entropy alloys is still done on Cantor's alloy.

1.6.2 Hardening mechanisms

To understand the exceptional properties of Cantor's alloy and compositions belonging to the same family various tests have been performed on both CoCrFeMnNi and alloys from systems of lower order (containing fewer elements) to define the mechanisms of deformation.

As first approximation it can be presumed that fcc HEAs behave like solute-strengthened dilute fcc alloys. There are three main contributions to strengthening in such systems: 1. a grain-size-dependent Hall-Petch strengthening (σ_{HP} with length scale equal to d, average grain size); 2. solid solution strengthening in the random alloy (σ_{ss} with length scale $\zeta_c \sim 10$ nm, where ζ_c is the wavelength of a dislocation in a random alloy); 3. dislocation-dislocation interactions in the form of forest hardening (σ_f with length scale $l = 1/\sqrt{\rho}$, inversely proportional to the dislocation density). The scales at which those contributions operate are very different: $d \gg l \gg \zeta_c$ and so it can be assumed that their effects are additive. Activation volume can give us information about which of these mechanisms is operational and dominant as it reveals length scale at which the plastic deformation occurs.

First attempts at measuring the activation volume V, were performed by Wu et al. [80] by strain rate jumps during tensile tests. The authors have obtained values for the CoCrFeMnNi alloy ranging between 20 - 80 b^3 for temperatures from 77 K to 293 K, which is much smaller compared for example to pure Ni or NiCo with V > 300 b^3. They suggest that short range effects like lattice distortion, reduced stacking fault energy or short-range ordering have greater impact on the deformation mode. Moreover the lack of dependence of activation volume on plastic strain has been reported in this study, which is highly unusual for fcc metals. Similar conclusions were drawn from the strain rate jump tests performed by Hong et al. [90]. The activation volumes were calculated at the order of 10 - 10^2 b^3 for T > 300 K; they are more comparable to bcc materials than what can be seen in fcc metals ($10^2 \sim 10^3$ b^3). Contrarily to Wu et al., Hong et al. reported increase of activation volume with plastic strain. It is again a deeply unexpected result. High friction stress for dislocation motion was attributed to presence of nanoscale inhomogeneities for example short range order. Unfortunately in both those studies big underestimations were hypothesised in latest paper by Laplanche et al. [22]. The authors suggest that strain rate jumps of only one order of magnitude performed in previous studies are not reliable to characterise fcc metals, specially that Cantor's alloy have already been reported as insensitive to deformation strain rate in this range [22, 73]. Furthermore the choice of $\sqrt{3}$ factor as a conversion between normal and shear stress seams inappropriate in Wu's et al. study [80] since they performed uniaxial tensile tests. This choice leads to additional underestimation by a factor 1,7 of the activation volume. To support their comments, Laplanche et al. [22] have performed their proper activation volume measurements using the repeated load relaxation method [91]. Their results are presented in Figure 1.19.

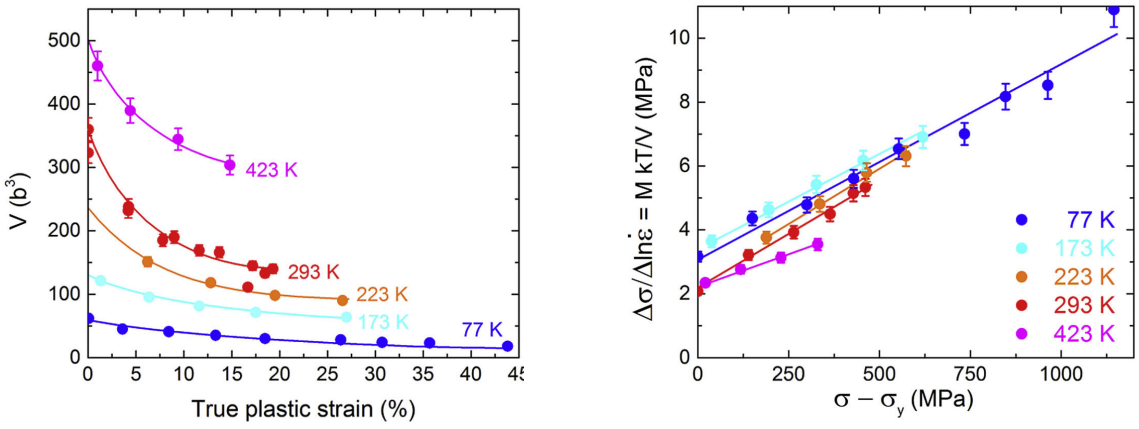

(a) **(b)**

Figure 1.19: *a)Physical activation volume, obtained at different temperatures, as a function of the true plastic strain; b) "Haasen plot", M k T/V versus the offset flow stress $\sigma - \sigma_y$. showing a positive offset at zero indicative of solute strengthening and linear increase with stress indicative of forest hardening [22]*

First of all, Figure 1.19a shows the evolution of physical activation volume as a function of true plastic strain for different temperatures. It is easily observed that V decreases with increasing strain. Upon straining the dislocation density increases leading to decreased dislocation spacing ($l = 1/\sqrt{\rho}$) which is a physical explanation of lowered V. Secondly the values of activation volume at yielding (true plastic stress ≈ 0) can be considered as an indication of interactions dislocation - solutes due to relatively low dislocation density at the initial state ($\rho = 3.2 \cdot 10^{12}$ m^{-2}). Values vary from about 460 b^3 at room temperature to 60 b^3 at liquid nitrogen. So finally the influence of temperature can be seen. With increasing T activation volume value increases. It is in agreement with dislocation creation and stability in function of temperature (higher T leads to lower ρ increasing the activation volume). Thereafter the authors have plotted the data in the form of so-called Haasen plot depicting MkT/V as a function of plastic stress, Figure 1.19b. Positive intercept of this plot is associated with solute strengthening and its slope with forest hardening. There is no clear temperature dependence nor does the mechanism of deformation influence the activation volume (continuous linear trend). In particular, authors suggest that twinning activated during deformation has no influence on V as the twin size is much bigger than spacing between dislocations [92]. Final conclusion of this study are that dominant deformation mechanisms in CoCrFeMnNi is the same as those found in other known fcc materials despite the high atomic complexity of the high entropy alloy. The plastic flow is controlled by a combination of three mechanisms: 1. rate-independent Hall-Petch strengthening, not analysed at this level of study; 2. thermally activated solid solution strengthening; 3. forest hardening that evolves with plastic strain.

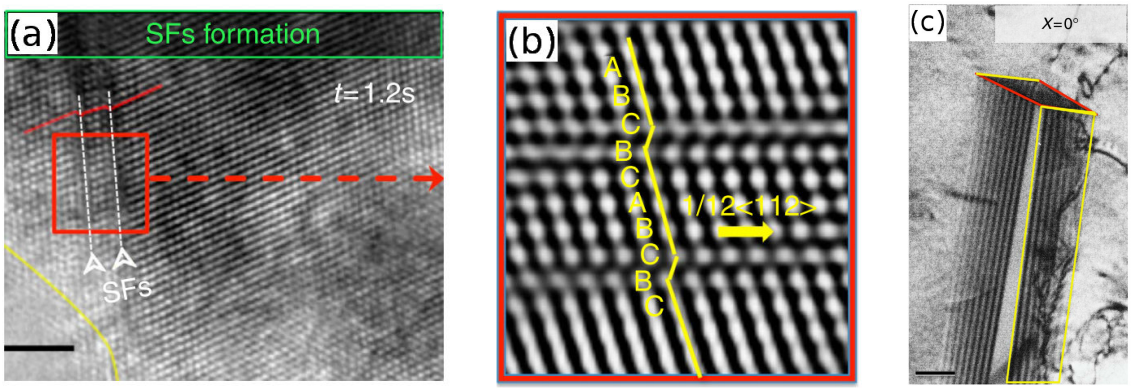

Figure 1.20: *a)High-resolution TEM image captured from the in situ high-resolution TEM movie (scale bar, 2 nm). The formation of multiple SFs at the crack tip (bottom left-hand corner) was observed at the atomic scale; b) is the magnified inverse fast Fourier transform image showing the atomic structure and stacking sequence (marked in yellow) of the SFs, surrounded by the red box in a); c) TEM image of the stacking-fault parallelepiped structure (with faces lying on three sets of {111} planes, scale bar equals 500nm) [78]*

Dominant mechanisms during various stages of deformation were analysed and described in different publications [76–78, 82]. At the early stages of deformation

the glide of 1/2<110> dislocations dissociated into two 1/6<112> Shockley partials on {111} planes is prominent accompanied by stacking fault (SF) formation. In situ observations by Okamoto et al. [77] showed numerous nucleations and annihilations of SFs playing a critical role in accommodating the strain at the beginning of plastic deformation. Moreover, interactions between partials form additional obstacles for dislocations resulting in further hardening. After activation of slip on multiple {111} planes three-dimensional obstacles appear with the form of "stacking fault parallelepipeds" as shown in Figure 1.20c. Dislocations are prompt to block on those volume defects. In this study partial dislocations move with ease; on the other hand the movement of perfect dislocations (undissociated 1/2 ⟨110⟩ type) is rather segmented with low velocity. It was shown that they need to overcome continuous activation barriers, possibly due to high friction stress: as a consequence, they move in localised bands and lead to planar slip. Same mode of deformation was determined as the dominant mechanism in Cantor's alloy by Patriarca at al. [82]. The authors have observed the band formation during compression of CoCrFeMnNi $[5\bar{9}1]$ oriented single crystals. They have found the presence of two slip systems: primary $[01\bar{1}](\bar{1}11)$ with Schmid factor 0,50 and secondary $[0\bar{1}\bar{1}](1\bar{1}1)$ with Schmid factor 0,44. They have concluded that slip is the dominant mechanism of deformation even at 77K. In general strong and complex interactions between dislocations were observed in CoCrFeMnNi HEA. They are considered as an important intrinsic strengthening mechanism. Another essential source of internal reinforcement are solute atoms and the interaction energy on individual dislocation. If energetically favourable, the dislocations can attract the randomly distributed solutes leading to local fluctuations in their concentration.

HEAs are complex alloys in which distinction between principal and solute atoms does not have a physical sense. Varvenne et al. [23] propose in their model of solution strengthening mechanisms to create an average matrix around a specific solute atom. It would contain average properties of the true alloy like lattice constant a, elastic constants $\{C_{ij}\}$ including shear modulus μ and Poisson's ratio ν as well as stacking faults based on average composition. The regularised matrix does not exclude formation of local fluctuations that indeed can be observed in the simulation at atomic scale. The model proposed by Varvenne answers some questions about solid solution strengthening in HEAs. First of all, it does not directly depend on number of components and most certainly is not maximised by equiatomic composition. To increase materials strength one needs to maximise the concentration-weighted misfit volume quantity and/or increase the shear modulus. Further on, authors have come to conclusion that stacking fault energy has little influence on yield strength. Finally, additional strengthening may occur due to local chemical environments and structural disorder. Unfortunately these parameters are very hard to measure.

Influence of individual elements on solid solution strengthening was modelled by Toda-Caraballo with Rivera Diaz del Castillo [25] and calculated as well as experimentally verified by Stepanov et al. [83]. According to the simulations the highest contribution in the CoCrFeMnNi system comes from the balance between chromium and nickel. Stepanov et al. performed a series of tensile tests on non - equiatomic $Fe_{40}Mn_{28}Ni_{32-x}Cr_x$ system (with x = 4, 12, 18, 24) to quantify the influence of chromium on its strength. Alloy with highest Cr content proved to be dual phased with large amount of Cr-rich /*sigma* phase. As a consequence it has not been taken under consideration. Other alloys were fcc single phased. It was shown that yield strength, YS = 210 MPa, and ultimate tensile strength, UTS = 310 MPa, for $Fe_{40}Mn_{28}Ni_{28}Cr_4$ increase with increased content of Cr to YS = 310 MPa and UTS = 605 MPa for $Fe_{40}Mn_{28}Ni_{14}Cr_{18}$. The result was in good agreement with calculated solid solution strengthening using Labush approach. As a consequence mechanical properties of alloys from CoCrFeMnNi family can be designed by varying the proportions between elements. Just like Varvenne's model predicts, the maximal strength is found in non - equiatomic compositions. Further optimisation can be done by adjusting the composition for tailoring the stacking fault energy to enhance twinning (TWIP effect) and controlled microstructure.

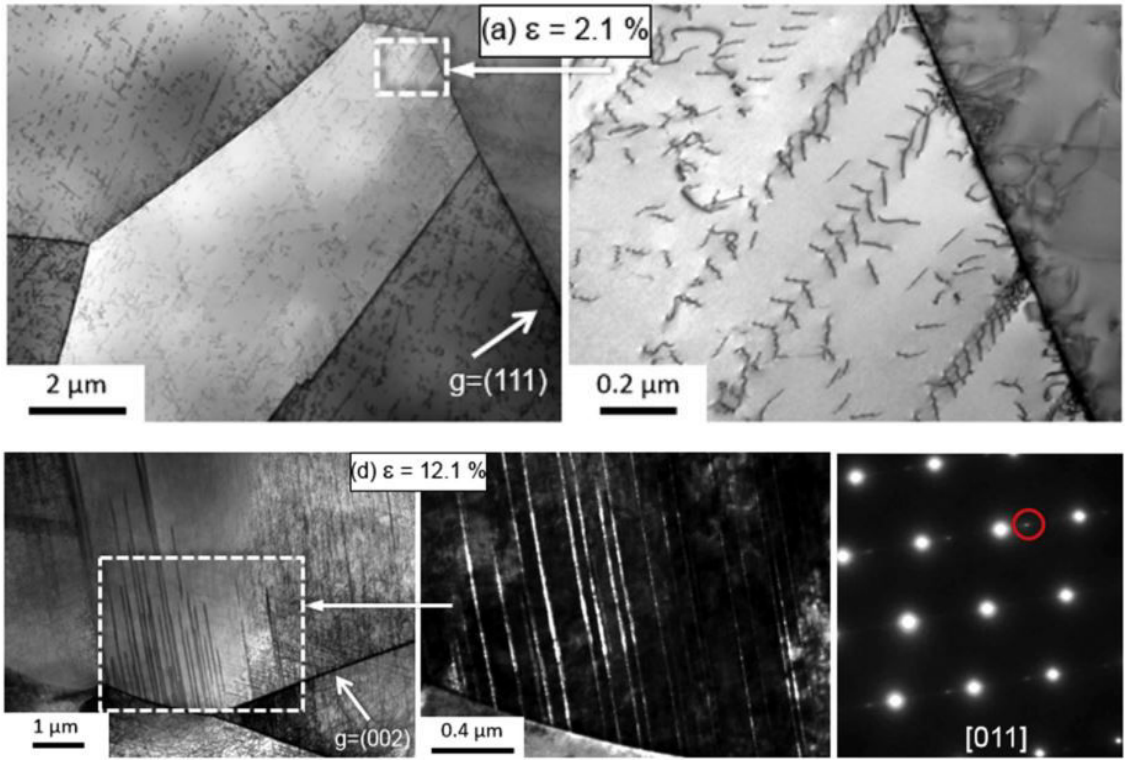

Figure 1.21: *TEM micrographs showing twin evolution with true tensile strain at 77 K. a) Both figures are bright field images. b) Figure on the left is a bright field image while in the middle is presented the dark field image with SAD pattern on the right. Diffraction spot circled in red in the SAD pattern was used to obtain the dark field image. The dashed rectangles in the left delineate the area that was magnified [92]*

Twinning, as a source of increased ductility at cryogenic temperatures, was proposed by Laplanche et al. [92]. The authors have performed a series of TEM observations on tensile samples after various strains both at room and liquid nitrogen temperatures. Part of their observations after interrupted tensile test at 77 K is presented in Figure 1.21. At low strain only dislocations activity is present and their pile ups at grain boundaries are observed. For strains above 6.0% twinning appears (clearly seen in the dark field image in Figure 1.21b). At room temperature twinning did not appear until much higher strains above 22.0%. This observation leads to reasoning that a critical stress has to be reached to launch deformation by twinning. At 77 K this critical true stress, σ_{tw}, is of the order of 720 ± 30 MPa. Straining specimens at room temperature just below this value (680 MPa) and above (820 MPa) indeed lead to the same conclusion, a critical stress needs to be reached to initiate twinning. At lower strain only dislocations were observed, whereas at higher one twins started to appear. Similarly twinning was observed at cryogenic temperature deformation in fracture toughness specimens in work of Gludovatz et al. [74]. No such phenomenon was reported by Otto et al. [10] for tensile tests at room temperature and it can be hypothesised that it is due to the fact that critical twinning stress was not reached. Further papers have also reported presence of twins upon deformation at various conditions (hot/cold rolling, compression, tensile) for Cantor's alloy and other compositions from the same family [75, 93–96]. Twinning deformation can be designed by chemical composition of an alloy. If desirable, addition of elements lowering the stacking fault energy could enhance twin formation during plastic deformation leading to further increase of plasticity. Deng et al. [97] have attempted and succeeded in developing a new composition in the CoCrFeMn family where twinning is activated even at room temperature. For the original composition $Fe_{40}Mn_{40}Co_{10}Cr_{10}$ with TWIP effect activated at lower stresses, properties similar to Cantor's alloy could have been obtained without any addition of nickel.

In fcc materials twinning is a commonly observed secondary mechanism of deformation. They are a locally inverted planes sequence going from ABCABC to ABCBCA [98]. Tendency of a material to form twins depends among others on its stacking fault energy (SFE) since it is hypothesized to be proportionate to the energy difference between the fcc and hcp phases. As a general rule the lower the SFE the more energetically favourable are twins. First measurements of SFE in the quinary CoCrFeMnNi and alloys of lower order were reported by Zaddach et al. [87]. The equiatomic composition presented the value of SFE close to 20 mJ/m^2 - 25 mJ/m^2 which is nearly four times lower than that of pure Ni but quite comparable to that of common stainless steels (AISI 304L SFE = 19 mJ/m^2 [99]). Same values were presented from a calculation by Beyramali Kivy and Asle Zaeem [100] from DFT simulations. Okamoto et al. [77] deduced the SFE from distance between

dissociated dislocations. They obtained an average value of 30 mJ/m^2. Those are all relatively close values. Nevertheless, Smith et al. [101] have observed an uncommonly high variation in observed distances which could imply complex solute configuration. Zaddach et al. [87] have suggested that the SFE can be tailored in a wide range of values in this specific family of alloys. In explicit, lowering Ni content significantly lowers SFE. Increasing Cr content also decreases the SFE but on smaller scale. They have managed to design a new composition $Ni_{14}Fe_{20}Cr_{26}Co_{20}Mn_{20}$ with extremely low SFE of the order of 3,5 mJ/m^2.

Twinning can have a desirable effect not only to enhance ductility. It can also lead to strengthening of the material through formation of new interfaces that reduce the dislocation mean free path. This phenomenon is commonly referred to as "dynamic Hall - Petch" [92,102] and results in strain hardening. Possibility to tailor the ability of an alloy to form deformation twin boundaries by change of SFE through chemical composition is an important advantage of CoCrFeMnNi family. It makes HEAs potential structural materials.

1.6.3 Microstructural evolution

Microstructure plays a crucial role in material engineering. It influences mechanical properties and is a part of the transformation process. Knowledge of recrystallisation, grain size or texture evolution allows the choice of proper state for specific applications. In literature many HEA compositions have been analysed after casting and homogenisation since at first, phase identification was the goal. For mechanical testing the alloys were most often cold or hot rolled and annealed to obtain a recrystallised structure with a defined grain size (see Figure 1.13). Recrystallisation is one of the most efficient ways to modify the microstructure. Its conditions, like time, temperature and initial deformation rate, are significant parameters to be defined. In HEAs the recrystallisation seams to be difficult, in explicit high temperature and long time of annealing are necessary. Sluggish diffusion may be at the origin of this phenomenon.

Recrystallisation of cold rolled samples with various thickness reduction was observed [103–106]. Depending on the thickness reduction of the samples recrystallisation begins at different temperatures. Otto et al. [103] have not observed any recrystallisation up to 500°C 1h for any of the deformations (21% to 96%). Haase and Barrales-Mora [104] reported no signs of recrystallisation up to 600°C 1h with unchanged texture character and initiation of recrystallisation at 650°C 1h for thickness reduction of 50%. Similarly Bhattacharjee et al. [105] report nearly fully recrystallised samples upon 1h annealing at 650°C (90% thickness reduction). The partially recrystallised structure presents a bimodal character with elongated deformed grains and heterogeneously distributed recrystallised grains on prior grain boundaries and

triple junctions of the deformed matrix [104]. Moreover, deformation twins formed during cold rolling proved not only to be thermally stable but also to remain in the microstructure up to high recrystallised volume fractions. Fully recrystallised structures were reported after 1h annealing at 900°C for thickness reduction 40% - 50% [103, 104] and at 800°C for higher deformations [103–106].

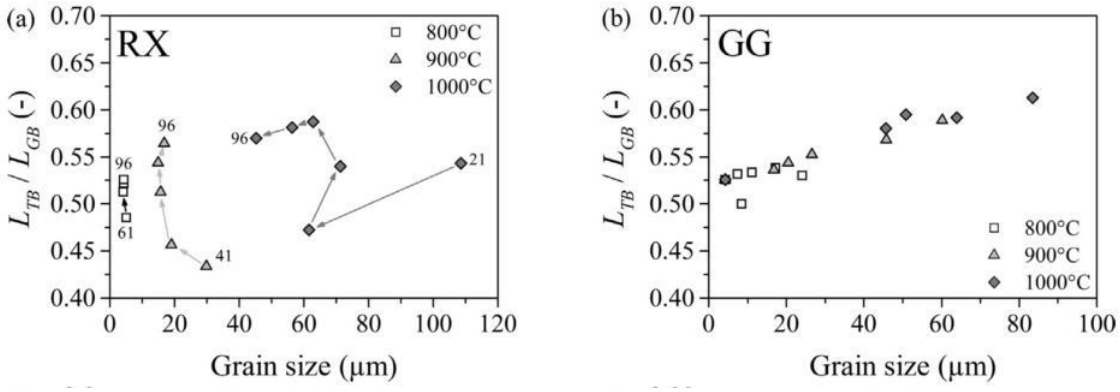

Figure 1.22: *Twin boundary fractions plotted as a function of grain size: a) recrystallization samples (RX) cold rolled to various final thicknesses and recrystallized for 1 h at temperatures of 800, 900 and 1000 °C. For a given annealing temperature, the arrows between the symbols point in the direction of increasing cold work with the minimum and maximum percentage rolling reductions given as numbers at the ends of each curve. b) grain growth samples (GG) cold rolled (96% thickness reduction), recrystallized for 1 h at 800° C and subsequently annealed for different times at temperatures of 800, 900 and 1000 °C [103]*

Annealing twins play an important role in microstructural evolution. They are noticeably present reaching up to 43-58% of all grain boundaries [103]. Otto et al. [103] have shown that twins amount depends highly on grain size as well as on the initial state prior to annealing. For samples that were recrystallised directly after cold rolling no obvious relationship between fraction of twin boundaries and grain size can be found (Figure 1.22a). On the other hand if change of twins fraction for fully recrystallised samples is observed (only grain growth occurs), the relation is clearly linear (Figure 1.22b). This means that twin boundary fraction is solely dependent on final grain size in case of grain growth. Likewise in the study of Sathiaraj and Bhattacharjee [106] for Cantor's alloy and binary Ni-Co alloy, similar twins densities are observed for comparable grain sizes. Formation of twins is possible provided that the grain boundaries move; yet, it supposes that the phenomena will be different, depending on initial state of the material: is it still deformed or fully recrystallised. Similar results were observed in α-brass where Hu and Smith [107] reported that twin density was solely determined by final grain size when the twin growth occurred in fully recrystallised samples. The linear dependence between density of annealing twins and grain size implies that formation of new twin boundaries during grain growth is related to internal microstructural length scale, which is the basis of the classical theory of Fullman and Fischer [108]. In their view twins are created at

migrating grain boundary triple points to lower the total system energy. In consequence number of twins formed during grain growth is higher than the number of twins that vanish. This approach is further validated in Cantor's alloy by common presence of terminal twins at triple points, that share only one coherent twin boundary with their mother grain [150].

Grain growth kinetics have been analysed on samples directly after cold rolling [18] and starting from a recrystallised structure with specific grain size $d_0 = 4.3\ \mu$m [103]. Annealings at different temperatures and various times have been performed to obtain a large spectrum of grain sizes. It was found that with increasing time and temperature the grain size increases monotonically. Furthermore in both studies grain growth exponent equal to 3 was found and the activation energy Q was determined to be equal 322 - 325 kJ/mol as presented in Figure 1.23. Liu et al. [18] concluded that such an activation energy is due to sluggish diffusion, but it is still unproven and requires additional investigations. Nevertheless close results in both studies suggest similar mechanisms responsible for grain growth.

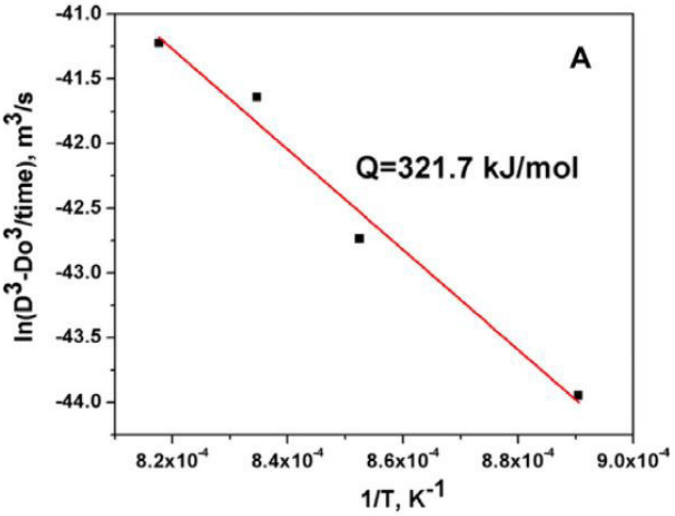

Figure 1.23: *Grain-growth constant, C, as a function of the reciprocal of absolute temperature in the CoCrFeMnNi alloy [18]*

Cold rolling leads to a certain texture evolution, highly dependant on stacking fault energy. It is common for low SFE materials to form strong Brass-type texture upon heavy deformation [109, 110]. This is also the case for CoCrFeMnNi alloy [104–106]. Haase with Borrales-Mora [104] report transition from Cu-type to Brass-type texture at approximate rolling degree of 50% due to formation of deformation twins. This texture transition occurs at higher deformations in HEA compared to other low SFE alloys most probably because of its lower twinning activity at room temperature. Annealing following cold rolling results in recovery and recrystallisation. Microstructure evolution in Cantor's alloy is at first dominated by nucleation of new grains at grain boundaries. It does not change the texture significantly as

the newly formed grains maintain the orientation of primary deformed grain. The TEM image in Figure 1.24 shows a small nuclei in a parent grain and diffraction diagrams for both areas. Orientations of both are very similar.

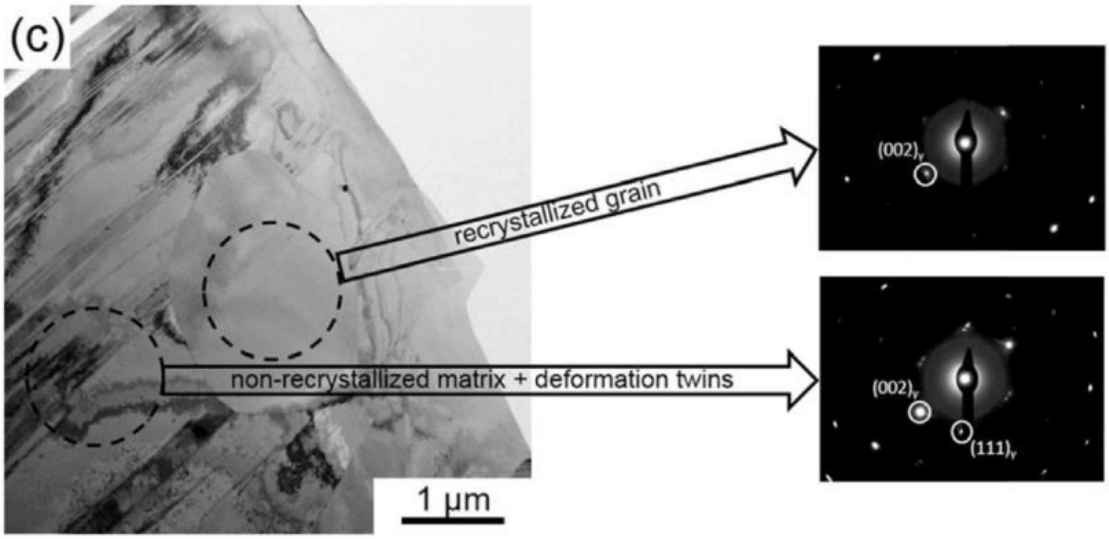

Figure 1.24: *TEM BF images of the material after 50% cold rolling, annealing at 650 °C for 1 h and tensile testing until fracture. The SAED pattern with [-110]g zone axis reveal that the recrystallized grain has a very similar orientation to the non-recrystallized matrix [104]*

Randomisation of texture happens mostly due to formation of annealing twins. Sathiaraj and Bhattacharjee [106] noted that the CoCrFeMnNi alloy presented less variation in texture components and more homogeneous grain growth compared to Ni-Co alloy that showed abnormal grain coarsening leading to enhanced α-fiber orientations. They attribute the differences in texture evolution in both alloys to sluggish diffusion in HEA which would diminish the mobility of boundaries and effectively prevent preferential growth of grains.

1.6.4 Phase stability

Even if the CoCrFeMnNi equiatomic alloy is considered as a model high entropy alloy with enhanced phase stability in a wide range of temperatures, thermodynamic calculations predict a decomposition of this material. At temperatures below 900°C, besides the initial fcc phase, presence of Cr - rich sigma phase, bcc Cr - rich phase, $L1_0$ MnNi - rich phase and B2 ordered FeCo - rich phase can be expected [38]; however, the precision of calculations at lower temperatures deteriorates. On the other hand, the phase transformation kinetics could make the difference between calculated equilibrium and reality, and in HEAs the kinetics are suspected to be slowed down. At the same time, most of the studies up to date report phase composition of alloys after high temperature homogenisation / annealing which would explain presence of single phase.

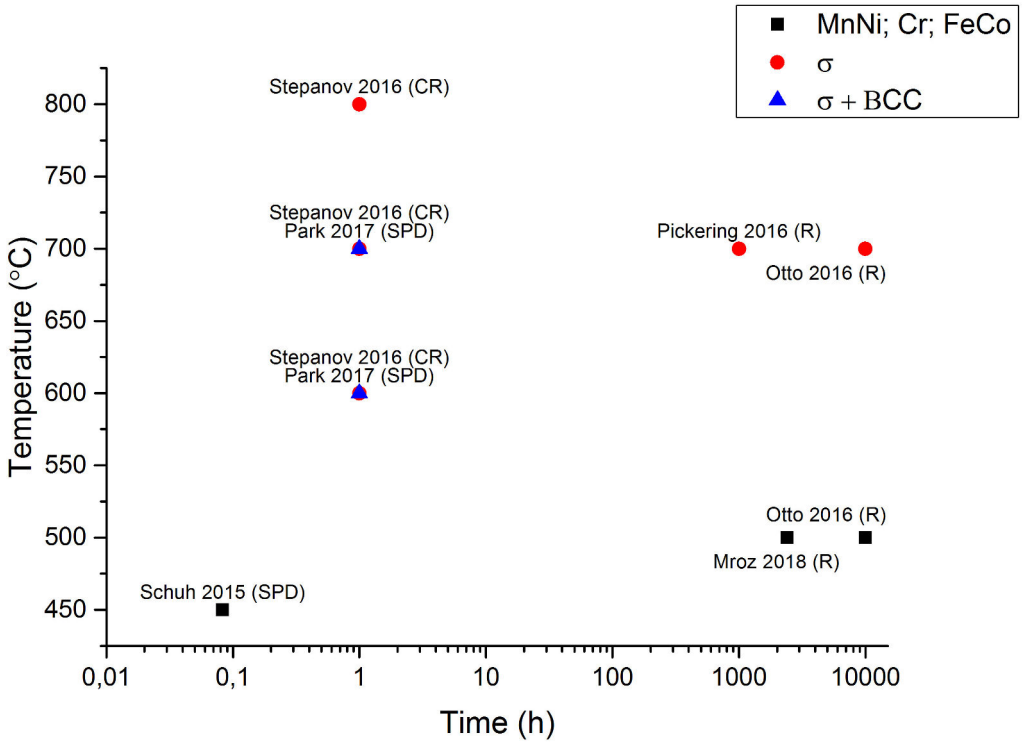

Figure 1.25: *Summarised observations of secondary phase formation in CoCrFeMnNi comming from [17, 111–115]; Abbreviations stand for initial state: CR - cold rolled, SPD - sever plastic deformation, R - recrystallised [115]*

Some of the recent publications state the appearance of secondary phases upon annealing at low temperatures, between 450°C and 900°C [17, 111–115]. First of all, Pickering [113] points out the presence of chromium carbide $M_{23}C_6$ after heat treatments at 700°C. It would seam that contamination of melting equipment plays an important role and even small presence of carbon induces carbides precipitation. Further more appearance of σ phase was observed for longer time annealings at 700°C in coarse grain samples [17,113]. The same σ phase was also present for shorter

times of annealings for temperatures between 600°C and 800°C for samples that were intensely deformed either by cold- or cryo-rolling or by sever plastic deformation [111, 112]. It would suggest that high deformation and therefore high density of dislocations and presence of many grain boundaries (reduced grain size) facilitate diffusion and thus phase transformation. All those observations are summarised in Figure 1.25 under the form of a temperature vs time graph proposed by Mroz [115].

Some lengthy heat treatments were also performed by Otto et al. [17] on the Cantor's alloy. They annealed the samples at 500°C, 700°C and 900°C for 500 days (12000 hours). At 900°C no secondary phases were seen, the fcc solid solution remained stable. At 700°C the Cr-rich σ - type precipitation on the grain boundaries was found. Finally at 500°C, except the fcc matrix, 3 distinct phases were observed as presented in Figure 1.26. NiMn - rich phase showed the $L1_0$ ordered structure, the Cr - rich phase had a bcc structure and the FeCo - rich phase was B2 ordered. Mean values of chemical composition of these phases are presented in Table 2.1 from measurements on TEM samples. Similar results were obtained for equiatomic composition by Mroz [115] already after 100 days of annealing at 500°C. On the other hand, another composition being the topic of his PhD (non-equiatomic $Co_{20}Cr_{15}Fe_{26}Mn17Ni_{22}$, patented under the name of A3S) proved to be much more resistant to decomposition and only slight presence of secondary phases was detected after 300 days of annealing at 500°C.

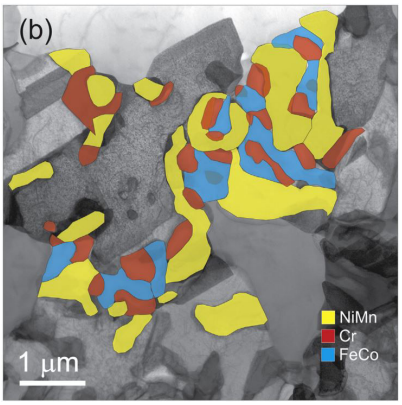

Figure 1.26: *EDX maps superposed on STEM image show that the precipitates have three distinct chemical compositions [17]*

Table 1.3: *Chamical composition of secondary phases in at.% [17].*

Phase	Cr	Mn	Ni	Fe	Co
MnNi	2	**37**	**55**	2	4
BCC Cr	**86**	4	1	5	4
FeCo	2	5	1	**46**	**46**

Phases found by most of the authors [17,111,113–115] are not foreseen by Thermo-Calc at all, showing that its predictions are in disagreement with those experimental observations. Only in few cases shown by Park et al. [112] presence of a bcc phase is in accordance with thermodynamic simulations.

Otto et al. [17] summarised the decomposition route of Cantor's alloy under a hypothesised TTT curve presented in Figure 1.27. It is only schematic and further

work needs to be done to improve the data set but general trends of phase formation can be read. At temperatures close to 800°C, σ phase is formed even for time of annealing below 500 days. For lower T no σ phase is formed but another Cr - rich bcc phase precipitates just after formation of NiMn - rich phase, and followed by appearance of B2 ordered FeCo - rich phase for longer times of annealing. All of these results suggest that careful consideration needs to be given in the future to the application temperatures as prolonged maintain at medium temperatures can cause phase decomposition.

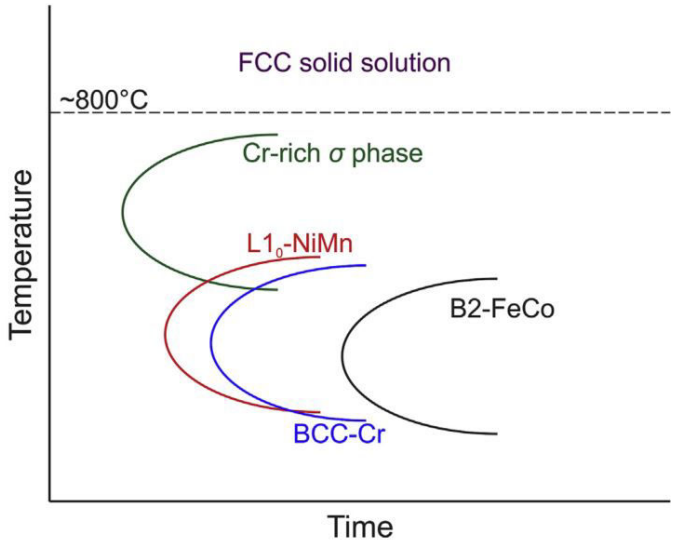

Figure 1.27: *Schematic (hypothesized) TTT curve for the CrMnFeCoNi high-entropy alloy [17]*

1.6.5 Non-equimolar grades from CoCrFeMnNi family

Equiatomic CoCrFeMnNi alloy has already been proved to have interesting mechanical properties with hope for high temperature phase stability and exceptional elongation at cryogenic temperatures with no martensitic transformation. Nevertheless, it stays a single phased solid solution whose resistance, in particular mechanical one, can still be enhanced. Increasing number of research is done on some modified grades of Cantor's alloy by changing the proportions [87, 115], substitution of one of the elements or addition of other metallic elements [34, 44, 70, 95, 116–123], elimination of one of the elements [83, 124–126] or addition of non-metallic elements [123, 127–131]. Even though those modified compositions are more probable to be applied in the industry, the equiatomic alloy stays the reference alloy and a base for fundamental research.

One could expect it possible to induce a martensitic transformation during deformation at low temperatures in those austenitic alloys, as commonly seen in metastable austenitic stainless steels [132–134]. It is one possibility of many to increase

the mechanical resistance of those alloys. Cantor's alloy does not present any traces of martensitic phase even after tensile tests at cryogenic temperatures, but changing its composition can lead to such behaviour. Li et al. [124] have managed to develop a non-equiatomic HEA that shows the TRIP effect due to metastable fcc solid solution. They have completely eliminated nickel, lowered the cobalt and chromium content to 10 at.% and varied the amount of manganese from 30 at.% to 45 at.%. Already after quenching some hcp phase is detected for 35 at.% of Mn and even more for lower Mn content. Fine grained (4.5 μm) $Fe_{50}Mn_{30}Co_{10}Cr_{10}$ shows increased YS, UTS and total elongation compared to the equiatomic quinary alloy. Its origin lays in changed primary deformation mechanism due to a martensitic transformation. Evolution of content of fcc and hcp phases during deformation at room temperature is presented in Figure 1.28. Over 80% of martensite after necking is a clear proof of deformation induced phase transformation. Further optimisation of this composition is possible and necessary, but those preliminary results place dual phase TRIP HEAs as important future research goals.

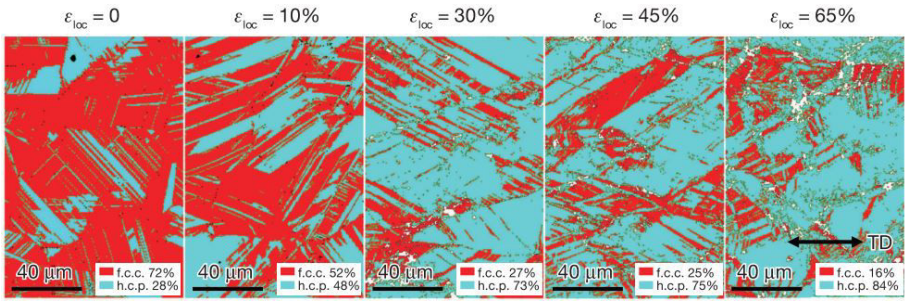

Figure 1.28: *EBSD phase maps revealing the deformation-induced martensitic transformation as a function of deformation. ϵ_{loc} is the local strain and TD is the tensile direction [124]*

The idea of dual phased alloys was developed also in another group of alloys, those containing Al. It was already pointed out that addition of aluminium leads to formation of bcc phase next to already known fcc solid solution (Figure 1.6a). He et al. [34] tested the influence of Al both on microstructure and tensile properties in the $(CoCrFeMnNi)_{100-x}Al_x$ alloys. It was found that up to 8 at.% of Al the fcc single phase is maintained with somewhat increased YS and UTS due to solid solution hardening by added Al atoms. Those compositions systematically loose some of their elongation with increasing amount of Al. For Al content between 8 at.% and 16 at.%, the alloy becomes dual-phased with cubic shaped B2 ordered particles embedded in fcc matrix. It results in significant increase of YS and UTS (up to 800 MPa and nearly 1200 MPa for 11 at.% Al). Tensile tests for high amounts of aluminium were impossible due to brittleness of the alloy. Further increase in Al content leads to solely bcc structure composed of disordered spherical precipitates in B2 ordered matrix, probably due to spinodal decomposition [34]. It is clear that

dual-phased alloys when properly designed can have increased mechanical properties while keeping reasonable ductility.

Similar multiphased microstructures were observed in further studies in other compositions containing aluminium [44,70,116–118]. Chen et al. [70] and Manzoni et al. [116] report bcc + B2 mix as shown in Figure 1.29a and more precisely Cr-Fe rich bcc precipitates (marked as B in Figure 1.29b) in an Al-Ni rich B2 ordered matrix (A in Figure 1.29b). In the six elements equiatomic AlCoCrCuFeNi analysed by Singh et al. [44], presence of those two phases was also reported. Olszewska et al. [117] have observed precipitation of cuboid B2 ordered phase in fcc matrix as shown in Figure 1.29c for the AlCrFeMnNi equiatomic alloy.

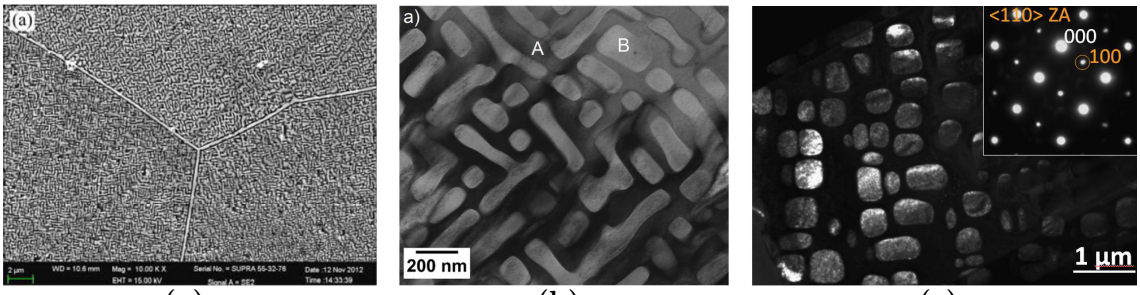

Figure 1.29: *a) SEM image of interdendritic zone of as cast AlCoCrFeNi HEA [70] b) BF TEM image of the microstructure in the interdendritic zone of the as-cast AlCoCrFeNi alloy [116] c) TEM DF image in <110> ZA and illuminated (100) spot view on dendritic zone with visible B2 ordered cubes [117]*

Lowering the Al content can lead to controlled precipitation and ageing hardening. Such compositions were developed by Chen et al. [118] with following proportions $Al_xCrFe_{1.5}MnNi_{0.5}$ with x equal to 0.3 or 0.5. Initially after casting and homogenisation, the alloy consists of fcc phase in the previous interdendritic zones and B2 precipitates in a bcc matrix in the early dendrites. Cold rolling followed by ageing heat treatment allows to additionally precipitate the $Cr_5Fe_6Mn_8$ ρ phase. Its presence allows to increase hardness from 300 HV to 800 HV. Those alloys show higher softening resistance than high speed steels, and good wear resistance compared to commercial alloys. Unfortunately its corrosion resistance in acidic environments with Cl^- ions is decreased with increasing content of Al [119].

Other elements have been also added to CoCrFeMnNi to induce precipitation of second phases as hardening factors. Stepanov et al. [122] have checked the addition of vanadium to the Cantor's alloy. It lead most of all to formation of σ phase and V was found to be a sigma forming element even stronger than Cr. $CoCrFeMnNiV_x$ alloys with $x \geq 0.5$ show continuous strengthening with yield strength reaching up to 1660 MPa. Unfortunately the loss of ductility is immense since it drops to 0.5% elongation to fracture in tensile test. Liu et al. [131] show that addition of Mo to the quaternary CoCrFeNi leads to precipitation of σ and μ phases. For

$CoCrFeMnNiMo_{0.3}$ at aged state the yield strength can surpass 800 MPa with total elongation of 19%. Including Nb to Cantor's alloy $CoCrFeMnNiNb_x$ can lead to precipitation of Laves phase [129, 130] or even to fully eutectic microstructure [135]. Presence of Laves phase leads to yield strengths exceeding 600 MPa but with very low ductility [130], whereas for eutectic alloys σ_y can go up to 1600 MPa in compression tests [135]. Finally addition of both Ti and Al can lead to fairly balanced tensile properties [127, 128]. Presence of $L1_2$ Ni_3(Ti, Al) and $L2_1$ (Ni, Co)$_2$TiAl Heusler precipitates contribute to both strengthening (up to $\sigma_y = 1$GPa) and loss of ductility (down to 17%).

Searching for precipitation-hardened or dual-phased alloys is not the only reason for addition of other elements to HEAs matrices. It can improve mechanical properties by influencing the deformation mechanism, for example facilitating twining at higher temperatures. This effect was observed by Komarasamy et al. [120, 121]. The authors have reported high work-hardening ability in $Al_{0.1}CoCrFeNi$ alloy due to presence of nano-scale deformation twins already at room temperature. In the coarse grained alloy they have also shown low activation volumes comparable with other fcc materials with ultra fine grain suggesting intrinsic strengthening mechanisms. Similarly Jo et al. [95] have reported possibility of inducing deformation twins at room temperature to enhance mechanical properties at cryogenic tensile tests by adding vanadium. They have developed the single fcc phased $Co_{10}Cr_{15}Fe_{35}Mn_5Ni_{25}V_{10}$ that can reach up to 970 MPa yield strength with elongation of 46% at 77K in the annealed state. Addition of carbon leads to increased strain hardening and strength in the $CoCrFeMnNiC_{0.5}$ according to Wu et al. [94]. The authors argue that it is due to increased twinning ability enhanced by presence of interstitial carbon atoms, most probably lowering the intrinsic stacking fault energy like in austenitic steels [136]. Some equally promising results were obtained on a non-equiatomic $Co_{20}Cr_{15}Fe_{26}Mn_{17}Ni_{22}$ (also referred to as A3S) alloy after hot deformation [115]. This newly developed composition shows some particular dislocations behaviour with cells formation and high stability after hot deformation. This nanometric substructure can lead to yield strength reaching 800 MPa with elongation to fracture up to 30% at room temperature.

Industrialisation of high entropy alloys can be problematic due to high number of alloying elements that increase the cost of fabrication significantly. Expensive and strategic elements are currently used in those alloys. The improvement of mechanical properties should be considerable to justify their cost at sale. Even though these alloys are still in a basic stage of research it is an aspect that should be considered and solutions to reduce the price are not to be neglected. Possible ways of rising the competitiveness of HEAs compared to classical alloys is for example the optimisation of chemical composition, in explicit lowering the amount of critical elements like

cobalt [137]. Little research is done on Co-free compositions in the Cantor's family of alloys even though it is costly and strategic. At the same time it can cause problems during irradiation as cobalt forms high levels of the ^{60}Co radioisotope during neutron irradiation [125]. Nevertheless some researchers have made effort to meet the problem [83, 125, 126]. The equiatomic CrFeMnNi after homogenisation exhibits multi-phased microstructure [20, 72], in consequence research was done on alloys with Cr content decreased to 18 at.% [125, 126] or variable Cr content [83] to maintain the single phase. Wu et al. [125] performed some tensile tests at various temperatures on cold rolled and recrystallised samples and compared the results to equiatomic CoCrFeMnNi. Values of yield strength and uniform elongation are plotted in Figure 1.30 (two samples coming from this study shown in dashed lines and a full line representing Cantor's alloy from [72]). Values for both alloys are generally comparable and similar temperature dependence trend is observed. However, for Cr_{18}FeMnNi a minimum of ductility is noted for intermediate temperatures (around 473 K). Just like for Cantor's alloy, deformation twins are observed in samples after tests at low temperature, but they are not found for tests at room temperature or higher. Presence of twins is a sign of low stacking fault energy that was measured to be of the order of 30 mJ/m^2 at 77K [77,87] for CoCrFeMnNi and that concentration of Co and Cr can decrease this value. Lower Cr and absence of Co most probably lead to higher SFE in Cr_{18}FeMnNi compared to Cantor's alloy [125]. More study is needed to confirm that same mechanisms govern the deformation in the quaternary alloy but obtained σ_y and ϵ_f are quite promising.

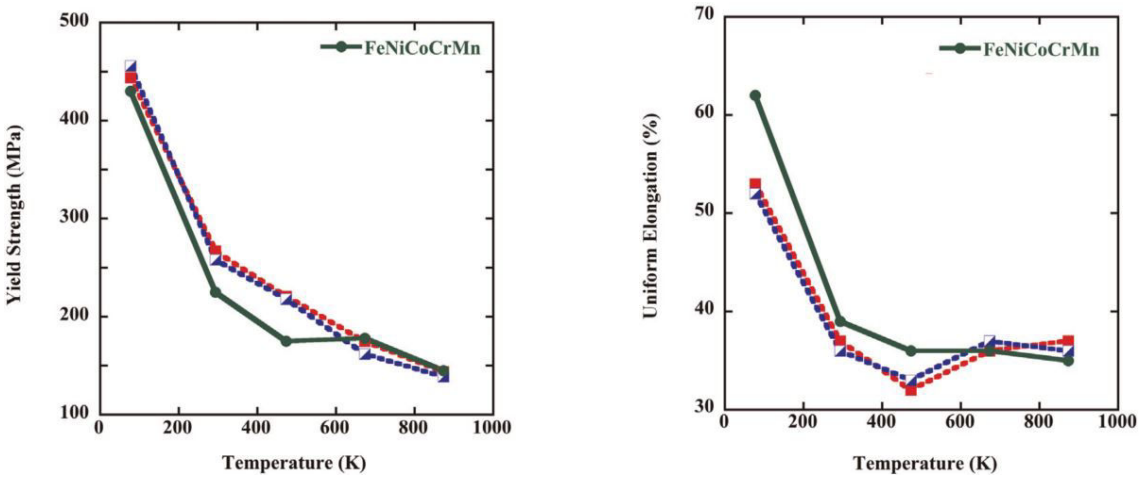

Figure 1.30: *a) yield strengths (σ_y) and b) uniform elongations to fracture (ϵ_f) as a function of temperature for Cr_{18}FeNiMn alloy (two samples, red and blue dashed lines); data for the equiatomic CoCrFeMnNi alloy (dark green solid line) [72] were also presented for comparison [125]*

One of possible application fields is the nuclear one, as it is hypothesised that HEAs may show better resistance to irradiation-induced damage due to their complex composition. Kumar et al. [126] have examined the microstructural and mech-

anical changes produced by irradiation in the $Cr_{18}Fe_{27}Mn_{27}Ni_{28}$ and compared it to conventional austenitic Fe-Cr-Ni alloys. Observation of newly created defects showed a much higher number of dislocation loops at elevated temperatures in HEA as shown in Figure 1.31. At the same time, the loops are much smaller, 6 nm compared to 110 nm in 316 stainless steel. As a result, coalescence of loops does not occur and no additional dislocations networks were formed. Consequently, the dislocation density stayed stable before and after irradiation. This result suggests sluggish diffusion kinetics in HEA compared to conventional Fe-Cr-Ni alloys with recombination of vacancies and interstitials as the dominant recovery process. As a consequence the resistance of HEA to void swelling, irradiation creep and other irradiation induced defects seams improved as compared to classical materials. Diffusion induced by irradiation in classical alloys usually leads among others to radiation-induced solute segregation on grain boundaries. This effect is significantly suppressed in HEA probably due to anticipated existence of short range ordering. In general the $Cr_{18}Fe_{27}Mn_{27}Ni_{28}$ and other alloys from the CrFeMnNi family are promising compositions for demanding nuclear energy application with better swelling resistance, reduced point defect mobility and limited segregation at grain boundaries. Absence of Co is an important criterion in HEAs development [125].

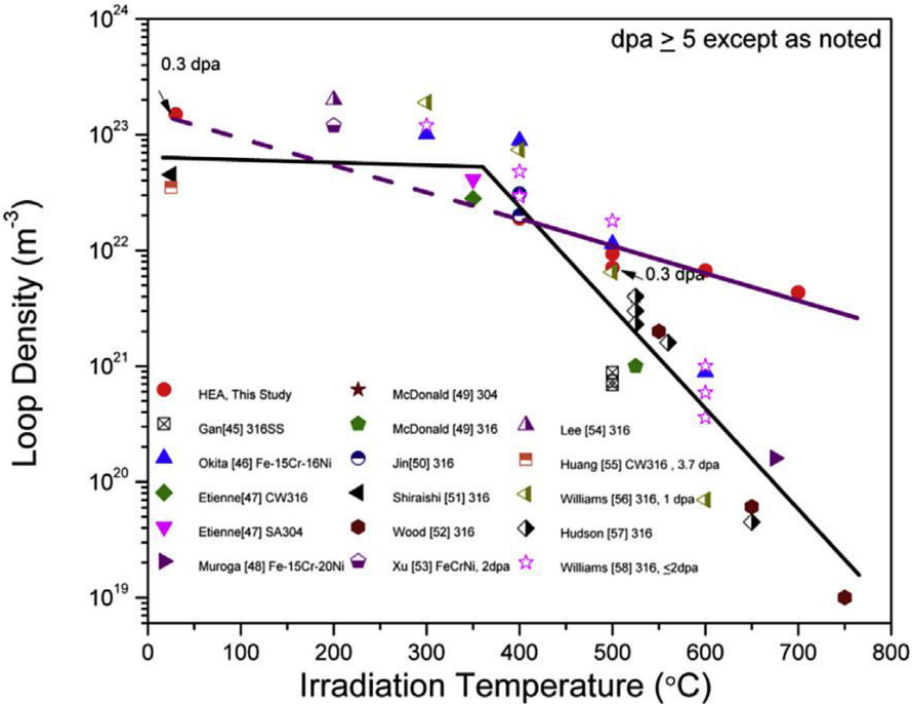

Figure 1.31: *Effect of ion irradiation temperature on dislocation loop density for Fe-Ni-Mn-Cr HEA compared to conventional Fe-Cr-Ni austenitic alloys irradiated at comparable doses and damage rates. The drawn lines are intended as guides for the reader's eye [126]*

Motivation and objective

High Entropy Alloys are a new promising approach in metallic materials. The phenomena occurring in this type of alloys are far from being fully understood and research is still needed. There are several groups of interest among HEAs, and the one based on 3d transition elements is the largest. The quinary equiatomic CoCrFeMnNi alloy, also called the Cantor's alloy, is part of this broad family of alloys. It is known for highly stable single fcc structure and interesting properties specially at cryogenic temperatures. The Cantor's alloy is treated as a model HEA. There have been some attempts of modification of the equiatomic composition with promising results pointing to the routes to follow: both by change of the stoichiometry, as well as, reinforcement by other mechanisms like secondary precipitation. Not all experimentally observed properties are fully understood yet. Microstructure, with dislocations being part of it, is found to be at the origin of phase stability and exceptional mechanical properties. Comprehension of its evolution is a source of optimisation possibilities. Finally, economic aspects are not to be neglected in the research. In the particular case of CoCrFeMnNi family, cobalt is the problematic element, primarily because it is an expensive and strategic one. Additionally, Co presence is at the origin of some technological difficulties. As compared to stainless steels, it is probably the major defect of Cantor's alloy for any industrial applications.

The aim of this work follows the logical approach of HEAs development. It is focused on design and optimisation of new fcc HEAs from Cantor's family, with major specifications of decrease or total elimination of cobalt while keeping high stability of single fcc phase and good mechanical properties also at cryogenic temperatures. In addition, lack of phase transformation under stress at liquid nitrogen, allows to keep the amagnetic properties of the fcc phase. This approach needs an in-depth comprehension of elemental mechanisms at the origin of mechanical properties such as: phase stability, recrystallisation phenomena or dislocations behaviour.

The choice of composition was done based on Thermo-Calc calculations and previous research work performed in the Ecole des Mines de Saint Etienne (EMSE). Alloys prepared both at EMSE laboratory and at research centre of APERAM

were studied. Multiple techniques of microstructural observations were used: SEM, EBSD, TEM, as well as numerous mechanical tests were performed: HV measurements, compression and tensile tests. The combination of those techniques allowed to thoroughly characterise the selected alloys and bring further insight into observed mechanisms of recrystallisation and plastic deformation.

Chapter 2

Methods and procedures

Contents

Alloys that have been designed and analysed in this work were designed and prepared according to the procedures described in this chapter. First the composition was selected on the basis of Thermo-Calc simulations. The casts to be studied were prepared mainly by the technique of cold crucible melting followed by hot forging in the EMSE laboratory. Part of the casts were prepared by vacuum induction melting in the APERAM research centre. They were later transformed by hot and cold rolling. Many heat treatments were performed directly after forging or additional cold rolling. Alloys in different states were characterised by microscopy techniques: SEM, EBSD, EDX, TEM. Mechanical testing of selected materials in different structural states consisted of hardness measurements, toughness, compression and tensile tests.

2.1 Thermodynamic calculations

First approach to definition of promising alloy compositions was to analyse phase stability calculated by Thermo-Calc software. It is commonly used by both academic community and industry to predict possible phases formation, phase transformations, solidification conditions calculate driving forces for phases formation [48, 49]. Thermo-Calc is a thermodynamic software based on CALculation of PHase Diagrams approach, CALPHAD. Minimisation of Gibbs free energy is at the basis of those calculations according to its general expression for multi-component phases, equation 2.1, where G^0 is the contribution from chemical mixing of pure components, G^{ideal}_{mix} is the ideal mixing contribution, and G^{xs}_{mix} is the excess Gibbs energy of mixing due to non ideal interactions [138].

$$G = G^0 + G^{ideal}_{mix} + G^{xs}_{mix} \tag{2.1}$$

The value of G can be defined individually even in heterogeneous systems with multiple stable phases, since properties of each phase are completely independent of the others. The Gibbs energy of the whole system, G_{system}, is the sum of the energies of each phase, G_i, multiplied by its amount, c_i, as expressed by equation 2.2 [139].

$$G_{system} = \sum_{i=1}^{n} c_i \cdot G_i \tag{2.2}$$

CALPHAD approach consists of several steps. The first consists in collection of experimental data to form empirical rules. Second, combination of obtained rules with fundamental theories leads to a model description of each phase and its thermodynamic properties. Gibbs free energies modelled for all individual phases in binary and ternary systems are collected in thermodynamic databases. Finally,

the model is extrapolated to higher order systems. As far as possible, the model is enriched with experimental data for continuous development of those databases.

Numerous databases are proposed by Thermo-Calc company starting with all major metallic alloy groups (Fe, Ni, Cu, Al, Mg), going through minerals to aqueous solutions. The databases are constantly under development and their improved versions are regularly released. In frame of this work three databases are of interest: TCFE5 and TCNI8 that were available at the beginning of this PhD thesis work (January 2016) and TCHEA1 that was released in late 2015. At present 3rd version of HEA database was released, but it was not available in the scope of this work. Since in selected and studied alloys, decrease of content or total elimination of Co was balanced with Fe, use of the TCFE5 database seamed to be the most suitable for the calculations. All representation of thermodynamic simulations are made in form of quasi-binary phase diagrams as a function of concentration of one of the elements balanced by Fe.

The Scheil Calculator activity is used to perform simulations of Scheil (Scheil-Gulliver) solidification processes. By default, a Scheil calculation results in an estimation of the solidification range of an alloy. The calculation is based on the assumption that the liquid phase reaches its equilibrium and is homogeneous at all times and that the diffusivity is null in the solid state.

2.2 Investigated materials

Three compositions were investigated at first, they are presented below in Table 2.1 and are named as Y1 low-Co(V), Y2 low-Co and Y3 Co-free. Alloys were prepared by cold crucible melting technique in Ecole des Mines SMS Center laboratory. Components were introduced one after the other with purity minimum 99,99% for iron, chromium, nickel and cobalt that have been purified in the laboratory. Manganese was purchased commercially with a purity of 99,9%. The level of impurities, in explicit C, N, O, S is <50 ppm for each. The casting process together with following thermo-mechanical treatments will be described in more details in Chapter 3.3.

Table 2.1: *Composition of investigated alloys [at.%].*

Alloy	Co	Cr	Fe	Mn	Ni	Others
Y1 low-Co(V)	10	15	bal.	17	22	1 % V
Y2 low-Co	10	15	bal.	17	22	-
Y3 Co-free	-	15	bal.	17	22	-
Y3 Co-free(0.1Nb)	-	15	bal.	17	22	0.1 % Nb
Y3 Co-free(0.3Nb)	-	15	bal.	17	22	0.3 % Nb

After casting, 3000g ingots were cut to about 500g pieces, annealed at 1000°C for 3 hours and hot forged at about 1060°C. Forging procedure starts with ingot pieces with cross section of about 20 x 40 mm and finishes with a 12 mm diameter rod in several passes with intermediate reheating. Total deformation could be estimated at the order of $\epsilon = 0.85$ not taking into account the possible recovery / recrystallisation during reheating. Most of the tests were done on samples *as forged* (**AF**) or *annealed* at 1000°C 2h and water quenched (**RQ**). Part of the RQ rods were cold rolled with thickness reduction of $\sim 90\%$ (**CR**).

Additionally, Y3 Co-free and Y2 low-Co ingots of 2000g were made in APERAM Research Centre in Isbergues by melting and casting under vacuum (Vacuum Induction Melting, VIM) to verify the feasibility of this kind of concentrated (HEA) alloys in conditions approaching those of an industrial laboratory. The chemical elements of 99% purity were melted in small portions without previous cleansing, starting with iron and finishing with manganese. Carbon was added to carry out deoxidation, nitrogen was used to purify the chamber after deoxidation. Afterwards, the ingots were hot rolled with the thickness reduction of 90% with quenching at the end of the process. Later they were heated to 1000°C and cooled down, as it is conventionally done for austenitic stainless steels for softening before cold rolling. Finally, cold rolling with reduction of thickness of 64%, down to 1 mm, was performed.

Heat treatments

Numerous heat treatments were performed on as forged or cold rolled samples to investigate the temperature influence on microstructural evolution. List of heat treatments is regrouped below in Table 2.2. Most of those annealings were done for samples in AF state or CR state. For treatments longer than 24h, samples were closed in evacuated quartz capsules; for short treatments if possible, pure argon atmosphere was applied to avoid oxidation. Most annealing treatments were performed in cylindrical furnaces in EMSE. The temperature was controlled with a thermocouple (+/- 5°C) before putting samples in the furnace; time of heat treatments was counted starting at putting the sample in a hot furnace.

Table 2.2: *List of temperatures and times of annealings.*

Temperature [°C]	Time
500	100, 200, 300, 400, 500 days
600	2, 14, 28 days
650	2, 14 days
700	2, 14 days
800	0s, 30s, 60s, 180s, 300s, 8h
1000	0s, 30s, 60s, 180s, 300s, 2h, 24h

A series of short annealing treatments was performed in APERAM laboratory. The temperature (800°C or 1000°C) was controlled by thermocouples welded on the surface of thin (1 mm) samples (either AF or CR state). Holding time was started when the slope of temperature change reached 4°C/s, giving the treatment profiles as presented in Figure 2.1. No protective atmosphere was applied and the samples were observed at the cross section for microstructure analysis through the whole sample thickness.

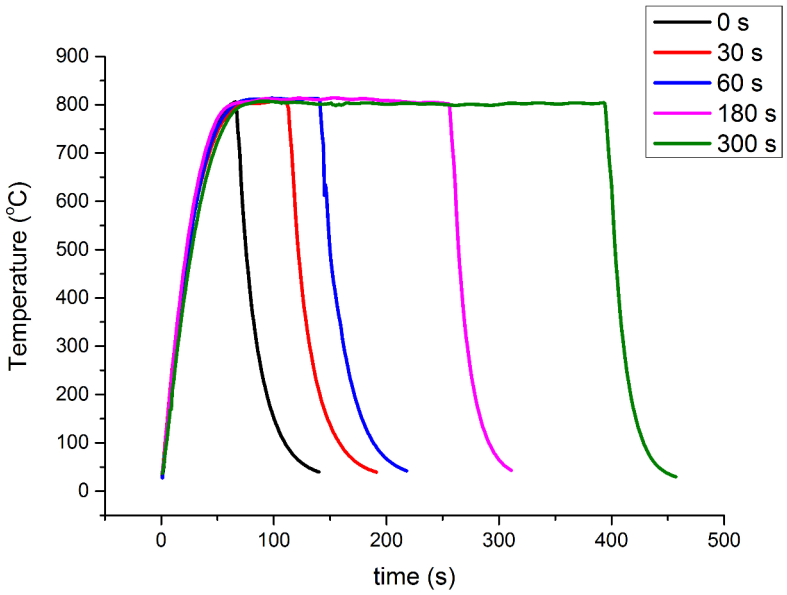

Figure 2.1: *Temperature profile during short annealings at 800°C*

2.2.1 Hot cracking tests

The capacity to undergo hot deformation of as cast alloys was verified by hot cracking tests. The tests were performed in the APERAM research centre using the Gleeble machine with tensile module. Samples in the as cast ingot were prepared according to the plan presented in Figure 2.2. The test consists of heating of the specimen locally, where the section is reduced. The applied heating rate was 50°C/s. The temperature was controlled by thermocouples welded on the surface. When the required temperature is reached, the sample is pulled with strain rate 10 s^{-1} and the maximal force is measured. Both critical drop in mechanical resistance and decreased necking are signs of "burned" material: local liquefaction. Tests performed at various temperatures allow to define precisely the temperature for hot deformation. In our case, the tests were performed at temperatures ranging from 950°C to 1200°C every 50°C. Later on, the samples were cut in two and the cross sections' microstructure was observed via light microscopy.

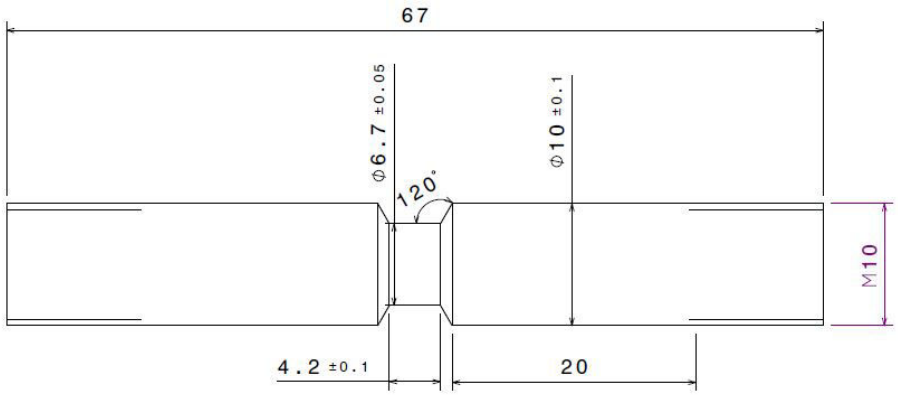

Figure 2.2: *Hot cracking test specimen; schematic drawing.*

2.3 Microstructure observations

Microstructural observations were always performed as close to the centre of the rod as possible or on the surface of CR samples (unless specified). All samples were prepared by mechanical abrasion followed by electro-polishing as described below.

2.3.1 Samples preparation

For all observations, surfaces were prepared by manual grinding with SiC (P240 - P1200) paper, followed by electro-polishing in a 10% solution of perchloric acid ($HClO_4$) in ethyl alcohol (C_2H_5OH), under 25-30V for 20-40s at room temperature. The so obtained state of the surface was generally satisfactory for further observations by electron microscopy or XRD, with some occasional pits. Microstructure for light microscopy was revealed by electrolytical etching in oxalic acid under 6V for 60s at room temperature.

2.3.2 X-Ray Diffraction

Crystal structure and phase identification for samples at different states were determined using an X-ray diffractometer (MDR PANALYTICAL) with Cu K_α radiation operated at 40 mA and 45 kV. Same conditions were applied for dislocation density measurements, this time using Co K_α radiation. The analysed angle was between 50° and 52° for {111} peaks with a step size of 0.0125° and time of counts of 10 000 s/point. The dislocation density was later determined according to the variance method based on the moments of intensity profiles, developed by Borbely and Groma [140].

2.3.3 Scanning Electron Microscopy

SEM Zeiss SUPRA55VP was used for microstructure observations in backscattered electrons (BSE) mode operated at 20kV. The same microscope was used for electron backscatter diffraction (EBSD) analyses with the step size between 0,06 and 0,1 μm. The EBSD data were analysed with the HKL Channel5 software (Oxford Instruments NanoAnalysis, version 5.11.10405.0). In this work, a *grain* was defined as an aggregate of data points that have relative misorientation smaller than 2°. The minimum size of the aggregate was set depending on specimen; for example for *as forged* samples, collection of at least 4 pixels with relative misorientation <2° were considered as a *grain*. Grain boundaries were set as a change in orientation over 15° and subgrain boundaries as over 2°. Twin boundaries were included in the measurements.

Local chemical composition was analysed by the SEM microscopes equipped with energy dispersive spectrometers (EDX): JEOL 6500F equipped with silicon diode detector Princeton Gamma tech; and Zeiss SUPRA55VP equipped with Oxford's SDD detector XmaxN 80.

2.3.4 Transmission Electron Microscopy

TEM samples were prepared by cutting small discs of $\phi = 3$ mm, thickness = 100 μm and later twin-jet electropolishing with Struers TenuPol-5 device. The bath was a 10% perchloric acid solution in ethanol ($HClO_4$ + C_2H_5OH), the potentials were between 14-18 V and the temperature was between -4°C and 0°C. The observations were made on Philips CM200 TEM operated at 200 kV.

Part of the observations was done on samples prepared by FIB to enable analyses in selected areas of heterogeneous materials. The microscope used was a Jeol 3010-LaB6, operated at 200 kV, held in SIMaP, Grenoble. It is equipped with ASTAR, *Automatic phase and orientation mapping*, allowing scanning in transmission mode [141]. The EDX, being also part of the equipment, was used for chemical composition maps.

2.4 Mechanical tests

2.4.1 Vickers Hardness measurements

Vickers hardness was measured under a load of 10kg. At least five equally spaced indents were made and the average values were calculated.

2.4.2 Compression and tensile tests

Compression tests were performed on cylindrical samples, h = 9mm, ϕ = 7mm, at temperatures 25 - 1050°C with strain rate of 10^{-1} s^{-1} and 10^{-3} s^{-1} in a Schenck compression machine. Strain was later defined as follow:

$$\bar{\epsilon} = -ln\frac{h_{cur}}{h_0} \tag{2.3}$$

where h_{cur} is the current and h_0 initial sample height. Since height during uni-axial compression tests changes and surface of the sample is in direct contact with pistons, friction between the sample surface and the piston has to be taken into account. The experimental stress should be corrected according to the equation 2.4:

$$\sigma = \sigma_{exp}\left[1 + \frac{2}{3\sqrt{3}}\bar{m}\frac{r_0}{h_0}exp\left(\frac{3\bar{\epsilon}}{2}\right)\right]^{-1} \tag{2.4}$$

where $\sigma_{exp} = F/S_{cur}$ is the stress for the current cross section of the sample, $\bar{m}$ is a friction coefficient (value of 0.1 was taken), $\frac{r_0}{h_0}$ is the slenderness ratio that influences the friction, where r_0 is equal to $\phi/2$, and $\bar{\epsilon}$ is the applied strain.

Tensile tests were performed on threaded-headed cylindrical specimens, l = 50mm, ϕ = 4mm (as shown in Figure 2.3), at the strain rate of 10^{-3} s^{-1}. Both behaviour at room temperature and in cryogenic conditions was tested. For the latter case, a temperature of -150°C was obtained in an isolated chamber by evaporated liquid nitrogen. The experimental machine was a screw-driven Schenck test machine. An extensometer was used to measure engineering strain. True strain can be defined as:

$$\bar{\epsilon} = ln\left(1 + \frac{\Delta l}{l_0}\right) \tag{2.5}$$

where Δl is the increased in length and l_0 is the initial length of the sample. True stress can be determined hypothesising that the volume of the sample is constant and it can be described according to the equation 2.6:

$$\bar{\sigma} = \sigma\left(1 + \frac{\Delta l}{l_0}\right) \tag{2.6}$$

where $\sigma = F/S_0$ is the engineering stress. All curves were drawn as a relation of true stress vs true strain. The totality of the curve was shown, even though once the necking begun, it has little physical sense.

Work hardening coefficient p for curves coming both from compression and tensile tests was calculated from the Hollomon equation:

$$\sigma = K\epsilon^p \tag{2.7}$$

$$log\sigma = logK + p \cdot log\epsilon \tag{2.8}$$

where σ is the stress, ϵ is the plastic strain and K is a material constant. The coefficient p was determined from the slope of a plot of logσ vs logϵ, in the linear area.

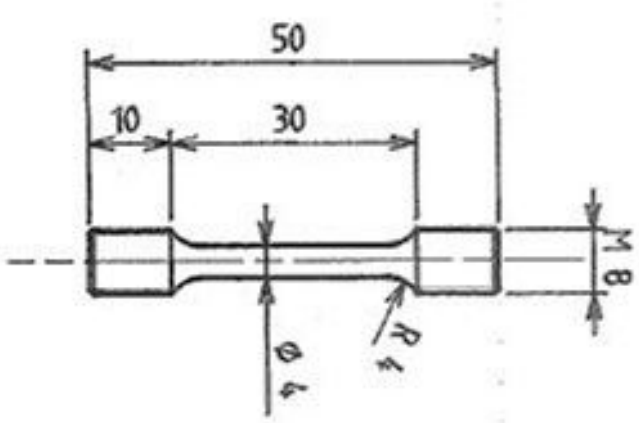

Figure 2.3: *Schematic specimens for tensile tests*

A set of relaxation tests was performed on cylindrical tensile samples on the same screw-driven Schenck test machine. Example of cycle of stress measurement as a function of time reading during one relaxation set is presented in Figure 2.4. A series of 5 relaxations of $t = 30$ s each were done for various loads, following the Spatig procedure [91]. Upon reaching the imposed load, pistons were stopped for time t, after which strain was applied again on the sample until the same load was attained. This action was repeated 5 times. After last relaxation of the set, the sample was strained till next imposed load value and the process was repeated. More details about analysis of these results are presented in Appendix 1.

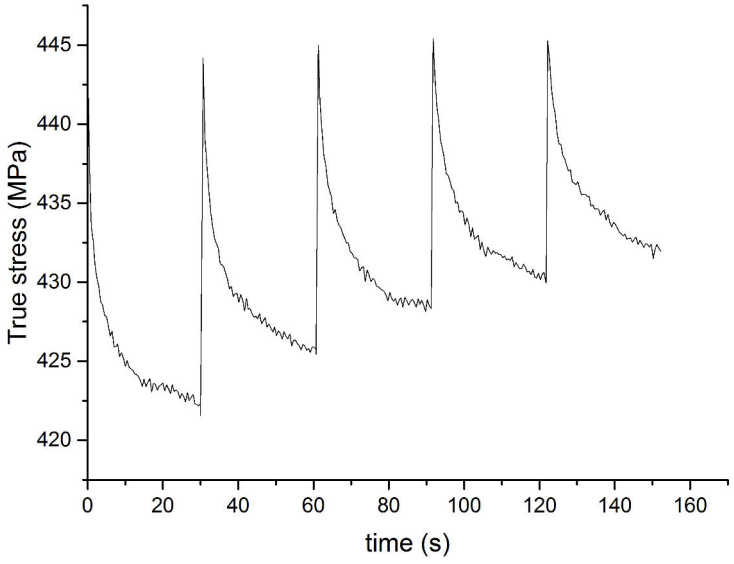

Figure 2.4: *Representation of a relaxation set at 445 MPa*

2.4.3 Charpy impact toughness

Charpy impact toughness tests were performed on V-notched samples with square cross section of dimension 5mm x 5mm and the notch depth of 1mm (Figure 2.5). One reference test at room temperature was performed. Two samples were tested in cryogenic temperatures. To cool down, the specimens were immersed in liquid nitrogen for 6 minutes. Charpy impact toughness KCV was calculated from the 2.9 equation, where KV in the energy absorbed by rupture and S_0 is the surface of the sample in rupture zone.

$$KCV = \frac{KV}{S_0} \tag{2.9}$$

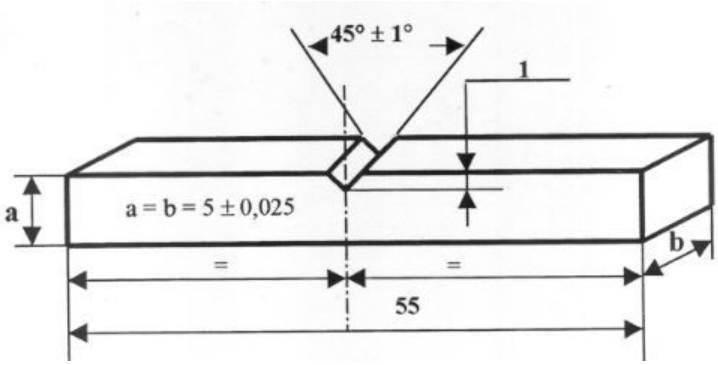

Figure 2.5: *Schematic specimens for Charpy impact toughness tests*

Chapter 3

Selection of original HEAs and their first evaluation

Contents

Goal of this work is to design and evaluate new alloys, based on the CoCrFeMnNi family with decreased or totally eliminated Co addition. First step on the path of searching for such possible grades of alloys was computational design. Based on thermodynamic calculations, phase stability can be predicted. This initial approach allows to narrow down the number of compositions and experimentally analyse only the most promising ones. Once the alloys are cast and transformed, their microstructure and mechanical properties are verified. Those primary results allowed to identify the most encouraging composition as well as some unusual phenomena occurring in this family of alloys.

3.1 Computational design of new HEAs

Choice and optimisation of new compositions often starts with thermodynamic simulations. In the case of this study, Thermo-Calc software, together with its databases, was used. Available databases and extrapolations to high order systems allow a preliminary insight into possible phases formed at equilibrium in a large range of compositions and temperatures. Obviously, those calculations do not fully represent the reality and their credibility depends on number of fully assessed lower order systems included in the available databases [50]. Especially σ phase appears to be the most problematic in the CoCrFeMnNi system and is often underestimated in the predictions [38]. In case of present study, due to high number of elements and their elevated contents, various databases could have been applicable among those proposed by Thermo-Calc, the software used for simulations. The databases that were considered are for iron based alloys, TCFE, for nickel based alloys, TCNI, and latest database for high entropy alloys, TCHEA. In this work most phase diagrams were calculated in the TCFE5 database and compared with the first version of high entropy alloys database TCHEA1.

Decrease or even total elimination of Co content while keeping the fcc single phased structure was a priority in the search of new compositions. To do that quasi-binary phase diagrams were simulated. The main criteria imposed during alloys selection were: 1. large domain of single fcc stability and its minimal temperature as low as possible; 2. absence of secondary phases, in particular σ phase, or their appearance for temperatures as low as possible to decrease the driving force of precipitation; 3. to keep high Cr content, for sufficient corrosion resistance of the alloy.

As it was previously shown in the literature, the quaternary equiatomic CrFeMnNi alloy exhibits a multi-phased structure [20, 72]. This outcome is well predicted by Thermo-Calc where single fcc domain is not present for this composition, as shown in Figure 3.1a. To ease the comparison of presented phase diagrams, two characteristic

points were defined: the minimal temperature of fcc stability, T^{fcc}_{min}, and the maximal temperature of σ phase appearance, T^{σ}_{max}. Change of their position will be followed across analysed diagrams.

Substituting Co entirely by Fe, leading to $Cr_{20}Fe_{40}Mn_{20}Ni_{20}$ composition, does not influence much the phase diagram, Figure 3.1b. The predicted phases are the same with only slight change of position of characteristic points. Stability of fcc phase is predicted down to around 850°C, which is still very high. Formation of σ phase is prompt to appear in a wide range of temperatures specially for Cr content above 18 at.%, where the maximum temperature of its stability can be found. The risk of multi-phased structure is quite high for this composition.

Substitution of Co by Ni was also analysed and the result is presented in Figure 3.1c. Strong decrease of temperature of fcc stability can be noticed. At the same time this point appears for very low Cr contents around 5 at.%: such limited Cr content in an alloy can lead to dramatically lowered corrosion resistance. On the other hand the $Cr_{20}Fe_{20}Mn_{20}Ni_{40}$ does not present any σ phase, at any range of temperatures. Its presence is limited for low Cr content. However, for compositions with Cr > 6 at.%, the bcc phase predicted next to the fcc one is nearly pure Cr (90 at.%). It not only decreases the Cr content in the fcc solid solution but at the same time puts the alloy at risk of brittleness. Large domain of appearance of the bcc phase leads to high driving force for precipitation in large range of temperatures, increasing the probability of presence of this second phase.

Further focus in research of new compositions was put on non-equiatomic alloys. It was already reported that increasing Cr content can lower fcc stability and lead to σ phase formation [83, 125, 126]. Let us note that the Cr content in the searched alloys may be considered as one of principal criteria for which a compromise needs to be found. Firstly, it is necessary at elevated concentration for good corrosion resistance. On the other hand, increased Cr content results in elevated T^{fcc}_{min}, as seen in phase diagrams presented in Figure 3.1. Such good compromise was achieved by Mroz for a quinary non-equiatomic composition $Co_{20}Cr_{15}Fe_{26}Mn_{17}Ni_{22}$, also called A3S [115, 142]. This composition presents a large fcc zone with a minimum stability temperature at about 550°C for 15 at.% Cr, Figure 3.1d. Additionally, formation of σ phase is strongly suppressed. It is limited to a narrow range of temperatures (500 - 550 °C), meaning that its formation can be easily avoided through appropriate heat treatments. Moreover, this composition was confirmed to have a stable fcc phase even upon long time annealings due to slow transformations kinetics: only trace amounts of second phases were observed after 300 days at 500°C).

Since proportions between elements as designed in the A3S composition proved to be profitable for increased fcc stability, this basis was used for further search of new compositions. The Co content was gradually decreased up to total elimination.

Attempts to substitute it by other transition metals outside of CrFeMnNi family were done. However, their poor solubility in the fcc solid solution did not allow for their increased concentrations; only slight doping could have been considered. As a consequence, the Co content needed to be substituted by one of the initial four elements. For obvious reasons substitution by chromium was not considered, as it is a strong bcc stabiliser and its increased content leads to high presence of σ phase. Manganese was also omitted due to its negative influence on corrosion resistance as well as, the problems it brings into the technological process of alloys preparation: high evaporation and facility of oxides formation. Finally, Ni was not considered either as it leads to fcc stability for low Cr content only, not sufficient for good corrosion resistance (Figure 3.1c). The choice was made to fully substitute Co by iron fixing all the other elements.

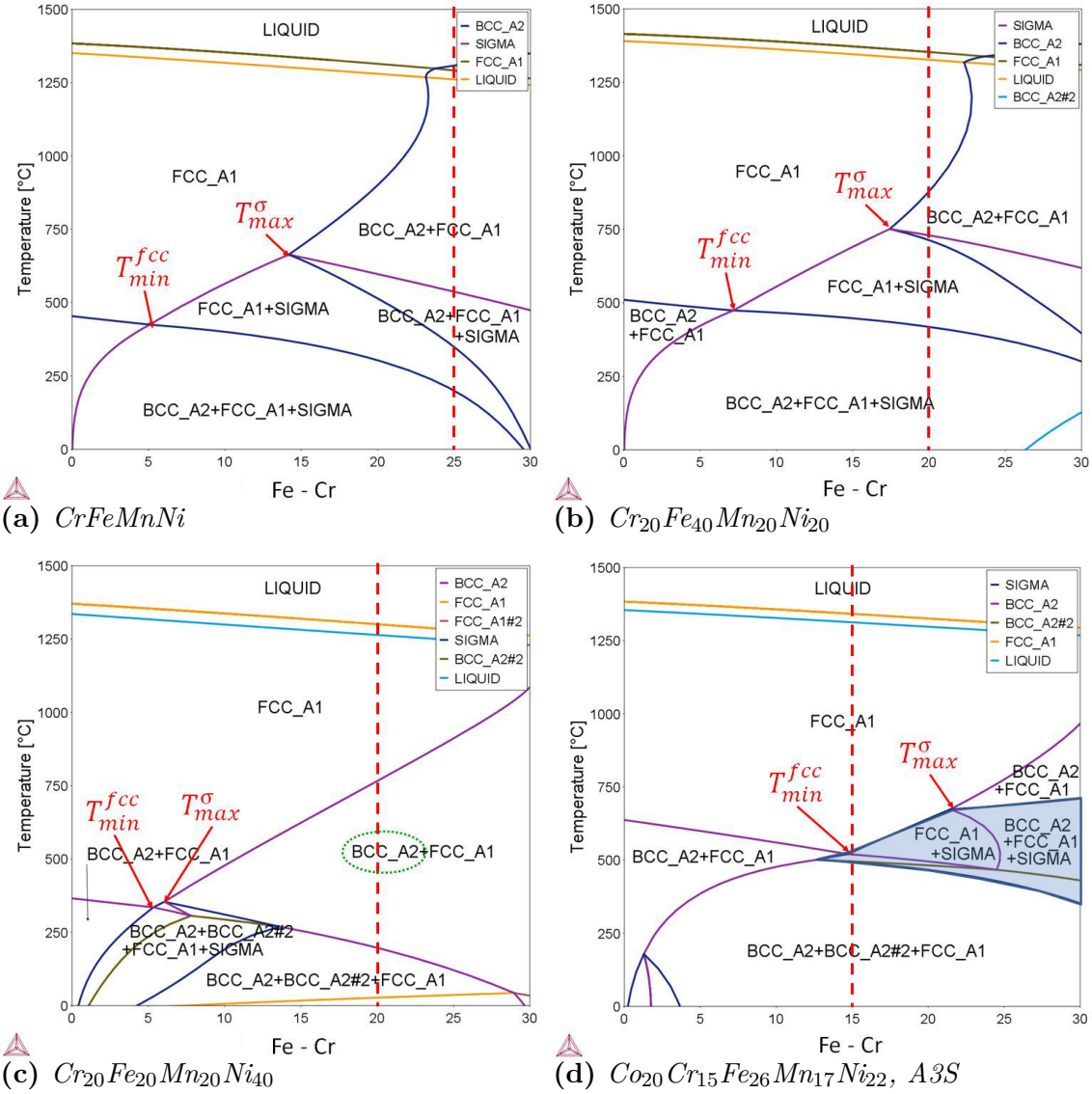

(a) $CrFeMnNi$ **(b)** $Cr_{20}Fe_{40}Mn_{20}Ni_{20}$

(c) $Cr_{20}Fe_{20}Mn_{20}Ni_{40}$ **(d)** $Co_{20}Cr_{15}Fe_{26}Mn_{17}Ni_{22}$, *A3S*

Figure 3.1: *Quasi-binary Fe-Cr phase diagrams of a) equiatomic CrFeMnNi, b) $Cr_{20}\mathbf{Fe}_{40}Mn_{20}Ni_{20}$, c) $Cr_{20}Fe_{20}Mn_{20}\mathbf{Ni}_{40}$ and d) $Co_{20}Cr_{15}Fe_{26}Mn_{17}Ni_{22}$, A3S. All diagrams calculated in iron TCFE5 database.*

As presented in Figure 3.2, the relatively low temperature of fcc phase stability is maintained within the wide range of Co content. Between 0 - 30 at.% Co, the T_{min}^{fcc} varies from 500 - 660 °C. Those values are still much lower than for other compositions previously presented in this study (Figures through 3.1a to 3.1c). At the same time, it can be noted that the decrease of Co in the A3S composition leads to reappearance of σ phase. It either totally replaces or accompanies the Cr-rich bcc phase. However its T_{max}^{σ} lower than for other compositions should lead to slowed down precipitation kinetics and thus lower probability of its presence.

For further study, three compositions were chosen based on the A3S alloy. For the first two compositions, Y1 low-Co(V) and Y2 low-Co, the Co content was decreased down to 10 at.%. In the Y1 low-Co(V) composition 1 at.% of V was added compared to Y2 low-Co. The purpose of this approach was to verify the efficiency of enhancing the solid solution strengthening. However, due to limited solubility, higher concentration could not be considered. Finally, the cobalt content was completely substituted by Fe in the Y3 Co-free alloy. The three chosen alloys, Y1 low-Co(V), Y2 low-Co and Y3 Co-free, whose detailed compositions can be found in Table 2.1, were further cast and the formed phases were identified.

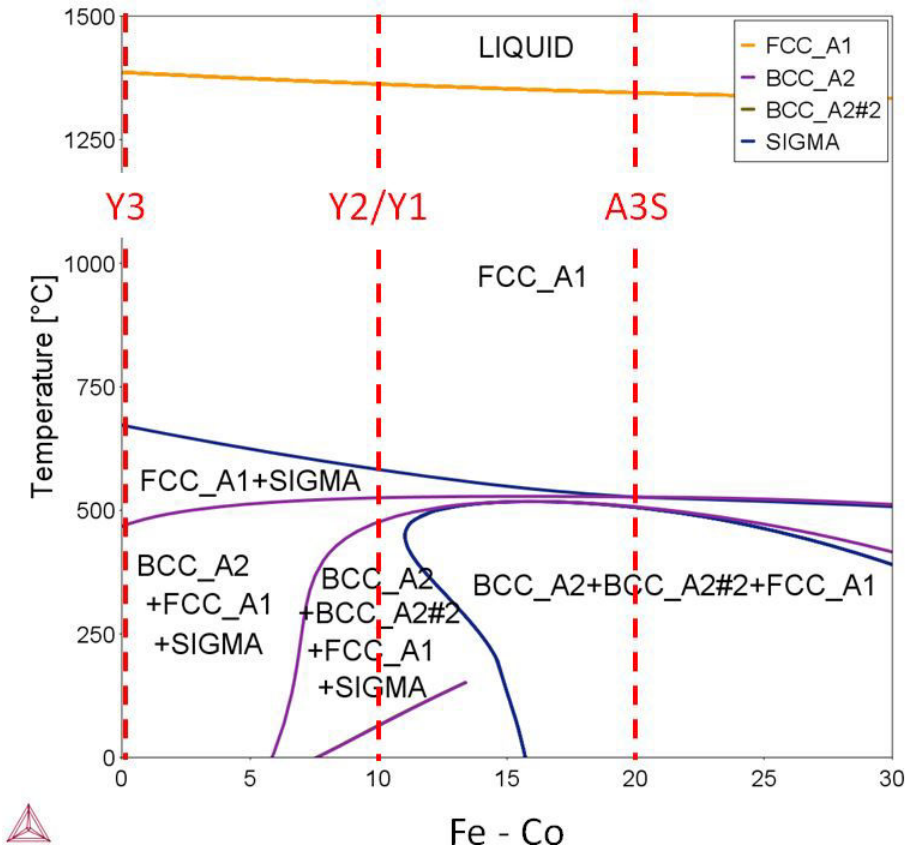

Figure 3.2: *Quasi-binary Fe-Co phase diagram representing Y2/Y1 and Y3 alloys next to the A3S composition. Diagram calculated in the TCFE5 database.*

When the phase diagram for Y3 Co-free composition as a function of Cr content is considered, Figure 3.3a, it can be noted that the formation of high temperature

bcc phase was shifted to increased Cr concentration further from the nominal 15 at.%. For this composition the T^{σ}_{max} was decreased to about 660°C, which is over 100°C lower than for other, previously considered Co-free compositions.

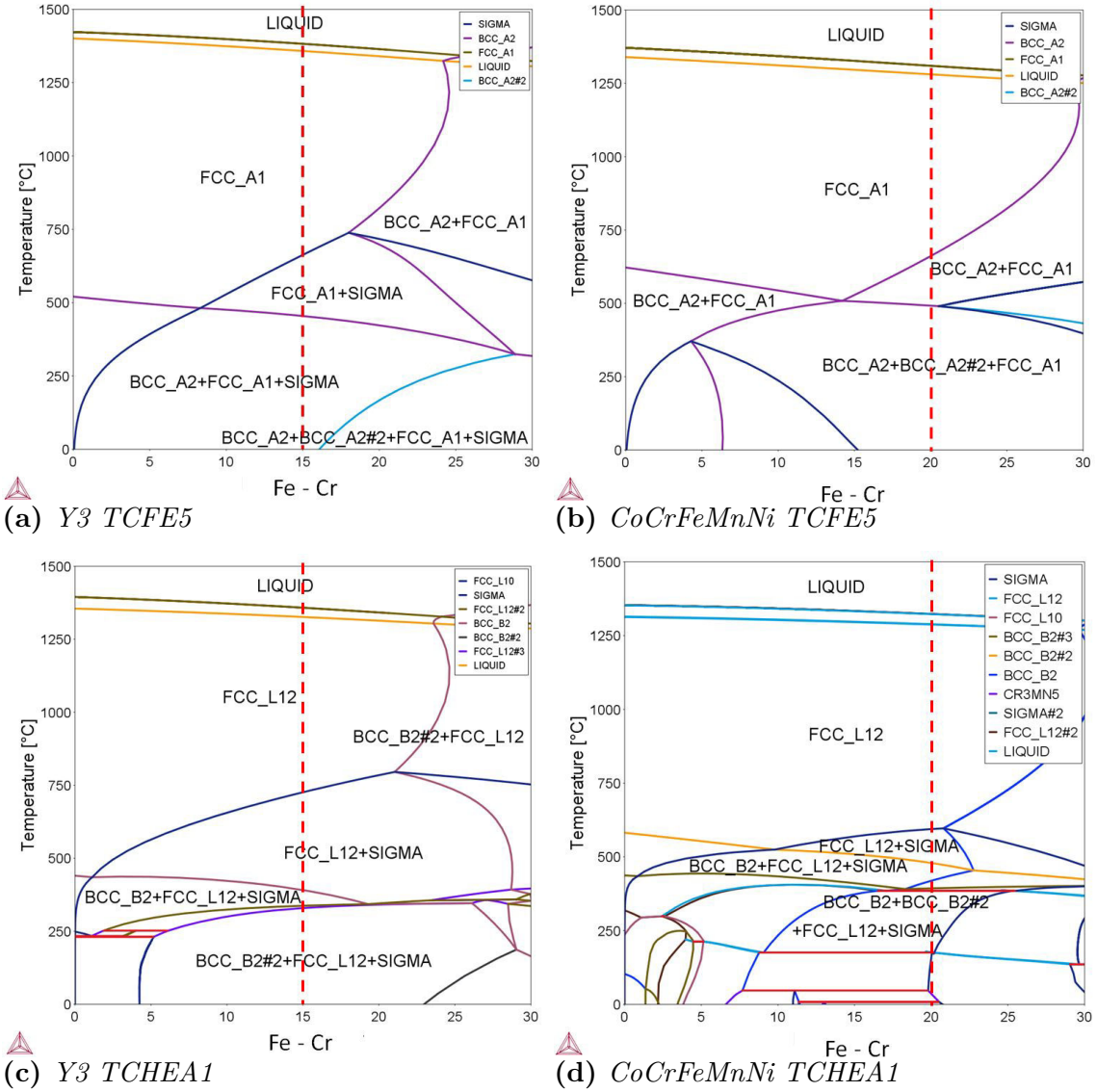

(a) *Y3 TCFE5* **(b)** *CoCrFeMnNi TCFE5*

(c) *Y3 TCHEA1* **(d)** *CoCrFeMnNi TCHEA1*

Figure 3.3: *Quasi-binary Fe-Cr phase diagrams of Y3 and equiatomic CoCrFeMnNi in two databases: iron TCFE5 (a, b) and HEA TCHEA1 (c, d)*

Once the new High Entropy Alloys database, TCHEA1, was released in late 2015, the phase diagrams for chosen compositions were verified again. Comparison of equilibrium phase diagrams for Y3 and Cantor's alloy calculated in both TCFE5 and TCHEA1 databases is presented in Figure 3.3. Let's note that the TCHEA1 database results suggest apparent ordering of both fcc ($L1_2$) and bcc (B2) phases. In fact, this is an artefact coming from the database description, where both ordered and disordered fcc/bcc structures are modelled as one phase labelled equivalently. If one verifies detailed information about the predicted phases, it becomes obvious that specific composition for each sub-lattice is exactly the same and equal to nominal

composition. It means that the phases are perfectly disordered at the atomic scale.

Furthermore, the complexity of the diagrams increased for the new database, more phases are permitted at lower temperatures. For calculation in both databases, higher number of phases is present in the quinary alloy than in the quaternary non-equiatomic Y3. For TCHEA1 the difference is even clearer. It is due to a more complex system with an additional element for the Cantor's alloy. For both alloys formation of σ phase is emphasised in TCHEA1: not only its stability begins at higher temperatures but it is also present through a wider range of Cr content. Nonetheless, the large single fcc domain is maintained. Both alloys are predicted to solidify into fcc solid solution that is stable down to 600-700°C. In all four diagrams in Figure 3.3 the temperatures of solidus and liquidus are similar (slightly higher for Y3 than CoCrFeMnNi) and the solidification range is narrow.

An easy to understand representation of phase stability in alloys is shown in Figure 3.4a, for the Y3 composition. It allows to see clearly all the temperatures at which phase transformations take place; both with the fraction of each phase present. Solidus temperature is predicted at about 1360°C, σ formation starts at 660°C and bcc Fe-rich phase just below 500°C. Yet, these computational results need to be checked: phase stability of the Y3 Co-free alloy at 500°C will be addressed in the next paragraph. Anyhow, compared to the melting temperature obtained via mixing rule, which is at the order of 1830°C for Y3 and similar for other compositions (see Table 3.4), Thermo-Calc prediction indicates a much lower value. Measurements by Differential Thermal Analysis (DTA) for Y3 alloy confirmed the accuracy of calculations with the value of solidus temperature for melting $T_M = 1343$°C. Verification of temperature during alloy preparation shows that casting done at $T \approx 1400$°C ensures fully liquid state and good fluidity of the melt, which confirms as well the validity of thermodynamic calculations.

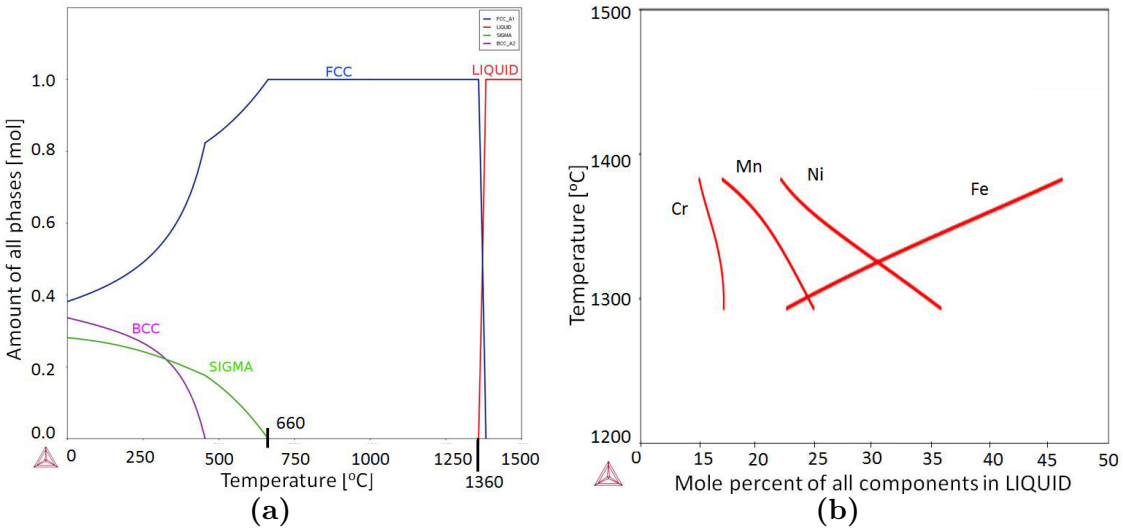

Figure 3.4: *Thermo-Calc diagrams of Y3: a) equilibrium phase composition and b) change of chemical composition of liquid during solidification according to Scheil-Guliver model. Calculations done in TCFE5.*

Thermo-Calc also foretells presence of chamical segregation during casting according to Scheil-Guliver model, Figure 3.4b. First, liquid solidifies with chemical composition close to the nominal one. Later on, with temperature decrease, the composition of remaining liquid changes through classical mechanisms of equilibrium between solid and liquid phases. When the temperature decreases, liquid becomes depleted of Fe and enriched in Mn and Ni. It is clear that the last liquid present at the end of solidification process, at about 1300°C, contains high amount of manganese and nickel, while the iron content drops drastically. There is little difference in Cr content throughout the solidification process. The segregation leads to variation in local composition and consequently change of local equilibrium. It is the reason for extended solidification range predicted by this model, compared to the equilibrium phase diagram. At the same time, it can be noted that the variation in elements content is continuous, confirming that no second phase is present upon solidification. The cast is predicted to be fully single phased.

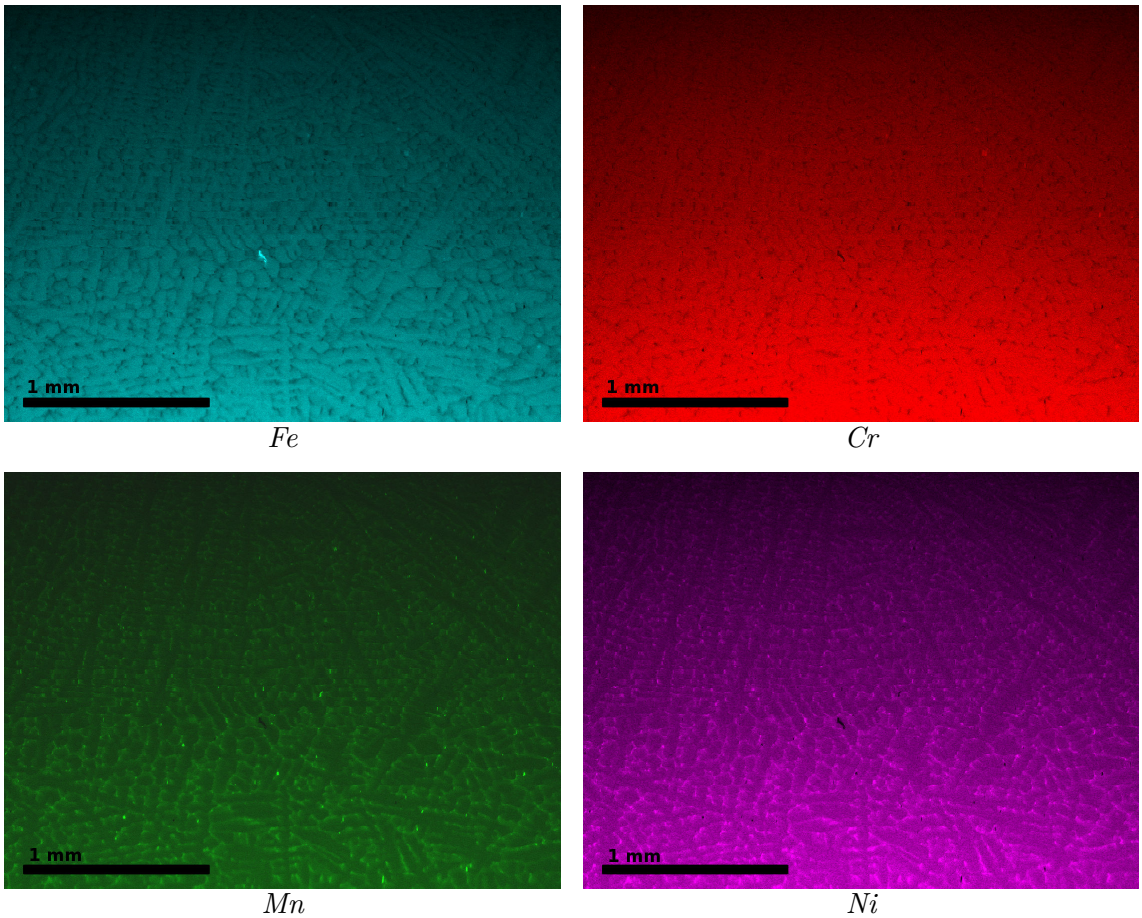

Figure 3.5: *EDX map analysis of as cast Y3 alloy with visible dendritic segregation.*

Thermo-Calc predictions have been experimentally confirmed by microstructural observations together with EDX mapping of Y3 alloy at the *as cast* state. Clear dendritic structure with presence of solidification segregation is presented in Figure 3.5. Long time of data collection allows to distinctly see the dendritic structure due

to differences in chemical composition. The interior of dendrites is highly enriched in Fe, whereas interdendritic zones present elevated content of Mn and Ni. Cr is dispatched in a more even way with little differences noticeable. It is encouraging to confirm that both experimental and theoretical data comply up to a certain level and existing thermodynamic calculations can be used as an insight into promising compositions, at least to determine the high temperature stability.

To summarise this part, in the frame of this work various quasi-binary phase diagrams were simulated by Thermo-Calc and thoroughly analysed in the search for new compositions. Finally, in preselected alloys, the substitution of Co was made by Fe atoms significantly increasing its content up to 46 at.%. As a consequence the use of TCFE5 seams justified and any further reference to TC calculations implies the use of iron database. In any case, the quasi-binary phase diagrams are an indication of equilibrium phases in the alloy and they should be used as initial tool for choice of composition. Three selected compositions were further analysed in the context of phase formation by calculation of empirical parameters.

3.1.1 Low temperature (500°C) phase stability: verification of thermodynamic calculations

Some recent publications showed that the equiatomic CoCrFeMnNi can be subjected to decomposition in certain conditions, as it was already presented in chapter 1.6.4. Despite being reported as a single fcc alloy in most studies, when exposed to temperatures below 800°C, besides the fcc matrix phase, four secondary phases were found: 1. σ Cr-rich phase, 2. bcc Cr-rich phase, 3. $L1_0$ ordered NiMn-rich phase and finally 4. FeCo-rich phase [17, 111–115]. The decomposition can be induced either by prolonged heat treatments, 100 days or more, but also strongly accelerated by severe plastic deformation due to increased number of fast diffusion paths (grain boundaries, dislocations). However, Thermo-Calc phase diagram simulations for Cantor's alloy do not predict most of those phases. Only σ Cr-rich phase is correctly foretold.

In the case of Y3 alloy, absence of fcc-stabilising Co, could lead to a decrease of single phase stability, which should be verified. Thermo-Calc quasi-binary phase diagram, as presented in Figure 3.6 (an insight into the diagram already shown in Figure 3.2), predicts presence of additional σ CrFe-rich phase upon reaching equilibrium below 650°C, and supplementary bcc Fe-rich phase below 480°C. A previous study by Otto et al. [17], where prolonged annealings of Cantor's alloy at various temperatures were performed, was the basis for setting conditions of this analysis. The temperature of 500°C was chosen, as highest degree of decomposition was found for this temperature in [17]. For Y3 Co-free alloy, Thermo-Calc predicts a presence of 10% σ phase next to the matrix at this temperature. Detailed chemical

compositions of both phases are presented in Table 3.1. To compare the correctness of those predictions as well as the phase evolution of Y3 alloy with respect to Cantor's alloy a series of heat treatments at 500°C up to 500 days was performed. The samples were in two initial states: directly *as forged* or *annealed* at 1000°C 2h, to check the influence of microstructure on decomposition kinetics.

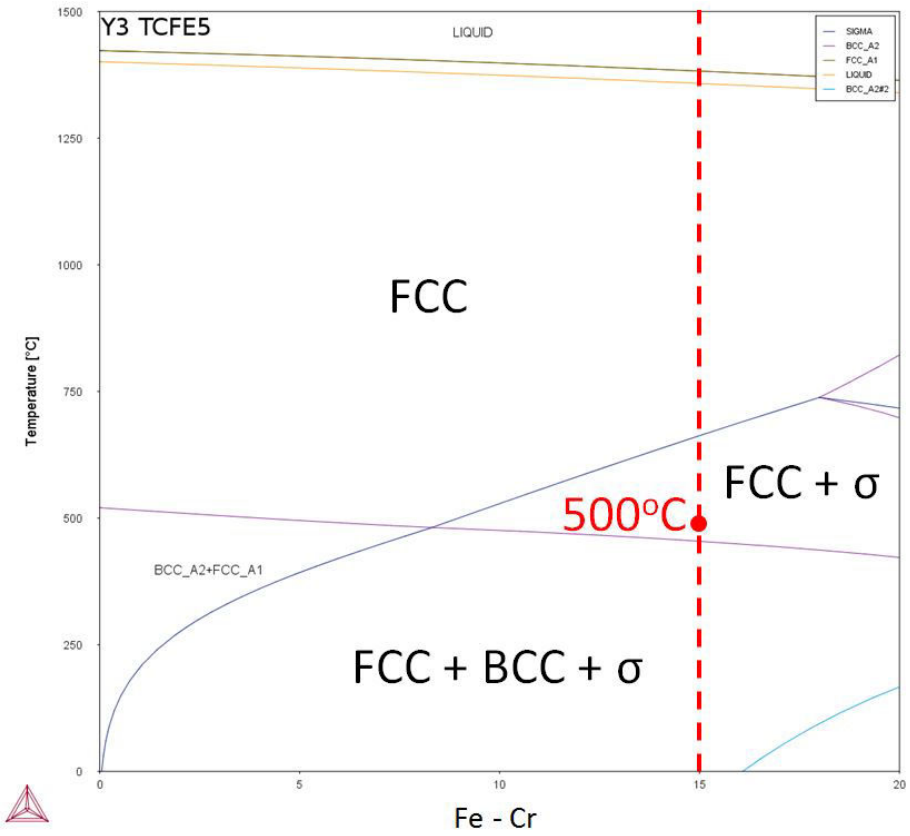

Figure 3.6: *Quasi-binary phase diagram of Y3 alloy calculated by Thermo-Calc TCFE5 database.*

Table 3.1: *Chemical composition (at.%) of phases predicted by Thermo-Calc and those observed by TEM EDX after annealing at 500°C 300 days.*

Method	Phase	Cr	Fe	Mn	Ni
Thermo-Calc, TCFE5	matrix (90%)	12	46	18	24
	σ (10%)	47	41	10	2
TEM EDX	matrix	11	38	25	26
	FeCr	84	16	-	-
	MnNi	4	1	48	47

Firstly, X-ray diffraction was performed on samples annealed up to 500 days at 500°C, presented in Figure 3.7. After any conditions of annealing, only peaks coming from the matrix fcc phase were detected, no additional peaks were found, in explicit: no σ phase was found. If Thermo-Calc prediction was to be believed, the formation of nearly 10 vol.% of this secondary phase should have been detected. It is clear that no

such amounts of secondary phase is present after 500 days at 500°C. The presented diffractograms come from samples with various initial states: *as forged*, AF, or annealed at 1000°C 2h, RQ. No particular differences were observed between the diffractograms, no matter the initial state of the sample. This result shows that even if any secondary phases are present, their volume fraction is below the 2% required to be detected by X-ray diffraction. It can be hypothesized that the fraction of secondary phases at saturation is indeed very low. Similar analysis was done on A3S and Cantor's alloys by Mroz [115]. X-ray analysis of A3S composition after 100 days at 500 °C gave the same result with only fcc phase detected. However, Cantor's alloy showed already the presence of multiple phases: next to the fcc matrix, the MnNi tetragonal phase, Cr bcc phase and FeCo B2 ordered phase were detected. After 200 days annealing analogous peaks were found with increased intensity suggesting higher volume fraction of secondary phases in Cantor's alloy. The identified phases were in accordance with those found by Otto et al. [17].

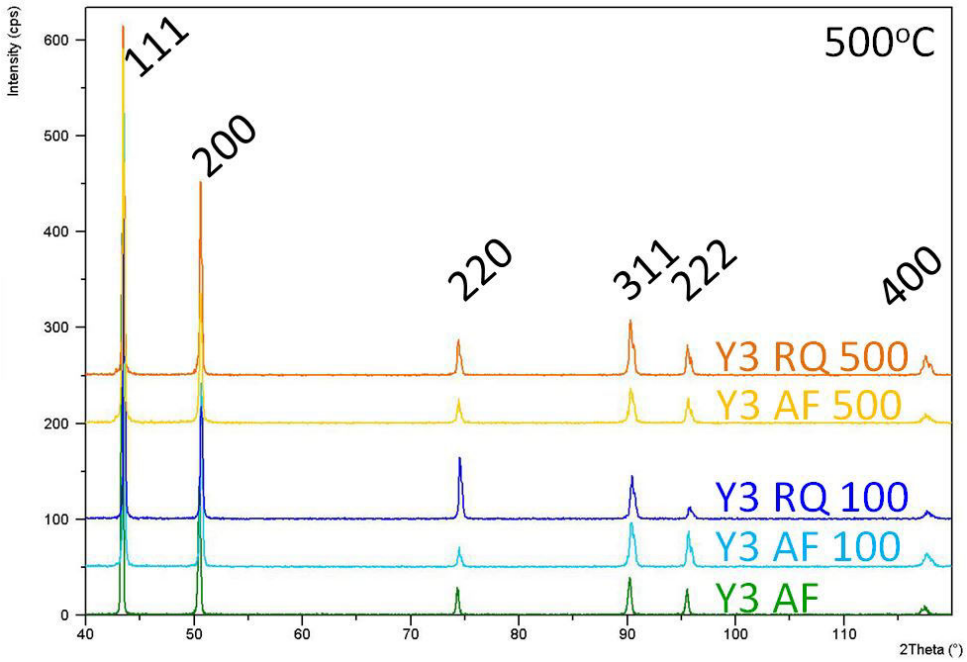

Figure 3.7: *Y3 alloy after 100 and 500 days annealing at 500°C, X-ray diffractograms. Alloy in two initial states: as forged (AF) or heat treated at 1000°C / 2h (RQ) prior to annealing. Comparison with initial as forged state.*

Next, microstructural observations of *annealed* Y3 at the scale of SEM were performed. Images of samples annealed for 100 days are presented in Figure 3.8. Y3 Co-free alloy is compared with Cantor's alloy [115]. The *as forged* Y3 alloy in Figure 3.8a shows a typical microstructure for HEA alloys prepared at EMSE laboratories: high misorientation in the grains leading to a difficulty to distinguish them. At the same time, pits due to electropolishing tend to follow a path that could easily be associated with grain boundaries (marked with arrows). It is an indication of pres-

ence of secondary phase, most probably on the grain boundaries, that was eroded during the process of samples preparation. Traces of precipitation were also found in the initially *annealed* state, however with lower fraction and not obviously on GBs, as indicated by arrows in Figure 3.8b. EDX analysis showed enrichment in Cr for most of them, and in MnNi for others. Yet, the volume fraction of those secondary phases for both *as forged* Y3 and *annealed* Y3 is low (not detected by XRD). In the case of Cantor's alloy the decomposition is much more pronounced. Images for a sample after forging and a sample after annealing coming from Mroz's thesis [115] are presented in Figures 3.8c and 3.8d. Here the distinction between single phased and decomposed area is clear. Zones with multiple phases are characterised by frequent change of colour from bright grey to black due to changes in chemical composition. It is evident that the volume fraction of secondary phases for Cantor's alloy is much more elevated than for Y3 Co-free alloy. Mroz reports total of 50% volume fraction of decomposed areas for Cantor's alloy, compared to certainly less than 2% in the Y3 composition. Same series of annealings for A3S composition shows that its decomposition is detected only after 300 days at 500°C, but again with volume fraction to low too be identified by XRD. Despite the absence of Co in Y3 alloy composition, it appears to be more stable than the equiatomic CoCrFeMnNi. However, compared to A3S alloy fcc stability was slightly decreased.

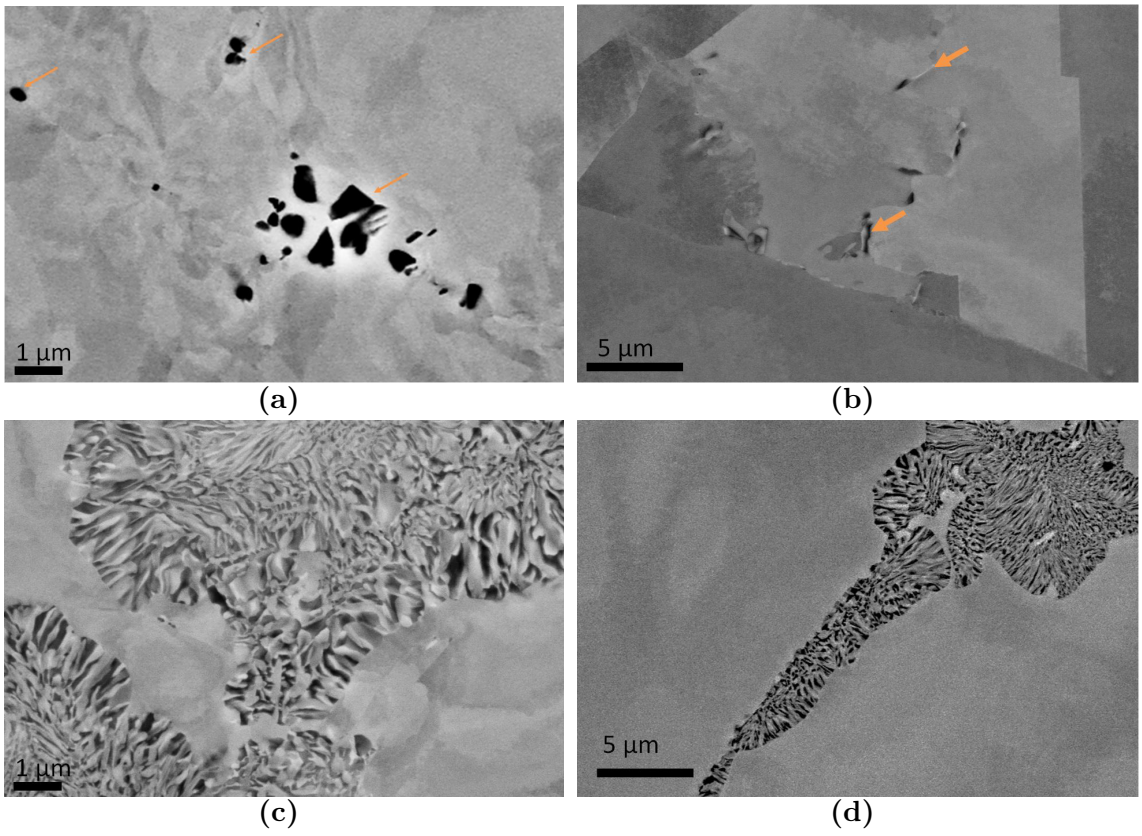

Figure 3.8: *Y3 Co-free alloy and Cantor's alloy [115] after 100 days annealing at 500°C. Two various initial states are compared: as forged and annealed (1000°C 2h). SEM BSE images of: a) as forged and b) annealed Y3 alloy; c) as forged and b) annealed Cantor's alloy.*

TEM thin foils of *as forged* Y3 alloy after 100 days of 500°C annealing, were prepared with the purpose of identification of secondary phases. A representative image is presented in Figure 3.9. Previous SEM observations suggested that precipitation may be preferentially placed on grain boundaries. This observation seams, in principle, confirmed by TEM. Unfortunately, foils preparation technique by electropolishing lead to preferential etching around the precipitates and their elimination. Numerous voids were found following the grain boundaries, however the precipitates could not be identified. At the same time, it is important to note that no traces of decomposition were found inside the grains. Moreover, the dislocations density remains elevated, and little change compared to the *as forged* state is visible. Despite annealing for 100 days at 500°C, the structure is still complex and did not evolve much compared to the initial state.

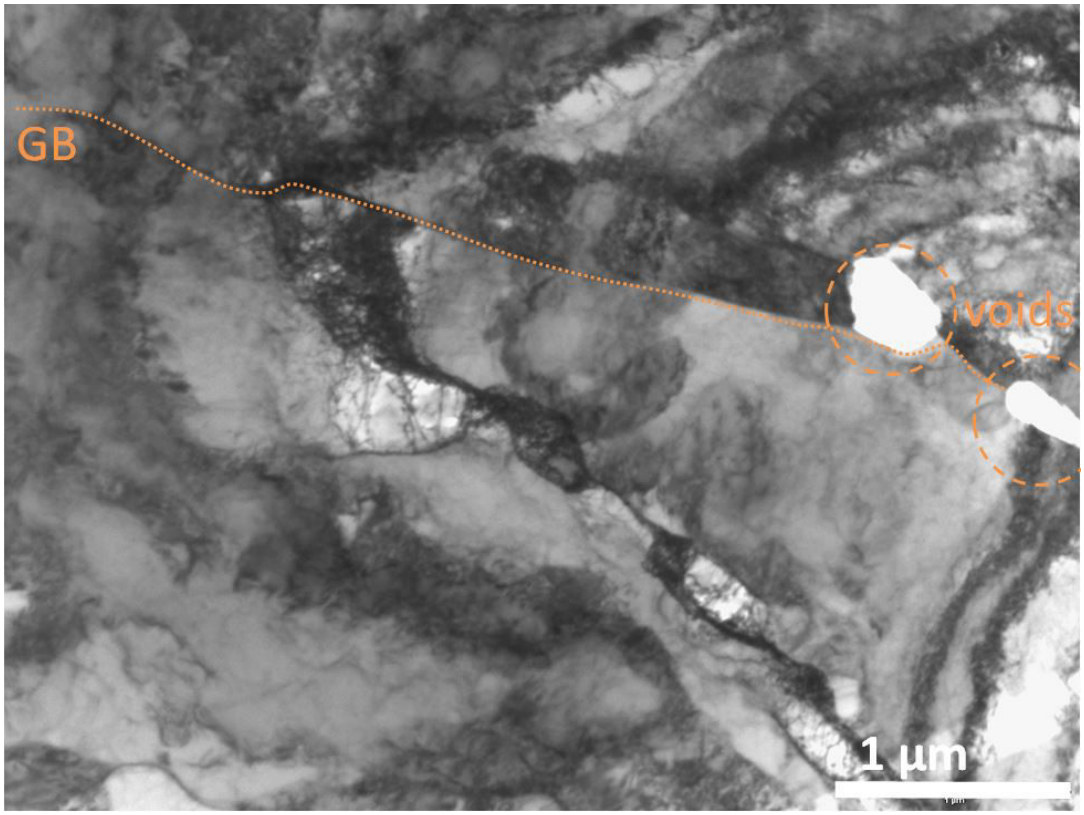

Figure 3.9: *As forged Y3 alloy after 100 days annealing at 500°C, TEM image.*

Since secondary phases could not yet be identified, neither by XRD, nor by TEM, samples after 300 days were further analysed by TEM together with ASTAR equipment in more detail. The structure obtained after this prolonged annealing is shown in Figure 3.10. Traces of secondary phases are clearly visible as numerous pits/voids are present due to preferential electropolishing around decomposed areas. To make sure that a zone with presence of the secondary phases is observed, an FIB thin foil was prepared. It was cut in the way to contain a grain boundary where most phenomena were detected, as shown in Figure 3.10 by an orange rectangle representing a zone of interest for thin foil extraction.

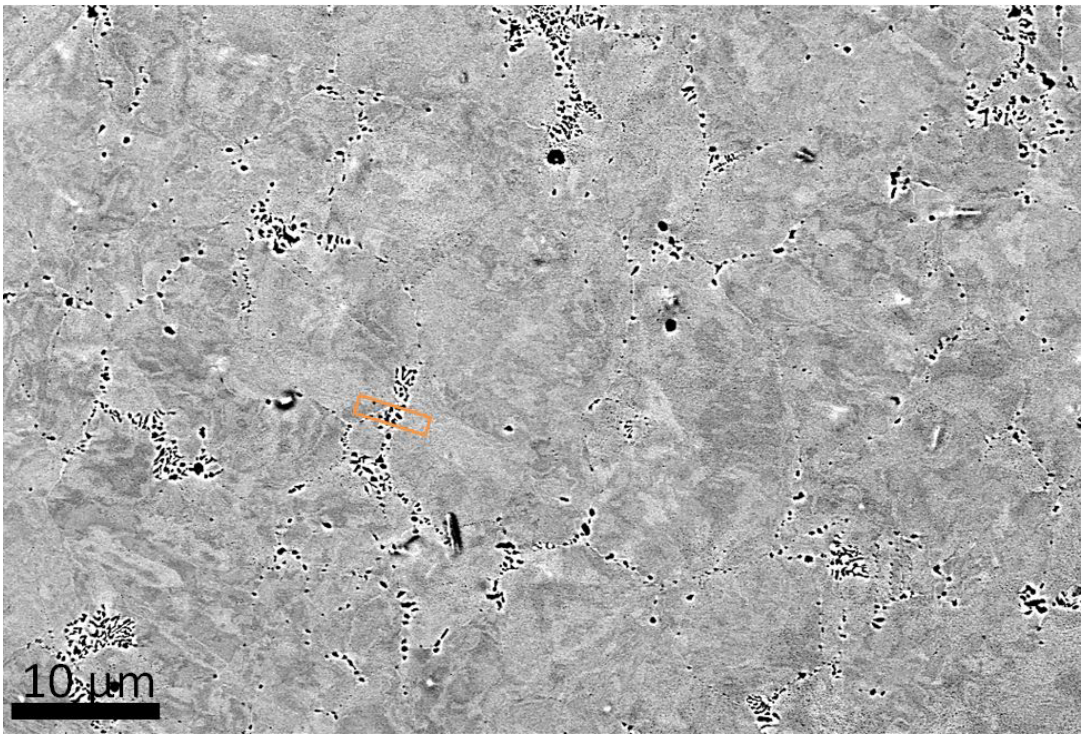

Figure 3.10: *As forged Y3 alloy after 300 days annealing at 500°C, SEM BSE image. Orange rectangle represents a zone of interest for thin foil extraction.*

A STEM image of the whole surface of the foil is presented in Figure 3.11a. The grain boundary is traced and numerous precipitates can be found in the upper grain. The ASTAR equipment allowed to perform an automatic phase identification in scanning mode. The result is presented in Figure 3.11b. Three distinct phases can be identified: in blue FeCr-rich phase, in green MnNi-rich phase and finally in red the fcc matrix. The dark filter represents the reliability of the identification. The darker the zone the lesser the reliability: therefore, other phases should be also considered. The identification is done based on previously indicated phase parameters from databases. The three phases were initially identified by analysis of TEM diffraction diagrams. Firstly, it was found that the FeCr-rich phase is a bcc phase $Cr_{70}Fe_{30}$ with cell parameter a = 2.87 Å that is not the σ phase as predicted by Thermo-Calc. Next, the MnNi-rich phase is the tetragonal $Mn_{50}Ni_{50}$ with cell parameters a = 2.61 Å, c = 3.49 Å. Finally, the matrix was confirmed to be the austenite with cell parameter a = 3.60 Å. The diffraction diagrams of fcc matrix and tetragonal MnNi in some orientations are very similar and differentiation between them is difficult. That is the reason for low reliability of the identification in certain zones of the matrix.

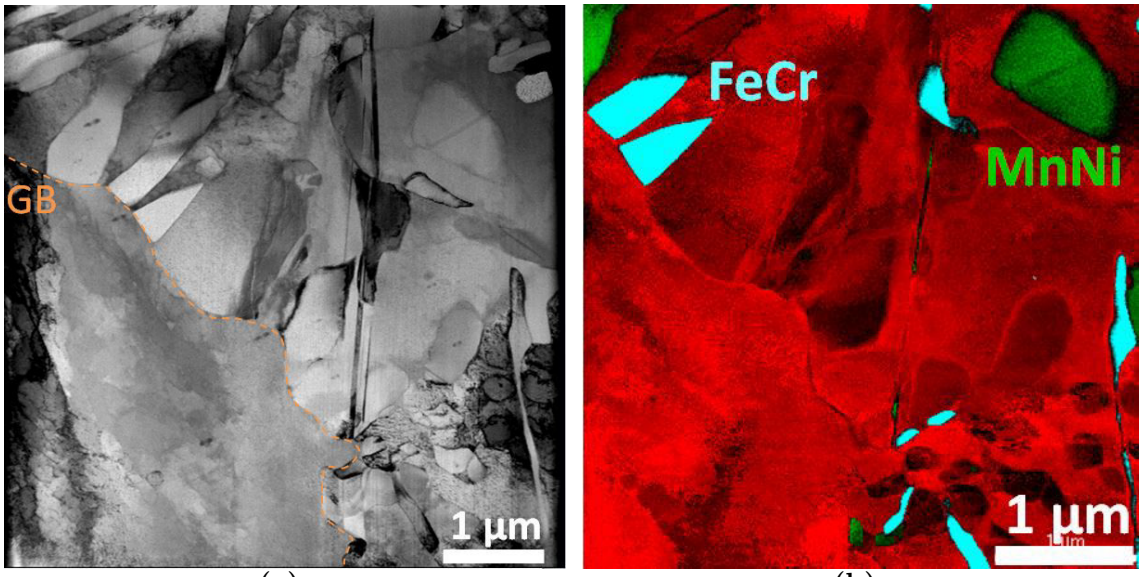

(a) (b)

Figure 3.11: *a) STEM BF image of the FIB thin foil coming from an as forged Y3 samples after 300 days at 500° C; b) Phase identification using the ASTAR equipment. Blue colour for FeCr-rich phase, green for MnNi-phase and red for fcc matrix. The superposed dark filter gives the information about reliability of the identification, the darker the zone the less reliable it is.*

To complete the obtained results of phase identification, EDX chemical elements mapping was done on the same zone. The results are presented in Figure 3.12. The difference in the shape of observed zones is due to the tilt of the sample necessary for EDX analysis. It can be clearly seen that the bottom grain contains no second phase and that all elements are distributed in an even way. All decomposition takes place in the upper part of the sample, most probably corresponding to a decomposed intergranular area. Presence of secondary precipitates is much higher than it would appear from the phase identification; in explicit, fraction of MnNi-rich phase is significantly increased in the analysed sample. At the same time the FeCr-rich phase was properly identified by ASTAR. The discrepancy for MnNi identification comes most probably from the similarity between the fcc matrix and the tetragonal MnNi phase diffraction diagrams. That is why simultaneous analysis of TEM phase indexation and distribution of elements is necessary. The distribution of two secondary phases is surprising. One would expect them to be in contact, next to each other as the elements from the single solution diffuse to one or the other phase. However, between each zone of secondary phase, fcc matrix is still present. The nature of secondary phases formation resembles to higher order precipitation.

More detailed chemical compositions coming from point analysis of individual decomposed zones are presented in Table 3.1. The values measured in the matrix derive compared to the nominal composition, but the measurement here was done on one small zone. Other measurements performed during TEM observations were reasonably close to required content. The chemical composition of CrFe phase is

richer in Cr than it could be expected according to phase identification. However, it confirms that it is not the σ phase predicted by Thermo-Calc. The composition of the MnNi phase is as expected according to phase identification from diffraction diagram, close to 50/50 proportions.

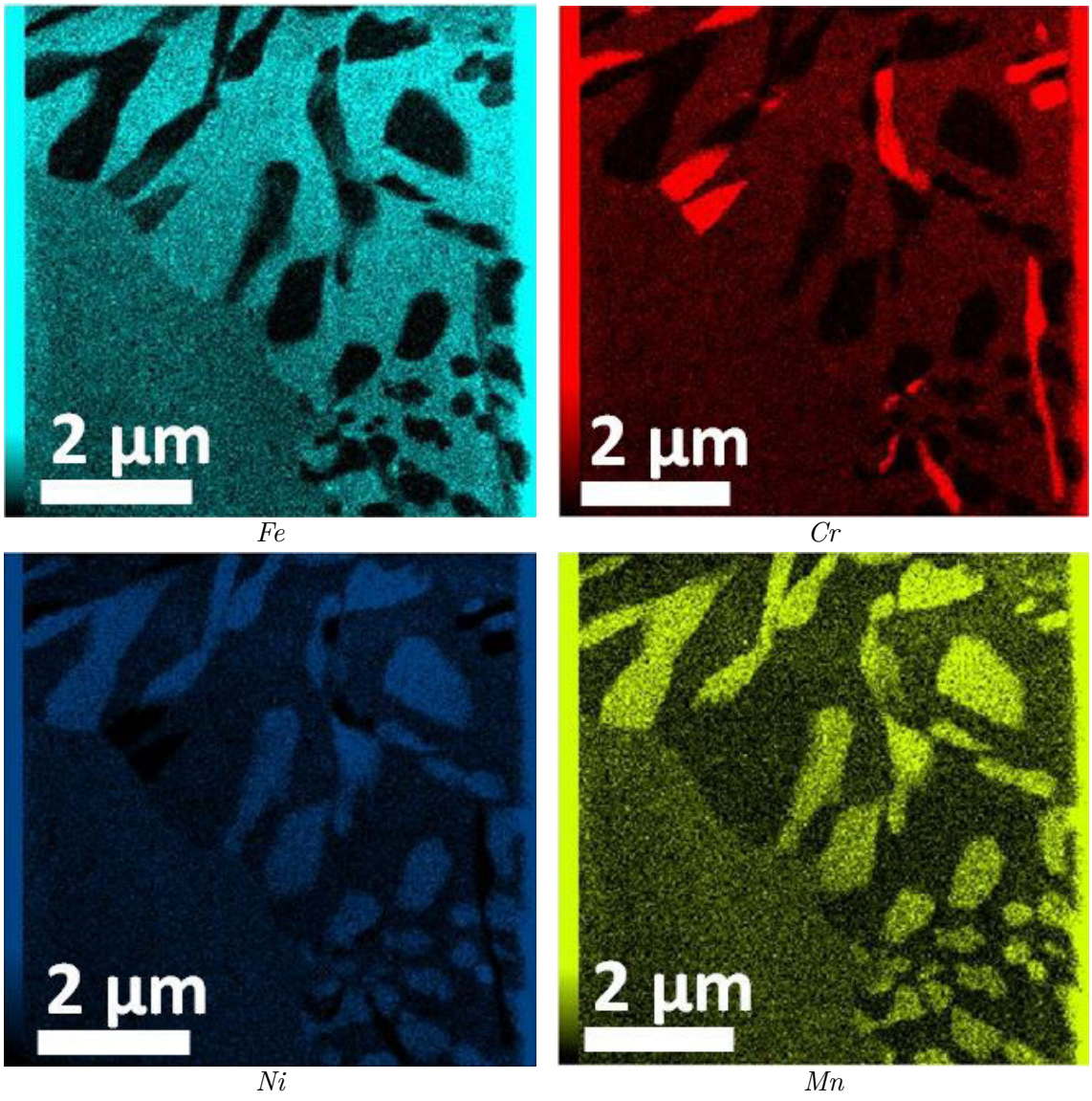

Figure 3.12: *Distribution of chemical elements in the FIB sample coming from as forged Y3 annealed at 500° C for 300 days, TEM EDX analysis.*

Prolonged annealing of Y3 Co-free alloy proved its increased phase stability compared to the equiatomic CoCrFeMnNi, although it is slightly decreased compared to A3S composition. Nonetheless, the result is very promising for the future.

It was proved that thermodynamic calculations performed with Thermo-Calc at 500°C, are in disagreement with observed phases. The phase equilibrium diagram did not correctly predict the formed phases, nor the created volume fraction. At this temperature the calculations are not viable and Thermo-Calc phase diagrams should not be considered for such complex systems at such low temperatures.

3.2 Verification of thermodynamic parameters for phase formation prediction in the specific HEAs

Thermo-Calc calculations allow an initial glimpse on possible phases present in chosen compositions, nonetheless other empirical parameters of phase prediction have been proposed specifically for HEAs. In literature, some fundamental thermodynamic criteria have been suggested to predict the phase formation in HEAs (already determined in Chapter1). Among them are: entropy of mixing ΔS_{mix}, enthalpy of mixing ΔH_{mix}, Ω parameter relating both entropy and enthalpy of mixing. Additionally, some physical parameters were determined as well: valence electron concentration VEC, electronegativity χ and atomic radius mismatch δ (all summarised in Table 1.1). To calculate those parameters for analysed alloys, some initial data is necessary for each chemical element as presented in Table 3.2. Also mixing enthalpies for binary systems present in the CoCrFeMnNi family are required for calculation of overall mixing enthalpy of each composition. They are grouped in Table 3.3.

Table 3.2: *Atomic radius, Allen and Pauling electronegativities, Valence Electron Concentration (VEC) and melting temperature of the constituent elements of the examined alloys [42, 143].*

Element	**Co**	**Cr**	**Fe**	**Mn**	**Ni**	**V**
Atomic radius [Å]	1.25	1.28	1.26	1.27	1.24	1.34
Allen electronegativity	1.84	1.65	1.80	1.75	1.88	1.53
Pauling electronegativity	1.88	1.66	1.83	1.55	1.91	1.63
VEC	9	6	8	7	10	5
Melting temperature [°C]	1531	1893	1571	1280	1489	1923

Table 3.3: *Mixing enthalpies for different binary systems [9].*

System	**FeCr**	**FeNi**	**FeMn**	**FeCo**	**CrNi**	**CrMn**	**CrCo**	**NiMn**	**NiCo**	**MnCo**
$\Delta \mathbf{H}_{AB}^{mix}$ $[kJ/mol]$	-1.5	-1.6	0.2	-0.6	-6.7	2.1	-4.5	-8.2	-0.2	-5.2

Results of calculations of phase prediction parameters are presented in Table 3.4. Values for Y alloys are compared with those calculated for A3S and Cantor's alloy. Firstly, melting temperatures values are based on the T_M of each element and its concentration (mixing rule). It gives quite high values compared to Thermo-Calc predictions and empirical measurements. Based on the quasi-binary phase diagrams, the solidus temperature is of the order of 1340°C for Y2 and 1360°C for Y3. The temperatures measured just before casting were as follow: 1390°C for Y2 and 1460°C for Y3, however overheating for cast Y3 was too high, since the precise melting

temperature was not known. The temperatures measured before casting show that Thermo-Calc estimations are reasonably valid, and are a better approximation than the approach based on simple mixing rule. To compare, the calculated T_M for SS 304L is 1858°C, but it is measured in the range between 1400°C and 1450°C depending on its precise composition.

Table 3.4: *Calculated values of average atomic radius $\bar{r}$, atomic radius mismatch δ, entropy of mixing ΔS_{mix}, enthalpy of mixing ΔH_{mix}, $\Omega = T_m \Delta S_{mix} / |\Delta H_{mix}|$, difference in electronegativity according to Allen $\Delta\chi_A$ and Pauling $\Delta\chi_p$, valence electron concentration VEC and melting temperature T_M of analysed Y alloys, as well as A3S [115] and Cantor's CoCrFeMnNi [30].*

Alloy	$\bar{r}$ [Å]	δ [%]	ΔS_{mix} $[\frac{J}{Kmol}]$	ΔH_{mix} $[\frac{kJ}{mol}]$	Ω	$\Delta\chi_A$	$\Delta\chi_P$	VEC	T_M [°C]
Y1	1.26	1.2	13.09	-3.31	7.13	4.44	7.47	8.17	1530
Y2	1.26	1.1	12.71	-3.34	6.86	4.06	7.29	8.20	1526
Y3	1.26	1.0	10.61	-2.62	7.41	3.97	7.13	8.31	1558
A3S	1.26	1.1	13.23	-3.87	6.09	4.13	7.41	8.17	1507
CoCrFeMnNi	1.26	1.1	13.38	-4.19	5.71	4.46	7.83	8.00	1517

For Y series of alloys, entropy of mixing, ΔS_{mix}, values are lower than for A3S or equiatomic CoCrFeMnNi. It is due to significantly decreased content of Co and thus, decreased complexity of the system. Nonetheless, those values are still in the empirical range for single phase formation suggested in literature, between 11 and 19.5 J/(K·mol). Obviously, the quaternary Y3 alloy presents ΔS_{mix} slightly below the minimum considered for all high entropy type alloys. Since the entropy of Y3 alloy is of only 1.28R, this composition should be considered as a medium entropy alloy. Nevertheless, no distinction will be made in this work and it will be considered as belonging to the large HEAs group.

Enthalpy of mixing, ΔH_{mix}, is slightly negative for all presented compositions and it is within the recommended range between -11,6 and 3,2 kJ/mol. Y3 composition presents the least negative value of ΔH_{mix} as well as lowest value of ΔS_{mix}. According to Gibbs free energy rule (equation 1.2), it may lead to lesser ΔG_{mix} compared to other HEAs and as a consequence, to a decreased relative phase stability, that may result in a demixion at lower temperatures. The single phase formation is in this alloy less certain among all analysed compositions. At the same time, the values of Ω parameter, that combines both entropy and enthalpy of mixing, easily fulfils the requirement of being ≥ 1.1 for solid solution formation. This combined with low atomic size mismatch places all analysed alloys in a zone with high chances of creating single solid solutions.

Finally, to assure that the formed solid solution is an fcc phase, the VEC and electronegativity parameters need to be considered. Values of the former one should

exceed 8 to increase the probability of fcc phase formation. All of the considered alloys fulfil this condition. When it comes to $\Delta\chi$, its values ought to be between 3 and 6 %. If Allen electronegativity is used, all analysed alloys fall in between those values. Yet, when Pauling electronegativity is chosen for calculation of $\Delta\chi_P$ all alloys exceed the maximal recommended value. As Poletti et al. suggested [30] the more recent Allen electronegativity expresses better, in a more physical way this parameter. The fact that both A3S and Cantor's alloy are confirmed single fcc phased material advocates also in favour of Allen electronegativity. This example shows that fundamental input data is not always clear. For some elements it might pose problems to define so the choice of various data may influence the final result. Even small deviations can lead to opposite interpretations of final calculations.

To summarise, all the Y alloys are prompt to form a single solid solution fcc phase. There are no critical indications of different phase formation probability between Cantor alloy, A3S and the Y series. However, Y1 and Y2 fulfil the HEA definition, while Y3 should be referred to as medium entropy alloy according to theoretical definitions. Anyhow, no distinctions will be made in the following chapters and all analysed alloys will be called HEAs.

3.3 Preparation of selected alloys: effects of process conditions

Alloy preparation plays an essential role in obtaining mechanical and microstructural results. Phase presence may be highly influenced by casting method and further thermomechanical transformations. In this study, alloys were prepared at Ecole des Mines de Saint Etienne (EMSE) by cold crucible melting, a standard procedure for high purity alloys developed in the laboratory. Afterwards, the casts were transformed by hot forging at EMSE. Feasibility of same alloys was verified in the industrial laboratory of APERAM Isbergues research centre. The materials were prepared by vacuum induction melting followed by hot rolling. Both procedures have given good results; at the same time some difficulties have appeared for each method.

3.3.1 Melting: effects of process of cast preparation

At EMSE the method of preparation of high purity alloys by cold crucible melting (CCM) was developed in the 1970s. It consists of induction melting of metallic elements in a horizontally placed crucible cooled by water. The crucible itself is made of welded together silver tubes, since silver presents no solubility within other elements, especially in the case of Fe-based alloys. The whole procedure is performed

in highly controlled atmosphere under vacuum or specific gases in a quartz tube. The controlled atmosphere allows purification of raw elements and alloys in liquid phase. The content of impurities like O, N, S, P is taken down below 20 ppm for each element in standard Fe-based alloys, and for alloys with extreme purity it can be decreased below 25 ppm for the totality of 75 analysed elements. The chemical composition of each ingot is controlled at the end of the casting process by X-ray fluorescence, infrared absorption or mass spectroscopy. To prepare alloys from Y series, purified raw materials were introduced one by one in the crucible starting with Fe + Cr, followed by Ni, Co and finally Mn. Metallic pieces are heated by induction ring moving along the tube which allows homogeneous distribution of elements. In the existing experimental equipment, ingots of 300g to 3000g can be prepared by CCM. The procedure was proved to be reliable and repetitive. Regular controls of chemical composition and level of impurities allow verification of robustness of this process.

In the family of the five transition elements present in the analysed alloys: Co, Cr, Fe, Mn, Ni, manganese poses most technical problems during casting. Firstly, it evaporates easily while melting, so its input should always be slightly overestimated to compensate for the possible loss. Additionally, it forms a stable oxide whose melting temperature is very high compared to other elements in the alloy (T_M(MnO) = 1839°C), making the alloy casting problematic. Such an oxide formed during melting becomes impossible to dissolve leading to cast contamination and change of chemical composition. This is a general problem that concerns all casting techniques. Among numerous casts prepared for this thesis at EMSE, formation of a piece of manganese oxide occurred only once, most probably due to oxygen pollution of the whole system.

Two selected compositions were cast as well in more industrial conditions at the APERAM research laboratory using Vacuum Induction Melting (VIM). In this technique, the alloy is prepared in ceramic crucible in a furnace under vacuum. The raw materials were of 99% purity and total weight of the cast was of 2 kg. Elements are melted portion by portion to ensure homogeneity. In this method some carbon is added to deoxidise the alloy. Carbon atoms recombine with oxygen to form gaseous carbon monoxide that escapes the alloy. Bubbles of CO form in the liquid alloy, float up and then they are removed by the vacuum system. In addition to deoxidation, vacuum treatment helps to remove hydrogen dissolved in liquid metal. Hydrogen diffuses into the CO bubbles and the gas is then evacuated by the vacuum pump [144]. When all elements are melted together, the temperature is measured by a thermocouple immersed in the liquid and the mix is cast into a mould still under vacuum. Alloy is cooled down with the furnace. No particular problems were observed during casting of Y2 and Y3 alloys by this technique.

Chemical composition of casts was verified by X-ray fluorescence for major elements and by infrared absorption for minor impurities. For both techniques, the obtained compositions are close to the nominal composition requested. The measurement results for one representative cast for each cast technique are presented in Table 3.5. The biggest disparity was in both cases seen for Ni reaching up to 0.8% for VIM casting. Anyhow, compositions reached for all elements are satisfactory. Impurities present in the casts are mostly C, S, N, O. In case of the EMSE casts their level is in the range of 10 - 50 ppm. Slightly elevated values for S and O come most probably with the addition of Mn, whose strong affinity to both sulphur and oxygen makes high levels of purification difficult. In this study, extreme purity of alloys was not required, so this level of impurities was acceptable. VIM technique allowed to reach values between 70 - 200 ppm for C, 10 - 20 ppm for S, 350 - 550 ppm for N, 30-40 ppm for O but also 0.1 wt. % for Si (not analysed in the case of CCM ingots). Those are typical values for casts prepared at APERAM research centre. The results are satisfactory as they show that control of chemical composition of major elements and level of impurities in prepared alloys is in agreement with expected values. Additionally the increased level of impurities did not influence the phase formation or did not induce any particular difficulties during casting preparation. The ingots were further homogenised and processed thermomechanically.

Table 3.5: *Chemical composition of Y3 casts prepared by cold crucible melting (CCM) at EMSE and vacuum induction melting (VIM) at APERAM Isbergues. Measurements by X-ray fluorescence for major elements, values in at. %, and by infrared absorption for minor impurities, values in ppm.*

	Cr	**Fe**	**Mn**	**Ni**	**C**	**S**	**N**	**O**
	at.%				at. ppm			
Nominal	15.0	46.0	17.0	22.0	-	-	-	-
CCM	14.7	46.0	16.9	22.4	12	52	25	31
VIM	14.6	45.7	16.9	22.8	70 - 200	10 - 20	350 - 550	30 - 40

3.3.2 Transformation of alloys: hot rolling at APERAM

To ensure good chemical homogenisation and proper microstructure (usually recrystallised equiaxed grains are sought), the casts are further processed. At APERAM thermomechanical processing is done by hot rolling. The rolling is performed after one hour homogenisation heat treatment at 1250°C. The thickness of the ingot is reduced to 2,5 mm within 6 passes between the cylinders. The whole process is finished by water quenching. Final stage of preparation of alloys in APERAM is annealing at 1000°C followed by cold rolling down to 1 mm thickness. First series

of casts was successfully transformed and final sheets were used for microstructural and mechanical testing. Unfortunately the second cast was found to be defective at the stage of hot rolling. The 2,5 mm thick sheets were burdened with a defect line in the middle of the thickness of the sheet. Its appearance and EDX map analysis are presented in Figure 3.13. In fact, approximately 20-40 μm thick oxide line was present in the centre. It was mostly rich in Mn and Fe, but at some places Cr rich oxides were found as well. Additionally, some smaller particles with similar chemical composition were found through the whole material thickness, dispersed due to rolling. These artefacts come probably from oxides formed during casting, which were later on wrapped and trapped at the stage of hot rolling. Unfortunately this type of defect disallows further analysis of the material, as presence of oxides will influence the overall chemical composition, microstructural evolution and mechanical properties. The cause of oxides creation during casting still needs to be determined. The control of atmosphere and/or purity of raw materials during casting may play a role in final result. The alloys fabrication process requires more control since high Mn content can be problematic.

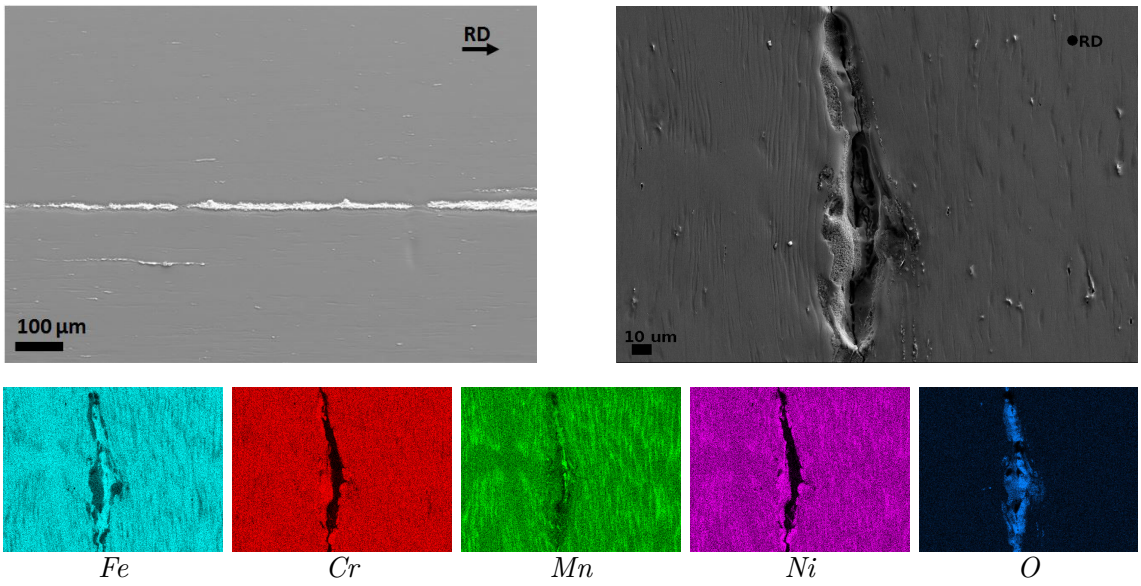

Figure 3.13: *Impurities embedded in the as rolled Y3 sheet*

3.3.3 Transformation of alloys: hot forging at EMSE

Standard procedure of alloy preparation at EMSE is CCM casting followed by homogenisation heat treatment and hot forging. For alloys from ferrous families, with melting temperatures between 1300 - 1400 °C, the temperature of transformation is of the order of 1060°C. Let's note that no temperature control is done during forging; therefore, the given value is just the temperature of the rod when it leaves the furnace after homogenisation treatment. Schematic representation of forging procedure is shown in Figure 3.14. A bar with final diameter of 12 mm is obtained through multiple section reductions by pounding and swaging with intermediate reheating of the material. It is a poorly controlled procedure, fully manual and based on technician's expertise.

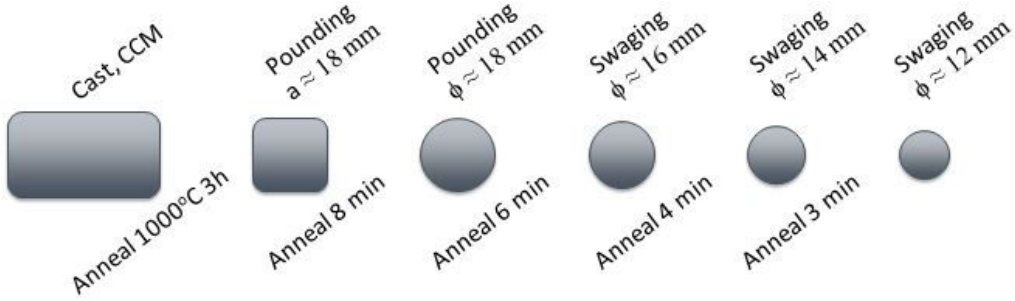

Figure 3.14: *Schematic presentation of hot forging process performed at EMSE.*

Table 3.6: *Forging conditions tested for Y3 alloy. Y3 1060°C* is the standard procedure according to which all other rods were prepared. Forging temperature represents the temperature of the material exciting the furnace.*

Name	Homogenisation annealing	Forging temperature	Final diameter
Y3 1000°C	1000°C / 3h	1000°C	ϕ12 mm
Y3 1060°C*	1000°C / 3h + 1060°C / 30 min	1060°C	
Y3 1100°C	1000°C / 3h + 1100°C / 30 min	1100°C	
Y3 1060°C	1000°C / 3h + 900°C / 30 min	900°C	

It may seam that the repeatability of this process is low, so a study of its robustness was done. A few rods were prepared with a focus on the forging conditions, in particular the change of temperature of homogenisation annealing just before processing, as presented in Table 3.6. The temperatures were selected to perform hot forging over the standard temperature, but not to close to the solidus of the alloy; and below the standard conditions to check the influence of cooling down the material upon processing. The standard conditions (1060°C) were applied as a reference. Since the initial and final shapes and sections were similar, it can be assumed that applied deformation is constant. Microstructure and mechanical properties were

subsequently analysed. Samples were taken from the centre or from the tip of the rod to verify its homogeneity.

Two EBSD IPF images are shown in Figures 3.15a and 3.15b for most extreme temperatures of forging, in explicit 900°C and 1100°C. General tendencies were as expected: finer and more deformed microstructure at the lowest temperature of forging and coarser grains with fewer sub-boundaries for 1100°C transformation. At higher temperature of transformation, some grains with no internal substructure were observed (marked in circles in Figure 3.15b). For all values of forging temperature, the typical microstructure consists of grains of couple to few tens of micrometers with highly developed substructure, regardless the position in the bar. To find details that may differentiate each rod, TEM observations were performed. Some specific elements of microstructure are presented in Figures 3.15c - 3.15f.

Firstly, the comparison between a "typical" austenitic and HEA microstructures is done. For standard materials recrystallised grains are obtained at the end of the transformation, as shown in Figure 3.15c. This micrograph comes form another alloy developed at EMSE, called ES1, whose composition still fulfils the HEA definition, but upon hot forging, it locally resembles classical austenitic steels. In case of HEAs analysed in this thesis, highly work hardened microstructures with dislocation cells of couple hundred nanometres were currently obtained as shown in Figure 3.15d. This image is a typical image of the microstructure after forging of Y3 alloy, in all analysed conditions and throughout the whole length of the rods. Typical observations were made both at the border and in the centre of the rods. Nonetheless, some exceptions to this microstructure were found in the rods forged at 900°C and at 1100°C. At lower temperature very fine recrystallised grains were occasionally found, Figure 3.15e. They measured few hundred nanometres and were free of dislocations. It is highly probable that the increased stresses (due to deformation at lower temperature) induce dynamic recrystallisation more easily. At higher temperature of transformation, some bigger grains, size between 5-10 μm, with no internal substructure were observed via EBSD. They show uniform orientation, no sub-boundaries but twins are present in it. At the scale of TEM those grains are easily distinguishable by their intrinsic dislocation structure, Figure 3.15f. Despite their appearance resembling recrystallised grains, they still present high density of dislocations, this time aligned following selected {111} planes. This curious behaviour will be addressed in more details in Chapter 4. It is important to note that those abnormal regions were a rarely occurring phenomenon and typical microstructure remains unchanged for the whole set of studied conditions of forging.

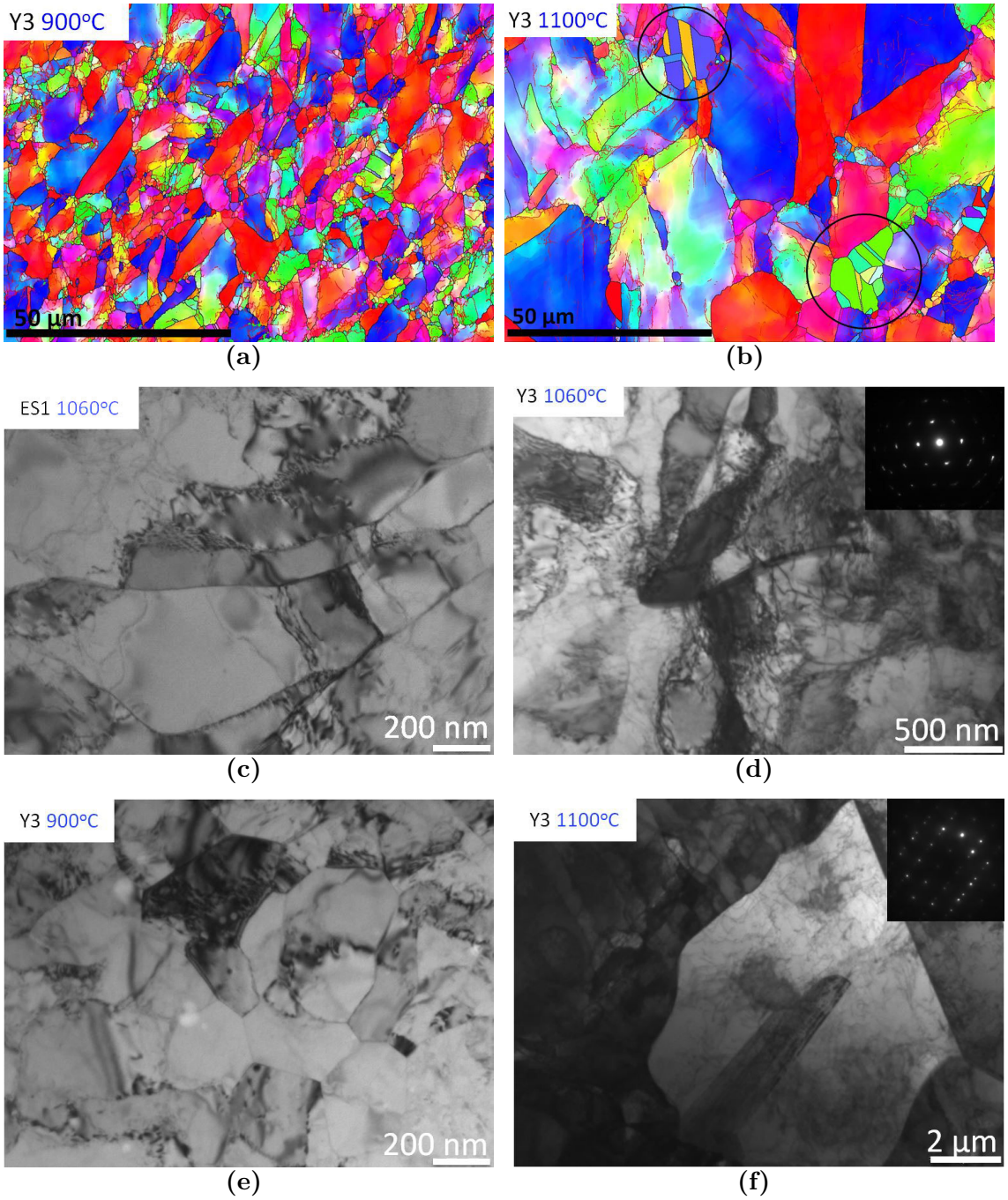

Figure 3.15: *IPFz images of as forged samples coming from the centre of rods forged at a) 900° C and b) 1100° C (in the circles grains with low internal misorientation). TEM micrographs for c) ES1, d) Y3 forged at standard conditions (typical microstructure found in observed HEAs), e) Y3 forged at 900° C, f) Y3 forged at 1100° C.*

Hardness measurements were performed both in the centre and at the tip of rods to verify possible inhomogeneities in mechanical behaviour. Results of these measurements are summarised in Figure 3.16, where black columns correspond to the centre of the rod, red columns to the tip and the dotted line connects the average HV values between tip and centre for each forging temperature. As expected, the HV slightly decreases between 900°C and 1060°C, with increasing forging temperature, and a drop is observed at 1100°C from 216 HV to 174 HV. It is due to probably to grain size and dislocations density. With increasing temperature, process of dynamic

recovery is facilitated and the sub-structure is less developed. At the same time grain coarsening takes place more easily. The differences between centre and tip of the rod are not much pronounced, between 2-6%. Oddly, the largest difference was found for the standard forging temperature with 15% deviation. Yet, no general trend between centre and tip differences were found. Nonetheless, it can be considered that hardness is homogeneous through the rod length and the influence of temperature of transformation is minimal.

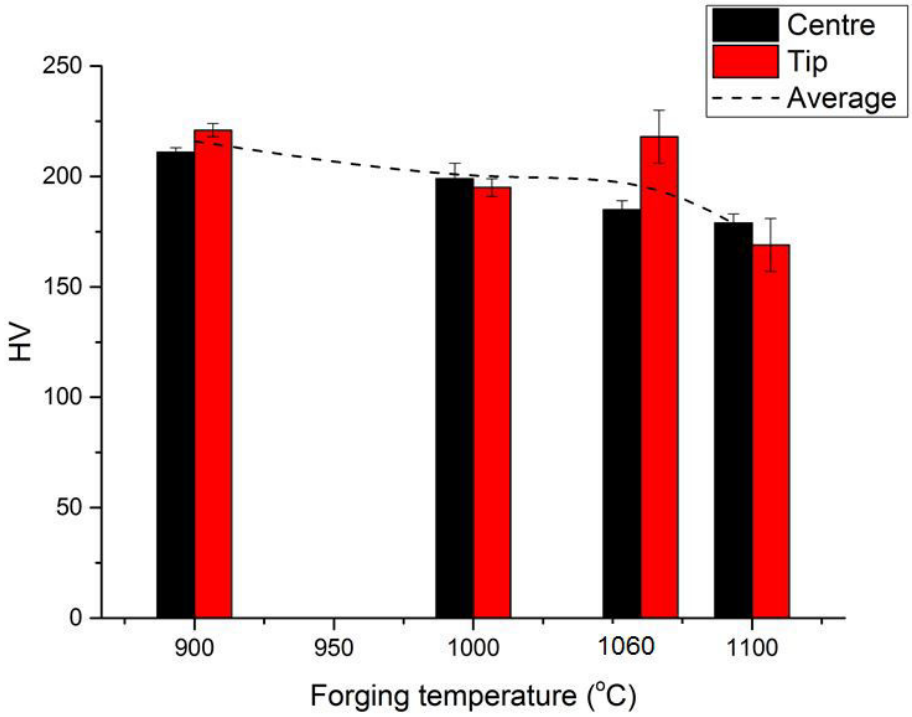

Figure 3.16: *Effect of forging temparature on hardness of Y3 alloys, forged at different temperatures. Dashed line represents the evolution of average HV for specific forging temperatures.*

Since HEAs from this family show particular behaviour at cryogenic temperatures, the tensile tests were performed both at room temperature and -150°C to check the main characteristics of Y3 alloy. True stress vs true strain curves are shown in Figure 3.17 and values of yield strength, ultimate tensile stress and elongation to fracture are recapped in Table 3.7. Forging at lower temperature (900°C) leads to increased YS and reduced ductility. Values of UTS are slightly higher for samples forged at 900°C compared to those prepared at a standard temperature (1060°C). Those increased values of YS and UTS are most probably due to higher degree of work hardening. Similar tendency was observed for hardness measurements, where values for rod forged at 900°C were higher than for rod forged at standard temperature of 1060°C. Consequently to increased strain hardening, the total elongation to fracture is decreased. Same tendencies between RT and -150°C are found for both temperatures of forging. Also elongation of samples forged at 900°C remains still satisfying reaching the value of 22%.

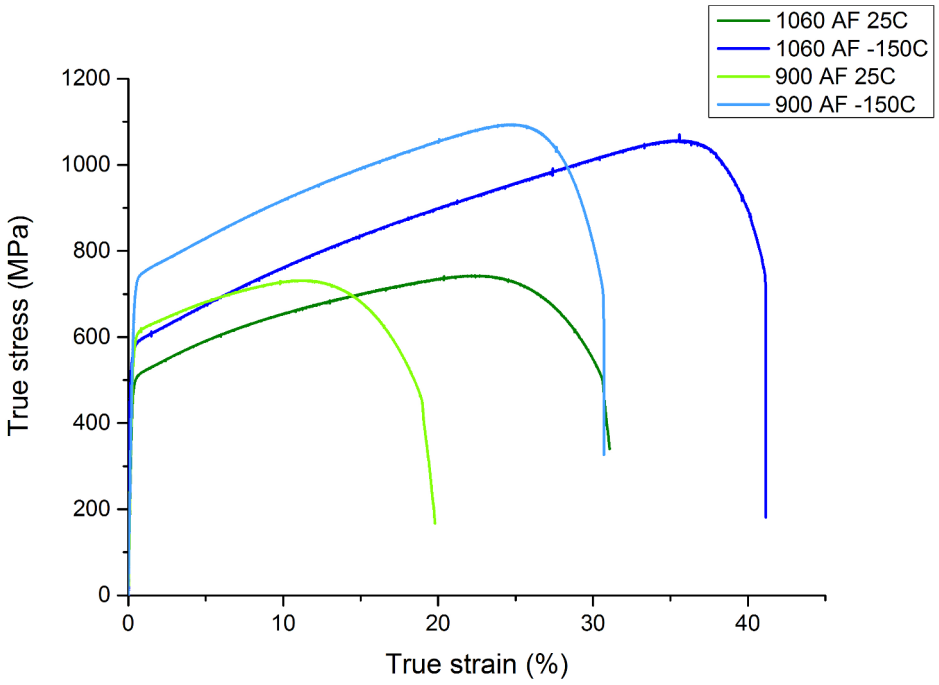

Figure 3.17: *Effect of temperature on tensile behaviour of Y 3 alloys forged at different temperatures. Tensile tests, $\dot{\varepsilon} = 10^{-3}\ s^{-1}$. Tests performed at room temperature (RT) and -150° C.*

Table 3.7: *Yield strength (YS), ultimate tensile stress (UTS) and elongation to fracture for Y3 alloy forged at 1060° C and 900° C.*

Forging T [°C]	**Test T** [°C]	**YS** [MPa]	**UTS** [MPa]	**El** [%]
1060	25	500	592	36
	-150	584	744	51
900	25	603	654	22
	-150	728	851	36

To conclude the forging procedure performed at EMSE stays a robust method. Microstructure of Y3 alloy shows little sensitivity to change of forging temperature with difficulty to recrystallise. Corresponding mechanical properties remain reasonably comparable bearing in mind that forging was performed in a wide range of temperatures between 900°C and 1100°C. For further study, results coming from multiple casts and rods forged at standard temperature (1060°C) can be compared without specific distinction. For all the series, no significant differences between microstructures coming from different forging conditions were observed at the scale of SEM or EBSD.

3.4 First evaluation of selected compositions: microstructure and mechanical properties

Upon thermodynamic calculations three compositions were chosen for further study: Y1 low-Co(V), Y2 low-Co and Y3 Co-free. First evaluation of those compositions was done on *as forged* rods prepared at EMSE. This thermomechanical transformation allows to homogenise the chemical composition of as cast alloys both with modification of grain size and morphology. It does not influence the phase stability and at the same time, facilitates reaching the equilibrium.

3.4.1 Microstructural characterisation

The selected compositions were specifically designed by Thermo-Calc calculations to form a single fcc phase: obviously for high temperatures starting at solidification and down to as low temperatures as possible (500 - 700°C). Results of X-ray diffraction measurements of *as forged* Y1 low-Co(V), Y2 low-Co and Y3 Co-free alloys are shown in Figure 3.18. They confirm the presence of a single fcc phase, with the uncertainty of the X-ray diffraction technique close to 2-3% of volume. The lattice parameter a was measured for all alloys, Y series, A3S and Cantor's alloy, in *as forged* state. The results are shown in Table 3.8. The lattice parameter for every alloy is of the order of 3,60 Å with negligible differences. They are in accordance with what was previously reported for Cantor's alloy: 3.5991 Å [80], 3.601 Å [24] and 3.606 Å [22].

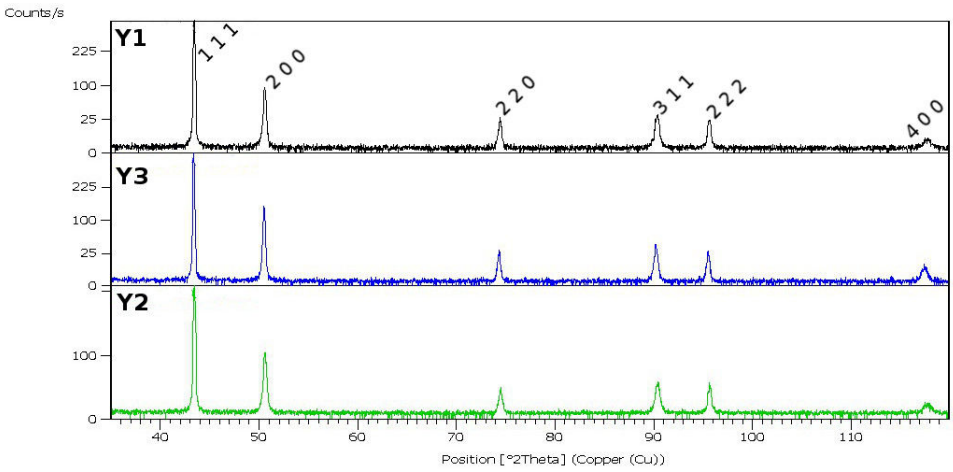

Figure 3.18: *X-Ray diffractograms of Y1, Y2 and Y3 alloys. Only one fcc phase is present in all materials.*

Table 3.8: *Values of lattice parameter measured by XRD for Y alloys, A3S and Cantor's alloy.*

Alloy	**Phase**	**Lattice parameter** [Å]
Y1	FCC	3.5992 ± 0.0001
Y2	FCC	3.5977 ± 0.0001
Y3	FCC	3.6030 ± 0.0001
A3S [115]	FCC	3.5903 ± 0.0003
Cantor's alloy [115]	FCC	3.5991 ± 0.0006

Presence of single fcc phase for Y alloys was confirmed by more precise TEM observations of *as forged* samples. No second phase was found at grain boundaries nor in the matrix. First of all, it is an indication that Themo-Calc predictions were correct, at least for the high temperature state of the material, therefore the simulated phase diagrams can be used as a first approach indication of phase formation in the alloys. Secondly, the choice of Allen electronegativity over Pauling proves to be accurate in the case of analysed compositions.

To verify the homogeneity of distribution of elements in samples at grain-scale, an Energy Dispersive X-ray Spectroscopy, EDX, in SEM, analysis was performed, on the *as forged* state. A representative mapping of elements distribution for Y2 sample is shown in Figure 3.19. No areas with difference in composition are visible (grain boundaries, inclusions, etc.). Similar results were obtained for the other two alloys, Y1 low-Co(V) and Y3 Co-free. This outcome confirms good homogenisation and lack of segregation of chemical composition upon annealing and hot forging (at the scale of SEM EDX). At the same time, the BSE SEM image confirms the disturbed internal structure of the *as forged* alloy; in explicit, no grains can be distinguished. These features can be seen in more detail in Figure 3.20b.

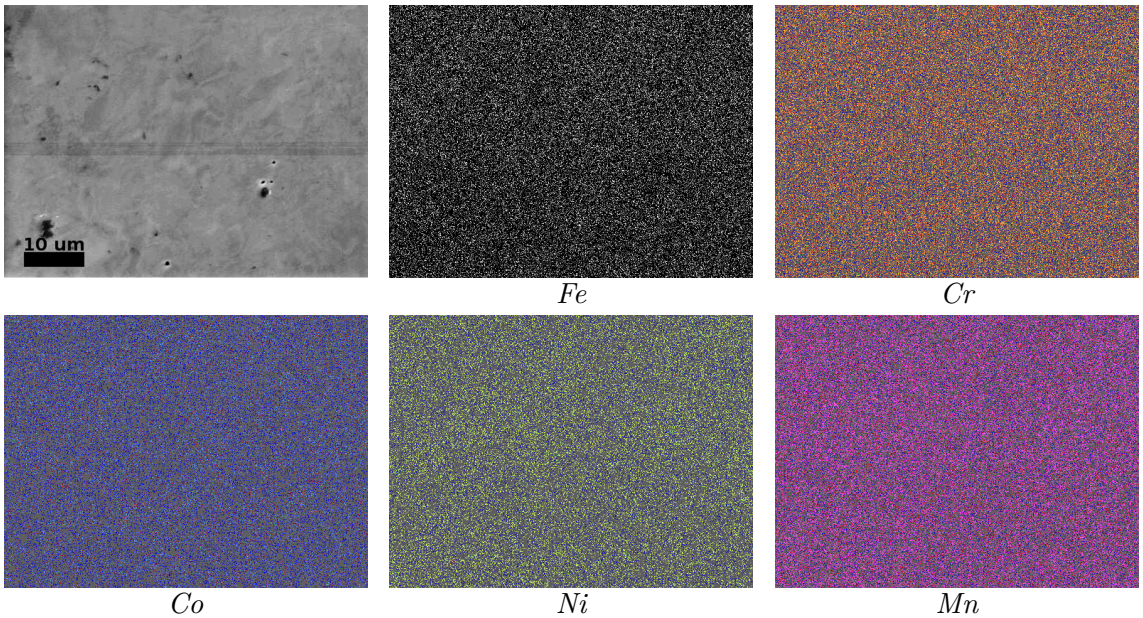

Figure 3.19: *Microstructural observations of as forged Y2 sample: BSE SEM image of the analysed zone with EDX mapping elements distribution.*

3.4 First evaluation of selected compositions: microstructure and mechanical properties

Microstructural analyses have been based on light microscopy (LM), SEM, EBSD and TEM observations to determine the microstructure at different levels. Firstly, LM observation were carried out on both non - etched (not shown here) and etched samples. No inclusions or impurities of importance were found before revealing the microstructure by chemical etching. The cast and forging procedure leads to obtaining rods of good quality without porosities or embedded inclusions through the whole alloy. Therefore, its microstructure and mechanical properties can be further analysed.

Etching the samples allowed to observe microstructures as represented in Figure 3.20a. A monophased structure is visible with occasional pits placed both inside the grains and at the grain boundaries. Their presence is due to electropolishing and electroetching. The grains are equiaxed in both longitudinal and cross sections of the rods for all alloy. Numerous twin boundaries can be observed as well, which is typical for an austenitic structure with low stacking fault energy when hot deformed. Grains shape suggests that dynamic recrystallisation took place upon hot forging.

As already pointed out, observation of grains in the BSE mode in SEM revealed to be problematic. BSE mode is sensitive to orientation and chemical composition. It was already shown that the alloys are chemically uniform, so only changes in crystalline orientation should be observed. Nonetheless, grains were indistinguishable. High degree of internal misorientation lead to an undefined mixture of shades of grey, as shown in Figure 3.20b. As a consequence, observations via EBSD and TEM were necessary to collect more precise information about the microstructure.

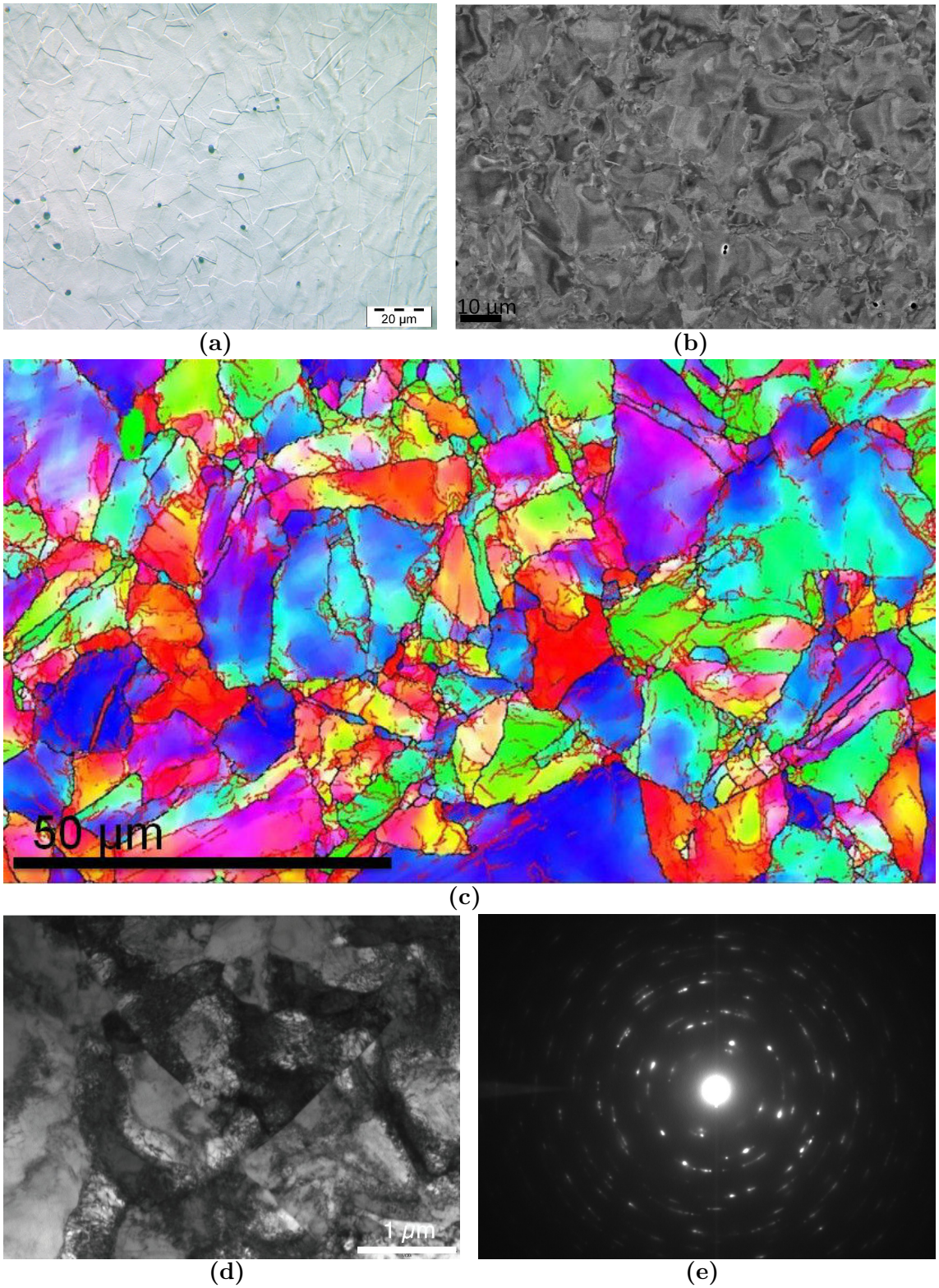

Figure 3.20: *Microstructural observations of as forged Y3 samples: a) light microscopy of an etched sample; b) SEM BSE image; c) EBSD IPFz image, with black lines representing high angle grain boundaries and red lines depicting subgrain boundaries; d) representative TEM image with e) local diffraction diagram.*

Good distinction of grains was possible via EBSD, as shown in Figure 3.20c. In this IPFz representation black lines trace the high angle grain boundaries and red lines indicate the subgrain boundaries. It is easy to notice that orientation within one grain is highly variable, presented by the change of colour. An elevated number of subgrain boundaries is visible as well. Those correlate with the change of colour indicating small changes of orientation (of more than 2° and less than 15°). Internal structure of the grains is complex and far from being at equilibrium. TEM observations confirm the presence of high density of dislocations, Figure 3.20d. Those dislocations form cells of couple hundred nanometres in diameter that are surely responsible for the complex image of the microstructure. The diffraction diagram shown in Figure 3.20e comes from a large area of 3 μm in diameter. Presence of multiple orientations in this zone is deduced from elongated diffraction points that start to draw circles. Obviously, full circles in diffraction diagram would have been formed for high number of randomly orientated grains diffracting in the analysed area: this is usual for nano-structured materials. This microstructure was found to be typical in the Y series of alloys prepared at EMSE by hot forging. The nano-sized substructure is most probably at the origin of high mechanical properties found in those alloys, as it will be presented in the next section.

Initial microstructure analysis did not show any significant differences between the three selected compositions. They are all single fcc phase, with very similar lattice parameter and no second phase precipitates or segregation of elements. A complex internal structure was found upon hot forging. It was shown by EBSD and TEM that the microstructure observed by LM has in fact a much more complicated internal structure than it would seem at first sight. That is why microstructure needs to be analysed at all scales to obtain its full characterisation, necessary for understanding the origins of properties of so designed materials.

3.4.2 Mechanical properties evaluation

Initial evaluation of mechanical properties was done by hardness measurements and compression tests. Hardness values of all Y alloys at the *as forged* state, Table 3.9, are relatively similar: 244 HV for Y2 low-Co, 232 HV for Y1 low-Co(V), and 190 HV for Y3 Co-free. The empirical α parameter showing the relation between HV and YS was calculated according to the following equation:

$$YS[MPa] = \alpha \cdot HV[Vickers] \tag{3.1}$$

Its values are between 2.5 and 2.6 which is slightly below the values for classical austenitic materials for which α approaches a value of 3. At the same time, it is not surprising: in the analysed HEAs, α value is certainly decreased by the very low

work hardening coefficient.

Compression true stress/strain curves are presented in Figure 3.21. For all alloys, the stress grows fast reaching high values of yield strength. Afterwards, upon deformation, the stress increases steadily with low slope indicating a low value of work hardening parameter. The Y2 low-Co shows the highest resistance measured by YS value, whereas Y3 Co-free composition is the weakest one. The difference in mechanical resistance between Y1 low-Co(V) and Y2 low-Co is very low (less than 100 MPa) in favour of the latter. Based on those first mechanical results, it seamed that there is no obvious interest in Y1 low-Co(V) composition. The addition of 1% V does not increase the mechanical resistance as expected, quite the contrary: it is decreased. On the basis of this result, study of Y1 low-Co(V) composition was put aside and the focus was laid on Y2 low-Co and Y3 Co-free alloys.

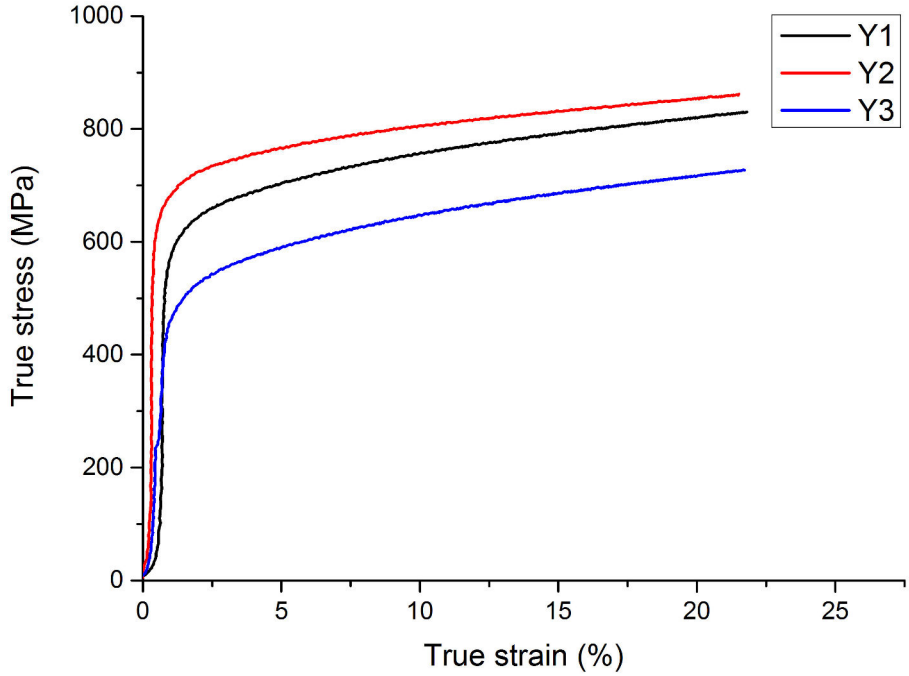

Figure 3.21: *Room temperature compression true stress vs true strain curves for Y alloys. Strain rate 10^{-3} s^{-1}.*

Table 3.9: *Compressive yield strength, hardness values and α parameter of Y alloys.*

Alloy	**YS** [MPa]	HV [Vickers]	α
Y1 low-Co(V)	573	232	2.47
Y2 low-Co	640	244	2.62
Y3 Co-free	483	190	2.54

From the mechanical tests Y3 alloy is considered as a highly promising one, due to very good compromise between mechanical resistance and reasonable fabrication costs due to Co elimination. This single phased alloy shows high mechanical resistance at the *as forged* state and was selected for further research.

3.5 Partial conclusion

Three new compositions of high entropy alloys have been designed by thermodynamic calculation with the use of Therm-Calc software. These alloys, denominated Y1 low-Co(V), Y2 low-Co and Y3 Co-free are non-equiatmic grades of HEA from (Co)CrFeMnNi family. They have been successfully cast, processed and basically characterised. Alloys were prepared in two laboratories according to two different procedures: CCM followed by hot forging at EMSE and VIM accompanied by hot rolling in APERAM. Both procedures are well defined and controlled; nonetheless, some difficulties were encountered. Those are mostly due to high content of Mn and its strong oxidation as well as segregations upon casting.

All analysed alloys are characterised by single fcc phase, with the lattice parameter of about 3,60 Å. It is in good accordance with Thermo-Calc predictions for high temperature phase stability. On the contrary, Thermo-Calc prediction has been shown inaccurate for low temperature (500°C) stability of single phase structure. The microstructure upon hot deformation was found to be highly complex demanding characterisation at multiple scales.

Basic mechanical properties of the so-designed alloys were analysed. High values of yield strength were measured in both compression and tensile tests: 600 MPa and 500 MPa for Y2 low-Co and Y3 Co-free at room temperature and 680 MPa and 580 MPa respectively at -150°C. At cryogenic temperatures simultaneous increase of yield strength and elongation to fracture was observed for all analysed compositions. This behaviour, typical for HEAs from Cantor's family, was found even in Y3 Co-free alloy characterised by lower entropy of mixing. Mechanical tests showed higher mechanical resistance in Y2 low-Co than in Y3 Co-free alloy. Nonetheless, the compromise between mechanical strength and predictive cost of production seams better for Y3 Co-free alloy. Elimination of Co lowers the overall price of the alloy, facilitates the process and enlarges application fields of the alloy. For all these reasons, the cobalt free Y3 composition was chosen for further in depth analysis.

Chapter 4

Microstructure: source of optimised mechanical properties of Y3-Co free alloy

Contents

Microstructure plays a major role in design of mechanical properties. To be able to create a desired microstructure it is necessary to first understand its evolution within various thermal, mechanical or thermomechanical treatments. In this chapter analysis of microstructure of Y3 Co-free alloy and its correlation with mechanical properties are presented. Microstructure is observed on the scale from grain morphology by light microscopy to characterisation of dislocations by transmission electron microscopy. Those observations lead to questions concerning recrystallisation: does it really take place in the Y3 Co-free alloy? Let's remind that previously, in A3S grade, Mroz [115] has shown that A3S alloy does not follow the classical rules for recovery and recrystallisation, in explicit at high temperatures recovery is preferential over nucleation of new grains. Is this phenomenon present in Y3 Co-free composition as well? Does the nucleation of new grains take place upon annealing? If so, in what conditions? Issues concerning recovery, recrystallisation and further grain evolution are approached in this chapter.

4.1 Initial states: grain size, dislocations density and mechanical resistance

4.1.1 Microstructure and mechanical behaviour of Y3

4.1.1.1 *As cast* state

For Y3 Co-free alloy, cold crucible melting results in a single fcc phased alloy, solidified in dendritic structure with big grains of the size of couple hundred micrometers eventually up to millimetric diameter, as observed on SEM micrograph in Figure 4.1a. Let's remind that dendritic structure and chemical segregation were already presented in Figure 3.5 in Chapter 3.1. Interdendritic zones enriched in Mn and Ni were correctly predicted by Thermo-Calc simulations of solidification. Further homogenisation and thermomechanical transformation eliminate successfully the chemical segregation.

TEM images of the *as cast* Y3 alloy, coming from samples from the centre of the ingot are presented in Figures 4.1b to 4.1d. At first sight it can be noted that the density of dislocations is surprisingly elevated. Numerous dislocation lines can be distinguished within the observed small surface of few micrometres. This observation is unexpected since in classical materials after casting only few dislocations should be distinguishable at this scale. At the same time, multiple interactions between dislocations can be distinguished in this state, due to their high density and short distances: entanglements, kinks and jogs, as well as pile ups. Most interesting feature found in the analysed state are the arrays of dislocations along selected {111}-type planes. Those arrays are composed of numerous dislocations within one

plane giving the impression of long segments of straight dislocations when the plane is parallel to the electron beam. Certain regularity in presence of such densely filled planes can be found, with distances between them of about 200-300 nm. In Figure 4.1b, a grid with cells of about 200 nm can be seen, formed by interaction of those {111}-type planes. It was found that many of those dislocations have the Burgers vector $\vec{b}$ (101) (all dislocations parallel to A in Figure 4.1b). It appears that creation of many dislocations is favoured in this material with high density.

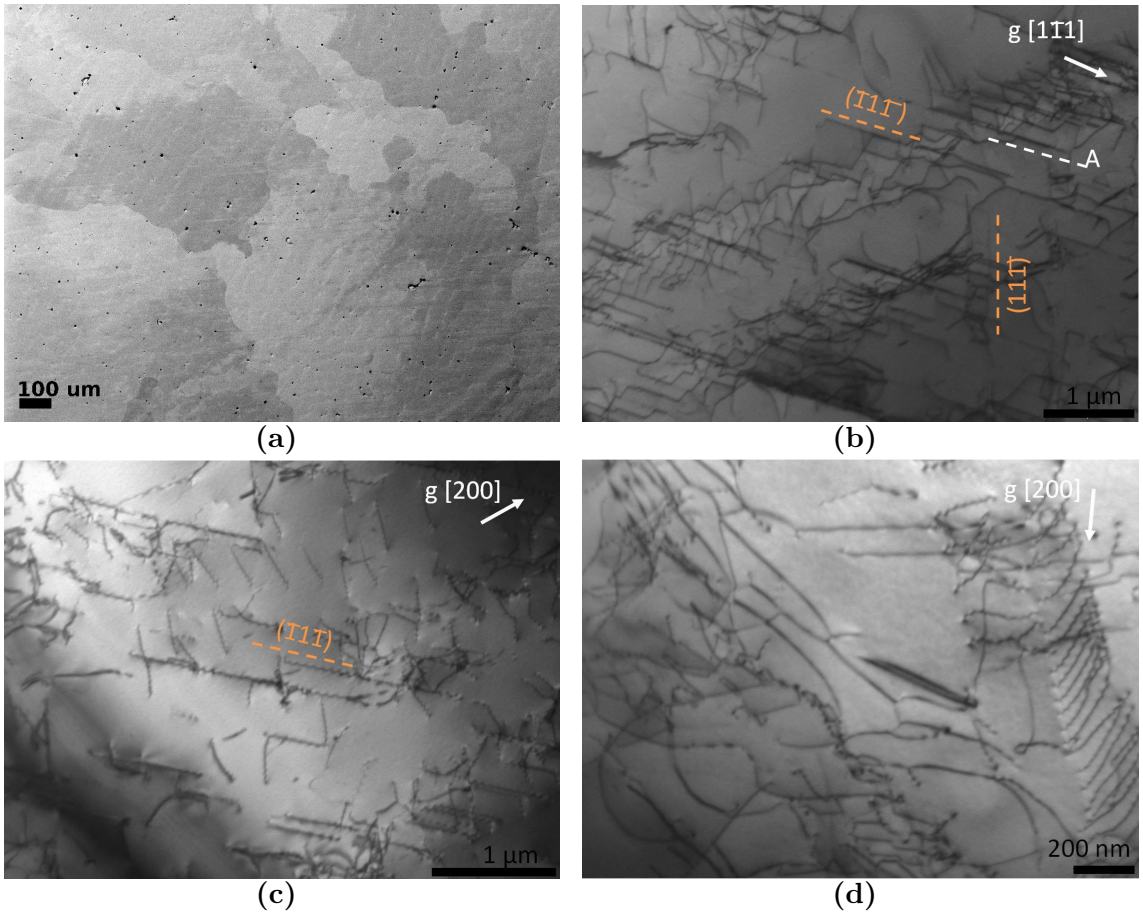

Figure 4.1: *Microstructure of as cast Y3 alloy. a) SEM image of grains; b) and c) TEM micrographs at [011] ZA; d) TEM micrograph at [001] ZA. "A" represents the trace of dislocations with* $\vec{b}$ *(101).*

4.1.1.2 *As forged* state

Multiple results presented for Y3 in the *as forged* state have been used for initial evaluation of this material and so were already presented in Chapter 3. Those results will be shown anew without excessive detail.

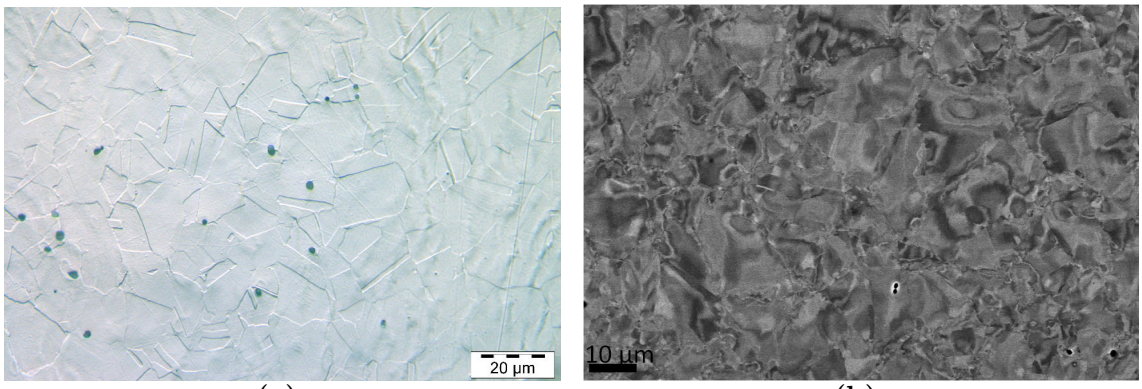

(a) **(b)**

Figure 4.2: *Microstructure of as forged Y3 alloy; a) light microscope image of etched sample; b) SEM BSE image.*

Hot forging according to the process described in part 3.3 results in a highly work hardened structure, Figure 4.2. Even if, at the scale of light microscopy the observations of an etched sample reveal equiaxed grains with presence of twins which would be a typical microstructure for an austenitic alloy upon hot forging, SEM BSE images show high misorientations inside the grains, Figure 4.2b. As a consequence it is impossible to distinguish individual grains. EBSD confirms the intricacy of grain structure with frequent changes in orientation of 0.5° - 1°. Misorientation profile through one of the grains is presented in Figure 4.3d. Aside from slight orientation changes, presence of numerous low angle boundaries is detected ($> 2°$ and $<15°$): they are represented by red lines on IPF images in Figure 4.3a. The frequent variation of orientation inside the grains is in agreement with elevated dislocations density observed by TEM, Figure 4.3b. Presence of dislocations forming a substructure in the grains is clearly visible. They form cells of 100 - 200 nm with boundaries composed of numerous entangled dislocations. Each cell has its own orientation that differs by a low angle from the neighbouring ones. As a result, multiple orientations are present in each grain. Selected area diffraction pattern confirms this phenomena as the spots become elongated and start forming circles like for nano-structured materials (well visible in Figure 3.20e).

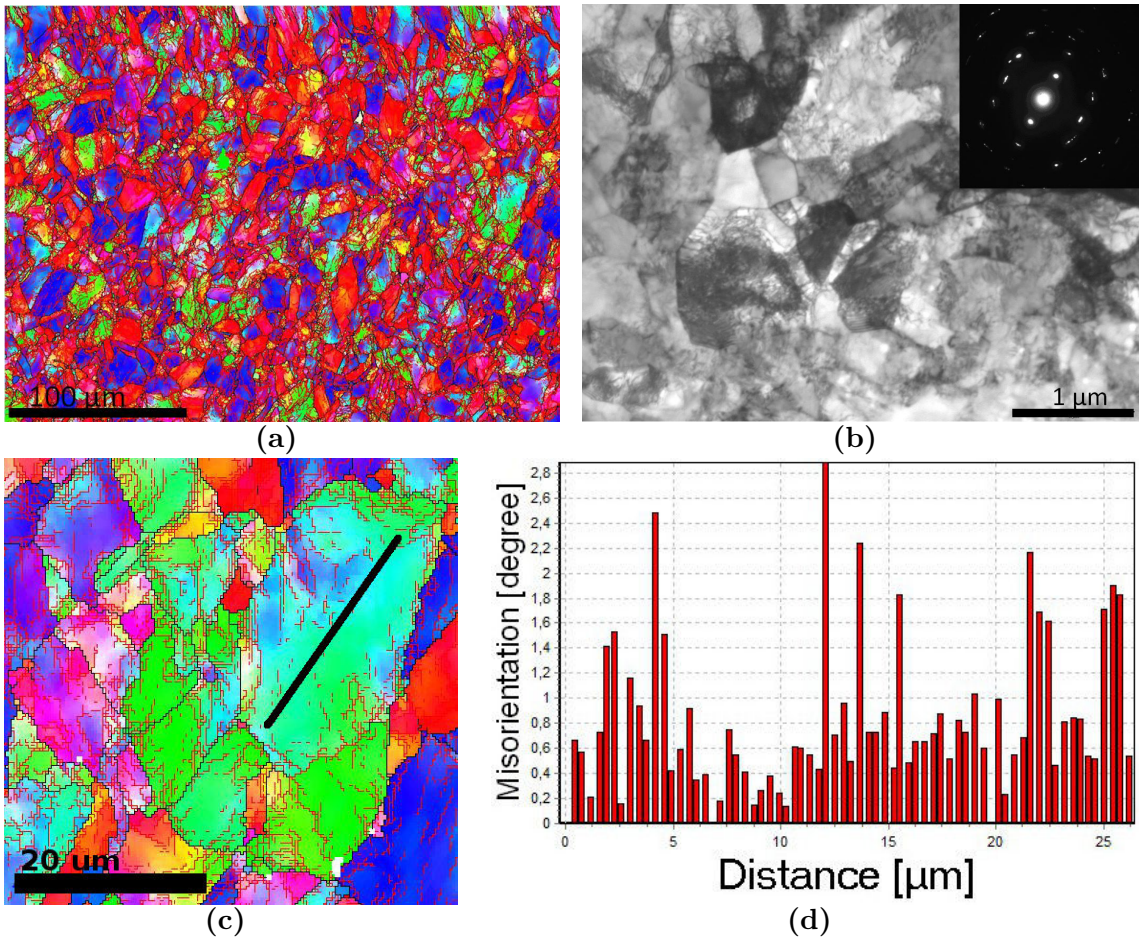

Figure 4.3: *Microstructure of as forged Y3 alloy; a) EBSD IPFz image, with black lines representing high angle grain boundaries and red lines depicting subgrain boundaries; b) TEM micrograph with local diffraction diagram; c) zoom on one of the bigger grains from EBSD with line along which the misorientation profile was done, presented on diagram d).*

Despite elevated temperature during forging (about 1060°C), microstructure of *as forged* Y3 alloy shows features typical for a work hardened material. It could be compared to microstructures obtained in 304L austenitic stainless steel upon severe hot deformation, like ECAP transformation shown in Figure 4.4 [145]. At the same time, this kind of thermomechanical transformation in classical composition results in mostly recrystallised microstructure (already shown Figure 3.15c). It would appear that the strongly disturbed microstructure characterises the analysed HEAs. Formation of dislocations and substructure as well as increased facility to work harden is a particularity that was observed in A3S [115], and is also present in the Y series of alloys. Cantor's alloy prepared in the same conditions shows the presence of substructure as well, but together with nano-cells, nano-twins can be clearly distinguished. Eased formation of twins is most probably due to somewhat lower stacking fault energy in Cantor's alloy than in A3S or Y3. Change in proportion between elements, in particular lowered Cr content and increased Ni content can lead to increase of SFE as it was calculated by Zaddach et al. [87].

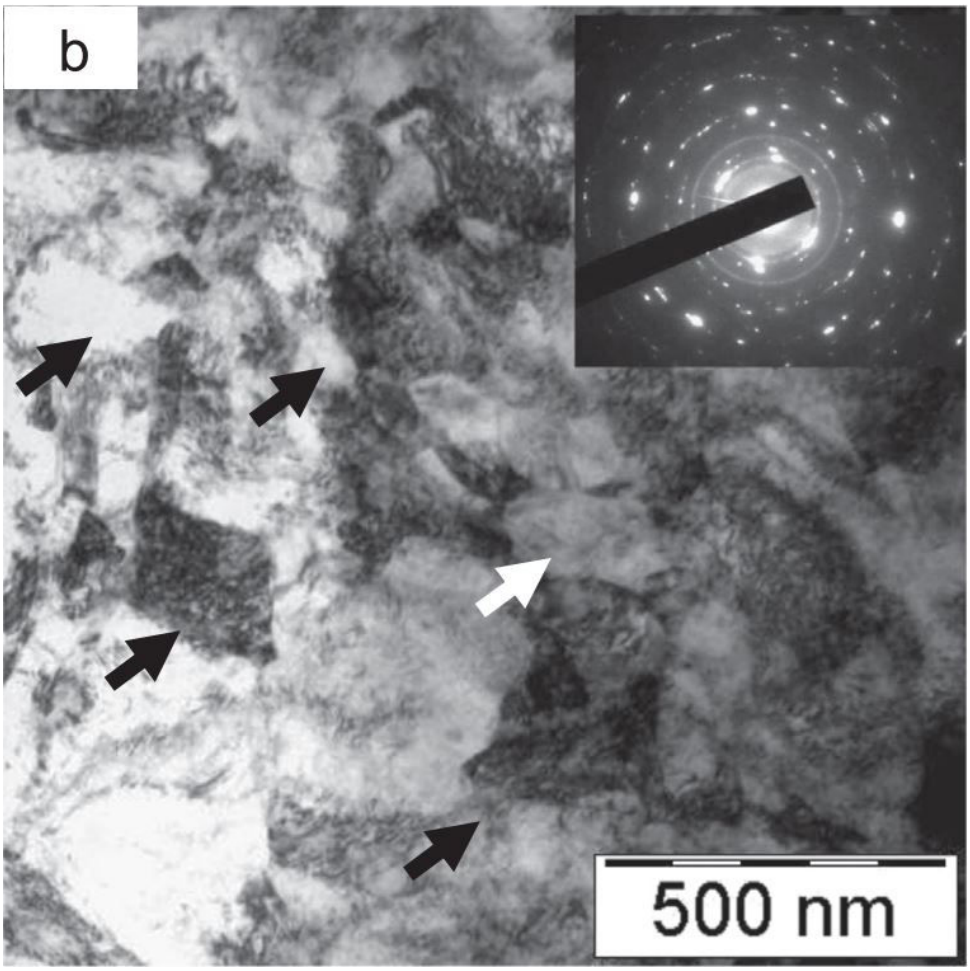

Figure 4.4: *Cellar sub-grained microstructure with the corresponding SAED pattern for 304L stainless steel after three ECAP passes at 500° C. Typical TEM image [145].*

Definition of grain size in *as forged* Y3 grade needs a specific consideration, due to elevated complexity of the structure. As the EBSD of *as forged* Y3 reveals, a high number of grains can be detected with a significant variation in size, Figure 4.5. Since the grain size follows the log-normal distribution, an arithmetical average highly influenced by the high number of grains between 0 μm and 3 μm, is far from being representative. That is why, two alternative approaches have been proposed for grain size determination expressed by equations 4.1 and 4.2. A mean value from log-normal distribution fit was estimated according to the equation 4.1, where x_c and wc are respectively location and scale parameters for the normally distributed logarithm. This approach gives a lesser impact on the average grain size to small grains, even if their number is elevated.

$$\bar{d} = exp\left(lnx_c + \frac{w^2}{2}\right) \tag{4.1}$$

$$\bar{d} = \frac{1}{A_T}\sum_{i=1}^{n} A_i d_i \tag{4.2}$$

In the second estimation, average grain size is based on the area occupied by each grain, as described by the equation 4.2, where A_T is the total surface, A_i is the surface occupied by i-th grain with d_i being its size. According to the surface represented by each grain a weigh is attributed to it.

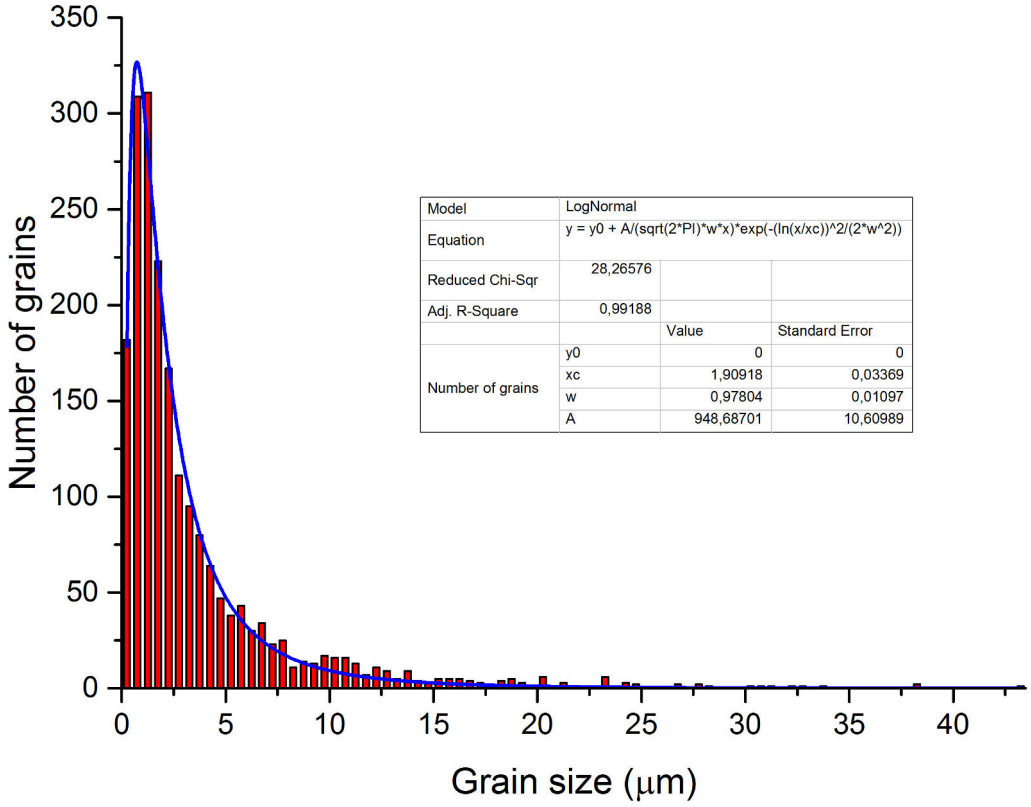

Figure 4.5: *Grain size distribution in as forged Y3 alloy with log-normal fit (blue line); class width 0.5 μm.*

In the studied case, in accordance with our expectations, high differences of average grain size have been found following those approaches. A mean value of 3.1 μm was obtained by log-normal approach, which is statistically correct but does not fully comply with effective grain size, while a weighted average was equal to 19.1 μm. The two average grain sizes are equally useful, since they represent distinct things: on one hand, simply statistical distribution; on the other, a more accurate description of grain size effectively influencing the properties.

Mechanical properties of *as forged* Y3 Co-free alloy were verified via tensile tests. Literature review showed an exceptional behaviour of Cantor's alloy, and other compositions from CoCrFeMnNi family, at cryogenic temperatures [10, 73]; with simultaneous increase of strength and elongation as well as effective phase stability (in explicit no martensitic transformation was observed even under stress). Tests in similar conditions were performed on Y3 composition. The true stress/strain curves are regrouped in Figure 4.6 and measured values of yield strength, ultimate tensile stress and elongation to fracture are summarised in Table 4.1. Results were compared to a standard austenitic stainless steel 304L. The obtained results confirm

in Y3 alloy the unusual behaviour previously reported in HEAs: in explicit drop of temperature to cryogenic conditions entails an increase of both strength and elongation to fracture. According to Otto et al. [10], this phenomena can be partially explained by the classical Considere's criterion, $d\sigma/d\varepsilon = \sigma$, where increased work hardening at low temperatures postpones necking increasing the plastic deformation. Authors also suggest that the increased work hardening rate in Cantor's alloy is due to appearance of twins at low temperatures, which via dynamic Hall-Petch, decreases the dislocations mean free path.

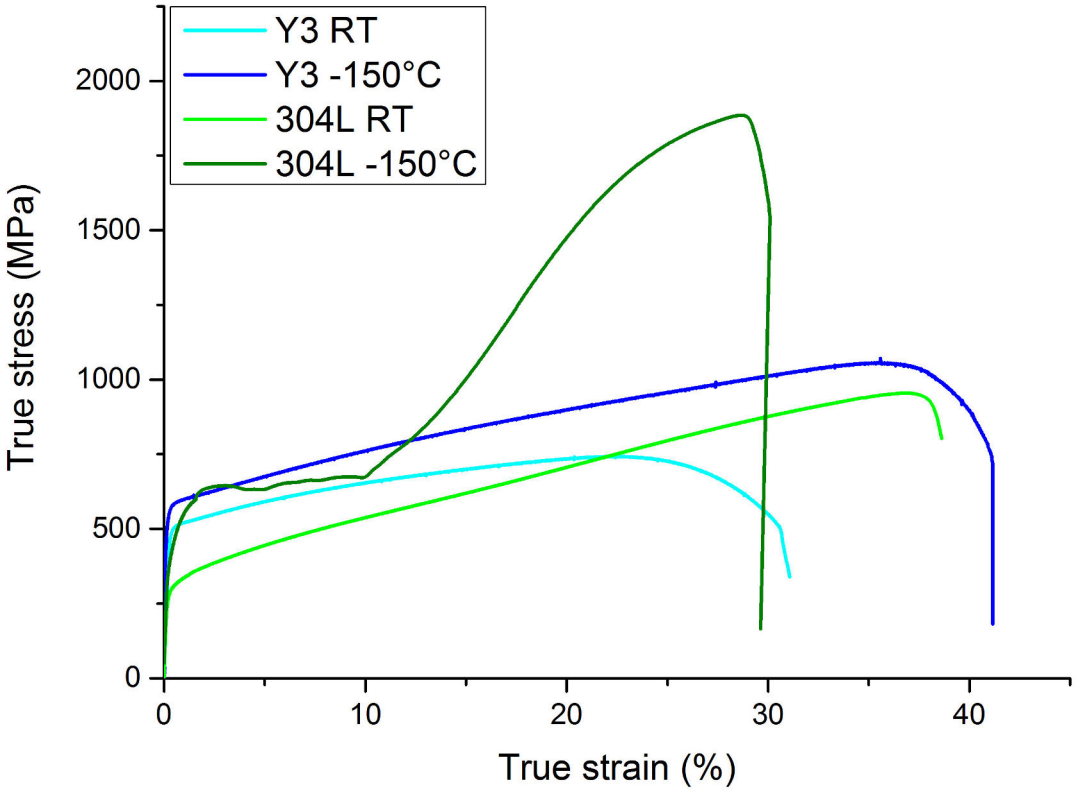

Figure 4.6: *Tensile true stress vs true strain curves for Y3 alloy (in blue) and 304L stainless steel (in green, courtesy of APERAM). Tests performed at room temperature (RT) and -150°C.*

It is also important to note that Y3 composition exhibits cryogenic phase stability, with no signs of phase transformation visible on the tensile curves. Curves for Y3 Co-free alloy, at both room temperature (bright blue curve) and -150°C (dark blue curve), present a steady slope with constant work hardening. Only slight increase in work hardening is observed for the test at cryogenic temperature, nevertheless the work hardening coefficient (WHC) is low. For comparison, tensile curves for 304L steel are presented. At room temperature, the tensile curve of 304L steel (bright green curve) shows similar behaviour with higher WHC. At -150°C (dark green curve) a martensitic transformation takes place. It is distinguishable due to a significant increase in stress, starting at about 10% strain. For higher deformation, a significant increase of stress is measured: it reaches the true UTS of nearly

1900 MPa. Such stress jump is a result of martensite formation upon deformation. Depending on the application it may be an undesirable effect: firstly, because the transformation is irreversible and secondly, it leads to loss of amagnetic properties of the material. Yet, the increased mechanical resistance of 304L steel is accompanied by reasonable elongation of 30% despite the presence of martensite. In case of Y3 Co-free alloy, a decrease in single fcc phase stability under stress, as compared to Cantor's or A3S alloys, could be expected due to absence of Co, a strong gamma-stabilising element.

Table 4.1: *Yield strength (YS), ultimate engineering tensile stress (UTS) and elongation to fracture (El) for as forged Y3 and 304L. Tests performed at room temperature and at -150° C.*

Alloy	**Test T** [°C]	**YS** [MPa]	**UTS** [MPa]	**El** [%]
Y3 *as forged*	25	500	592	36
	-150	584	744	51
304L	25	300	660	52
	-150	446	1408	30

If a comparison between Y3 alloy and the 304L steel is done it could be estimated that the HEA presents increased yield strength. However, the microstructural states of both alloys are clearly different. On one hand, the Y3 alloy is in the already work hardened *as forged* state, on the other, stainless steel is composed of recrystallised grains. Still, the fact that no ductility loss nor phase transformation were observed in the HEA at a hardened state, is a highly promising result. These observations lead to conclusion that gain in mechanical resistance via dislocation hardening can be easily obtained by hot deformation and no recrystallisation annealing is required to maintain good plastic properties. It could be imagined that this type of HEAs are used in work hardened state for increased mechanical properties.

Fracture surfaces after tensile tests, both at room temperature and at -150°C are presented in Figure 4.7. Typical fracture elements, characteristic for plastic deformation, are present for both samples. Centres of the samples are full of dimples and at the border of the fracture surfaces, lips of shear failure can be seen. Close up on the plastic deformation dimples shows the influence of cryogenic conditions. It is clear that the dimples size is significantly reduced with decreased temperature; the plastic zones around the voids are smaller than in the samples pulled at room temperature. It can be hypothesised that voids nucleation and growth differ within tested conditions. At RT, the resistance to local stress concentration is smaller, resulting in eased void growth and consequently enhanced dimples size. On the contrary, at cryogenic conditions, the stress needed to locally plastify the material is

increased so the void growth is suppressed therefore observed dimples size is lesser. It suggests that resistance to local stress concentration is enhanced at low temperature of -150°C. Similar conclusion can be drawn, when the necking is analysed. Area reduction in the neck is more pronounced for room temperature test than the one at -150°C. Even though total elongation to fracture is increased at cryogenic temperature, the failure once necking has begun is accelerated as compared to RT.

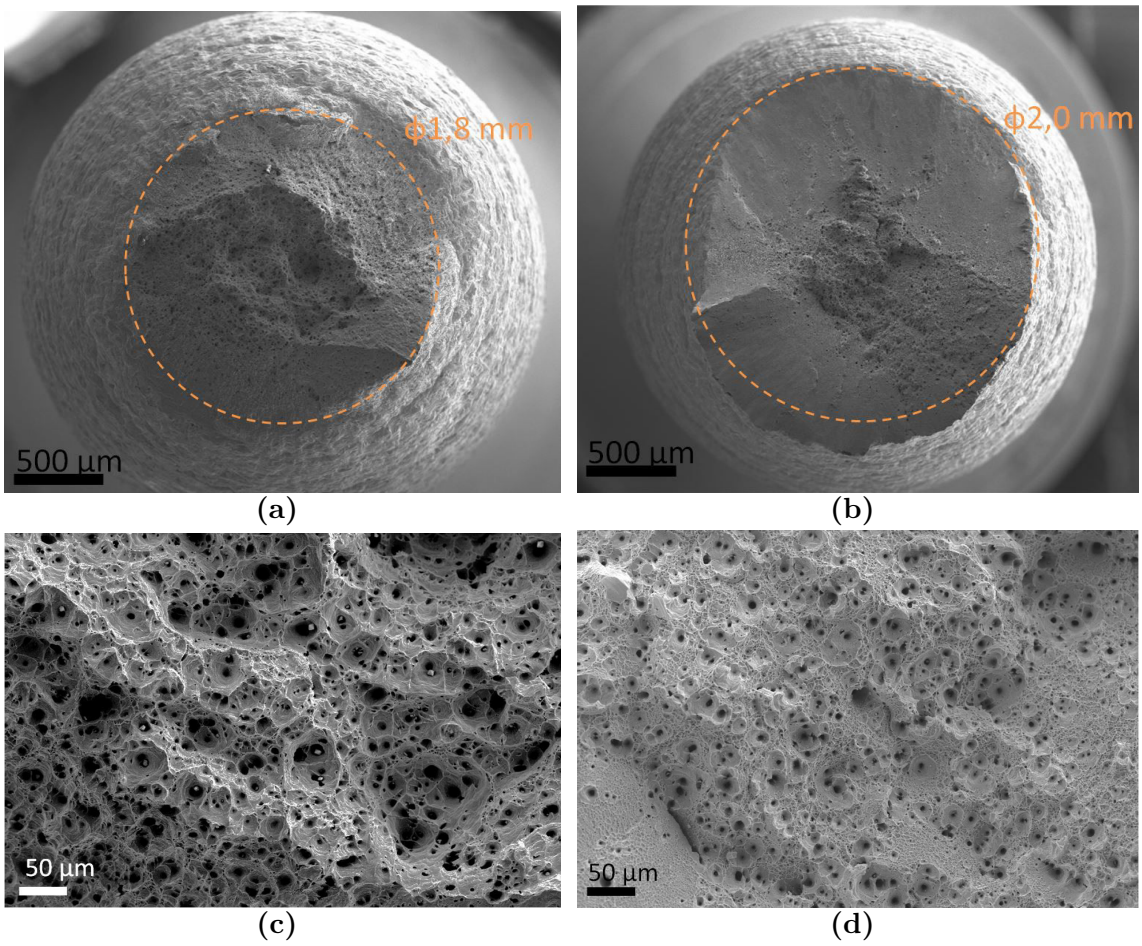

Figure 4.7: *Annealed Y3 tensile samples after fracture at room temperature (a, c) and at -150° (b, d). SEM SE images.*

Influence of the complex nanosized substructure of *as forged* Y3 Co-free grade on dynamic mechanical resistance was verified as well via Charpy impact toughness tests. The tests were performed at room and at liquid nitrogen temperature. The measured values of KCV_5 for Y3, A3S alloys and 304L stainless steel are presented in Table 4.2. Samples of reduced dimensions were chosen for those tests due to the size of initial forged rods, thus the index *5* next to KCV. Independently on test temperature, none of the samples broke upon impact, as shown in Figure 4.8. Large plastic zones on both sides of the notch were visible for Y3 Co-free alloy at both analysed conditions. Results of testing of reference 304L steel are slightly different. Fully plastic fracture was observed only at room temperature; at liquid nitrogen, the fracture surface presented more brittle character. This modification of fracture

conditions is also accompanied by a decrease of the KCV_5 values: a decrease in measured impact toughness resistance from 168 J/cm^2 at RT to 134 J/cm^2 at -196°C. Despite the loss of impact toughness resistance, the 304L steel maintains elevated level of resistance, higher than both tested HEAs in all conditions. Nonetheless, the impact toughness of Y3 and A3S alloys is still sufficient at the same time being stable throughout all testing conditions.

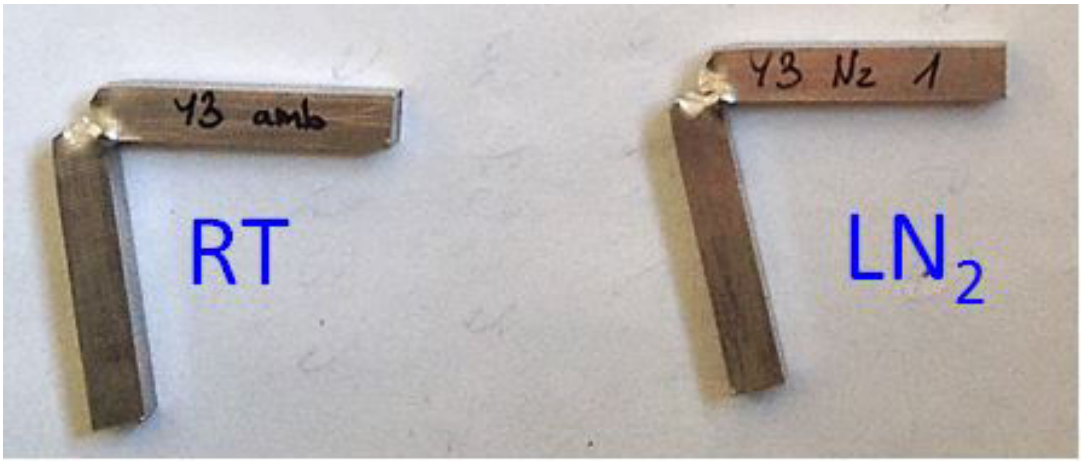

Figure 4.8: *Samples after Charpy impact toughness tests performed at room temperature (RT) and at liquid nitrogen (-196° C) for Y3 Co-Free alloy*

Table 4.2: *Impact toughness KCV_5 values obtained in Charpy test. Comparison between Y3, A3S and 304L alloys.*

Temperature	**Y3 Co-free** [J/cm^2]	**A3S [115]** [J/cm^2]	**304L SS** [J/cm^2]
25°C	138	126	168
-196°C	135	125	134

4.1.1.3 *Annealed* state

In this study, *as forged* state was often used as the initial state for analysis of microstructure evolution, recovery and recrystallisation. However, since it is a highly work hardened state, a comparison with an annealed, close to equilibrium state, was necessary. A heat treatment at 1000°C for 2h with subsequent water quenching was selected following the previous study by Mroz [115]. The chosen temperature is at about 0.8 T_M homologous temperature, which should be high enough to expect a fully recrystallised microstructure at the end. First observations of Y3 alloy in *annealed* state on the SEM scale and via EBSD are presented in Figures 4.9a and 4.9b. As it can be seen, the orientation is now uniform through each grain, which allows the observations by SEM BSE. Near equiaxed grains with straight grain boundaries are clearly seen. Moreover, presence of annealing twins is obvious. The grain size

was measured by EBSD and intercept method omitting the twin boundaries and the obtained values for both techniques were of the order of 48 μm, values are compared with *as forged* state in the Table 4.3. Those microstructural observations suggest that indeed recrystallisation took place during annealing treatment.

Table 4.3: *Mean grain size values after forging (from log-normal distribution fit / based on surface occupancy) and after annealing.*

		As forged	Annealed
Mean grain size	$\bar{d}$ [μm]	3.1 / 19.1	48.0

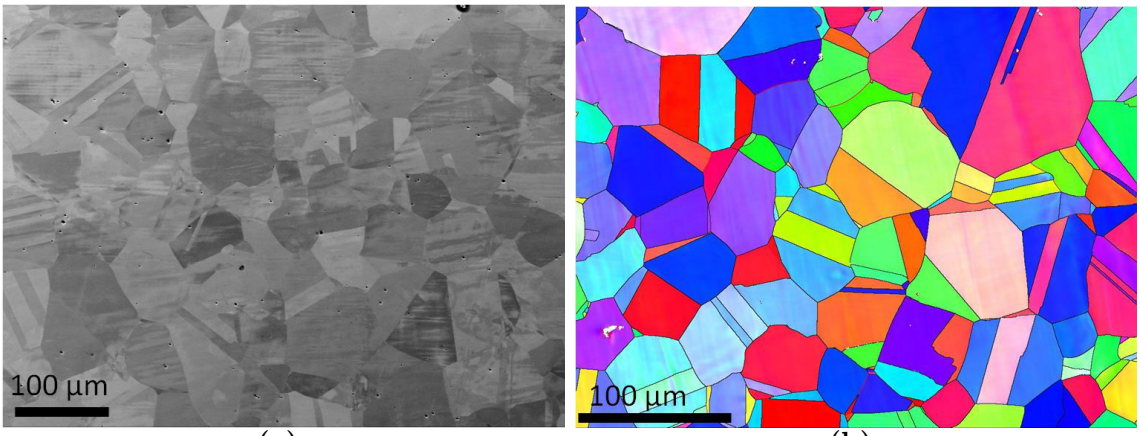

(a) **(b)**

Figure 4.9: *Microstructure of Y3 alloy annealed at 1000°C 2h, water quenched; a) SEM BSE image; b) EBSD IPFz image, with black lines representing high angle grain boundaries and red lines depicting subgrain boundaries.*

The evolution of microstructure between *as forged* and *annealed* states can also be seen through change in grain boundaries proportions, as shown in Figure 4.10. Information about all GBs was taken from EBSD analyses, where black lines stand for HAGBs, red lines for LAGBs and blue ones for twin boundaries. It is clear that in *annealed* state, number of LAGBs decreases drastically: it is close to 80% in *as forged* state and goes down to barely 4% among all boundaries present. At the same time the amount of HAGBs increases with a high fraction of $\Sigma 3$ twin boundaries, over 50%. Since the material was solely annealed, in explicit no deformation was applied, we can assume that the twins present in the structure are the annealing twins. Their formation is possible only during movement of HAGBs, which implies that grain growth has occurred during heat treatment [108]. This analysis suggests again a full recrystallisation of the material upon annealing.

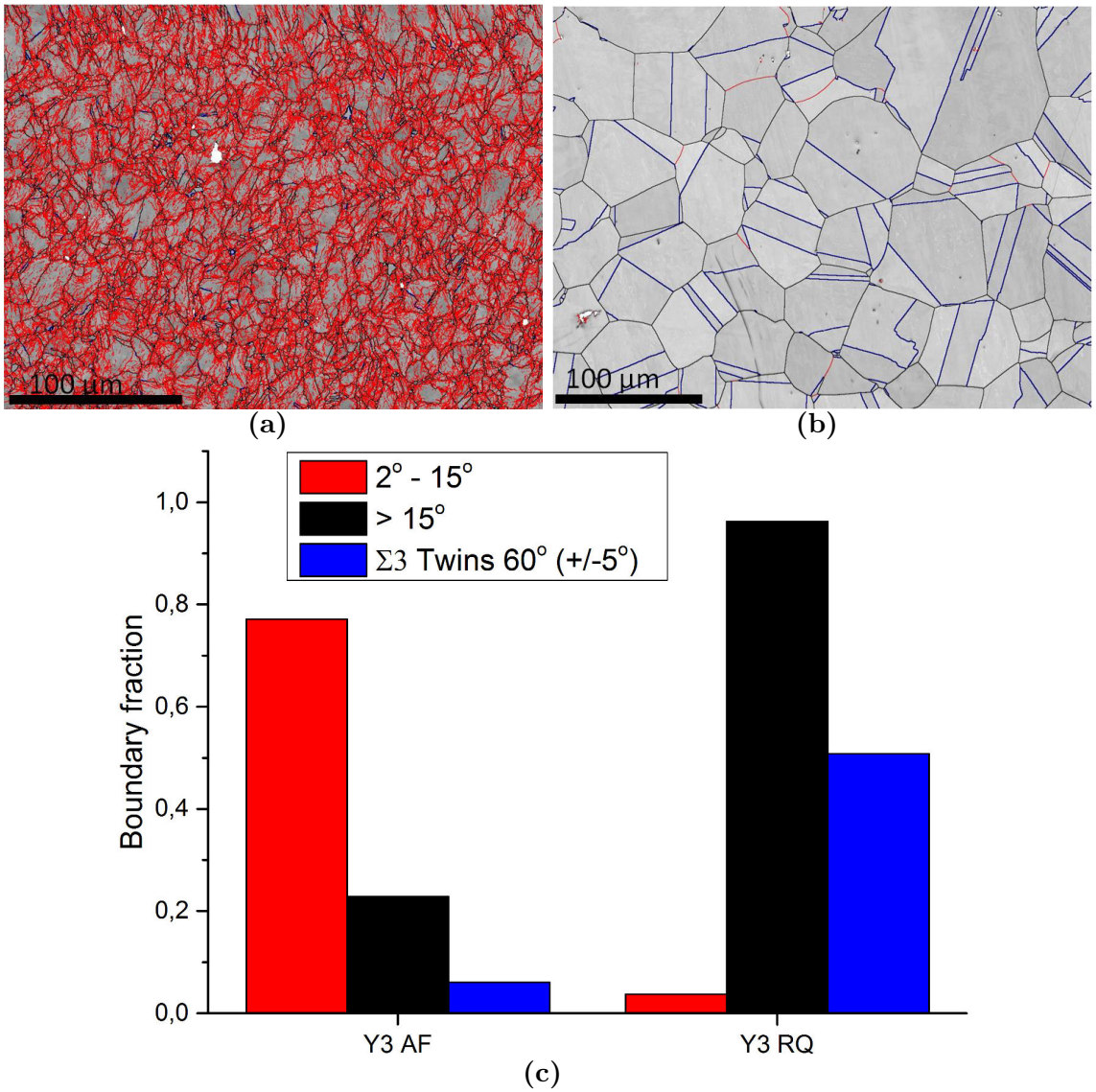

Figure 4.10: *Grain boundaries presented on band contrast images in Y3 alloy at a) as forged state and b) annealed state, 1000°C 2h. Black lines represent high angle grain boundaries, red lines represent low angle grain boundaries and blue lines depict Σ3 60° twin boundaries; c) fraction of HAGBs, LAGBs and twins for both as forged and annealed states*

The influence of the microstructure modification is clearly seen on mechanical properties: between *as forged* and *annealed* states, a strong change of shape of stress/ strain curves, is observed (Figure 4.11). Curves from tests at room temperature (bright blue curves) and at cryogenic conditions (dark blue curves) are displayed, the *as forged* curves have already been shown previously. It can be easily seen that the yield strength after annealing decreases over two times as compared to the *as forged* state; the values are regrouped in Table 4.4. This result is not surprising, since the *annealed* microstructure is relaxed, close to equilibrium. Its mechanical resistance is no more increased due to high work hardening of the material, like it was the case for *as forged* state. At the same time, decrease in UTS after annealing can be noted despite increased work hardening coefficient. Slope of plastic parts of

the *annealed* Y3 curves increases, but the high values of UTS are not reached and necking begins for lower stresses. Nevertheless, the total elongation to fracture has increased in the *annealed* state.

It is reassuring to note that same tendency, already found in the *as forged* state, to simultaneously increase mechanical resistance and elongation at cryogenic temperatures, is also observed upon annealing. Finally, no signs of martensitic transformation are visible on the -150°C curve: the fcc phase stability is maintained. This behaviour, characteristic for the studied HEA family, is preserved. In fact, this phenomenon is due to the matrix properties, not related to the microstructure.

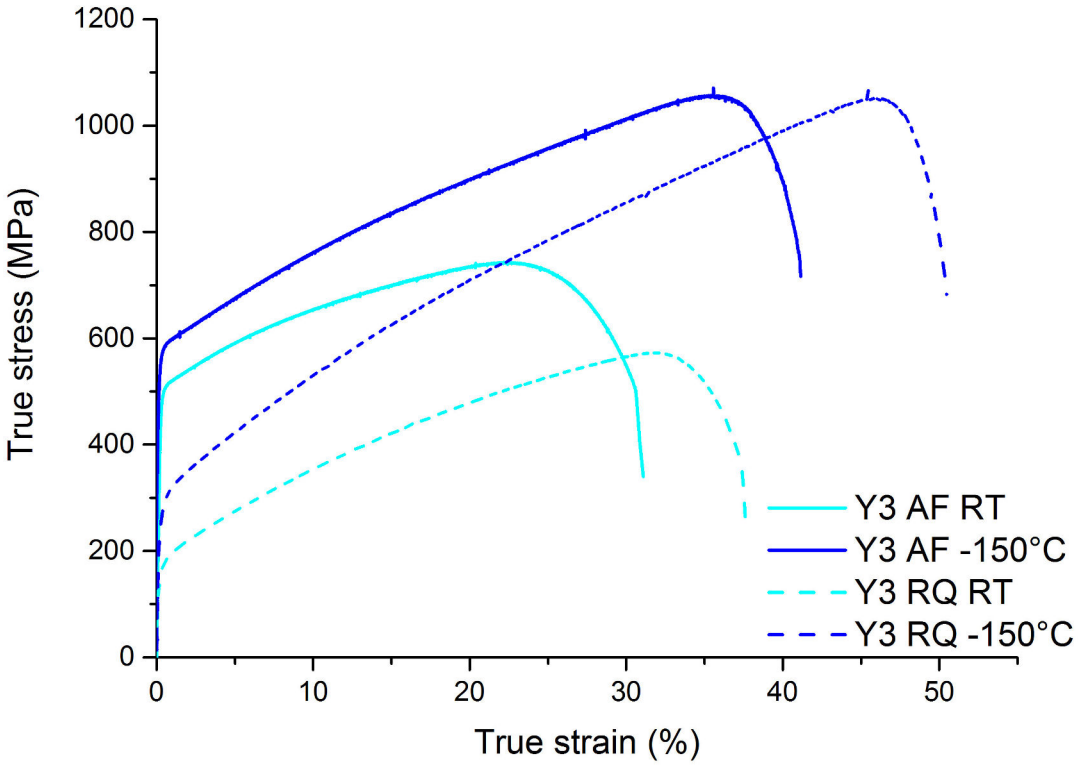

Figure 4.11: *Tensile true stress vs true strain curves for Y3 alloy with various initial states: as forged AF (solid lines) or annealed RQ (dashed lines). Tests performed at room temperature (RT, bright blue) and -150° C (dark blue).*

When hardness of both *as forged* and *annealed* states is analysed, the change of behaviour is also visible, Table 4.4. A significant drop from 190 to 118 HV is observed upon annealing. At the same time, the ratio between YS and HV, represented by α parameter, decreases. It is due the fact that hardness measurements account also for plastic response of the material, about 10% strain. Since the slope of the plastic part of the curve after annealing is increased, the impact of plastic part during hardness measurement is greater than for *as forged* state. As a result the HV and YS values in their respective units are closer and the α parameter is decreased.

Table 4.4: *Yield strength (YS), hardness (HV), α parameter (α = YS/HV), ultimate engineering tensile stress (UTS) and elongation to fracture (El) for as forged Y3 and annealed Y3. Tests performed at room temperature and at -150°C.*

Alloy	**Test T** [°C]	**YS** [MPa]	**HV** [Vickers]	α	**UTS** [MPa]	**El** [%]
Y3 *as forged*	25	500	190	2,63	592	36
	-150	584			744	51
Y3 *annealed*	25	207	118	1,75	475	46
	-150	287			675	66

Analogous change of tensile behaviour was observed by Mroz for both A3S and Cantor's alloys [115]. Samples after forging showed high YS with low work hardening coefficient, while upon annealing for 2h at 1000°C, the YS dropped drastically and the WHC increased. The author explains the initial behaviour by nanosized microstructure that is lost upon annealing, since alike data was reported by Valiev et al. [146] on ultra-fine-grained copper. Knowing that *as forged* Y3 Co-free alloy presents a complex substructure with network of dislocations cells and similar mechanical behaviour, analogous to the one observed for A3S, the same explanation can be attributed in this case.

To let a better insight on the mechanical behaviour of Y3 alloy, all tensile and compression tests performed on this alloy are summarised in Figure 4.12. Influence of temperature, strain rate and initial state on yield strength are shown. Firstly, as already pointed out, the YS values after forging are over two times higher than after annealing in the tested range of temperatures from -150°C to 500°C. This significant drop can be attributed to the change of microstructure with low density of LAGBs and bigger grain size. Secondly, the influence of strain rate can be defined. It is clear based on the *as forged* samples that no strain rate dependency is visible up to 500°C; purple and blue triangles overlap nearly perfectly. Likewise, the same independence from strain rate in this range of temperatures was found to be true for both A3S and Cantor's alloys [73, 115]. This result is not surprising: in classical materials, and in accordance with models of mechanisms of plastic deformation, it is expected to see little influence of strain rate in range of temperatures, below 0.5 T_M, as the thermal mechanisms should not be activated. Yet, as the testing temperatures increases to 850°C, 0.69 T_M, and 1050°C, 0.81 T_M, increased impact of thermally activated processes can be distinguished. It is an expected outcome, since for $T > 0.5\ T_M$ thermal activation takes place. It leads to increased yield strength if the deformation rate is accelerated, due to less time available for diffusive processes to intervene. The observed influence of strain rate in the range of temperatures 850°C to 1050°C is in accordance with literature for Cantor's alloy [73]. At the same time, it is not

very pronounced since 10^{-3} s^{-1} is still a relatively fast deformation rate. The study for Y3 alloy at high temperatures was done only in its *annealed* state; it could be expected that if analogous tests were performed fo the *as forged* Y3 the strain rate dependency would be more evident due to modification of nano-structures present in this state. Nevertheless, only one deformation rate was selected for most tests, just like in many other studies [10, 22, 73, 115] the mechanical tests were done with rate 10^{-3} s^{-1}.

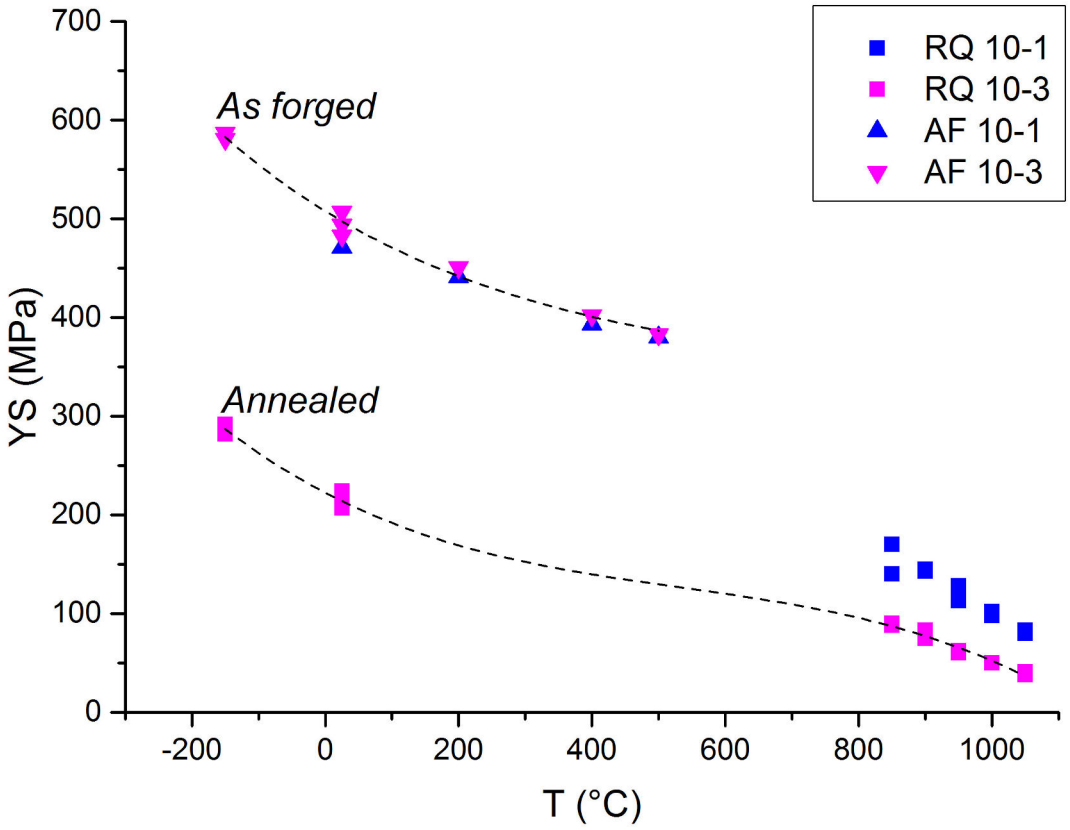

Figure 4.12: *Variation of yield strength with respect to temperature. Alloy's initial state is represented by triangles for as forged AF, or by squares for annealed RQ. Influence of deformation strain rate is depicted by colours: blue for 10^{-1} s^{-1} and purple for 10^{-3} s^{-1}. Dashed lines ar drawn through point corresponding to each state as a guide for readers eye.*

Finally, the influence of temperature on YS values can be determined. In general, as expected, the yield strength decreases with temperature. Relatively high YS of the order of 400 MPa is maintained for the *as forged* state up to 500°C and no drastic drop is observed in the analysed range of temperatures. The evolution of YS values is rather monotonous. However, for recrystallised Cantor's alloy, Gali et al. [73] reported a change of rate of YS evolution at about 200°C, after a fast decrease, the YS values reach a certain plateau to further drop again less drastically. Ultimately, the YS values decrease down to about 50 MPa at 1000°C, 0.8 T_M, in both cases, for Cantor's alloy [73] and for Y3 Co-free alloy in this study.

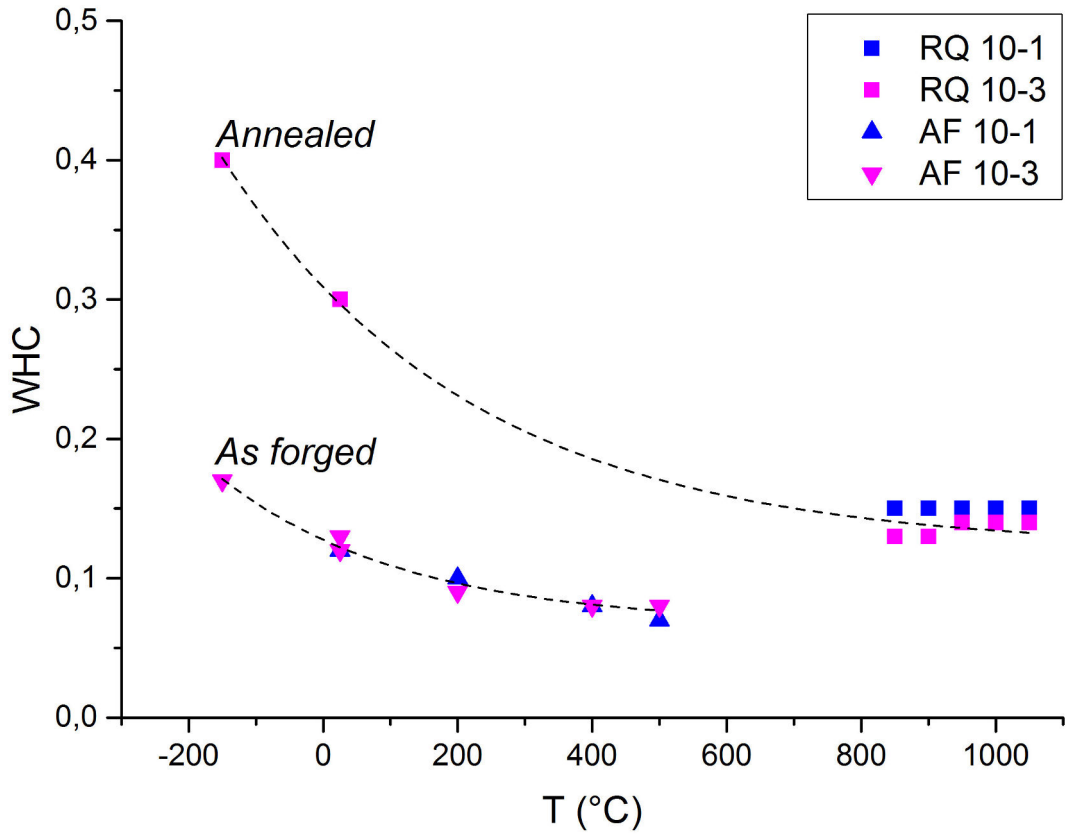

Figure 4.13: *Variation of work hardening coefficient with respect to temperature. Alloy's initial state is represented by triangles for as forged AF, or by squares for annealed RQ. Influence of deformation strain rate is depicted by colours: blue for 10^{-1} s^{-1} and purple for 10^{-3} s^{-1}. Dashed lines ar drawn through point corresponding to each state as a guide for readers eye.*

Effects of temperature, strain rate and initial state on work hardening coefficient, WHC, are presented in Figure 4.13. Again, all tests are grouped together and same symbol/colour codes are preserved. Firstly, as mentioned before, the *as forged* state shows significantly lower values of WHC compared to the *annealed* state. It can be explained by the complex structure of dislocation cells in the *as forged* state, due to nanosized structure [146]. It can be hypothesised that dislocations are prompt to move through a cell and annihilate with other dislocations they meet. This allows to create new dislocations that will further cross next cells. As a consequence, little additional stress is needed to move the dislocations in this structure that is in general complex and changes dynamically but in the end, if globally analysed, does not evolve significantly. Secondly, as expected, little to nearly no influence of strain rate on WHC is visible. Points overlap for both *as forged* and *annealed* states in the whole range of temperatures. Finally, asymptotic decrease of WHC is found through the wide range of temperatures and for both states; no drastic change of behaviour was found.

Initial microstructural observations as well as mechanical tests suggest that the Y3 alloy undergoes classical recrystallisation upon annealing. However, when one

observes the *annealed* Y3 alloy at the scale of TEM, stating that recrystallisation took place is not straightforward any more, Figure 4.14. The microstructure appears to be much more complicated than supposed on the basis of SEM observations. Despite clear proof of movement of grain boundaries, high density of dislocations is maintained. It is uniform though grains and in particular, it is maintained in the close neighbourhood of HAGBs.

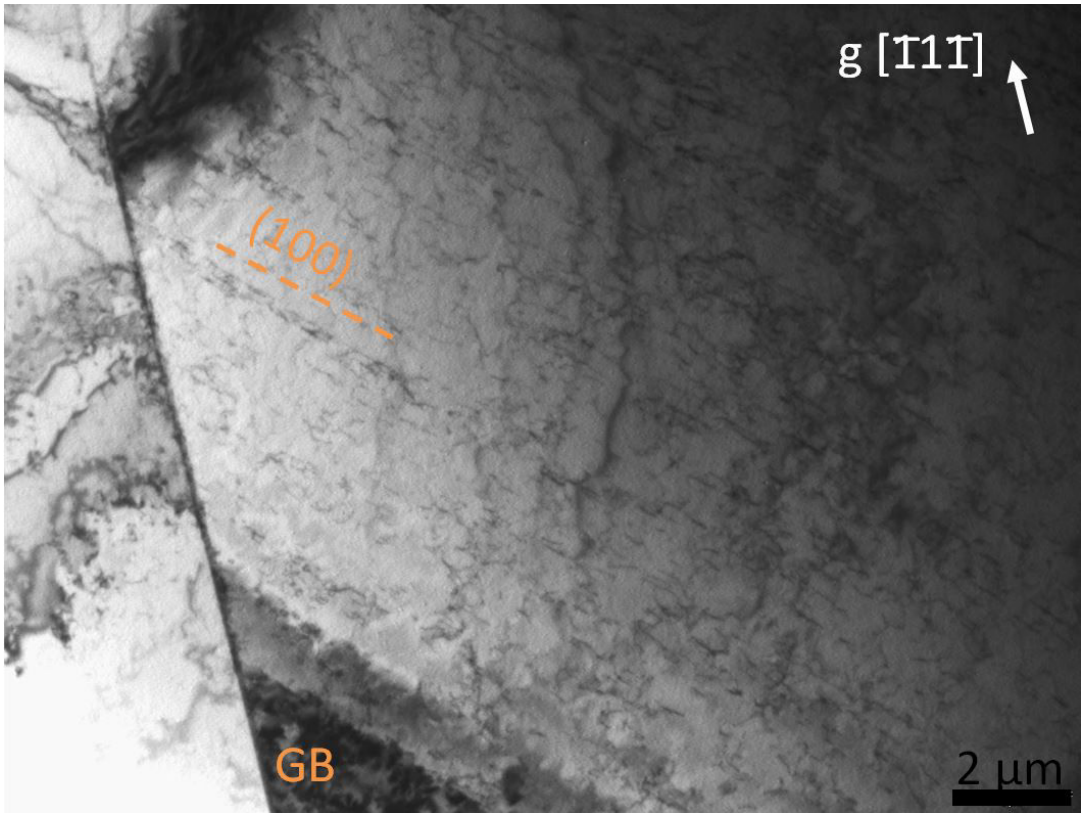

Figure 4.14: *Microstructure of Y3 alloy annealed at 1000°C 2h, water quenched, TEM BF micrograph at [011] ZA.*

Once again, like in the *as cast* state, the arrangement of dislocations following selected {111} - type planes is clear, Figure 4.15a. Those arrangements look like numerous long dislocations when the {111} plane is up during observations. However, when the same plane is tilted, the previously lines become aggregates of multiple dislocations, Figure 4.15b. There is an elevated number of dislocations in selected {111} planes, with numerous interactions. The distance between those arrays of dislocations on {111} planes is of about 200 nm. This span is coincidently similar to the size of cells formed during forging. It is interesting to note that the same phenomenon was found in A3S alloy [115], where upon high temperature annealing dislocations were found to organise themselves along the {111}-type planes. It suggests that this characteristics is uninfluenced by absence of Co in Y3 alloy but is typical for this family of non-equiatomic HEAs.

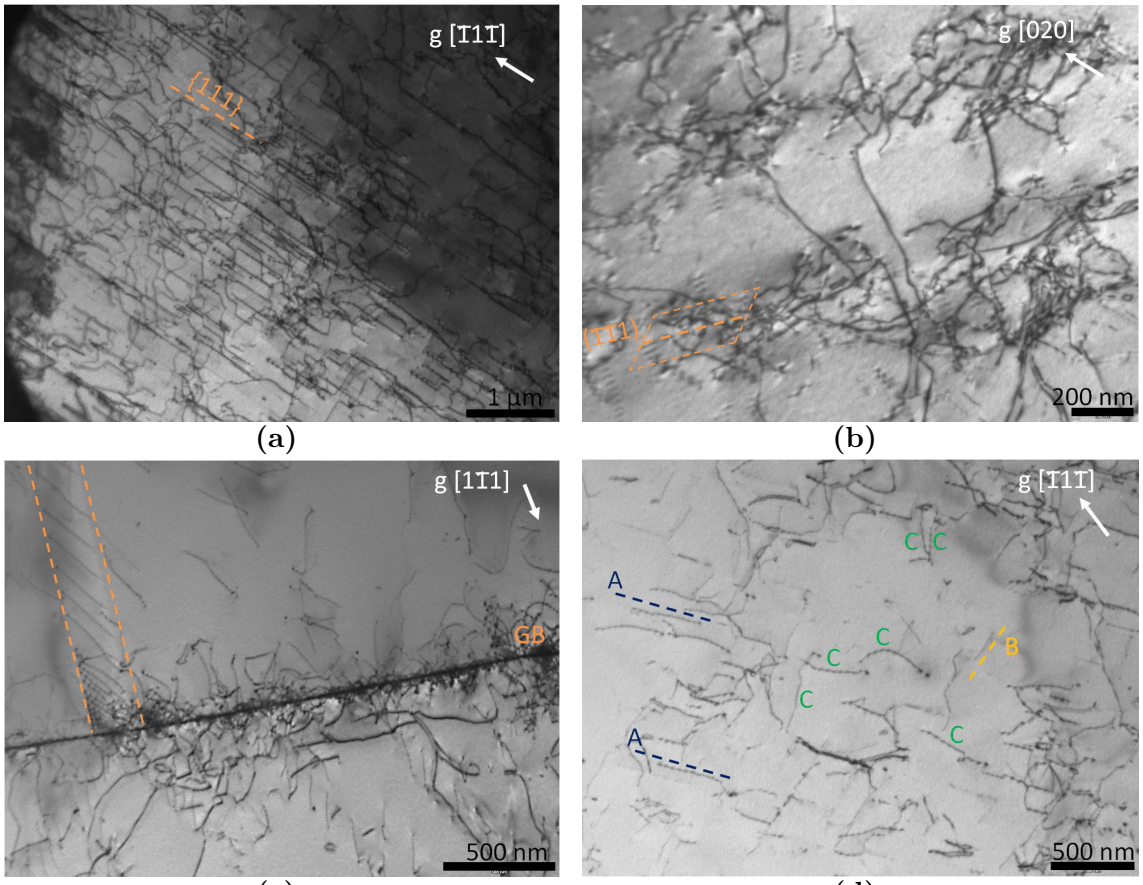

Figure 4.15: *TEM micrographs of Y3 alloy at annealed state. a) alignement of dislocations at {111}-type planes ([011] ZA); b) the same dislocations alignements at {111}-type planes that are laid down; c) grain boundary and a pile up ([011] ZA); d) thin zone with identified dislocations types ([011] ZA)*

Numerous interactions between the dislocations as well as their pile ups at grain boundaries were observed, Figures 4.15c and 4.15d. Character of some of the dislocations present in the latter Figure was defined. Dislocations marked as A could have been fully described with their Burgers vector $\vec{b}$ $(1\bar{1}0)$, line vector $\vec{t}$ $(\bar{1}01)$ and the angle between them $\measuredangle\,(\vec{b},\,\vec{t}) = 60°$. This is a whole family of long and straight mixed dislocations with their slip plane being (111), which is typical for fcc materials. B dislocation is a screw dislocation with $\vec{b}$ $(1\bar{1}0)$ and $\vec{t}$ $(1\bar{1}0)$. The $\vec{b}$ of all C dislocations was found to be $(01\bar{1})$ but due to their curvature no line vector could have been defined.

An example of detailed method of definition of dislocations character is presented in Figure 4.16. The same zone is photographed in TEM at various bright field two beam conditions close to at least two different zone axes. "Two beam" conditions mean that only one plane, with vector $\vec{g}_{hkl}$, is in diffraction conditions. In presented Figure, the observed zone axes are [011] and [001]. Fulfilment of diffraction condition $\vec{g}\cdot\vec{b} \neq 0$ leads to visible dislocation contrast and its trace can be noticed in the TEM image, like in Figure 4.16a. However, when $\vec{g}\cdot\vec{b} = 0$, the dislocation contrast

disappears like in Figure 4.16b. Some residual contrast can be seen due to elastic interactions, nevertheless the dislocation is considered as extinguished. Observations with other $\vec{g}$ vectors lead to definition of all conditions of extinction which allows to precisely describe the Burgers vector $\vec{b}$. Such analysis is presented in Table 4.5. This specific configuration is possible for only one Burgers vector $[1\bar{1}0]$.

Table 4.5: *Analysis of dislocations extinction conditions according to $\vec{g} \cdot \vec{b}$, where "+" means that the dislocation is visible and "-" means its absence.*

Zone axis		**[011] ZA**			**[001] ZA**		
$\vec{g}$	$\bar{1}1\bar{1}$	$\bar{1}\bar{1}1$	$\bar{1}00$	$\bar{1}00$	$\bar{1}10$	110	$\vec{b}$
	+	-	+	+	+	-	$[1\bar{1}0]$

Source of high density of dislocations upon annealing is yet to be defined. How come that upon clear signs of grain boundary movement, the dislocations are still present? The same question was found during the work on A3S alloy by Mroz [115]. As well as for the Y3 Co-free alloy, he reported arrangement of dislocations along some {111}-type planes after heat treatments at high temperatures. Mroz proposed a hypothesis based on short range ordering and increased Peierls stress. He suggests that if fluctuations of local chemical composition were to be confirmed, they could be the pinning points for the dislocations leading to their stability. At the same time, more distorted lattice could result in fluctuations of Peierls potential causing elevated friction stress. As a consequence, the dislocations movement would be disturbed. It is a working hypothesis that could be also applied to the Y3 Co-free composition. However, up to now, no proof of deep Peierls valleys were observed. TEM observations rather suggest a normal fcc behaviour, making the question about high stability of dislocations still open.

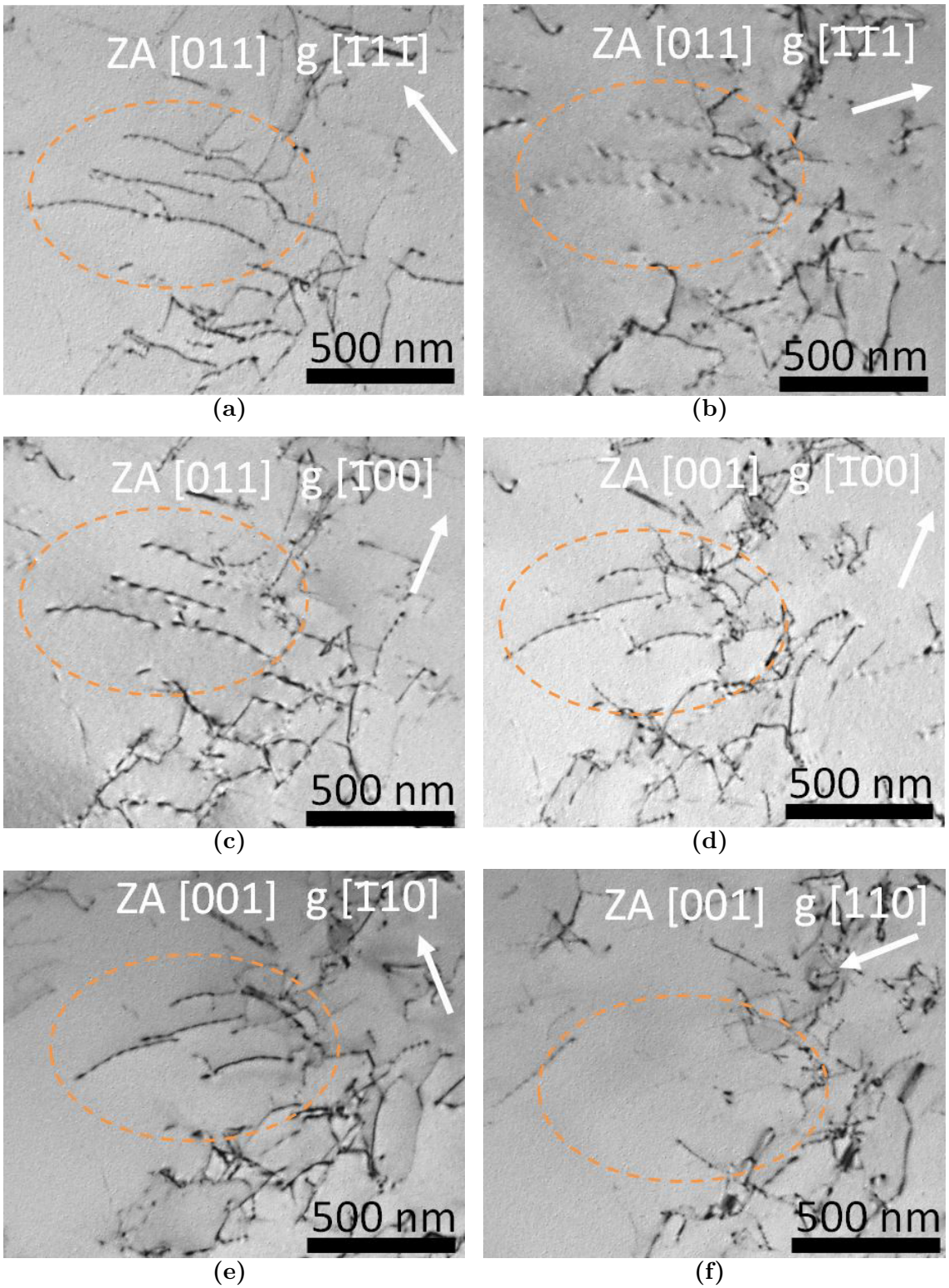

Figure 4.16: *Dislocations observations at various conditions for definition of extinction aspects according to $\vec{g} \cdot \vec{b}$ rule. The orange ring defines the observed area,, the same in all images.*

4.1.2 Estimation of dislocation density in initial states

The microstructural observations show a complex dislocation structure in all states, starting from as cast one to the annealed one. In general it was found that density of dislocations is elevated in respect to the analysed material states. However, measurement of dislocation density in such complex materials is problematic. Two basic standard techniques were used to evaluate the density of dislocations, starting with intercept method on TEM images and going to XRD measurements. Both techniques have their positive and negative sides. First, the TEM intercept method, is a reliable one for relatively low dislocation densities. Since it is a visual assessment, it depends on the observation conditions; there will always be a part of dislocations that is extinct. Additionally, if numerous dislocations are superposed or are difficult to distinguish the measurement can be badly estimated. At the same time, difficulty within this technique lies with measurement of foil thickness necessary for dislocation density estimation. The measurement is not direct and an approximated error of about 10% is to be expected. Despite all those sources of uncertainty, the method stays the most straight forward one.

Second technique, the XRD measurement, is based on the X-ray diffracted peaks widening at their basis. The dislocations density is measured based on a mathematical model of variance method based on the moments of intensity profiles, developed by Borbely and Groma [140]. This technique being more global, gives better statistics. Nevertheless, despite all possible precautions, the configuration of dislocations influence is not eliminated from the measurement and is a possible source of inaccuracy. Since none of the techniques is fully reliable, both were compared together for more accurate estimation of dislocations density.

Finally, a complementary solution for dislocations density estimation was proposed, based on mechanical tests and Taylor's equation 4.3, where M is the Taylor's factor (close to 3 for fcc materials with random orientation [147]), A is a constant between 0.1 and 1.0 (in this work set to 0.3, following [148]), μ is the shear modulus, b is the magnitude of Burgers vector (0.255 nm in the case of analysed HEAs) and ρ is the dislocation density. According to equation 4.4, ρ can be estimated for a given stress. It can be assumed that when the value of flow stress is reached, the dislocation structure is in dynamic equilibrium, creation and annihilation is constant (steady state stress was assumed to be reached at $\varepsilon = 0.8$). Consequently, the dislocation density corresponding to a value of dislocation density of a material at equilibrium could be estimated. Of course this approach does not allow the measurement of real dislocation density but can give an estimated idea, which should fall close to the measurements giving a final confirmation of measured values.

$$\sigma = MA\mu b\sqrt{\rho} \tag{4.3}$$

$$\rho = \left(\frac{\sigma}{MA\mu b} \right)^2 \tag{4.4}$$

Measurements of dislocations density performed based on TEM images, as well as using the XRD and Taylor's equation are presented in Table 4.6. Each measurement technique was used wherever possible, so that the values can be compared and a good estimation could be made. The differences between values from all measurement techniques come from their specificities as described above. Elevated density of dislocations was confirmed in all analysed states. Y3 alloy after casting and after annealing is characterised by similar dislocations density of the order of 10^{13} to 10^{14} m^{-2}, depending on the measurement technique used. Compared to classical fcc materials upon casting or recrystallisation, the observed dislocation density is extremely high, at least 4 orders of magnitude difference. Normally, a density of the order of 10^9 m^{-2} is found in such alloys and 10^{13} - 10^{14} m^{-2} rather corresponds to highly work hardened materials, not relaxed ones [149]. To illustrate how this difference in dislocations density can be seen in TEM micrographs one have to imagine that for classical materials individual dislocations are present every 1 μm or so. In the case of *as cast* or *annealed* Y3 alloy, numerous dislocations can be observed with the distances of about 100 nm between them.

Y3 alloy in the *as forged* state shows a somewhat increased dislocations density as compared to the *as cast* or *annealed* states, and is of the order of 4 x 10^{14} m^{-2}. The obtained value comes solely from the XRD measurement, as the intercept method could not be applied in this state. Due to complex substructure observed by TEM, distinguishing individual dislocations proved to be futile. Again, such elevated density of dislocations is typical for highly deformed materials [149].

Table 4.6: *Dislocations density in Y3 alloy at various states: as cast, as forged and annealed at 1000° C 2h. Comparison of measurements between XRD and intercept method on TEM images. Estimation from Taylor equation also presented for the annealed state.*

		As cast	**As forged**	**Annealed**
ρ [x10^{13} m^{-2}]	XRD	20 ± 0.1	42 ± 0.5	9 ± 0.1
	TEM	2 ± 0.5	-	3 ± 0.5
	Taylor	-	-	3 ± 1.0

In Table 4.7 a comparison between Y3, A3S and Cantor's alloys is made. For ease, all results come from XRD measurements. The Y3 Co-free alloy shows the lowest density of dislocations in both compared states: *as forged* and *annealed*. After hot forging the difference is of one order of magnitude, whereas after annealing the disparity is less pronounced. Little difference is found between A3S and Cantor's alloy.

Table 4.7: *Dislocations density in Y3 alloy, A3S [115] and Cantor's alloy [115] at various states: as forged and annealed. All measurements coming from XRD method.*

		Y3 Co-free	A3S [115]	Cantor's [115]
ρ [x10^{14} m^{-2}]	*As forged*	4.2	15	11
	Annealed	0.9	2.0	2.7

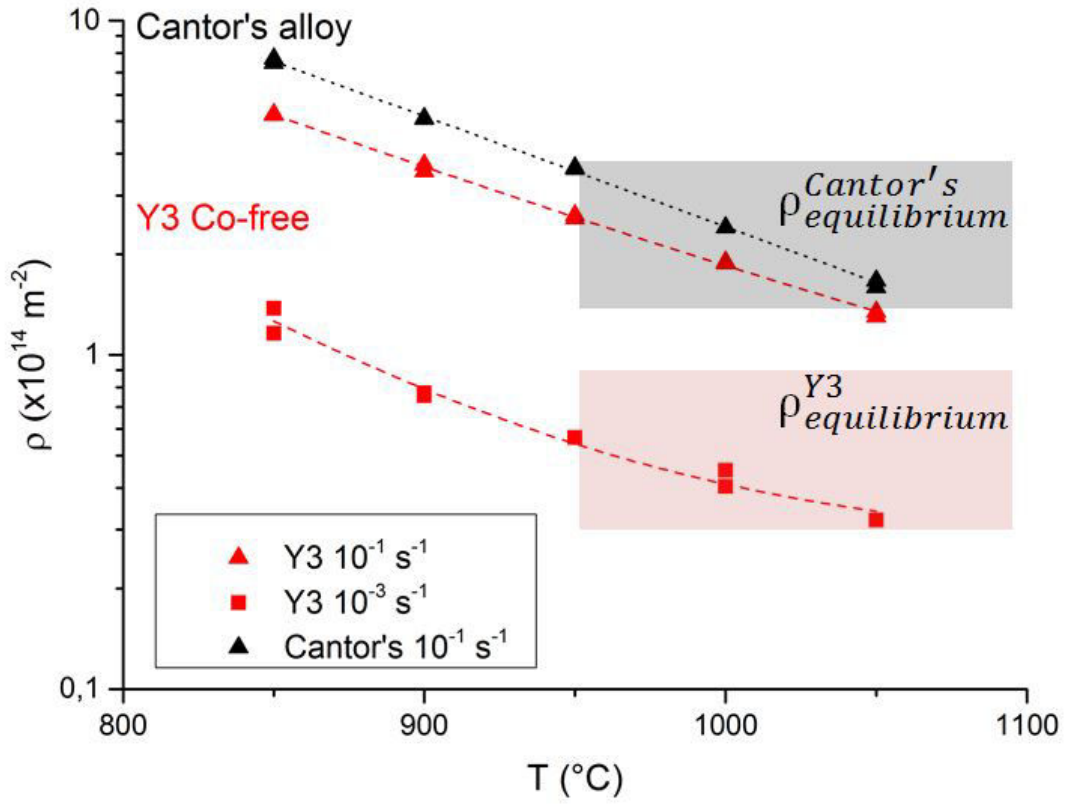

Figure 4.17: *Evolution of estimated dislocations density for high deformation compression tests and temperatures between 850°C and 1050°C. Comparison between Y3 Co-free and Cantor's alloys. Range of equilibrium dislocation density ρ measured in annealed samples is shown.*

Variation of estimated density of dislocation with temperature, coming from high temperature, and high deformation compression tests, is presented in Figure 4.17. Results for both Y3 Co-free (in red) and Cantor's alloys (in black) are compared. For Y3 alloy two different strain rates are represented. For all conditions the dislocation density decreases with increasing temperature. This outcome was expected and is due to presence of dynamic recovery. It is interesting to note that for high temperatures, between 950°C and 1050°C, the ρ values calculated from Taylor's equation are in the range of values measured via XRD or TEM for annealed samples for both Y3 Co-free alloy and Cantor's alloy. It would appear that at those elevated temperatures, a dynamic equilibrium is reached which is relatively close to the static equilibrium, $\rho_{equilibrium}$. Once again the density of dislocations for the quinary alloy

exceeds the one of Y3 alloy. It could be hypothesised that it is due to differences in chemical compositions between the two compared alloys. Could it be that more elements in the quinary alloy lead to higher number of equilibrium dislocations? The fact that the same orders of magnitude, as well as same tendencies were found via all measurement techniques confirms the correctness of measurements and it can be clearly stated that both HEAs are characterised by abnormally high density of dislocations.

Unusually high dislocations density is a common characteristics between Y3 Co-free alloy, Cantor's alloy [22,115] and the A3S composition [115]. The order of 10^{13} - 10^{14} m^{-2} is maintained through a wide range of heat treatments. Once again, those values are typical for highly deformed material in case of classical alloys and are surprising to be found in an annealed material [149]. In Y3 Co-free alloy, mainly defect-free structures were never observed and the elevated dislocations density was always preserved even in recrystallised grains. It stays unexplained why despite the clear proofs of grain nucleation and grain growth the dislocations are still present in so high density. Grain boundaries mobility should help dislocations annihilation but it is not the case in Y3 alloy, in agreement with previous observations in A3S composition. Dislocations formed during deformation are highly stable. It was hypothesised by Mroz that their stability is due to elevated energy of a perfect crystal of HEA compared to pure metals. The energy of HEA crystal with the addition of dislocations is very close to the defect-free crystal making dislocations presence not disturbing. In that case the annihilation of dislocations is not crucial for the system and only their rearrangement takes place. It is a hypothesis that still needs to be confirmed.

4.1.3 Effects of temperature of thermomechanical processing on microstructure

The question of initial deformation and driving force for recrystallisation needs to be approached as well. Does the temperature of initial deformation play a role? Change of SFE with temperature could lead to variation in dislocation structure that later could influence the structures found after annealing. In particular, is the elevated density of dislocations always present? Up to know, in literature, the microstructure observations were done mostly at the scale of SEM [20, 89, 103] and rarely on the scale of TEM [101]. The "recrystallised" appearance of the structure at this scale was always reported, with uniform orientation, straight grain boundaries and numerous twins. Similarly, observations of Y3 alloy at the SEM scale give the same result, but TEM analyses proved a complex internal structure. Is it the same when the deformation temperature changes?

4.1 Initial states: grain size, dislocations density and mechanical resistance

In parallel with recrystallisation study for *as forged* material, selected heat treatments were performed for Y3 alloy after severe cold rolling. The thickness reduction of the initial material of 90% was applied without any difficulties. The material did not show any cracks or failures.

Firstly, the standard annealing at 1000°C 2h was done and the microstructures at the scale of SEM were compared. The BSE images for both hot forged and cold rolled samples after heat treatment are shown in Figure 4.18. Each of the microstructures show grains close to equiaxed with straight boundaries and apparent uniform orientation. Numerous Σ3 twin boundaries can be found as well. The fraction of all types of grain boundaries is presented in Figure 4.18c, were HAGBs play a considerable part and nearly no LAGBs are present. Elevated fraction of twin boundaries is confirmed reaching nearly 60% of all HAGBs. At this scale of observations no significant differences in microstructural evolution can be determined between hot forged and cold rolled materials.

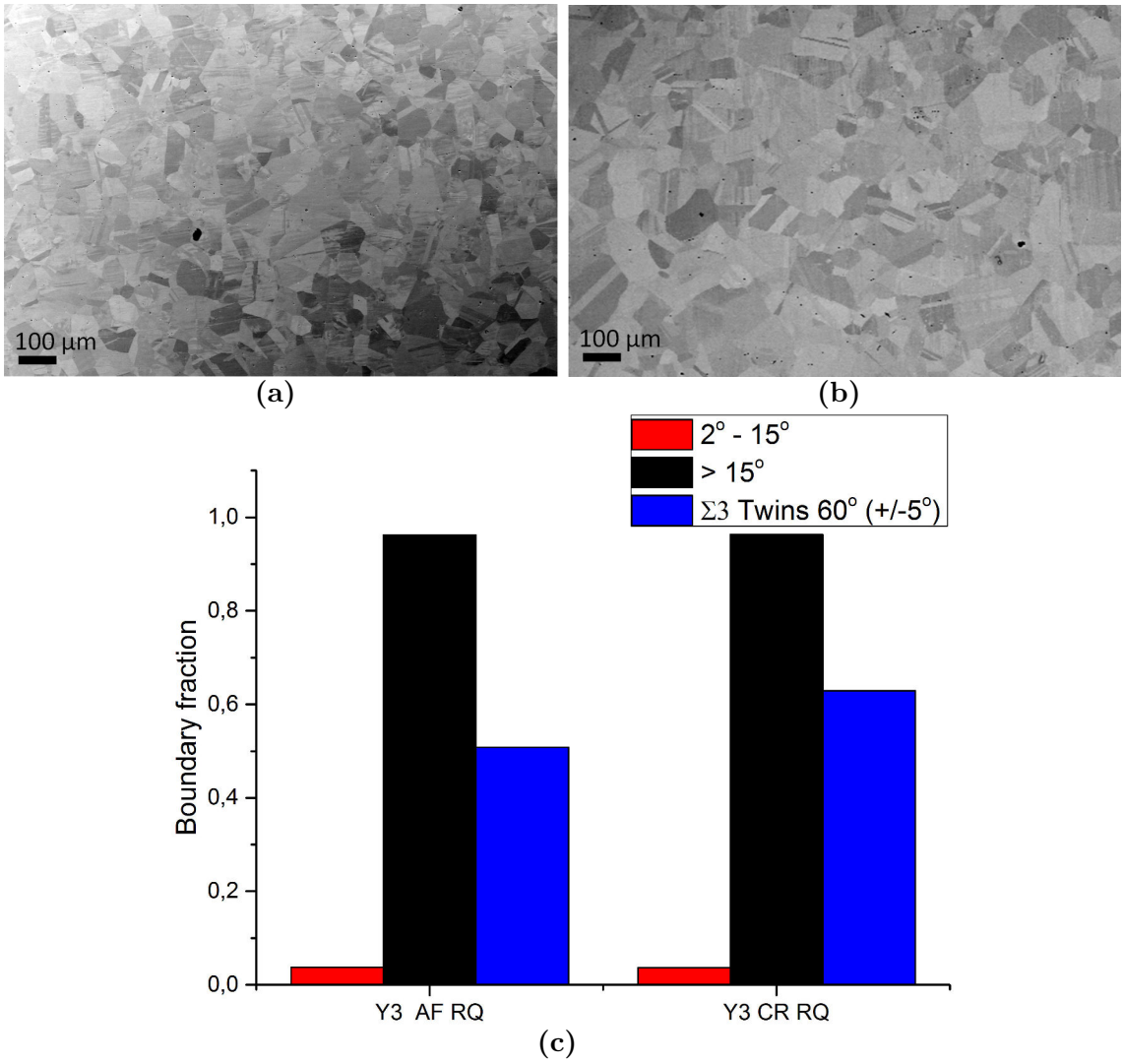

Figure 4.18: *Microstructure observations of Y3 alloy annealed at 1000°C 2h with two different types of initial deformation. SEM BSE micrographs of a) hot forged and b) cold rolled. c) fraction of HAGBs, LAGBs and twins for both states.*

TEM observations were performed for cold rolled Y3 alloy after short time annealings: 800°C 180s and 1000°C 0s, to verify if any differences at the level of dislocations appear. Two representative micrographs are presented in Figure 4.19 and they should be compared with Figures 4.26 and 4.27. Presence of high density of dislocations can be noted for both temperatures of annealing. Organisation of dislocations has started and it resembles the one found in *as forged* material. In both cases, hot or cold deformation prior to heat treatment, dislocation cells can be distinguished in the structure. Furthermore, again despite signs of grain growth and movement of grain boundaries, high density of dislocations is present in the structure. It suggests that dislocations formed upon hot or cold deformation are stable and there is little driving force for their annihilation.

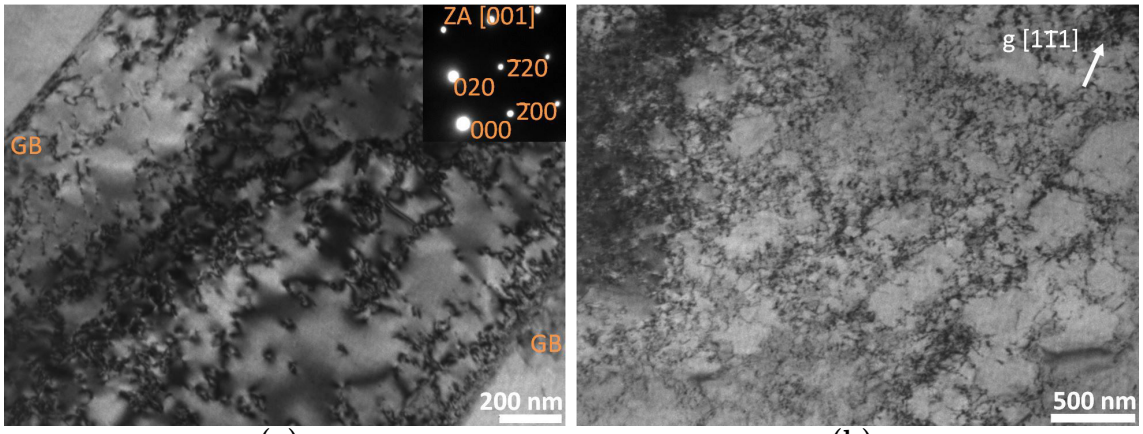

(a) **(b)**

Figure 4.19: *TEM images of cold rolled Y3 alloy after annealing at a) 800° C 180s ([001] ZA) and b) 1000° C 0s ([011] ZA).*

No particular influence of temperature of initial deformation was found. Microstructures for both hot forged and cold rolled material resemble themselves at both scales of observations: SEM and TEM. It reinforces the suggestion, that dislocations created upon deformation at high or room temperature, are stable and not prompt to annihilation. The facility of stabilising dislocations is a remarkable feature of analysed HEAs.

4.2 Effects of annealing temperature of thermomechanically processed alloy: analysis of recrystallisation conditions

Microstructural observations of Y3 Co-free alloy at various states bring us to question the recrystallisation process, specific to this grade of austenitic HEAs. High density of dislocations upon high temperature annealing, uncommon for a relaxed structure, would rather suggest their reorganisation, so: a kind of recovery. However, at the scale of SEM observations it seams obvious that recrystallisation took place. So does recrystallisation, in the classical sense of this term, really happen in the Y3 alloy? Since the doubt persists, the *annealed* states, where microstructure with low density of sub-boundaries and uniform orientation is observed, will be called "recrystallised", until a clear answer is obtained. Signs of recrystallisation can be found in various places. Indications can come from mechanical behaviour, grain size evolution or even texture.

At the same time, one should wonder if the equilibrium structure for the Y3 Co-free alloy needs to be redefined? Elevated density of dislocations in the *as cast* state as well as in the *annealed* states would suggest that this is the favoured configuration. The fact that high density of dislocations is maintained upon movement of grain boundaries during grain growth, favours the hypothesis of peculiar equilibrium structure in the HEA.

4.2.1 Microstructural evolution with temperature of annealing

Typically, in initially deformed metallic alloys two different phenomena can be found upon annealing. Firstly, for low temperatures, usually below 0.5 T_M, organisation of dislocations inside the grains takes place and is called recovery. When the temperature of annealing increases, and if the initial deformation was high enough (leading to increase of stored energy), another event occurs: nucleation of new grains followed by their growth called recrystallisation. It is an effect dependant on the initial deformation of the material and on the energy stored in it which further influences the temperature and time of annealing necessary for recrystallisation. As a result a microstructure with little defects is obtained with increased elongation and decreased mechanical resistance.

To determine the conditions of recovery and/or recrystallisation of Y3 alloy, a series of annealings at various temperatures ranging from 600°C to 1000°C were performed with times ranging from 2 hours to 4 weeks. The durations of heat treatments were chosen following the work of Mroz [115], where unexpected behaviour was observed.

Compression curves from tests at room temperature of samples *annealed* in various conditions are presented in Figure 4.20. They are clearly assembled into two groups: 1) high resistance regime, with low work hardening coefficient (WHC) and 2) low resistance regime, with high WHC. In fact, only samples annealed at 600°C, independently of time of heat treatment, present the first type of behaviour, quite similar to that obtained in the *as forged* state. Only slight decrease of YS with increasing time of annealing at 600°C is measured (from 527 MPa to 455 MPa). Similar mechanical behaviour suggests little to no change in the microstructure between those states.

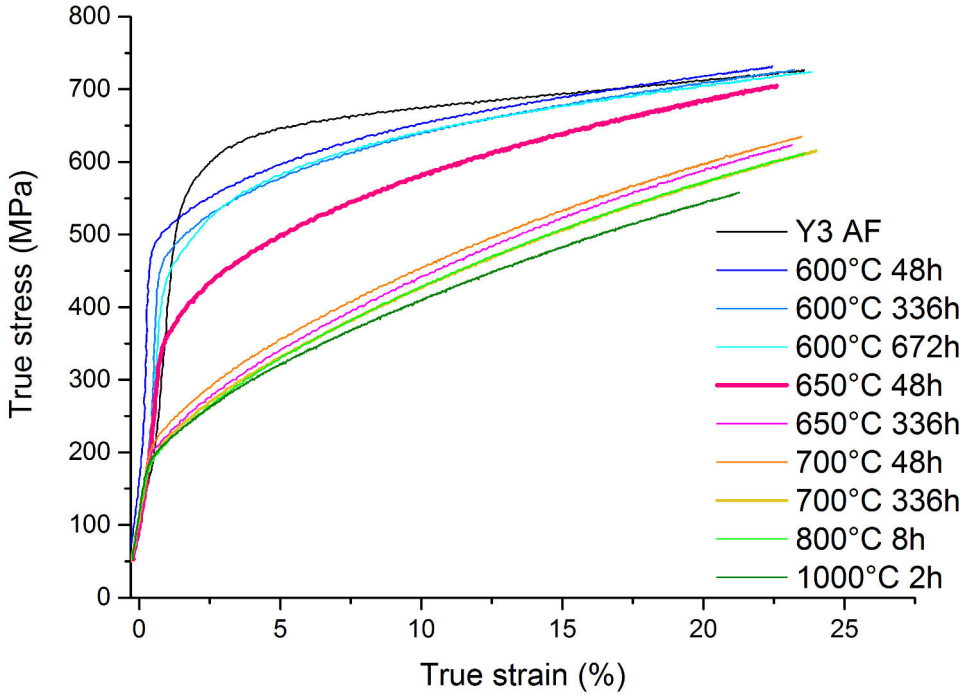

Figure 4.20: *Effect of annealing on compression behaviour at room temperature for Y3 alloy. Deformation rate* 10^{-3} s^{-1}.

A significant decrease of YS and a simultaneous increase of WHC can be observed for the sample annealed during 48h at 650°C (pink curve). This behaviour implies initial stages of microstructure modification. When the alloy is further annealed for longer time or at higher temperatures, it reaches a low resistance regime, with YS ranging form 220 MPa to 250 MPa and high values of work hardening coefficient equal to 0.36 - 0.4. Let's note that these characteristics are close to what was considered until now as the *annealed* state. All the various heat treatments presenting the second type of behaviour result most probably in the same microstructure. Therefore, it is reasonable to consider that a significant microstructural modification takes place between 600°C (0.53 T_M), and 650°C (0.57 T_M).

The modification in compressive behaviour can be resumed by yield strength

comparison shown in Figure 4.21a. The change in mechanical resistance is also reflected in the results of hardness measurements, Figure 4.21b. HV values are maintained at a level comparable to initial *as forged* state up to 48h at 650°C. When the time or temperature slightly increases, a significant drop is observed from 194 HV to 130 HV. Those observations suggest a significant change in microstructure at around 650°C. If the analysed HEA were to behave like a classical alloy, at 0.57 T_M beginning of recrystallisation would be suspected. Similar change in behaviour was observed by Mroz [115] on both A3S and Cantor's alloy.

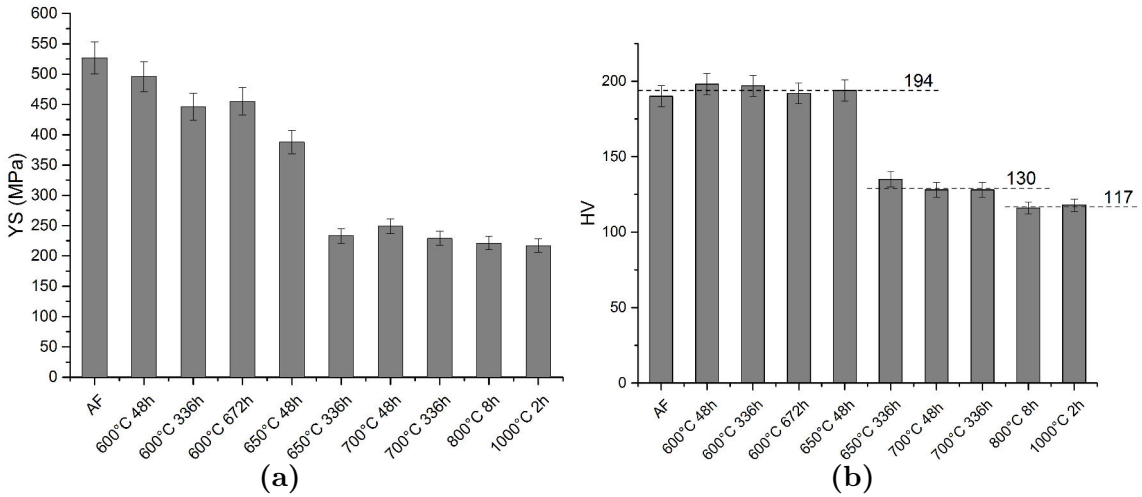

Figure 4.21: *Effect of annealing on a) compressive yield strength for Y3 alloy and b) Vickers hardness.*

EBSD observations allowed to determine the modifications in the microstructure upon annealings, specially those which resulted in changed mechanical behaviour. One could expect a "recrystallised" microstructure, in explicit with low fraction of LAGBs and increased presence of twin boundaries, when the low resistance regime is reached, if it were a classical material. Figures presenting grain boundaries on a band contrast image for selected annealing conditions are regrouped in Figure 4.22. Annealings at temperatures up to 600°C can be mostly represented by Figure 4.22a. Nearly no difference is visible between this microstructure and initial *as forged* state. Only occasional "recrystallised" grains are present upon very long annealing (4 weeks; 672h). However, even with presence of such grains, proportions between all types of GBs are not altered, as it is presented on the histogram in Figure 4.22d. One can notice that those proportions start to shift in the favour of HAGBs at 650°C already after 48h of annealing. Large part of the microstructure resembles now a "recrystallised" one with numerous grains free of sub-grain boundaries and presenting many twin boundaries, Figure 4.22b. This type of microstructure is in accordance with observed mechanical properties. Some areas showing grains with presence of LAGBs are still visible, although the density of sub-boundaries has decreased compared to *as forged* state or the ones annealed up to 600°C. If the annealing is prolonged to 2 weeks, the structure shows solely grains that could be

described as "recrystallised", Figure 4.22c. LAGBs are nearly non-existent and twin boundaries present more than half of all boundaries. Microstructures observed for higher temperatures of annealing are similar to this image: at the scale of SEM observations no distinction can be made between samples annealed above 700°C; grain boundaries fractions are comparable and only the grain size somewhat increases.

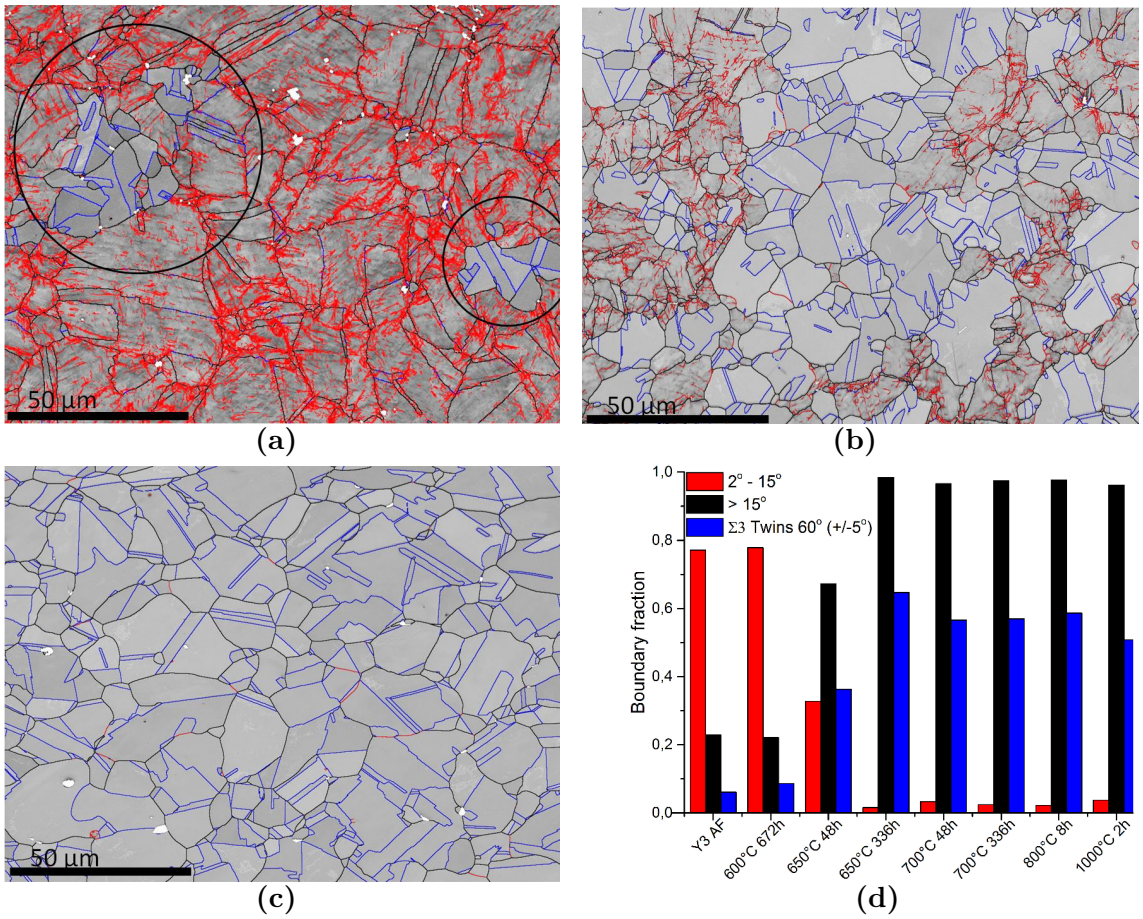

Figure 4.22: *Grain boundaries presented on band contrast images in Y3 alloy after annealing at a) 600°C 672h; b) 650°C 48h; c) 650°C 336h and d) comparison of grain boundaries fractions for all annealing conditions. Black represent HAGBs, red represents LAGBs and blue stands for twins*

The mechanical testing combined with EBSD observations images suggest a "recrystallisation" process that would start at 650°C, in *as forged* Y3 alloy. No changes are visible at 600°C, and very long time is necessary for the process to start at 650°C at least in the applied deformation conditions. To confirm, or not, this hypothesis, series of TEM observations has been performed on selected annealed samples. Representative micrographs are shown in Figure 4.23. Firstly, complex internal structure with high dislocations density maintained upon long time annealing at 600°C can be found, Figure 4.23a. Presence of dislocations cells and numerous orientations inside grains are still observed just like for the *as forged* state. Yet, a slight organisation of the substructure must have occurred, as the diffraction diagram from a wide zone shows only one crystal orientation. This substructure maintained even upon long

time annealing is now considered as responsible for high mechanical resistance of the samples during compression tests, in agreement with our already achieved comprehension of studied material. However, the TEM observations of sample annealed at 650°C for 2 weeks, Figure 4.23b, is more surprising. According to SEM and EBSD this should result in a fully "recrystallised" structure. Nonetheless, it presents a high density of dislocations that barely started to reorganise, as traces of {111} planes can be guessed. Contrarily to classical materials, where recrystallised structure does not keep such elevated levels of dislocations density, in the HEA dislocations have barely moved. Presence of some annealing twins could have been observed as confirmed by the diffraction pattern. For annealing at 700°C, Figures 4.23c and 4.23d, the organisation of dislocations is further advanced. It can be hypothesised that dislocations do move between the cells, leading to their partial annihilation. This in return, allows for creation of new dislocations during deformation what explains the increased WHC observed on compression curves. Still, despite the movement of GBs dislocations are present with elevated density. Similar structures are obtained for all other annealings at high temperature ($\geq$ 700°C) regardless the time of the heat treatment. Those are the dislocation structures that have also been found in the *annealed* state considered as initial state for most of studies (1000°C 2hours).

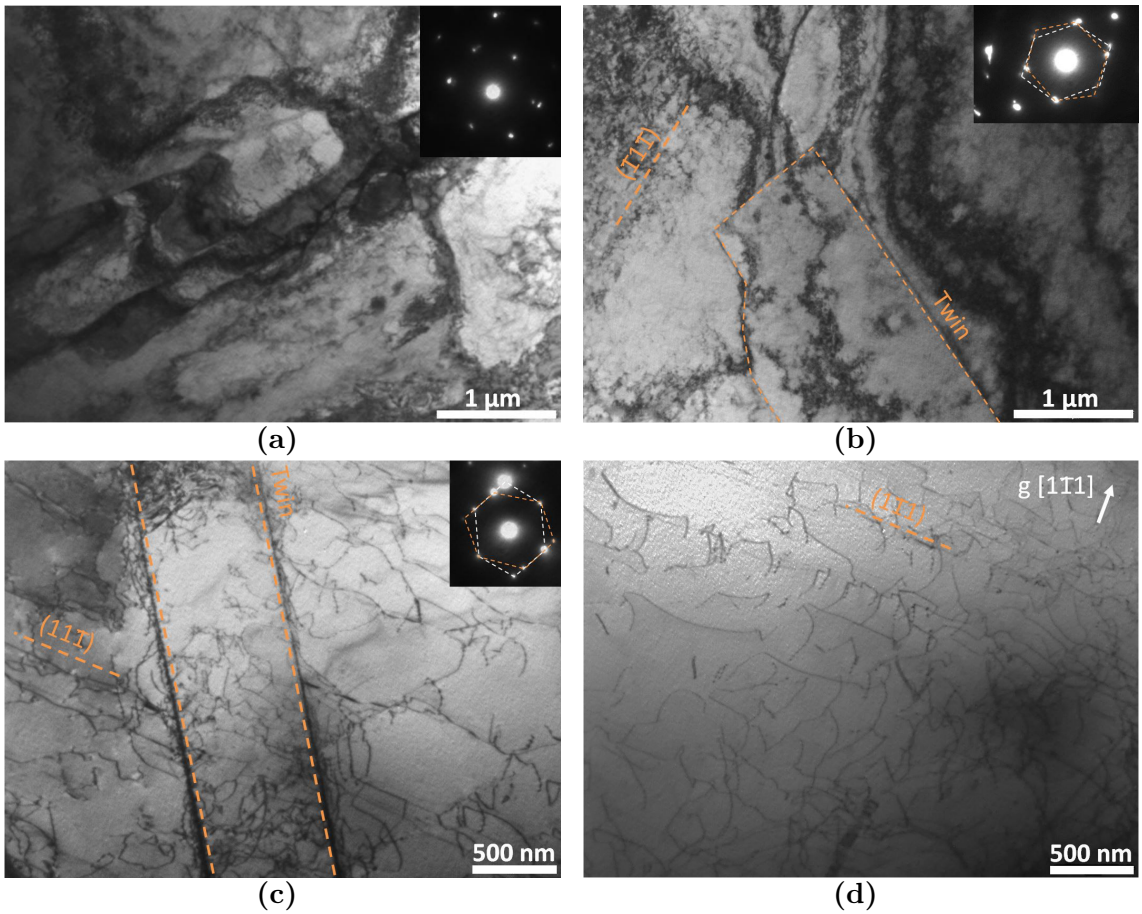

Figure 4.23: *TEM images for Y3 alloy after annealing at a) 600° C 672h; b) 650° C 336h; c) and d) 700° C 48h. Twins and traces of {111}-type planes are marked with dashed lines. All images are taken close or at the [011] ZA.*

The behaviour observed for Y3 alloy differs from what was previously reported by Mroz [115] for A3S. In his thesis the microstructural evolution of *as forged* A3S was divided into three stages. Below 600°C, substructure after forging was maintained even after long time annealings. However, after heat treatments in the range from 600°C to 700°C, the presence of micrometric grains free of dislocations considered as truly recrystallised, according to the classical definition, were reported. Finally, for temperatures above 700°C, big grains with high density of organised dislocations were found. Mroz concluded that for A3S alloy true recrystallisation occurs for medium temperatures in a narrow range of 600°C to 700°C, whereas only process of recovery takes places upon high temperature annealings. This is not the case for Y3 Co-free alloy. For this composition micrometric dislocations-free grains were never observed; no annealing resulted in a structure composed mostly of such grains. It could mean that the recrystallisation never took place or that its result differs from the expected one as in classical alloys.

Usually, in classical alloys recrystallisation temperature is considered to be in the range of below 0.5 T_M depending on the deformation rate. In the case of analysed HEAs temperature where significant change in microstructure is found is of the order of 0.6 $_M$ and requires quite long annealing times, 2 - 14 days. These observations suggest slow kinetics of whatever process happens. It can be hypothesized that the dislocation motion, necessary for either recovery or recrystallisation to take place, is low as compared to classical fcc alloys. Wouldn't recovery followed by grain growth be a better supposition according to the observations? The answer will come if the nucleation of new grains could be confirmed. This problem will be approached in the following section.

4.2.2 Experimental evidences of nucleation of new recrystallised grains

Process of recrystallisation in metallic alloys is a consequence of a driving force coming from stocked energy, introduced to the material and accumulated during its thermomechanical treatment. The aim of the system is to reduce its total energy: in recrystallisation transformation, it is achieved through nucleation and growth of new grains. Approaching equilibrium state, these new grains should be defects-free. Currently, their crystal orientation is different from that of the "mother grain". Nucleation is a phenomenon difficult to observe, but some indirect indications of its presence can be found upon microstructural observations. It can be expected that when formation of new grains takes place, the average grain size will decrease at some point, to later grow again. Another source of proof for nucleation is the change of crystallographic texture. Finally, in rare cases and a significant part of luck, nuclei can be directly observed. The purpose of this part of our work is to

establish if nucleation is present upon annealing in the Y3 alloy to determine if recrystallisation truly takes place.

The evolution of grain size was analysed for very short time annealings, between 0s and 300s, in the temperature range where the recrystallisation was supposed to take place, at 800°C and 1000°C, as observed by EBSD and at which the kinetics of the transformation should be relatively fast. Given times are the total length of maintain upon reaching the required temperature: thus, the time "0 seconds" corresponds to a situation in which the sample was put in the furnace at the nominal temperature, and took out as soon as this temperature was reached according to the thermocouple reading.

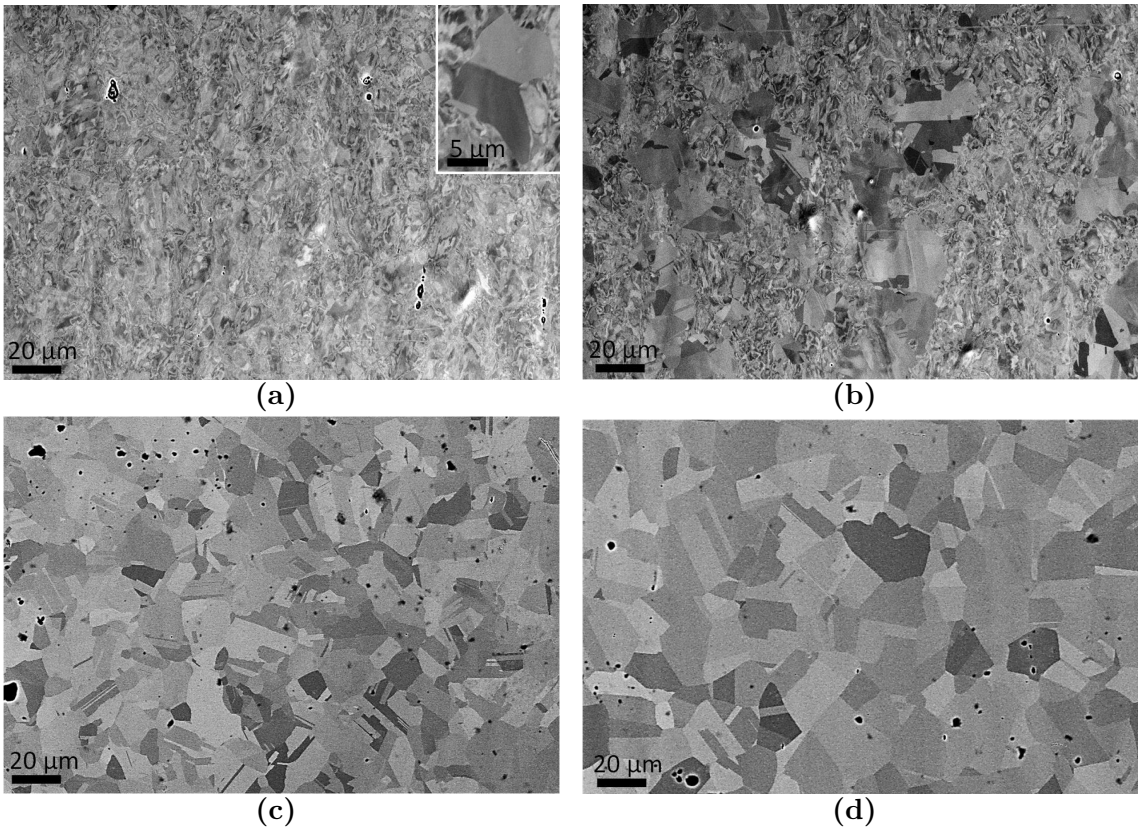

Figure 4.24: *Evolution of as forged Y3 microstructure upon short annealings: a) 800°C 60s, zoom on a grain with uniform orientation found within the structure shown in the upper right corner; b) 800°C 180s; c) 1000°C 0s and d) 1000°C 180s. SEM BSE micrographs.*

SEM BSE micrographs of four chosen states of shortly annealed samples are presented in Figure 4.24. It is clear that at 800°C the short time is not sufficient to obtain a fully "recrystallised" microstructure for the level of deformation reached after forging. Upon 60s at this temperature, Figure 4.24a, the microstructure does not change. High degree of misorientation is present as before annealing and distinguishing the grains is close to impossible. Only occasional "recrystallised" grains of few micrometers can be found with uniform orientation and twin boundaries.

Increasing the holding time at 800°C to 3 minutes leads to a higher "recrystallised" fraction embedded in the deformed material, Figure 4.24b. It is now possible to measure the average size of the "recrystallised" grains, which is of the order of 5.7 ± 1.9 μm. It is already a considerable grain size and it is difficult to talk about nucleation. We could suspect a heterogeneous nucleation that would explain presence of grains of such size embedded in the "non-recrystallised" matrix.

On the contrary, heating the *as forged* material to 1000°C results in fully "recrystallised" structure regardless the time, Figures 4.24c and 4.24d. The result of 0 seconds at 1000°C is particularly interesting regarding the previous observations at 800°C where little "recrystallisation" was found. Additional 20 seconds that pass during heating between 800°C and 1000°C are sufficient to fully transform the structure. At the same time, the observed grain size is already significant, much too large for us to be able to conclude about the presence or not of nucleation.

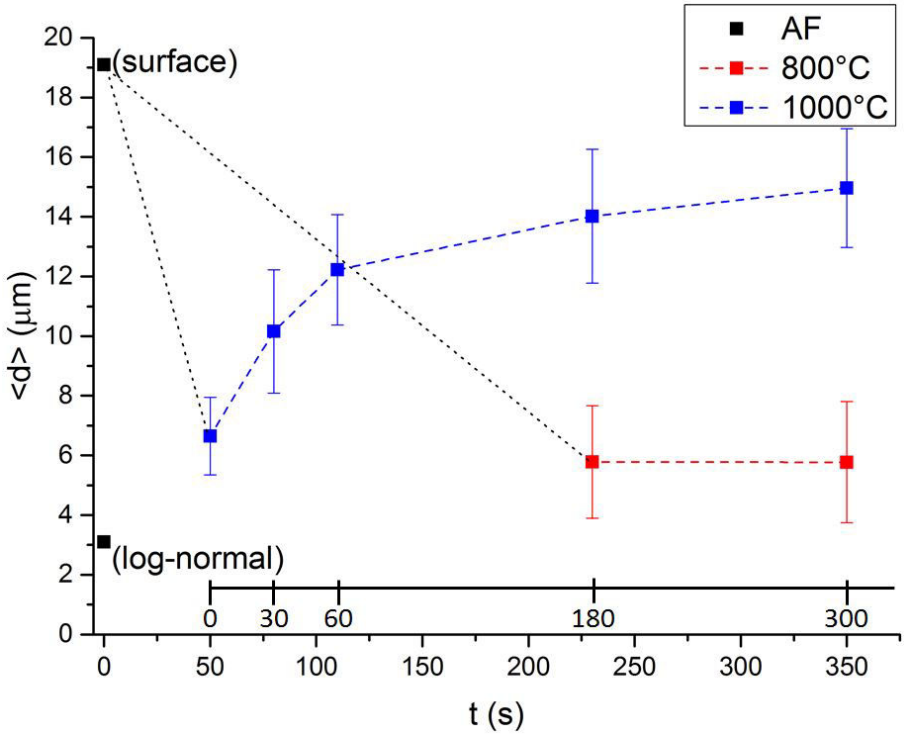

Figure 4.25: *Evolution of grain size for Y3 as forged alloy at two temperatures: 800°C and 1000°C for very short annealings. Initial grain size after forging is marked in black and dotted lines are drawn as a guide for the eye to show the drop of grain size.*

The evolution of grain size was defined for the series of samples annealed at 800°C and at 1000°C. The results are presented in Figure 4.25, where measurements of average grain size (excluding twin boundaries) are shown as a function of time. Time required to reach the annealing temperature, 50s, was added, hence the shift in respect to the time axis. As expected, for the fully "recrystallised" samples, annealed at 1000°C , the grain size increases with the increasing time of annealing (blue points). For only partially "recrystallised" samples, shortly annealed at 800°C, the grain growth did not take place yet (red points). However what is important is

the comparison with the initial grain size of the material. As it was already shown, the definition of grain size in the *as forged* state proved to be complicated and two values of mean grain size were calculated. To be able to best compare average grain sizes at various states, the same method of measurement should be applied. In the case of short annealing study all "recrystallised" grains' size was defined by the intercept method, which was impossible in the case of *as forged* state. Even though the structure after short heat treatments at 800°C is close to the one after forging, only "recrystallised" fraction was taken into account, so intercept method could be applied here. No straightforward choice is available and both grain sizes are shown. As a consequence, conclusion whether a drop in grain size is observed, is not obvious. If we consider that the initial grain size of the *as forged* material was 19 μm, as calculated from the surface weighted average, the drop is present and quite significant, as a uniform grain size of 6 μm was observed. Nucleation and consequently recrystallisation would be then confirmed. However if the mean grain size for *as forged* Y3 calculated from the log-normal distribution is taken under consideration, the decrease in grain size is not seen. The initial size of about 3 μm could grow with further annealing. The results of grain size analysis are unfortunately not conclusive and clear answer about nucleation can not be given. Further observations were done in the search for more convincing signs of nucleation.

TEM thin foils were prepared for samples annealed in two different conditions: 800°C / 180s and 1000°C / 0s. Microstructure after 800°C 180s is presented in Figure 4.26. Dislocation cells can be seen, with areas between the dislocations walls free of dislocations, Figure 4.26b. The observed zone was very thin (about 100 nm) so the dislocations density and walls thickness may appear low. However, a great advantage to this observation is that the cell size is of the same order as the foil thickness. This way, no risk of superposition of cells in the beam direction is present and the size as well as shape of the cells can be clearly defined. Finally, several other features could be observed in these conditions. In Figure 4.26a a curved grain boundary can be distinguished. Its form suggest mobility in the direction marked by arrows: probably a "recrystallised" and growing grain is observed. Yet, let's note that numerous dislocations and cells are present inside this grain despite the signs of its growth.

Next, some rare stacking faults could have been observed, as presented in Figure 4.26c. Its size could not be measured since it originates or ends in the neighbouring grain boundary, nonetheless its length of couple hundred nanometres is a good indication of low SFE of the Y3 alloy. Finally, an image of a nanometric grain is presented in Figure 4.26d. Its boundaries are high angle grain boundaries and its orientation differs from the neighbouring grains: as the result, this grain shows very different contrast compared to surrounding areas. One of the GBs is curved

suggesting growth; and at the same time, its small size implies its recent creation. It is free of dislocations and positioned on a grain boundary, a preferential place for nucleation. Most probably the observed grain is a defects-free nucleus inside the deformed structure, a proof of creation of new grains and thus, proof of recrystallisation.

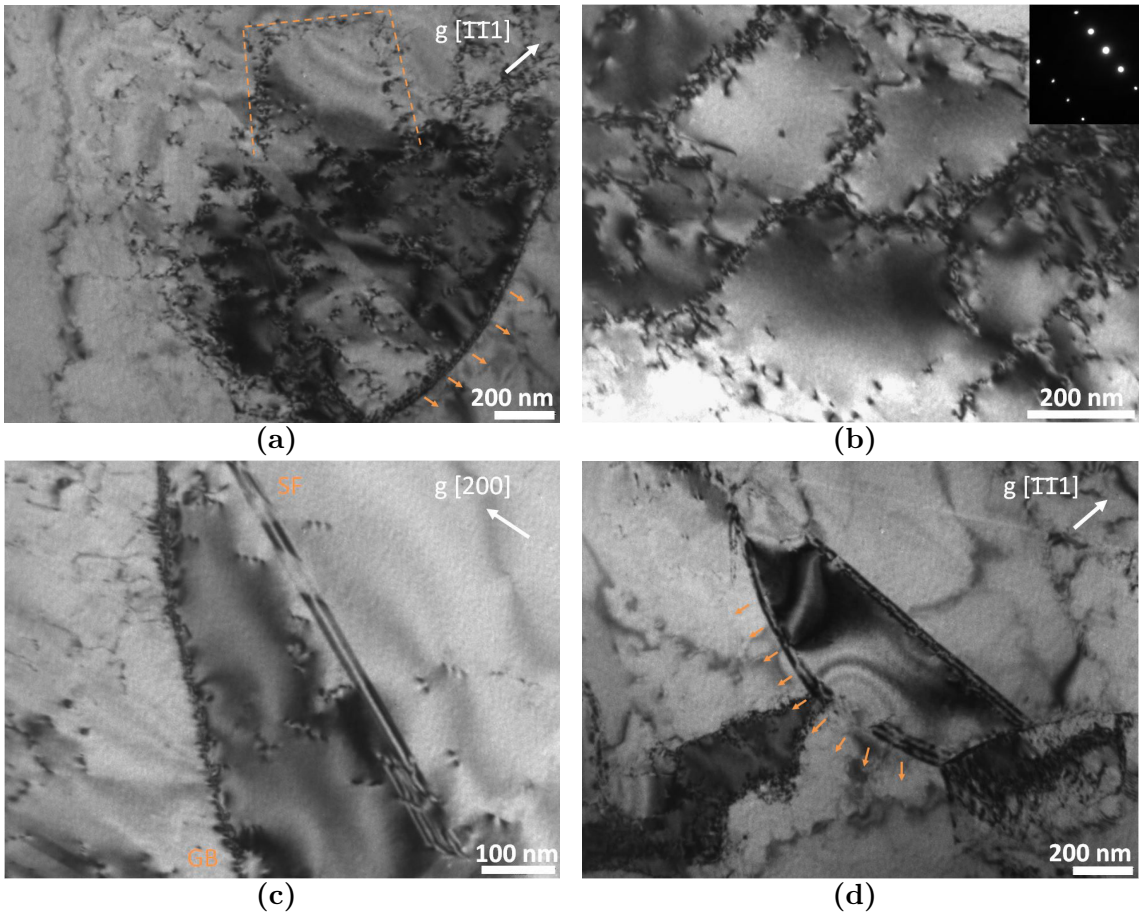

Figure 4.26: *Y3 in as forged state after annealing at 800°C 180s. TEM images showing: a) substructure at a proximity of a mobile grain boundary ([011] ZA), a dislocation cell marked by dashed line; b) dislocation cells; c) stacking fault originating or stopping at grain boundary ([001] ZA); d) new grain, free of dislocations ([011] ZA).*

Samples annealed at 1000°C for 0s are presented in Figure 4.27. The beginning of dislocation cell formation can be seen, Figure 4.27a. Defects-free cells, restricted by dislocation walls, started forming. Even though the overall density of dislocations is very high, interiors of the cells are rather dislocation-free, Figure 4.27b. Since the microstructure at the scale of EBSD resembled a fully "recrystallised" state, it was hard to expect to find nuclei. Nevertheless the observations allowed to confirm the presence of twins and arrangement of the substructure into cells. It is important to note that already after a short time at high temperature (time to reach 1000°C) the dislocation cells start to grow and the dislocations in the walls start to arrange themselves, which later might result in the already observed lines following the {111}-type planes. Looking at this structure with very high dislocation density it

is difficult to believe that recrystallisation took place in this sample.

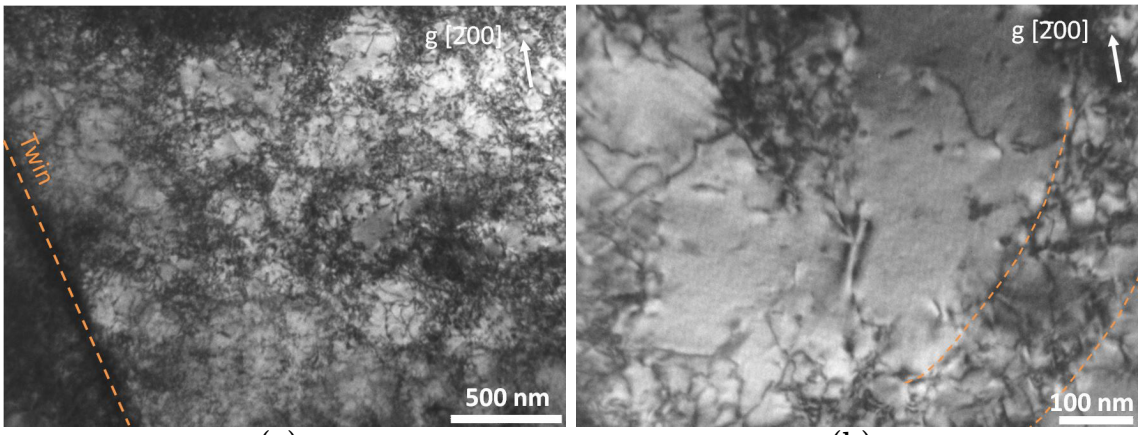

(a) (b)

Figure 4.27: *TEM images of Y3 AF after annealing at 1000°C 0s. a) substructure formed by dislocations and b) zoom on dislocation cells with a dislocations wall marked by dashed lines. [001] ZA*

A general proof of nucleation in the material would be of value. That is why analysis of texture was done by X-ray diffraction. Two samples were compared: *as forged* being the initial state, and *annealed* at 1000°C 2h, which at the scale of SEM resembles the "recrystallised" state. The standard *annealed* state was selected for these observations as the expected change in texture should be more pronounced after longer annealing time. At the same time it will allow to clearly state if what was chosen as the initial state for most studies is recrystallised or not. Observations were done on the surface perpendicular to the rod axis.

Pole figures for both states are presented in Figure 4.28. In the initial *as forged* state, the maximum in the centre of the pole figure for {111} Figure 4.28a, indicates that the rod axis is parallel to [111] direction. It is typical for "fiber" texture often found in low SFE fcc materials, in particular those processed by axisymmetric forming like swaging [115, 150]. Additionally, {220} pole figure, Figure 4.28b shows that the remaining <111> poles position themselves in preferential areas, represented by six maximums at the borders of the figure. Such image is found to be a single crystal texture. Evolution of the texture upon annealing at 1000°C 2h is shown in Figures 4.28c and 4.28d. It is clear that randomisation of orientations takes place. First of all, even though the central point of maximal intensity is kept, the initially concentrated intensities at 70° for 111 pole have disappeared suggesting already some randomisation in grains orientations. Secondly, no more intensity maximums at 90° are visible for 220 pole (at the borders of the pole figure). Those maximums have been replaced by presence of multiple orientations through the whole range of angles. At the same time a new maximum appears in the centre of the 220 pole figure 4.28d corresponding to the normal direction, parallel to rod axis. This change of texture, specially visible for the 220 pole, suggests nucleation of new grains that grow with a different orientations in respect to the initial state.

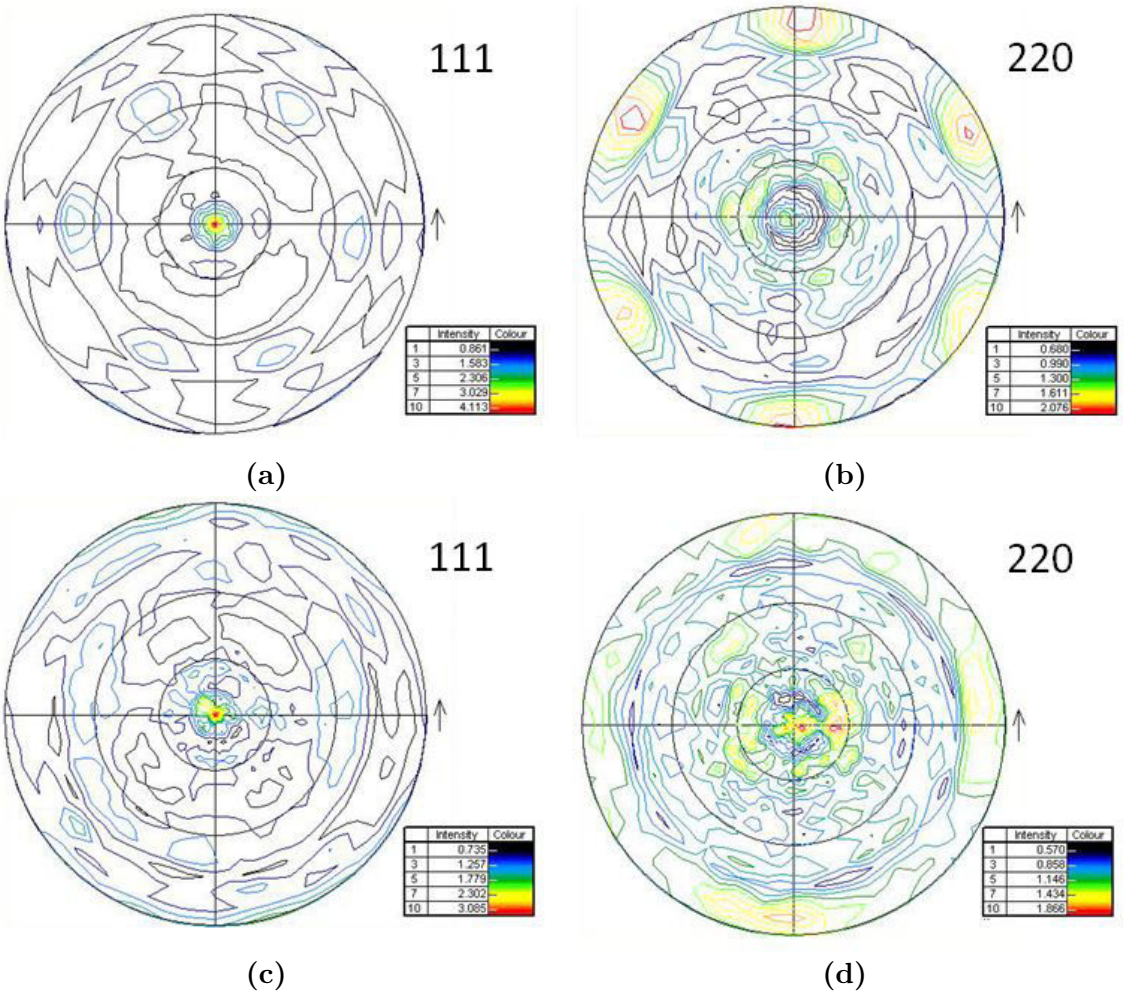

Figure 4.28: *Pole figures measured by XRD. Poles 111 and 220 represented for as forged Y3 alloy (a and b); annealed Y3 alloy at 1000°C 2h (c and d).*

Similar study was conducted by Mroz on the A3S alloy [115]. This material is as well characterised by high density of dislocations after annealings at temperatures >700°C. The short time annealings study did not show any signs of decrease in grain size, but one has to take under consideration that the shortest time applied was 6 minutes. The obtained mean grain size after 6 minutes for A3S was 11 μm, whereas for Y3 alloy after 5 minutes at the same temperature, it reached 15 μm. It was shown for Y3 alloy, at 1000°C, that grain growth starts already after 30s of maintenance at such elevated temperatures. The drop of grain size could have just been missed in Mroz's study. Yet, at the same time texture analysis was done for A3S, where initial *as forged* and annealed at 1100°C 10 minutes states were compared. Since no significant change of texture was observed, Mroz concluded lack of nucleation at high temperatures and only recovery followed by grain growth. It is an opposite outcome to what was seen in Y3 alloy. Grain size analysis combined with TEM observations and texture measurements for Y3 alloy allow to conclude that nucleation of new grains does take place upon annealing of hot forged samples. It is now possible to

say that the annealed state underwent recrystallisation after forging and annealing at 1000°C. This is where the two materials might show different behaviour.

Texture measurements brought clear proof that recrystallisation takes place in Y3 Co-free alloy upon annealing at 1000°C. Yet, the elevated density of dislocations, of the order of 10^{13} m^{-2}, upon recrystallisation is still to be explained. Elimination of Co from the A3S system lead to change of behaviour and recrystallisation previously limited to a narrow temperature range is now taking place even at high temperatures. Recrystallised state for the Y3 Co-free alloy can hence be defined as the one showing uniform orientation in the grain, with straight grain boundaries and presence of twins, and at the same time, high density of arranged dislocations.

4.2.3 Study of kinetics of grain growth in hot and cold processed Y3 alloy

Grain growth kinetics was studied for Y3 alloy after two different deformation conditions: hot forging (approximately 0.85 surface reduction) or cold rolling (0.9 surface reduction). The heat treatments were done at 1000°C for various times, starting with 0s of hold up in temperature up to 24 hours. The evolution of grain size with time is presented in Figure 4.29. For both initial states the curves follow the power law as in equation 4.5, which suggest analogous grain size evolution. The maximal grain size after hot forging is lower than the one reached for cold rolled material. It is a surprising outcome, since more energy stored in the cold rolled material should result in faster and more intense nucleation leading to a smaller grain size. On the other hand earlier onset of nucleation leads to earlier onset of secondary grain growth in such material, that as a consequence gives more time to the grain to grow. Hard to say which of these will have more impact on the grain size evolution.

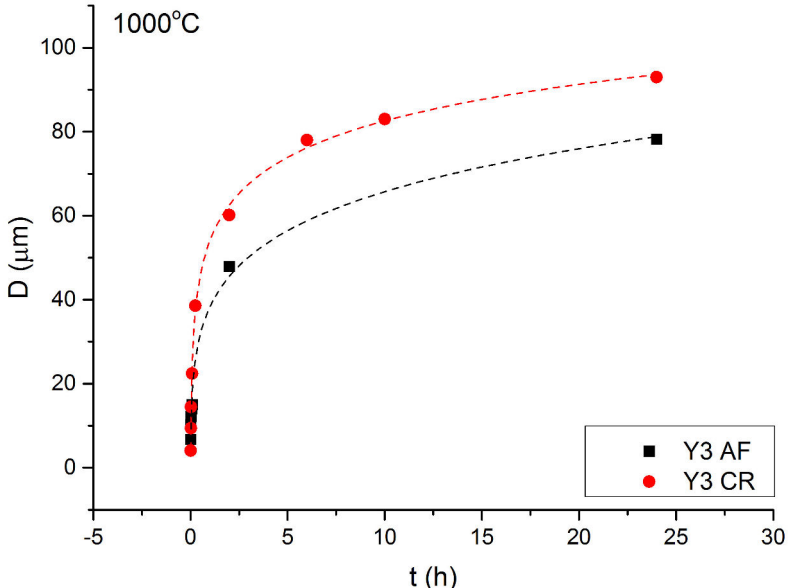

Figure 4.29: *Grain size evolution upon annealing at 1000°C for various times for Y3 alloy after forging (black points) or after cold rolling (red points).*

The kinetics of grain growth were analysed in accordance with the classical theory for grain growth [18] following the equation 4.5, where D is the instantaneous grain size, D_0 is the initial grain size, t is time, n is a grain growth exponent and k is a kinetic constant, which depends primarily on the temperature and grain boundary energy. The mechanism of grain growth is determined by n value. For most single phased materials its value is close to 2.

$$D^n - D_0^n = kt \tag{4.5}$$

It was shown previously that definition of initial grain size D_0 after hot forging is not straightforward. Presence of nanosized cells was found and for this study it can be taken as the initial grain size. Since few hundred nanometres is way below the obtained grain sizes after annealing it can be disregarded. For cold rolled samples the value of D_0 is experimentally uncertain. However, it can be as well ignored during the analysis of n from long time annealing data, especially at high temperatures, when $D \gg D_0$. It gives us the equation 4.6, from which the values of grain growth exponent can be obtained. The n parameter can be determined from a double logarithmic plot of the grain size as a function of annealing time presented in Figure 4.30.

$$D = kt^{1/n} \tag{4.6}$$

It has to be reminded that the applied model considers a constant grain growth leading to a single crystal for $D \rightarrow \infty$. If it were the case, the linear fit would well represent the data points. In reality however, grain growth does not follow such linear path, as the driving force for grain growth is not constant. With time and increasing grain size, the driving force decreases, leading to slowed kinetics of grain growth. In other words the grain tends to reach a critical value [151]. It can be clearly seen in Figure 4.30. At first the n factor close to 2 is found, however for longer time of annealing the grain growth slows down and an n factor of about 5 is found. Nonetheless, since the exponential law is commonly applied, an average value of n could have been defined. For hot forged and cold rolled Y3 alloy those values are respectively 2.72 and 3.15. These are comparable values to the ones obtained by W. H. Liu et al. [18] and F. Otto et al. [103] for the equiatomic CoCrFeMnNi, where it was reported to be close to $n = 3$. In classical materials this high power index seen in Y3 Co-free alloy, is said to be an indication of slow coarsening kinetics due to the migration of impurities or solute-drag of grain boundaries. This results is unexpected in the single phased fcc HEAs. No segregations have been reported for those alloys yet so the solute-drag has no reason to take place. Nonetheless, this result may suggest presence of short range ordering that still need to be put to evidence [18].

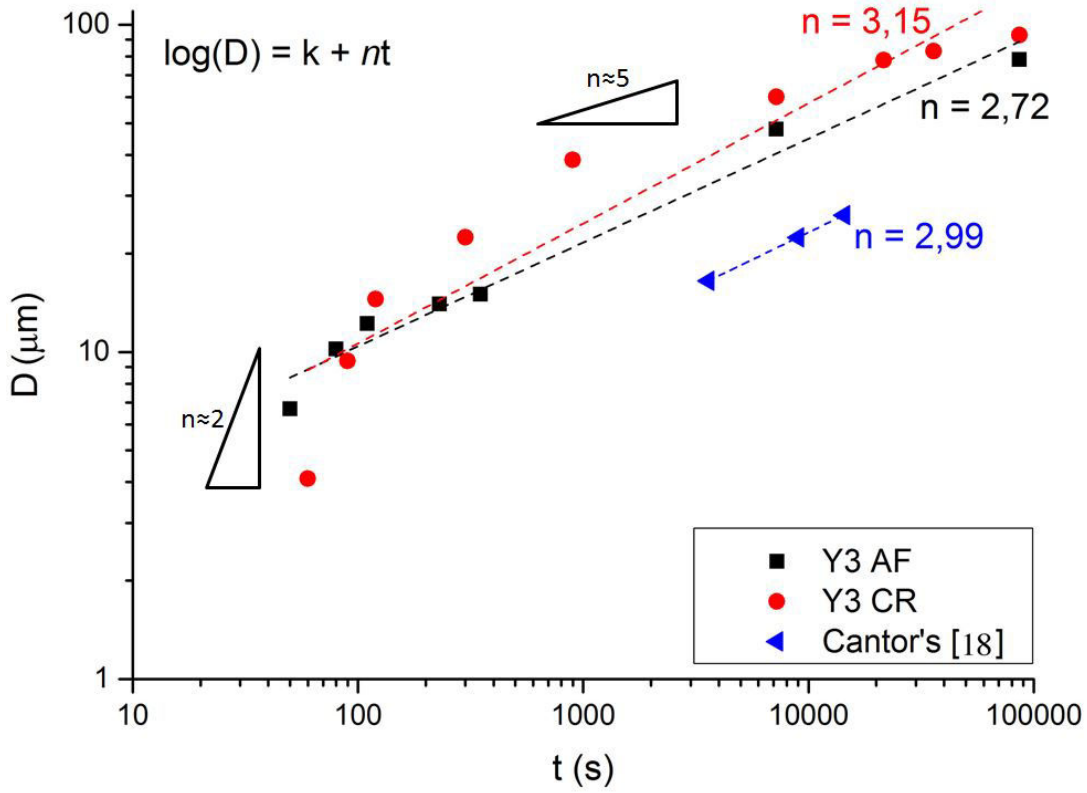

Figure 4.30: *Double logarithmic plot of the grain size as a function of annealing time for hot forged Y3 (Y3 AF), cold rolled Y3 (Y3 CR) and cold rolled Cantor's alloy [18].*

4.3 Partial conclusions

Study of the Y3 Co-free alloy showed the evolution of its mechanical properties with the changing microstructure. Two regimes could have been defined. Firstly, regime with high yield strength and low work hardening coefficient corresponding to highly work hardened states like the *as forged* one. Nonetheless, despite highly work hardened state after forging, the Y3 alloy maintains good levels of ductility suggesting its possible application in this non-recrystallised state. Secondly, the regime with low yield strength and high work hardening coefficient for the states *annealed* at temperatures above 600°C was observed. The change in mechanical behaviour was correlated to the modification of dislocation structure inside the grains from nanometric substructure to dislocations arranged on preferential planes.

The dislocations density was found to be abnormally elevated in all analysed states. Multiple techniques were used to measure the density of dislocations, and the results derived from all of them are coherent between each other. In the *as forged* state the dislocations density of the order of 10^{14} m^{-2} was measured. Density of the order of 10^{13} m^{-2} was found for both *as cast* and *annealed* states. Such elevated density of dislocations corresponds rather to severely deformed materials than to material close to equilibrium, For this reason, the recrystallisation phenomena in Y3 alloy seemed questionable.

The texture analysis of *as forged* and *annealed* states, allowed us to confirm that recrystallisation does indeed take place in the Y3 alloy upon annealing, at least at 1000°C. The recrystallisation temperature was found to be about 0.57 T_M, not so far from temperatures of recrystallisation for classical alloys. However, the kinetics of this transformation in the Y3 alloy was shown to be extremely slow. Additionally, the *recrystallised* state of Y3 alloy remains distinguished by surprisingly elevated dislocations density, that seams to be its characteristics and still needs an explanation.

Chapter 5

Strengthening mechanisms of Y3 Co-free alloy

Contents

Y3 Co-free composition is a single fcc phased alloy with a highly complex microstructure. As it was shown in the previous chapter, unusually high density of dislocations is easily formed and conserved even upon recrystallisation. Influence of this intricate microstructure on mechanical properties was shown, specially in the *as forged* state. Mechanical behaviours of Y3 composition were found to resemble the ones previously reported for A3S [115] and Cantor's alloy [10, 22, 73]. What is the strengthening impact on mechanical resistance of each microstructural element? Can other possibilities of enhancing those properties be considered? Finally, how much does the selected HEA differ from classical metals and alloys with same crystallographic structure? How should the high entropy alloys consisting of transition elements be positioned among the known alloys? Can the classical models of hardening be applied for these alloys? Those questions will be addressed in the following chapter upon initial definition of mechanical behaviour of Y3 Co-free alloy in various conditions and states.

5.1 Identification of in-grain strengthening mechanisms: activation volume measurements

Firstly, identification of scale at which the strengthening of the Y3 Co-free alloy takes place was done. Measurements of activation volume allow to define the major in-grain contributor to mechanical resistance. Since the Y3 alloy presents an elevated density of dislocations even after recrystallisation, it can be suspected that they play a significant role, but are they the most important factor? Comprehension of dislocations impact is primordial for understanding of mechanical properties. In crystalline materials plastic deformation is accomplished mainly by dislocation motion, however, description of this movement under stresses is quite complex. Dislocation structure is constantly changing during plastic deformation due to their motion, creation and annihilation, which lead also to strain hardening of the material. At the same time the plastic deformation is to some extent temperature and strain rate dependent, as the motion of dislocations may be controlled by thermally activated processes. Definition of influence of dislocations on plastic deformation will bring insight to the question to what extent the analysed HEAs are unusual.

Among all existing hardening mechanisms, the single fcc HEAs can be considered as solute-strengthened fcc alloys (in the dilute limit) and each of the strengthening mechanisms operates at different scale. Activation volume represents the volume of matter involved in the thermally activated processes during deformation and it reveals the operative size scale in the material at a given temperature, strain rate and stress. The inverse activation volume can be measured via strain rate jump tests and can be presented as the sum of inverse activation volumes for solid solution (V_{SS})

and forest strengthening (V_f) since the Hall-Petch mechanism does not contribute to the activation volume, equation 5.1 [152].

$$\frac{1}{V} = \frac{1}{V_{SS}} + \frac{1}{V_f} = \frac{1}{MkT}\frac{\delta\sigma}{\delta ln(\dot{\varepsilon})} \tag{5.1}$$

Activation volume can be thus defined from the 5.1 equation leading to equation 5.2, where M is the Taylor factor (about 3 for fcc materials [22, 147, 148]), k is the Boltzman constant ($1.38 \cdot 10^{-23}$ J/K), $\dot{\varepsilon}$ is the strain rate and $\delta\sigma$ is the stress jump. In fact, the activation volume represents the change of form of a crystal rather than the change of its volume. This change is proportional to the area scanned by the dislocation while crossing an obstacle (in the case of cross slip it is the critical size of the nuclei) [153].

$$V = MkT\left(\frac{\delta ln(\dot{\varepsilon})}{\delta\sigma}\right) \tag{5.2}$$

Since activation volume is represented as a function of strain rate sensitivity of stress necessary to deform the crystal, two techniques are possible for its measurement: strain rate jumps or stress relaxation at constant temperature [154]. As it was reported in the literature the Cantor's alloy shows little sensitivity to strain rate [73]: this is why relaxation tests have been performed to define the activation volume of analysed HEAs. This type of tests have already been carried out on Cantor's alloy by Laplanche et al. [22]. In the frame of this work, experiments were completed again on Cantor's alloy to validate the experimental set, and afterwards on Y3 Co-free alloy. Detailed description of experimental method, together with its validation are presented in Appendix 1.

The relaxation tests allow to measure only the apparent activation volume, since it does not account for strain hardening [154]. However, Spatig et al. [91] have developed a new procedure of measurement of effective activation volume, V_{eff}, that corrects the strain hardening. The method consists of performing a series of repeated stress relaxations with constant time span during tensile tests at constant temperature and at specific strain. The apparent activation volume is considered to be constant during the load relaxation test that must be analysed over "short duration" [91]. First relaxation allows to determine the value of apparent activation volume, V_{app}, and consecutive relaxations in the same set, allow to correct the influence of strain hardening, V_h, according to equation 5.3:

$$V_{eff} = V_{app} - V_h \tag{5.3}$$

Tensile curves with relaxation sets at various stresses for *annealed* Y3 Co-free alloy are presented in Figure 5.1. The tests were performed at three various temperatures, starting from room temperature, 20°C, down to cryogenic conditions, -100°C and

-150°C. It can be noted that with decreasing test temperature, the flow stress and work hardening rate increase. It is consistent with previous mechanical tests at low temperatures, where with decreasing test temperature the increased resistance is accompanied by increased elongation. Total of five sets of five consecutive relaxations were performed: first set was close to the yield strength and later for higher strain values.

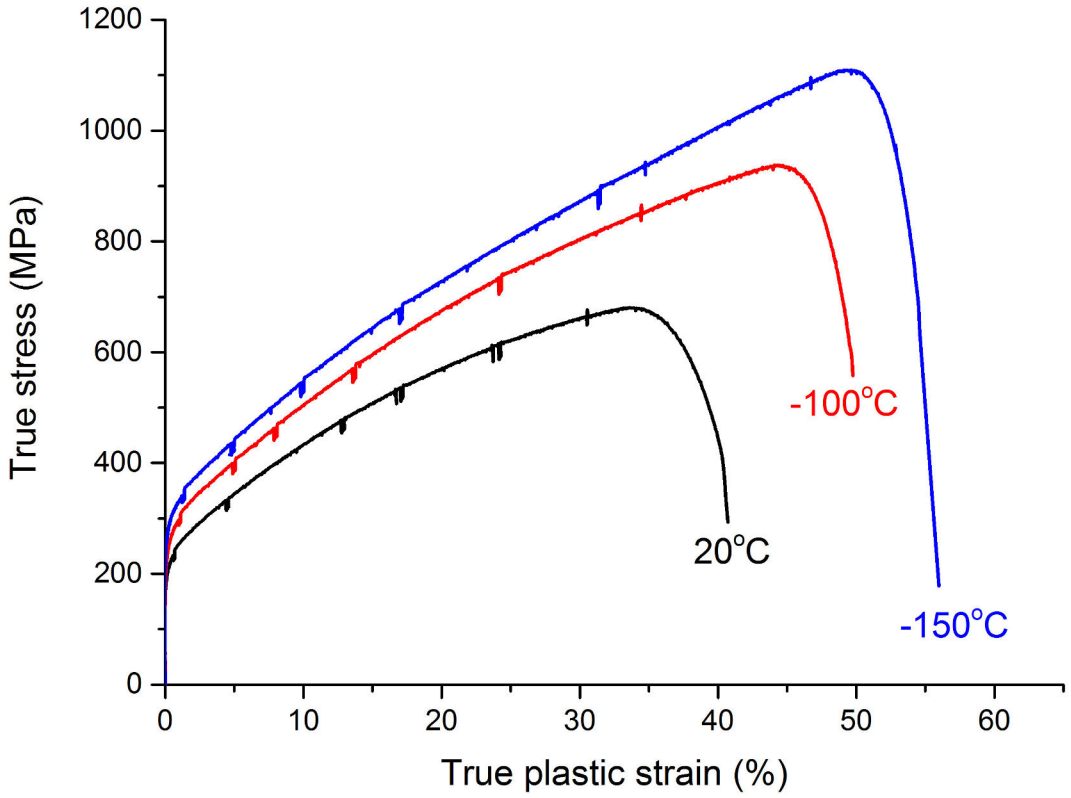

Figure 5.1: *Tensile curves with visible relaxation sets at various stresses. Tests performed at room temperature (20° C) down to cryogenic conditions (-100° C and -150° C) on annealed Y3 Co-free alloy.*

Effective activation volume measured during relaxation tests is represented as a function of strain in Figure 5.2. The obtained values vary from 330 b^3 to 140 b^3 starting at room temperature down to cryogenic conditions. Those values are in the same range as obtained by Laplanche et al. [22] and are comparable with pure Ni or NiCo, with V $\sim$ 300 b^3 at room temperature [80]. The temperature influence can be thus seen and is in agreement with dislocation creation and stability. It can be expected that with decreasing temperature the overall dislocations density increases which is reflected in decreased values of measured activation volume. Same tendencies can be observed for both analysed alloys.

Moreover, it was found that the activation volume decreases with true plastic strain for both Cantor's and Y3 alloys at all tested temperatures. This outcome reflects the dislocations density increasing with deformation. During tensile tests, despite constant competition between creation and annihilation of dislocation, their ac-

cumulation is unavoidable. As a consequence, spacing between dislocations, $l = 1/\sqrt{\rho}$, decreases.

Finally, by comparison between two alloys: Cantor's and Y3 Co-free, it can be deduced that the dislocation density varies between the two alloys. Somewhat lower values of activation volume for Cantor's alloy suggest smaller spacing l, and thus increased dislocations density. Difference in dislocations density between the two alloys was already shown and this observation only confirms its reliability. The lower values of activation volume could be further influenced by a hidden effect, such as increased solute hardening for Cantor's alloy. Since its composition is more complex than the one of Y3 Co-free alloy, it can be hypothesised that the lattice distortion is more pronounced, blocking dislocation's motion and thus having more influence on its mean free path. As a result the activation volume could be additionally reduced.

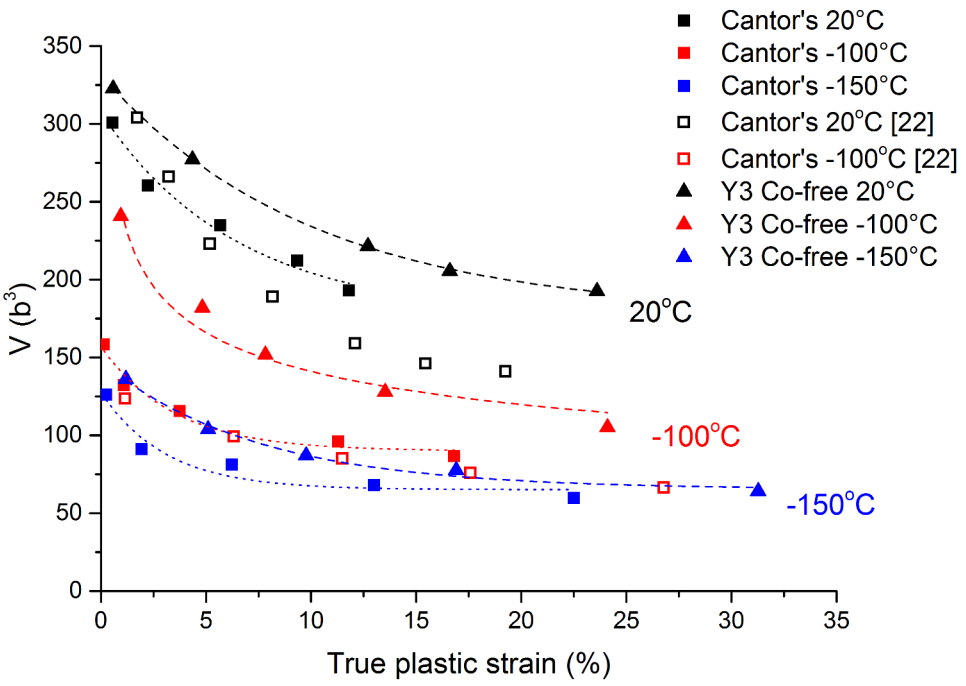

Figure 5.2: *Evolution of activation volume with strain at various temperatures. Comparison between Cantor's alloy (squares) and Y3 Co-free alloy (triangles). Empty squares represent results on Cantor's alloy obtained by Laplanche et al. [22].*

Further analysis of relation between activation volume and strain is possible by plotting $\delta\sigma/\delta\dot{\varepsilon} = \mathrm{MkT/V}$ versus offset of flow stress $\sigma - \sigma_y$ in the form of so called Haasen plot, as presented in Figure 5.3. The slope of obtained curves is associated with forest hardening, and the positive intercept with solute strengthening. Slopes of all lines are comparable, and so the forest hardening efficiency, in both Cantor's and Y3 alloy seam to be similar. However, there is a shift in the influence of solute strengthening. Intercept values are higher for Cantor's alloy suggesting more hardening coming form the lattice compared to the Y3 Co-free alloy. It can be again explained by lesser complexity of the quaternary Y3 system, and consequently less

distorted lattice.

At the same time, no specific temperature dependence of Haasen plots was found for neither of the alloys. It is consistent with applied model and suggests that a "standard" interpretation of the thermally activated flow of solute strengthened metallic alloys is applicable. As no discontinuities in relation between V and $\sigma - \sigma_y$ are seen, it can be concluded that no modification of activated deformation mechanisms takes place in the range of testes temperatures. Especially no evidence of twinning existence was shown in this analysis. Let us remind that twinning was proposed [10] in Cantor's alloy, as an additional deformation mechanism leading to increased damage resistance in liquid nitrogen temperature. According to Laplanche et al. [22], the absence of influence of twins on activation volume in Cantor's alloy, is due to much larger spacing between twins than between dislocations. Same hypothesis can be made for Y3 Co-free alloy.

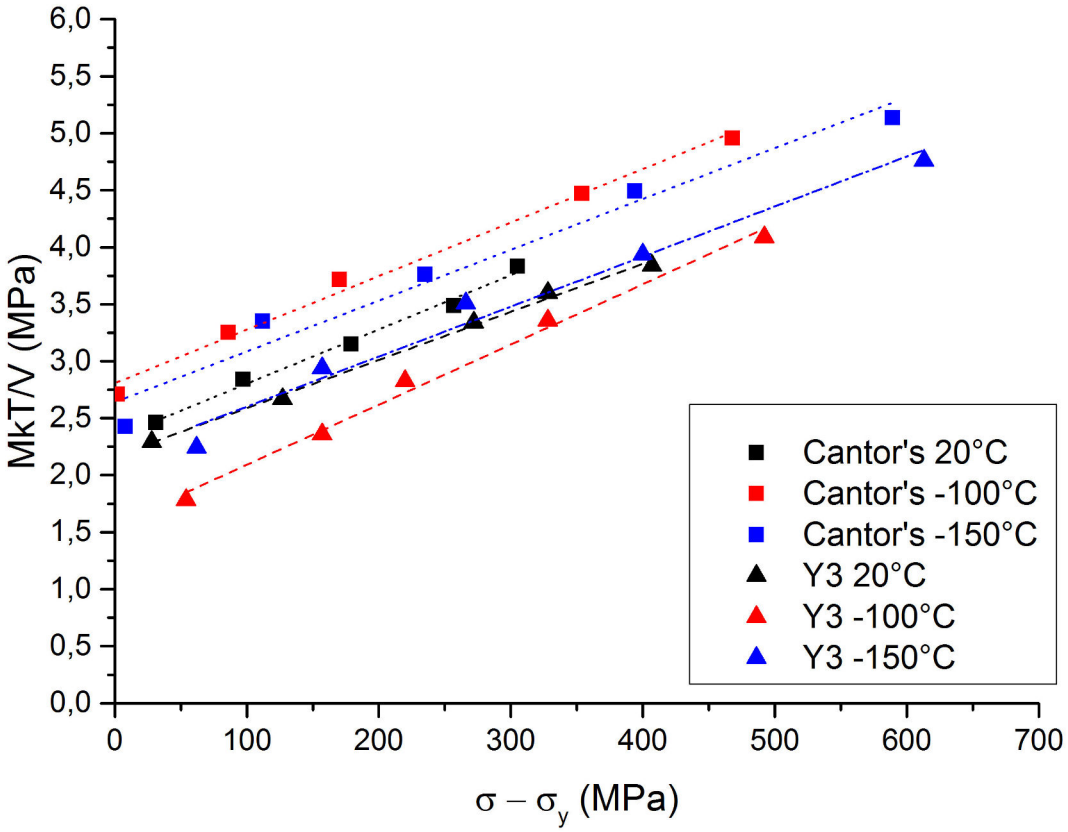

Figure 5.3: *"Haasen plot", M k T/V versus the offset flow stress σ - σ_y. Comparison between Cantor's alloy (squares) and Y3 Co-free alloy (triangles) showing a positive offset at zero indicative of solute strengthening and linear increase with stress indicative of forest hardening.*

In summary, the activation volume measurements lead to general conclusion that for both Cantor's and Y3 Co-free alloys standard solid-solution-strengthening theory applies. In both cases the plastic flow is controlled by a combination of thermally activated solid solution strengthening and forest hardening that evolves with plastic strain. The dominant deformation mechanisms in those HEAs are the same as found

in classical fcc alloys; no new mechanisms have been found despite the increased system complexity. The differences found between two compared alloy confirm lower dislocation density and suggest a decreased solute strengthening in Y3 Co-free alloy than in Cantor's alloy. It is in agreement with decreased complexity of the quaternary Y3 Co-free system.

5.2 Kocks-Mecking model of strain hardening

Stresses measured during deformation can be separated into two parts: elastic σ_y and plastic σ_p also called flow stress. The latter is dependant on dislocation structure which respectfully is relative to temperature T and strain rate $\dot{\varepsilon}$. In a more physical way, flow stress can be considered as a stress resulting from dislocations interactions with atoms, dislocations and boundaries. The relation between plastic stress and dislocation density was proposed by Taylor [155] under the form of equation 5.4, as presented previously.

$$\sigma = M\alpha\mu b\sqrt{\rho} \tag{5.4}$$

The dislocation structure is in constant evolution during deformation, even though their organisation is not represented by the Taylor equation. Plastic deformation implies creation of new dislocations contributing to strain-hardening. At the same time recovery of the material enhanced by increased temperature takes place, and some dislocations are eliminated. Both contributions are of importance and work in opposite directions. The balance between them can be expressed by general Kocks-Mecking-Estrin equation [147, 156]:

$$\frac{d\rho}{d\varepsilon} = k_1\sqrt{\rho} - k_2\rho \tag{5.5}$$

where the k_1 parameter corresponds to athermal storage of moving dislocations that are immobilised after having travelled a distance proportional to the mean free path $1/l \propto \sqrt{\rho}$, and the $k_2 = f(T, \dot{\varepsilon})$ parameter represents the rate of dynamic recovery. Combining equations 5.4 and 5.5 leads to the evolution of flow stress according to the Voce law, as expressed by equation 5.6 [147]. It represents the linear decrease of hardening rate θ with flow stress. The initial hardening rate θ_0 for strain $\varepsilon \to 0$ is temperature independent, as it is only a function of k_1. The saturation stress, σ_V = f(T, $\dot{\varepsilon}$), is the stress reached for high strain when no softening occurs.

$$\begin{aligned} \theta = \frac{d\sigma}{d\varepsilon} &= \theta_0\left(1 - \frac{\sigma}{\sigma_V}\right) \\ with\ \theta_0 &= \frac{M\alpha\mu b k_1}{2} \\ and\ \sigma_V &= \frac{M\alpha\mu b k_1}{k_2} \end{aligned} \tag{5.6}$$

$$\sigma = \sigma_V \left(1 - e^{\frac{-\varepsilon \cdot \theta_0}{\sigma_V}}\right) \tag{5.7}$$

Integration of Voce law in respect to strain, leads to a description of flow stress according to saturating exponential law, equation 5.7. The θ_0 and σ_V parameters can be determined experimentally from the evolution of hardening rate θ with stress. In Figure 5.4, evolution of θ is shown for five compression tests at high temperatures varying from 850°C to 1050°C. The curve is presented only in the domain where the linear part (marked in red) corresponding to uniform deformation of the sample, is seen. Change of shape of the curve for low θ is due to influence of dynamic recrystallisation together with friction present during compression tests. Nevertheless, the fit in the linear region can be done. If the Voce law stands, its intercept with y axis, for $\sigma \to 0$, will give the value of θ_0 which gives the information about initial hardening rate. The stress σ_V corresponds to the intersection point of the linear extrapolation of hardening rate with the x-axis.

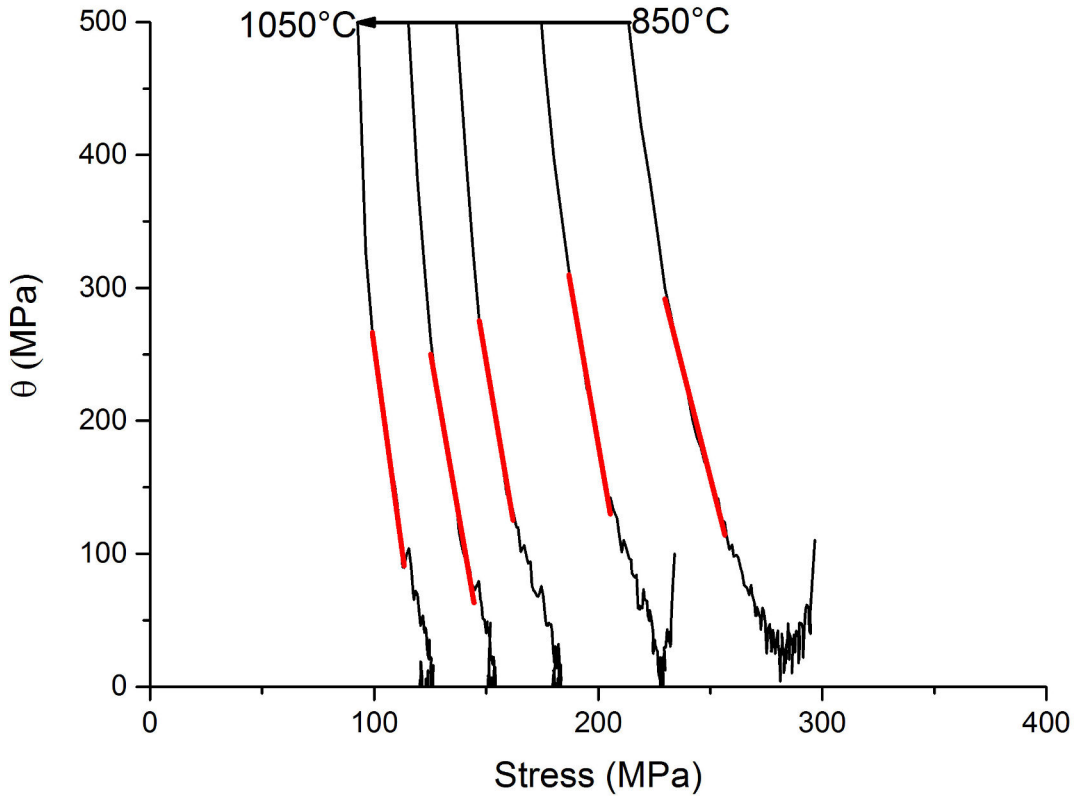

Figure 5.4: *Evolution of hardening rate θ with flow stress for annealed Y3 alloy. Results from high deformation compression $\varepsilon = 1.2$ tests at high temperatures from 850°C to 1050°C and strain rate 10^{-1} s^{-1}.*

A concept of single-parameter based description of work hardening was proposed by Kocks and Mecking [147]. Since flow stress is both temperature and strain rate dependent, the authors have gathered both contributions into one adimensional parameter noted g. Equation 5.8 describes the parameter g, with k the Boltzmann

constant, μ the shear modulus and $\dot{\varepsilon_0}$ a floating parameter. The floating parameter was chosen arbitrarily by the authors, so that all master curves for each metal could have been gathered on one graph. They have set it at the level of 10^{-7} s^{-1} for all metals. The same value was chosen in this work, to be able to position the analysed alloys on the master graph by Kocks and Mecking. According to the authors, flow stress normalised by shear modulus follows a power law with g parameter, and $\sqrt{\sigma_V/\mu}$ varies linearly with $\sqrt{g}$.

$$g = \frac{kT}{\mu b^3} ln \left(\frac{\dot{\varepsilon_0}}{\dot{\varepsilon}} \right) \tag{5.8}$$

The master curves: $\sqrt{\sigma_V/\mu} = \mathrm{f}(\sqrt{g})$ for pure metals are shown in Figure 5.5 for various pure fcc metals, where results for each element follow a single line. It has been pointed out by Kocks and Mecking that stacking fault energy plays a major role in controlling the level of normalised stresses to which the material can be work hardened in given conditions. This is finally found in the position of those master curves. All lines are ordered in the function of respective stacking fault energies. The two border lines for the values zero and infinity of the stacking fault energy indicate the direction of change of SFE (χ).

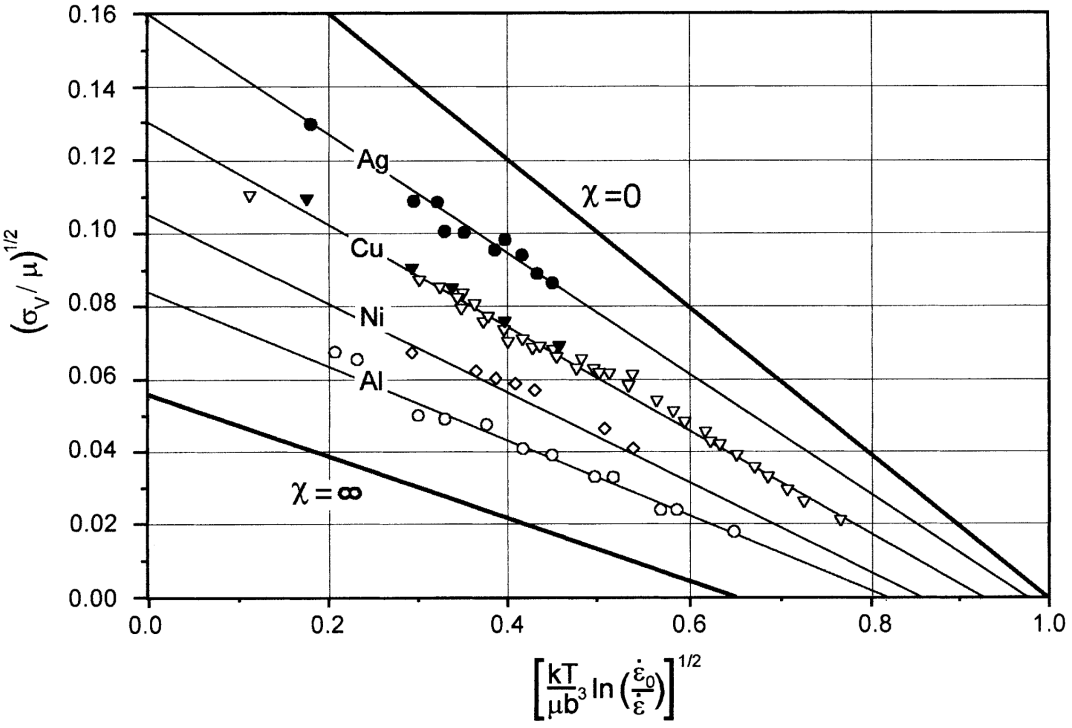

Figure 5.5: *$\sqrt{\sigma_V/\mu}$ versus $\sqrt{g}$ for pure fcc metals [147]. χ corresponds to stacking fault energy.*

The main characteristics of the Kocks-Mecking model is that all experimental data can be gathered into a single master curve representing the evolution of stress with deformation conditions for a given material. Data coming from numerous tests

at various conditions (different temperature and/or strain rate) can be considered together thanks to the g parameter that represents those conditions. This is a big advantage of the Kocks-Mecking model, as it can be applicable to large data sets. Finally, the extrapolation of the master curve can lead to flow stress estimation for any untested deformation conditions.

At the same time, to be able to compare various metals all values of Voce flow stress are regularly normalised by the shear moduli μ of respective elements. That is why definition of μ values for Y3 Co-free alloy was necessary to use the Kocks-Mecking model. Their evaluation has been done in the frame of Bawab's master internship at EMSE [157]. Laplanche et al. [89] have already reported an empirical relation of shear modulus μ [GPa] with temperature [K] for Cantor's alloy: $\mu = 85 - 16/(e^{448/T} - 1)$. It can be assumed that the evolution of μ for Y3 Co-free alloy will be similar. However to adapt this empirical formula to Y3 alloy, measurements at room temperature have been done. The measurements were performed by ultrasounds resonance frequency technique according to the procedure applied by Laplanche et al. [158], in agreement with the ASTM E228-11 standard test method [159]. The obtained value was close to the one of Cantor's alloy, and was equal to $\mu_{RT}^{Y3} = 83$ GPa. This measurement allowed to adjust the empirical relation proposed by Laplanche et al. [158] for Y3 alloy that is the object of this work. Final evolution of shear modulus with temperature for Y3 Co-free alloy is presented by equation 5.9. Values following this equation were implemented in the Kocks-Mecking model.

$$\mu = 87 - \frac{16}{e^{\frac{448}{T}} - 1}[GPa] \tag{5.9}$$

Numerous mechanical tests performed in the frame of this thesis were combined and analysed by the Kocks-Mecking model of work hardening. The results shown in this part come from both compression and tensile tests performed in a wide range of temperatures (from -150°C to 1050°C) with one of two selected strain rates, 10^{-3} s^{-1} or 10^{-1} s^{-1}. Detailed route of data analysis is described in Appendix 2. Results of analysis of all data for Y3 alloy are compared with Cantor's alloy and classical stainless steel 304L.

Firstly, hardening rate $\theta = d\sigma/d\varepsilon$ was analysed as a function of plastic strain. A representative curve is shown in Figure 5.6. This portrayal allows to see the evolution of θ during deformation, which can indicate if any change of dominant deformation mechanism is present. It is illustrated based on the example of tensile test at cryogenic temperature. The work hardening is constant upon reaching the yield strength suggesting that only one mechanism of deformation through dislocations motion is active. If twinning were to be activated a bump in the curve could have been expected [160], as depicted by the orange dashed line. Just like the meas-

urements of activation volume suggested, twinning in the Y3 alloy is not a dominant mechanism of deformation. Even if twins are present, their size is much larger than spacing between dislocations and consequently hardening is not active.

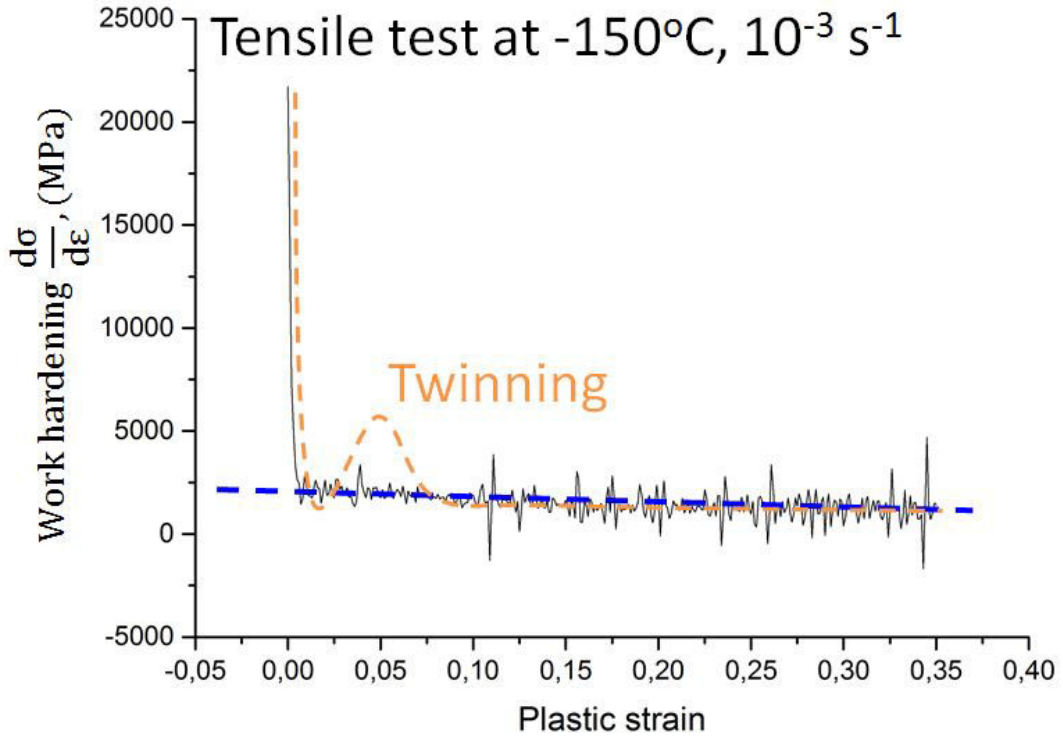

Figure 5.6: *Work hardening $\theta = d\sigma/d\varepsilon$ as a function of plastic strain for annealed Y3 alloy. Curve from a tensile test at -150°C and strain rate 10^{-3} s^{-1}. Orange dashed line depicts what the curve would look like if twinning were to dominate the deformation [160].*

As it was previously mentioned initial hardening rate θ_0 and steady stress σ_V values, representing the influence of recovery and dislocation creation, can be determined from the linear part of θ vs σ curves, Figure 5.4. The θ_0/μ represents the hardening taking place during deformation and is proportionate to k_1 parameter. For all analysed alloys the values of this parameter describing recovery are presented in Table 5.1. They were calculated as the average value from all experimental data and are of the order of 10^{-8} for each alloy. The θ_0 measurement is laden with high uncertainty as the definition of linear part of the curve lays fully at the appreciation of the experimentalist. However, since all obtained values are in the same range, it can be noted that the order of recrystallisation for all three alloys is similar. The input of these average values to the Voce law (equation 5.7) for calculation of theoretical stresses confirms the validity of the model.

In Figure 5.7, experimental curves (solid lines) are compared with theoretical ones (dashed lines) obtained via Voce law for Y3 Co-free alloy. Analogous curves were obtained for Cantor's alloy and 304L steel. It can be noticed that the theoretical curve exceeds the experimental one at the beginning of deformation. It means that the θ_0 parameter was overestimated in all those cases. It proves again that its

Table 5.1: *Values of average initial hardening rate normalised by shear modulus: $\theta_0/\mu \sim k_1$. Comparison between Y3 Co-free, Cantor's alloy and 304L steel.*

	Y3 Co-free	**Cantor's alloy**	**304L SS**
$\theta_0/\mu \sim k_1$	3.5 10^{-8}	4.9 10^{-8}	2.1 10^{-8}

measurement shows a high level of uncertainty. Nevertheless, at higher strains, the Voce law provides a suitable fit for the stress-strain curve, thus this law was finally applied to the analysed compositions.

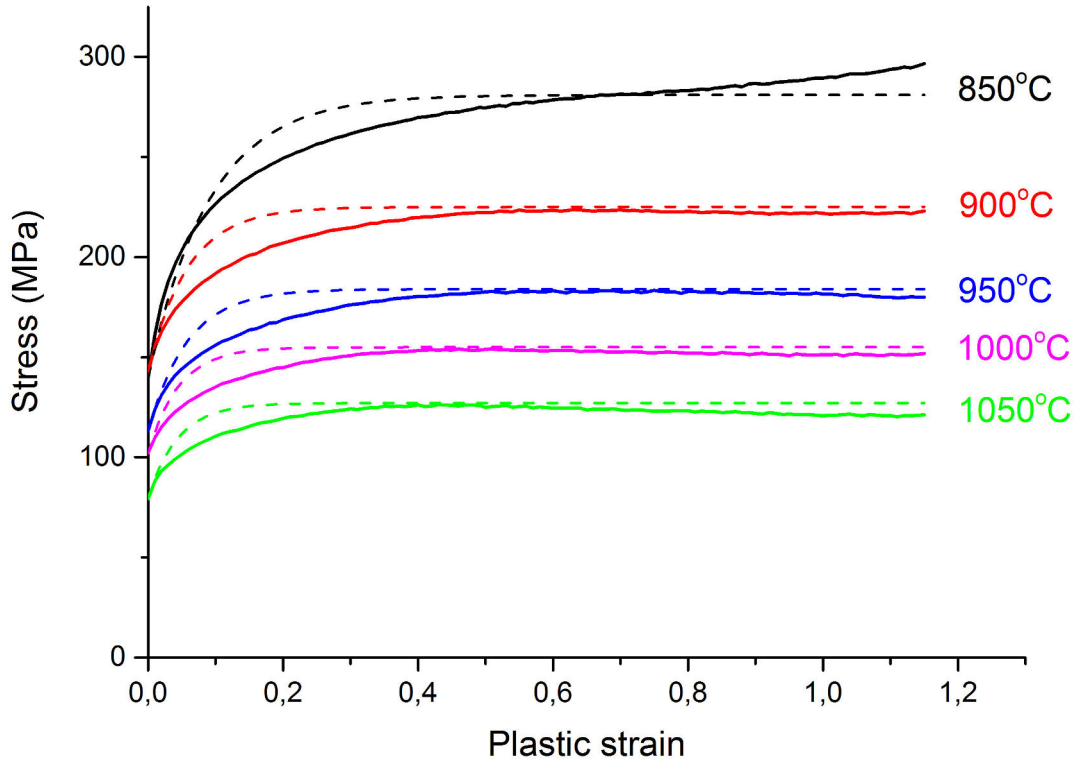

Figure 5.7: *Stress-strain curves of annealed Y3 alloy at high temperatures from 850° C to 1050° C and strain rate 10^{-1} s^{-1} (solid lines) and Voce fit law (dashed lines).*

Second parameter that can be obtained from the θ vs σ curve is the steady state stress σ_V that provides an estimation of stress in the absence of recrystallisation. This parameter describes the equilibrium between hardening that is proportional to k_1 and dynamic recovery that is proportional to k_2 (equation 5.6). Plot of the normalised σ_V/μ as a function of g parameter (equation 5.8) for Y3 Co-free composition is presented in Figure 5.8. The curve decreases linearly with g. For high values of g, when the temperature is elevated or the strain rate is low, the σ_V/μ values are low, close to zero. It shows increased influence of recovery over hardening during deformation. It is in agreement with enhanced annihilation of dislocations at higher temperatures, that results in a possibility to create new dislocations and further deformation, called the thermal activation. This observation is in accordance with

overall expectations, as increased temperature of tests and/or slower strain rate give time to the dislocation structure to react according to the imposed stress. On the other hand at small gs, the σ_V/μ is high and predicts reduced mobility of dislocation with deformation driven by preferential creation of new ones.

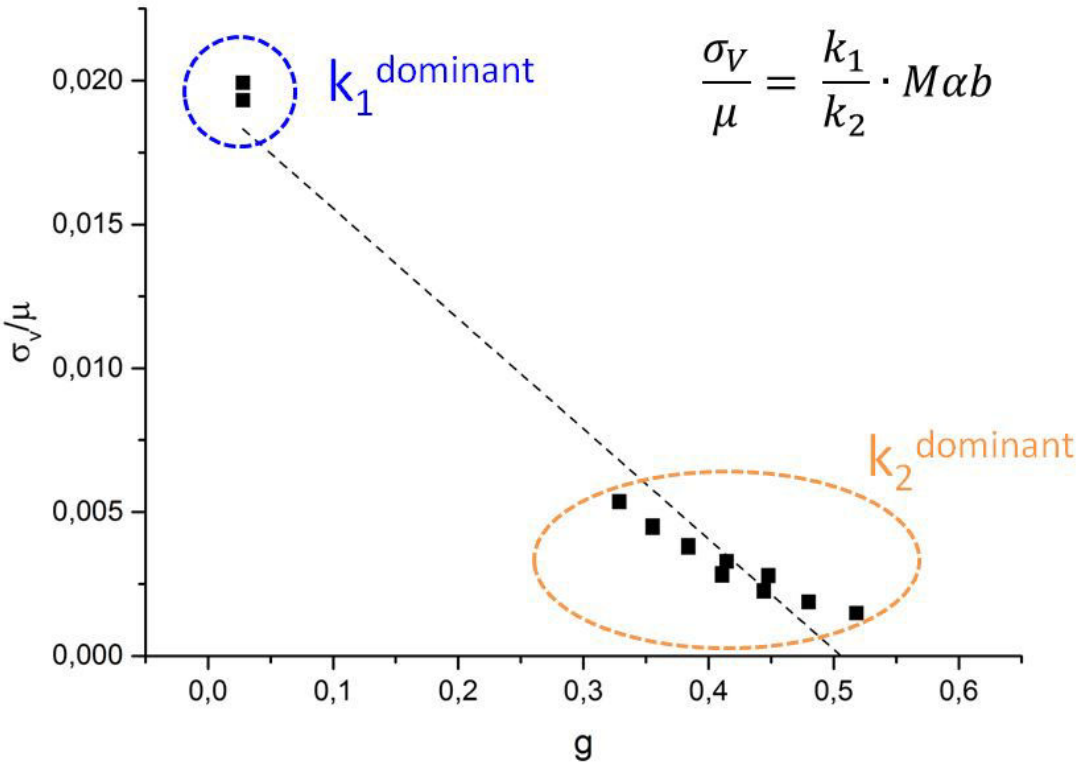

Figure 5.8: *Evolution of normalised σ_V/μ as a function of g for Y3 alloy. Dominance of hardening k_1 or recovery k_2 indicated for various g.*

This behaviour is in agreement with results obtained by Kocks and Mecking [147] for pure copper and other fcc metals. Master curves σ_V/μ vs g for Y3 Co-free alloy, Cantor's alloy and 304L stainless steel are compared with pure fcc metals in Figure 5.9. Line for $\chi = 0$ is also plotted in the same graph. It can be noticed that all analysed alloys are near each other in the close neighbourhood of silver, Ag, for which the SFE value is known to be of about 20-30 mJ/m^2. This position suggests relatively similar values of SFE for all alloys. Indeed, 304L stainless steel is reported to have the value of SFE at room temperature of about 19 mJ/m^2 [99], and the SFE for Cantor's alloy was measured in the range of 20-30 mJ/m^2 [77, 87]. It can be further deduced that Y3 Co-free alloy is characterised by similar value of stacking fault energy.

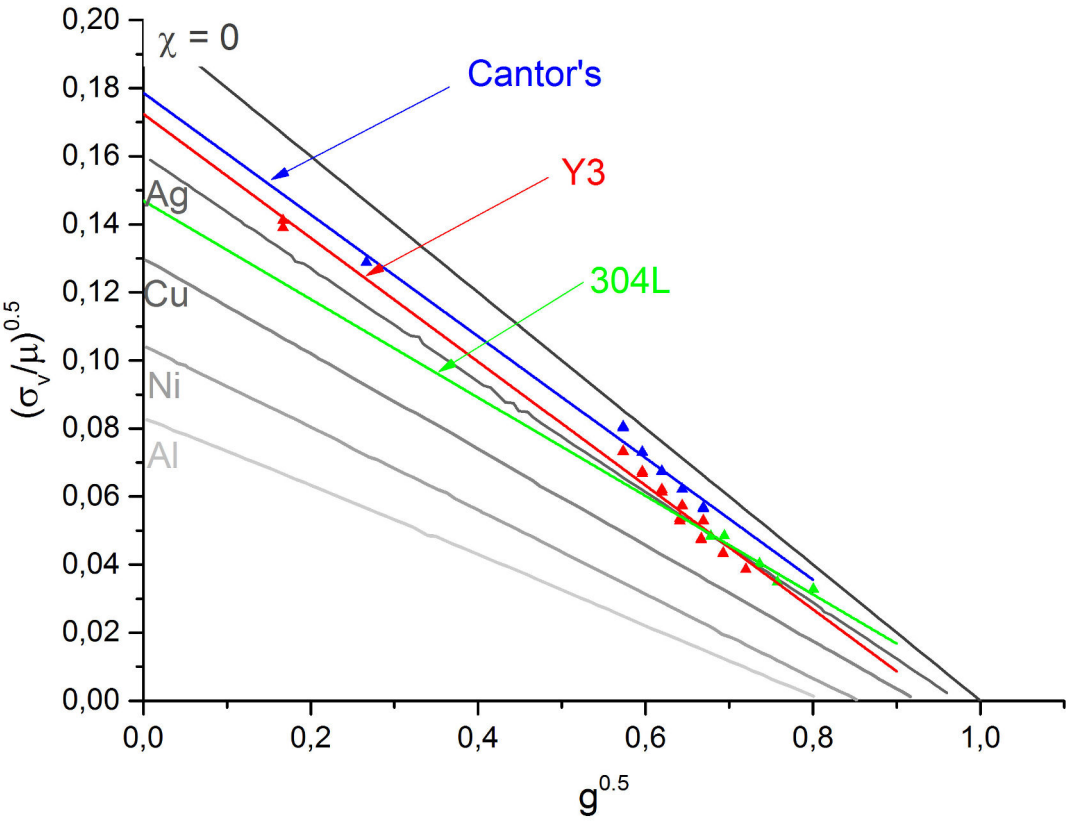

Figure 5.9: *Y3 Co-free alloy, Cantor's alloy and 304L stainless steel master curves plotted on the Kocks-Mecking* $\sqrt{\sigma_V/\mu}$ *versus* $\sqrt{g}$ *for pure fcc metals [147].* $\chi = 0$ *corresponds to stacking fault energy SFE = 0.*

Voce law together with Kocks-Mecking model enabled a relatively good prediction of deformation curves in a wide range of temperatures and strain rates with just two parameters. A master curve relating σ_V as a function of a single parameter g for each alloy could have been drawn. The Kocks-Mecking model allowed to roughly estimate the value of stacking fault energy. At the same time, hardening related to forest of dislocations and absence of influence of twinning on deformation could have been confirmed. It was shown that this approach that is current for fcc metals can be applied to the austenitic HEAs, showing that no hardening specific to HEAs is distinguishable. Selected HEAs behave like, and can be described by standard models for fcc materials.

5.2.1 Dynamic recovery and recrystallisation

It was shown that Y3 alloy is characterised by easy formation of nano-sized substructure upon hot deformation which is the source of high mechanical properties. The Kokcs-Mecking model of hardening showed that at high temperatures recovery/recrystallisation significantly influence the mechanical resistance. That is why evolution of microstructure upon high temperature deformation was analysed, to verify the conditions of substructure formation and dynamic recrystallisation in this alloy. The study was done via high deformation compression tests in the temperature range between 850°C and 1050°C with $\epsilon = 1.2$ and strain rate 10^{-1} s^{-1}. To avoid the influence of substructure formed upon previous forging, the initial microstructure of the samples is recrystallised by the heat treatment at 1000°C / 2h.

Stress strain curves for each temperature of deformation are reminded in Figure 5.10. Decrease of stress necessary to deform the sample with increased temperature is observed as well as a plateau upon reaching a critical value of stress for each condition. Stabilisation of the stress could correspond to a "steady state" of the structure and be a sign that dynamic recrystallisation begins. However, when the compression curves are compared to the one of 304L steel [161], it appears that the steady state is not yet reached within the applied deformation, as shown by an arrow in Figure 5.10. A hypothesis can be made that higher deformation to reach the steady state id needed in the case of the analysed HEA.

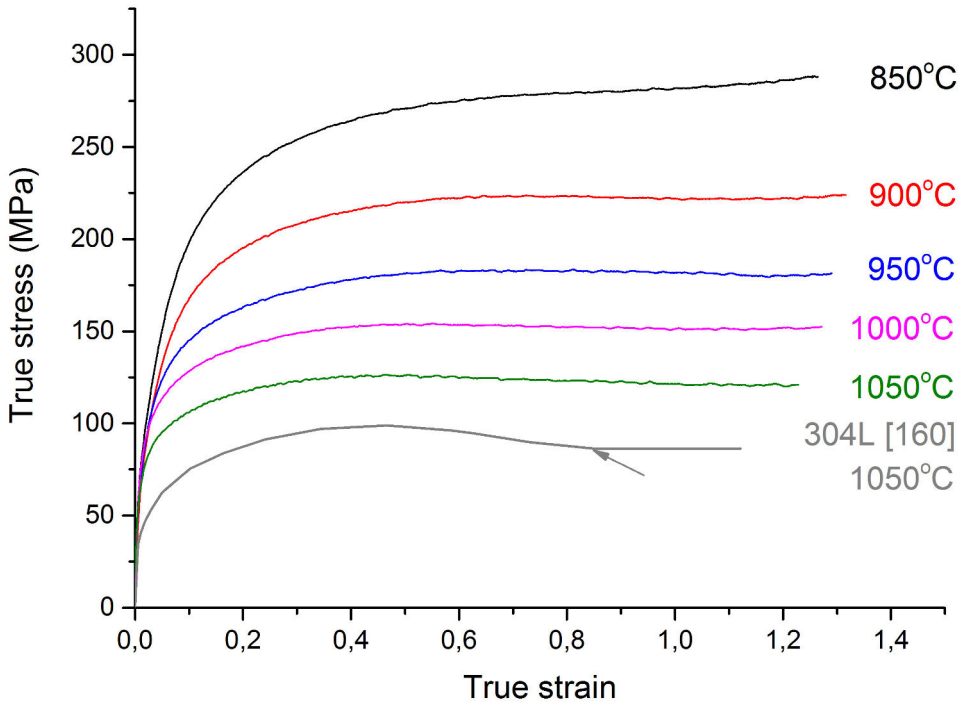

Figure 5.10: *Stress strain curves for Y3 alloy with high deformation $\epsilon = 1.2$ and strain rate 10^{-1} s^{-1}. A curve of 304L stainless steel compressed at 1050°C is presented for comparison [161], point where steady state is reached is marked with an arrow.*

Microstructural observations by EBSD confirm that recrystallisation takes places in all samples. In Figure 5.11 two images are compared, corresponding to compression at 850°C and 1050°C. Grains that underwent recrystallised are coloured to distinguish them from deformed grains represented by a band contrast image with the indication of grain boundaries (black for HAGBs, red for LAGBs and blue for twins). The grains are considered as recrystallised when their internal misorientation is below 2°. From presented images, it is clear that dynamic recrystallisation starts at the grain boundaries, leading to a typical necklace structures. With increasing temperature of deformation, the recrystallised fraction increases and the grains are bigger (note the change of scale between images). Eased diffusion together with earlier onset of recrystallisation at higher temperature lead to enhanced grain size. At the same time it can be noted that, contrarily to the deformed grains, the recrystallised grains do not have any sub-boundaries, however they show the presence of twin boundaries. It is clear that the imposed deformation was not sufficient to obtain a fully recrystallised structure.

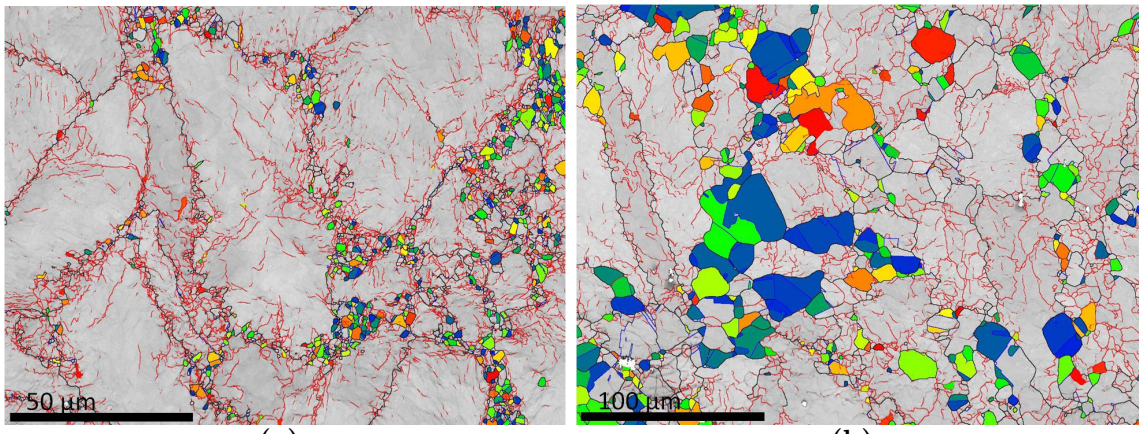

Figure 5.11: *EBSD bond contrast images with indicated grain boundaries (black for HAGBs, red for LAGBs and blue for twins) and coloured recrystallised grains (misorientation < 2°) after compression at a) 850° C and b) 1050° C.*

The microstructural evolution between samples from analysed conditions is reflected in the hardness values, presented in Figure 5.12 as a function of test temperature. The initial hardness of the material in the *annealed* state was of the order of 118 HV (in red). Compression at 850°C leads to reinforcement close to the one obtained upon hot forging, over 190 HV. The small fraction of recrystallised grains does not induce any softening compared to the *as forged* Y3. While the compression temperature increases, so does the recrystallised fraction which leads to softening and decreased hardness. HV values stabilise at about 160 for two highest test temperatures.

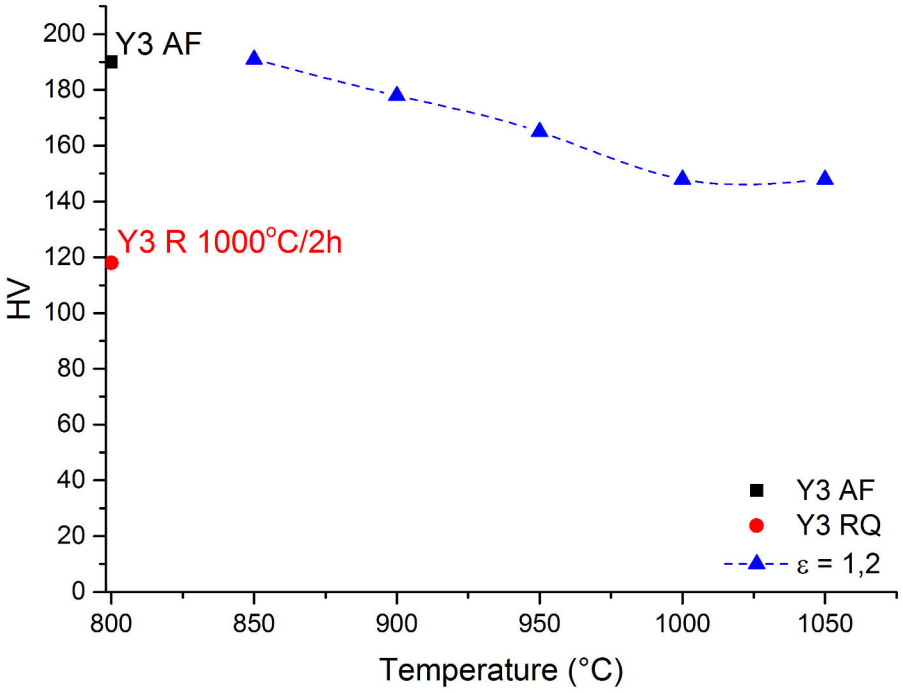

Figure 5.12: *Influence of compression test temperature on hardness, comparison with initial state, Y3 RQ, and as forged state, Y3 AF.*

The Y3 composition is characterised by high stability of dislocations and recrystallisation does not result in their classical elimination. Recrystallised grains were found to present a high density of dislocations following the {111}-type planes after forging and annealing. To verify if same behaviour is re-enacted for the compressive simulation of alloys' hot transformation, TEM observations were done. Micrographs for two extreme temperatures are presented in Figure 5.13. Generally, the local microstructure highly resembles the one found after forging, no matter the test temperature. It can be represented by microstructure from compression at 850°C shown in Figure 5.13a with high density of dislocations and nano-sized dislocation cells. Numerous orientations present within one grain are reflected in the elongated spots of diffraction diagram. Similarly, multiple spots can be found for the sample compressed at 1000°C, however with decreased intensity. The multitude of orientations is lesser at higher temperature suggesting that in-grain unification of orientations takes place.

Anyhow, for both compression temperatures some exception to this complex microstructure were observed. At 850°C presence of few grains free of dislocations was observed. As it can be seen in Figure 5.13b the presented grain has straight boundaries on one side and still not defined limit on the other as its growth was probably stopped. Its size is of few hundred of nanometres and its interior is free of dislocations. Similar occasional dislocation-free grains were found in Y3 alloy after forging at 900°C or after annealing at 800°C. However, no such grains were observed upon long time static annealing at 800°C. The reason behind it might be

that they are energetically not favourable and with time are consumed by grains with organised dislocation structure. Such relatively big grains, compared to the surrounding microstructure, were found after compression at 1050°C as shown in Figure 5.13c. The presented grain has little internal misorientation and dislocations organised along {111} planes. In Figure 5.13d enlarged view of the inside of this grain is shown with a trace of one of the {111} planes family. At the scale of EBSD this grain appears as a recrystallised with presence of twins. In the Figure 5.11 it would be one of the colour grains. Again, analogous microstructure was found upon forging at 1100°C.

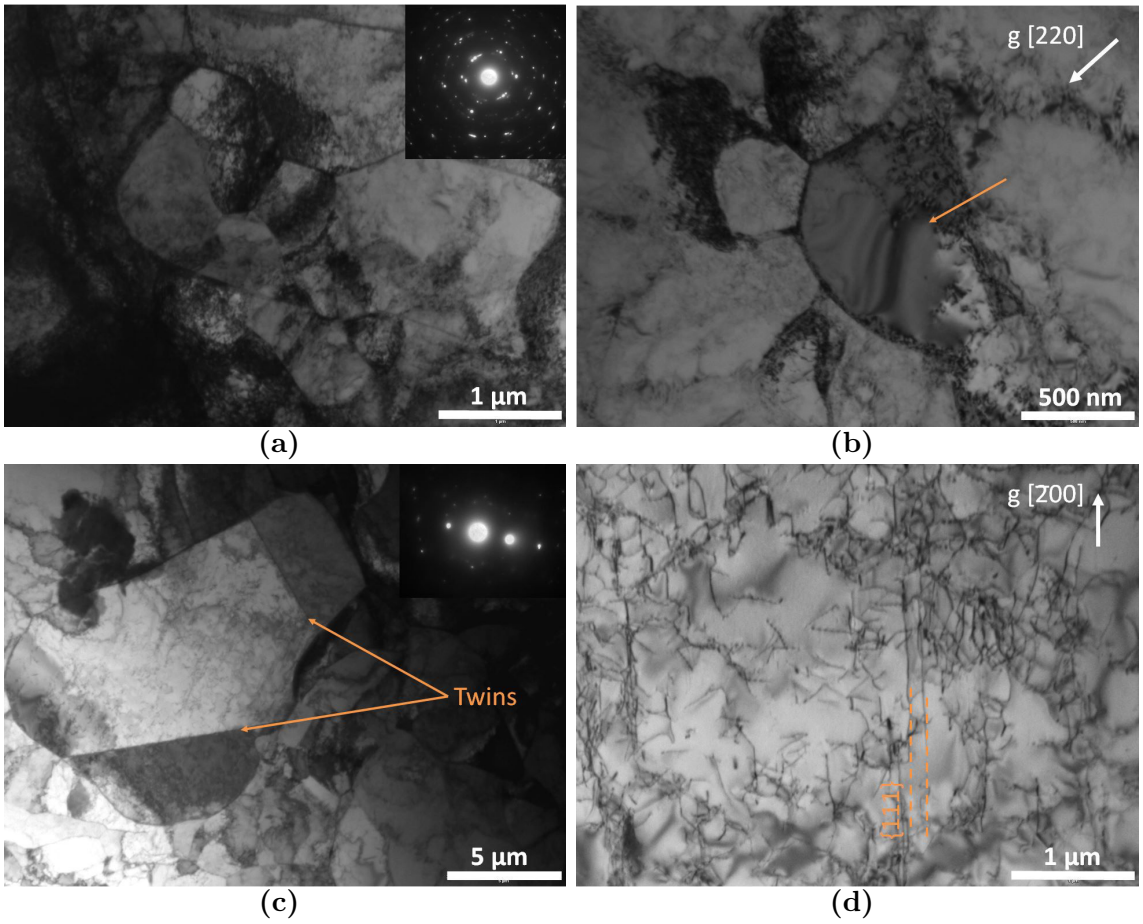

Figure 5.13: *Y3 alloy after high deformation, $\epsilon = 1.2$ at high temperatures: a), b) 850°C and c) d) 1050°C. BF TEM images.*

All those observation allow to conclude that formation of the substructure characteristic for those alloys in the *as forged* state is well recreated during hot compression tests. Creation of nano-sized dislocation-free grains is possible at lower temperatures, whereas at higher temperatures presence of recrystallised grains with typical structure of organised dislocations is found. The applied deformation of 1.2 is not sufficient to obtain a fully recrystallised structure, however the dynamic recrystallisation is initiated at both tested temperatures.

5.3 Grain boundaries hardening. Hall-Petch relation

As compared to features treated in previous paragraphs, grain boundary hardening is the structurally superior level of metallic materials strengthening. Magnitude of strengthening by the presence of grain boundaries can be defined via Hall-Petch relation as expressed by the equation 5.10, where D is the average grain size, YS_0 is the intrinsic strength representing the strength of a single crystal, and k_{HP} is the Hall-Petch coefficient describing the efficiency of hardening via grain boundaries. Since it is common to define a direct relation between yield strength and hardness measurements: YS = α·HV, very often Hall-Petch is presented as a function of hardness, as shown by equation 5.11, where HV_0 is the intrinsic hardness, and k_{HP} is again the Hall-Petch coefficient, but this time expressed in HV units. This approach eases the definition Hall-Petch relation, as hardness measurements are faster and less complicated to perform.

$$YS = YS_0 + \frac{k_{HP}}{\sqrt{D}} \tag{5.10}$$

$$HV = HV_0 + \frac{k_{HP}}{\sqrt{D}} \tag{5.11}$$

To properly assess the influence of grain size on mechanical properties of Y3 Co-free alloy, a series of severely cold rolled samples (90% thickness reduction) was prepared. After rolling the samples were annealed at 1000°C at various times, in the range of 2 minutes to 24h. These heat treatments allowed to obtain a variation of grain size from 14 μm to 93 μm. Grain size was measured by the intercept method (twins were not taken into account), based on SEM BSE observations. Vickers hardness was then measured on each sample. To be able to compare the results of Y3 alloy with A3S and Cantor's alloy all the hardness measurements were transformed into YS values, with the coefficient $\alpha = 1.75$ as previously defined for recrystallised samples. So obtained YS values were plotted as a function of $1/\sqrt{D}$ and are presented in Figure 5.14. A linear relation was found in the analysed grain size range, that can be described by equation 5.12:

$$YS = 144 + \frac{232}{\sqrt{D}} \tag{5.12}$$

The obtained results were compared with relations previously known for A3S [115] and for Cantor's alloy [72] and coming from tensile tests. As in the present study, in both those studies, the material was initially cold rolled and subsequently annealed to obtain a variation of grain size: therefore, an easy comparison of results is possible. Values of YS_0 and k_{HP} are presented in Table 5.2, 316L stainless steel [162] is also shown as a reference. Firstly, it can be seen that Y3 Co-free composition in general

presents lower strength for a given grain size than A3S or Cantor's alloy. However, when the values of intrinsic strength for a single crystal ($D \to \infty$) are taken under consideration, it appears that Y3 Co-free alloy shows somewhat increased resistance from all analysed HEAs. Nevertheless, it is the austenitic stainless steel that is characterised by the most elevated YS_0. Such surprising outcome could be due the purity of compared alloys. The industrial grade of steel is richer in interstitial atoms like C and N that highly influence the intrinsic hardness of the material, their effect is more pronounced than simple solid solution strengthening seen in HEAs.

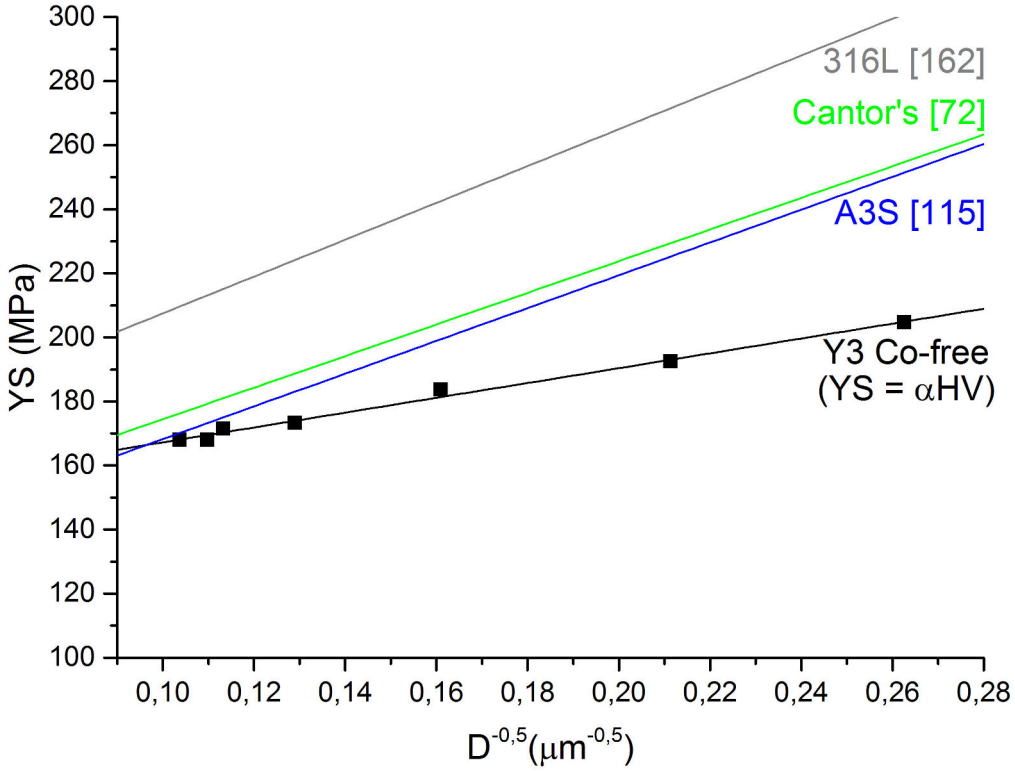

Figure 5.14: *Hall-Petch relation for Y3 alloy obtained for cold rolled samples annealed at 1000°C for various times. Comparison with Cantor's Hall-Petch relation [72], A3S [115] and 316L stainless steel [162].*

Table 5.2: *Values of intrinsic strength YS_0 and Hall-Petch coefficient k_{HP}. Comparison between Y3 Co-free, Cantor's alloy [72], A3S [115] and 316L steel [162].*

	Y3 Co-free	**Cantor's** [72]	**A3S** [115]	**316L SS** [162]
$\mathbf{YS_0}$ [MPa]	144	125	117	151
$\mathbf{k}_{HP}$ [MPa·μm$^{-0.5}$]	232	494	512	575

The Hall-Petch coefficient proved to be the highest for the 316L stainless steel. Values for Cantor's alloy and A3S show values close to the one of steel but largely exceed the one obtained Y3 alloy. The efficiency of grain boundaries hardening is significantly lower in the selected Y3 grade despite showing similar structure on the

grain level, as well as at the scale of dislocations. It could be hypothesized that the grain boundaries character is modified as compared to A3S, Cantor's alloy or the 316L steel. A study focusing on the grain boundaries character would be required to confirm or disprove this hypothesis.

The above definition of Hall-Petch relation was done on fully recrystallised samples and gives us the information solely on grain boundaries influence on mechanical resistance in the analysed grain size range. This information could also be used to define the hardening of the Y3 alloy due to high density of dislocations, especially observed in *as forged* state. It can be assumed that mechanical resistance of a single phased material comes from both its intrinsic hardness YS_0 and grain boundaries hardening. These two effects being independent and therefore, additive in this approach, the intrinsic hardness can be divided into two contributions: the one of a monocrystal at equilibrium with low density of defects YS_m, and the one due to dislocations forest hardening YS_ρ, as presented by equation 5.13. The extrapolation of Hall-Petch relation to a single crystal, for $D \to \infty$, allows to eliminate the contribution of grain boundaries, leaving solely two parts. If so, the efficiency of forest hardening can be estimated.

$$YS_0 = YS_m + YS_\rho \tag{5.13}$$

This approach is presented in Figure 5.15, where for the *as forged* Y3 the line representing Hall-Petch relation was slid upwards to go through corresponding YS value maintaining the same slope. It was done assuming that the efficiency of hardening via grain boundaries does not change between the two analysed states: *cold rolled* or *as forged*. One can see that a significant increase of YS_0 parameter is observed, from 144 to 447 MPa. Hot forging of Y3 alloy results about 3 times higher mechanical resistance than upon recrystallisation when the influence of grain boundaries is excluded. Since the intrinsic hardness of a single crystal is constant for the material (YS_m = const), independently of its state, only the hardening due to density of dislocations is a variable between those two states. It was previously shown that the dislocations density is roughly one order of magnitude higher after forging than at *annealed* state. According to Taylor's equation such difference in dislocations density should result in yield strength $\sqrt{10} = 3.16$ times higher. That is exactly the result that was found with the Hall-Petch approach. It can be thus confirmed that the high density of dislocations found in the *as forged* state is responsible for increased mechanical resistance.

Let's also analyse the other red points on the graph in Figure 5.15, corresponding to annealed samples with initially *as forged* structure. Those points regain the master curve of Hall-Petch relation for recrystallised Y3 alloy. Regardless the initial deformation type (hot forging or cold rolling), once the alloy is recrystallised, the

mechanical resistance is found to be the same for corresponding grain size. It confirms that the dislocation structure is not influenced by the temperature of initial deformation.

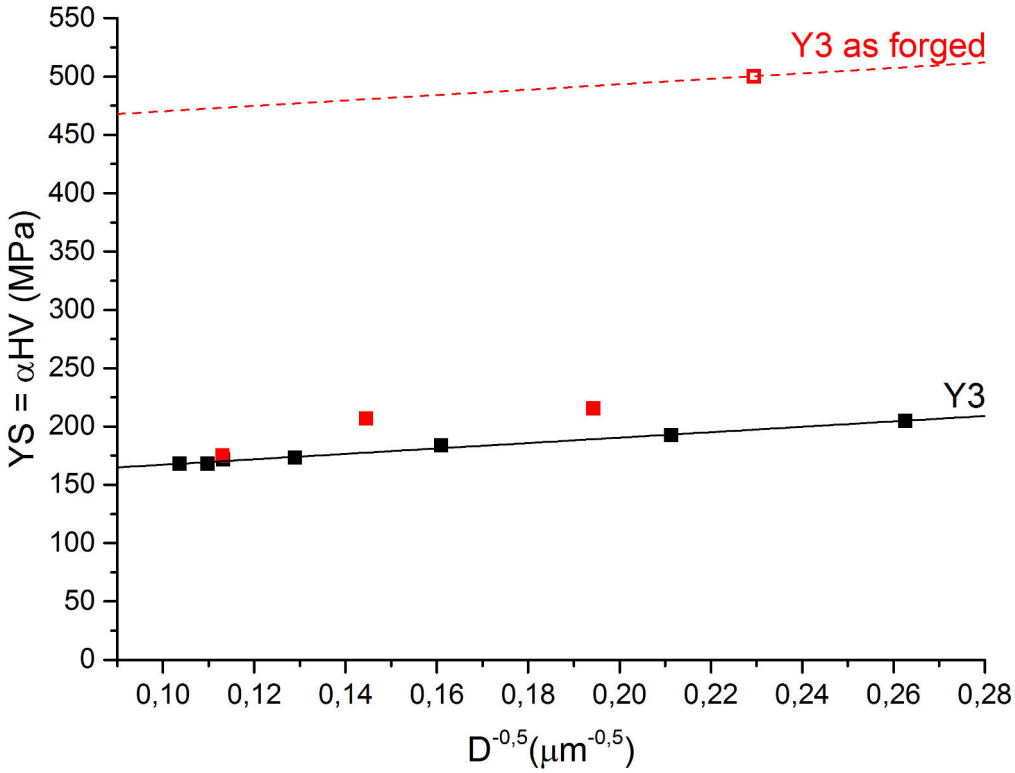

Figure 5.15: *Hall-Petch relation for as forged Y3 Co-free alloy assuming that k_{HP} is the same as for annealed state. For as forged Y3 sample the YS value comes from tensile test at room temperature (red empty square symbol). Other red points represent the YS values for as forged samples after annealing calculated from hardness measurements using the α coefficient equal to 1.75, since such relation was found after recrystallisation. Black points as previously present the fully recrystallised samples.*

The grain boundaries hardening seams to show little efficiency in the analysed Y3 Co-free alloy, with significantly lower Hall-Petch coefficient than classical 316L stainless steel, A3S or Cantor's alloys. However, the intrinsic hardness of Y3 alloy is increased compared to the quinary HEAs, but lesser than the austenitic steel. Increased mechanical resistance of the Y3 composition due to dislocations substructure created during forging could have been shown. Also lack of influence of temperature of initial deformation on resistance of recrystallised samples was shown.

5.4 Precipitation hardening

Selected Y3 Co-free composition is a single fcc phased alloy. Its mechanical properties have been shown promising; yet as in classical alloys, further increase of mechanical resistance can be thus contemplated by second phase precipitation. It is quite common in the field of analogous austenitic stainless steels to enhance their properties by secondary precipitation of carbides, nitrides or carbo-nitrides of elements like Ti, W, Nb. Such precipitates are not only obstacles to dislocations movement leading to increased resistance, but also they interact with grain boundaries. Presence of fine secondary particles can significantly slow down the grain growth by Zenner-pinning effect and consequently, further increase materials resistance thanks to Hall-Petch effect.

Similar approach was imagined for the analysed Y3 alloy with the same measures to its design as before. Several aspects are required from the phase diagram for the precipitation hardening to be efficient. First of all, at high temperatures, a single phased region is necessary to dissolve all elements in the matrix through solution annealing. It is best if the region is large enough in a wide range of temperatures and compositions so that in case of hazardous variation of any of these, the annealing still results in a single phased alloy. Secondly, change in solubility has to be present for precipitation to take place. It is preferable for the curve presenting such second phase formation, to be concave for higher driving force. Finally, the precipitation annealing temperature needs to be high enough for diffusion to be sufficiently fast so that its time can be reasonably short.

A series of Thermo-Calc calculations was performed for simulation of phase diagrams. Addition of various elements like W, V or Ti was tested, and calculated alloys have been simultaneously doped with carbon, nitrogen or both, at levels between 100 to 500 ppm. For most attempts, the solubility of the additional element in the HEA matrix was found not sufficient to contemplate its use. The single fcc region was then significantly reduced or even non existent. In some cases also convex solubility function was obtained, which is undesirable in the case of precipitation. Finally, the most promising result seamed to come from niobium alloying accompanied by carbon doping. The obtained phase diagram of Y3 Co-free composition doped with 200 at. ppm of carbon as a function of Nb content is presented in Figure 5.16. The choice of such amount of carbon was based on tentatives of variation of its content. When the C content was increased to 500ppm or more, the presence of $M_{23}C_6$ type carbides was significantly enlarged. It is not a targeted carbide, so when it precipitates it uses the carbon necessary for NbC precipitation and unables its formation. Additionally, it can be harmful to the alloy in numerous ways. Firstly, because it has the tendency to form on grain boundaries leading to material brittleness. Secondly it usually uses the available chromium, making the neighbouring area depleted in

this element and consequently leading to local decrease or total lack of corrosion resistance, as it is currently identified in classical stainless steels.

Several aspects need to be noted when analysing the obtained phase diagram, that is shown in Figure 5.16. First of all, the NbC phase is predicted by the thermodynamic calculations. Its presence is foreseen bellow 1000°C and is defined by a concave curve (yellow curve)as required for precipitation hardening. Secondly, another feature of importance for efficiency of precipitation, is the single phased area in the range of temperatures from 1000°C to 1350°C. For small size hardening precipitates and avoidance of big embritelling ones, full solubility in the matrix is preferable.

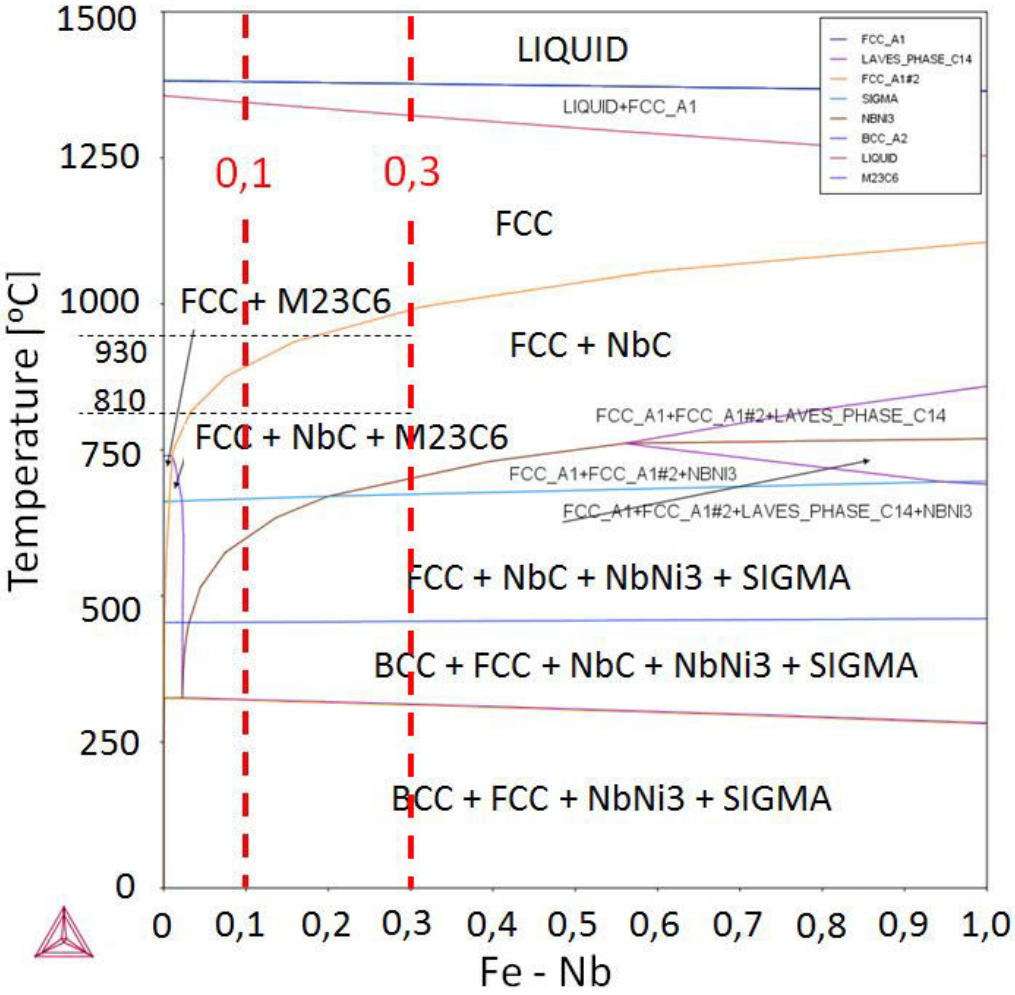

Figure 5.16: *Phase diagram of Y3 Co-free composition doped with 200 at. ppm C and with Nb, presented in at. %. Calculation done with the TCFE5 database.*

With all those elements in mind, two compositions were selected for casting and analysis: one with the addition of 0.1 at.% Nb and the other with 0.3 at.% Nb. Both compositions are doped with 200 ppm of C and present a possibility of solution annealing above 1000°C. The precipitation hardening heat treatment was proposed as follows, at temperatures ranging from 750°C to 980°C; according to Thermo-Calc

calculations it should lead to the presence of 0.14 - 0.19 vol.% of NbC at equilibrium state.

Firstly, the alloy richer in Nb was cast and its structure was observed directly after casting, Figure 5.17. A dendritic structure can be distinguished and EDX chemical analysis suggests primary segregation. Just like in the Y3 Co-free alloy, the interdendritic zones are enriched in manganese and nickel, and depleted in iron and chromium. Unfortunately, presence of primary precipitation of a Nb-rich phase is noted in the interdendritic zones: particles of sub-micron size are evenly spread between the dendrites. It is an undesirable outcome, that was not predicted by Thermo-Calc simulation of equilibrium state.

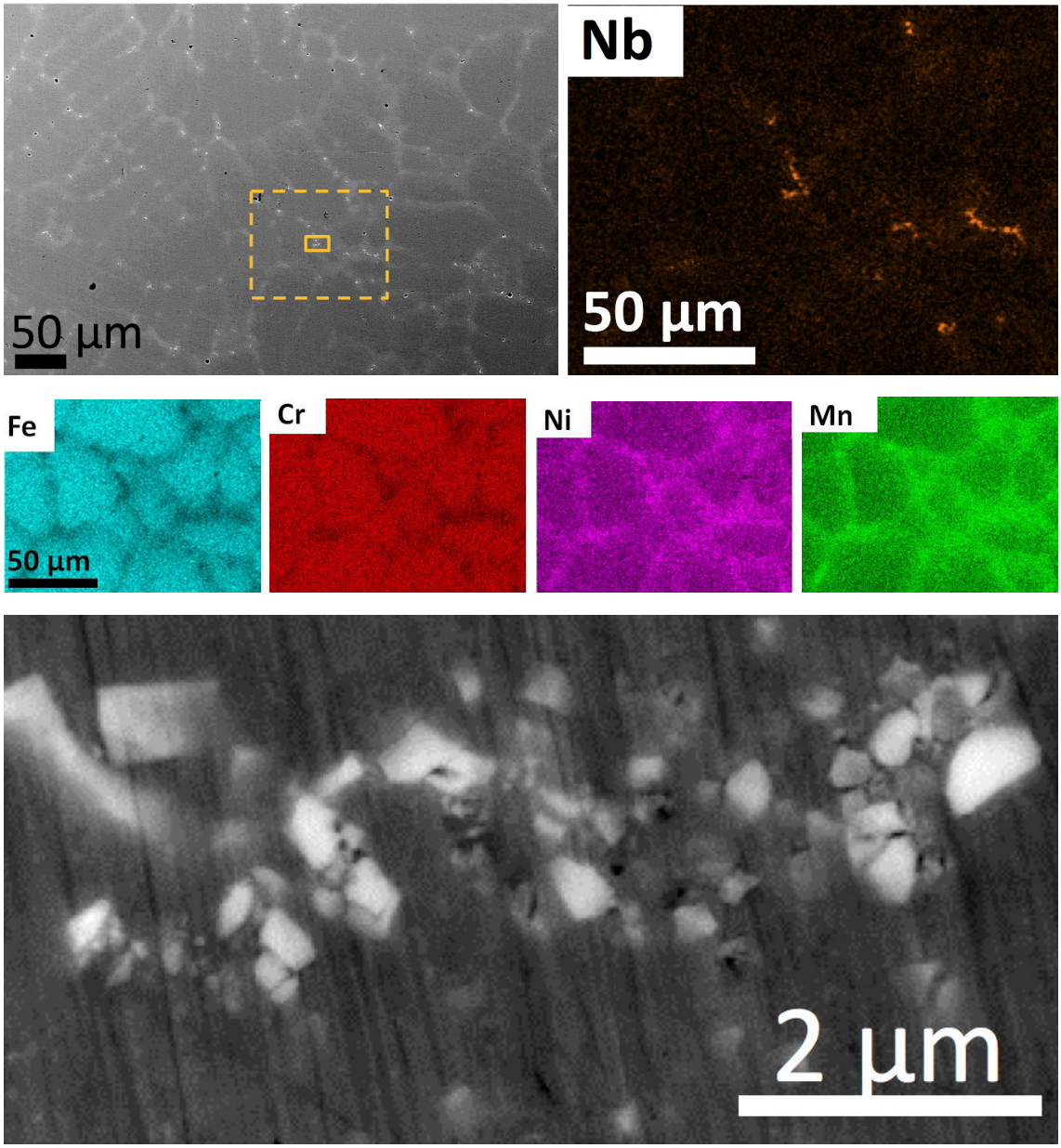

Figure 5.17: *As cast Y3 Co-free (0.3Nb) alloy with a zoom on Nb rich precipitates, SEM BSE image. Local EDX cartography coming from the zone in dashed square showing the chemical segregation through the dendrites as well as Nb-rich precipitates.*

Indeed, when the solidification simulation according to Scheil-Gulliver model is performed, significant segregation of elements is predicted to finally show second phase formation. Solidification profile, together with variation in chemical composition of liquid phase are presented in Figure 5.18. As in Y3 alloy, solidification starts as fcc phase at about 1380°C. Unfortunately, due to segregation phenomena, the range of solidification temperature is much larger than at equilibrium, where it should be finished at 1340°C. According to the simulations of real course of solidification, the range of coexistence of liquid and solid phases goes down to 1100°C; moreover starting from 1155°C, a primary NbC solidifies. Presence of this second phase, marked in green, is in agreement with primary precipitation observed experimentally. Such low temperature of solidification suggests that the final product might be an eutectic, mixture of fcc solid solution and NbC.

To verify the prediction of non-equilibrium solidification conditions, experimental measurements have been done by ATD technique and then, by hot cracking testing method on a Gleeble machine.

ATD measurements performed during heating of as cast Y3 Co-free (0.3Nb) alloy have shown the temperature of beginning of melting similar to that of pure Y3 Co-free alloy around 1347°C ±10°C: it is to be compared to 1344°C for Y3 alloy. ATD did not detect any low temperature event; in particular no feature was noted during measurements close to 1100°C. It is highly probable that, even if at this temperature some liquid phase was already present, its volume fraction was not sufficient and the emitted heat was not high enough to be detected. Those results suggest that the early onset of melting concerns only the suspected eutectic mixture, whose presence is minor in the alloy.

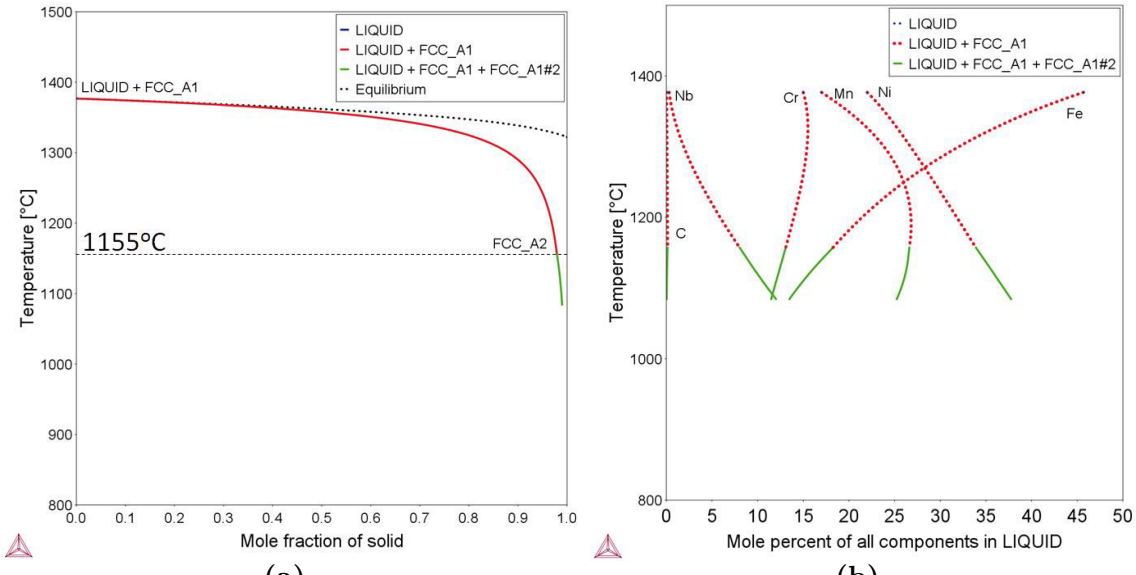

(a) **(b)**

Figure 5.18: *Thermo-Calc diagrams of Y3 Co-free (0.3Nb): a) phase formation upon solidification and b) change of chemical composition of liquid during solidification. Calculations done in TCFE5.*

Since the ATD measurements were not conclusive, hot cracking tests were performed on Gleeble machine in APERAM research laboratory, as a complementary technique for liquefaction temperature definition. The test consists of rapid heating (50°C/s) and pulling of cylindrical samples. Radical drop in force necessary to break the sample is a sign of local liquefaction and so, beginning of melting. Such tests were performed on as cast Y3 Co-free (0.3Nb) in the range of temperatures between 900°C and 1200°C. Microstructural observations of cross sections of samples after the tests, presented in Figure 5.19, allowed to clearly determine the starting temperature of melting. First, sample after test at 1000°C is presented in Figure 5.19b. It is a representative image for tests performed in the range of temperatures between 900°C and 1050°C. Elongated dendrites at the fracture tip are visible. They were clearly plastically deformed without any melted zones to be found on the surface. However, when the temperature was raised to 1100°C, the character of the fracture surface has changed, as shown in Figure 5.19c. Presence of melted zones could have been distinguished, characterised by fine dendritic structure due to rapid solidification after sample rupture. Melting was found to start as expected, in the interdendritic zones, for which local chemical composition shifts the equilibrium to lower melting temperatures. Thus, the solidification process simulation predicting low temperature freezing was confirmed to take place between 1050°C and 1100°C.

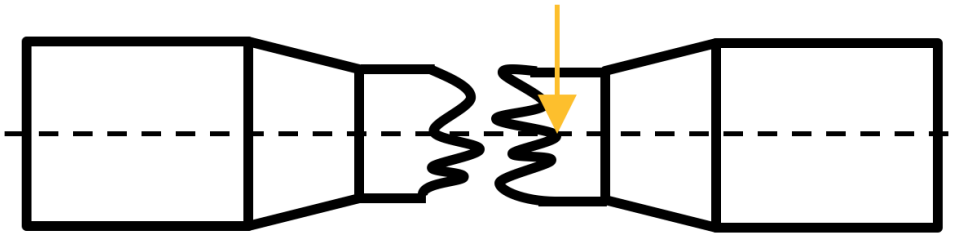

(a)

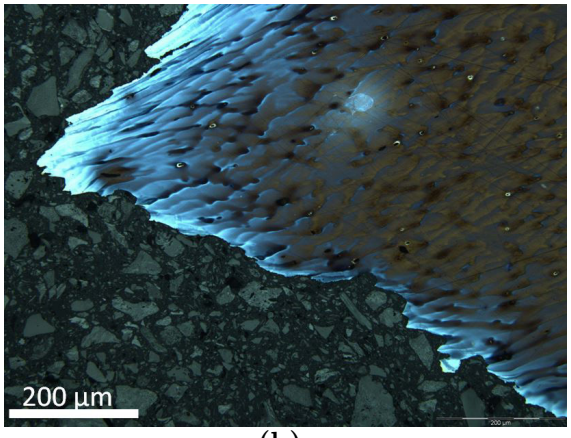

(b)

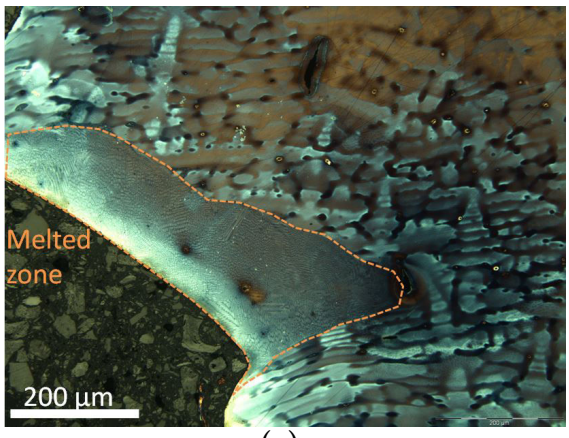

(c)

Figure 5.19: *Samples of as cast Y3 Co-free (0.3Nb) alloy after hot cracking tests: a) schematic representation of observed surface b) test at 1000°C and c) test at 1100°C with a clearly distinguishable melted zone; light microscopy on etched samples.*

Attempt of dissolution of those primary precipitates in the as cast state was done. A heat treatment of 3h at 1200°C was performed. The temperature was chosen as the highest possible, for which melting of only the eutectic zone happens. The expectation was that, due to a homogenisation of the local composition, primary NbC would be dissolved and upon re-solidification the eutectic would not form again. If the diffusion of Nb, as the slowest diffusive element is considered, the expectation for dissolution seams quite reasonable. Diffusion coefficient D can be defined according to equation 5.14,where D_0 is the maximal diffusion coefficient (at infinite temperature), Q is the activation energy for diffusion, R is the universal gas constant and T is the absolute temperature. As for Nb diffusion in an fcc matrix, bibliographic data [163] indicate $D_0 = 0.053$ m^2s^{-1} and Q = 344,6 $kJ{\cdot}mol^{-1}$; thus at 1200°C, the diffusion coefficient is equal to $3.19 \cdot 10^{-14}$ m^2s^{-1}. For 3 hours of annealing it can be approximatively calculated that the diffusion distance of Nb is of the order of 26 μm, assuming that the distance x is proportionate to $\sqrt{2 \cdot D \cdot t}$. This distance is high enough to allow local homogenisation of the material and further diffusion of Nb. It can be expected that in the case of HEAs, the diffusion will be slowed down, but even is one order of magnitude is considered and D decreases 10 times, the diffusion distance is still reasonably high, over 8 μm.

$$D = D_0 \cdot exp\left(-\frac{Q}{RT}\right) \tag{5.14}$$

Microstructural observations together with chemical analyses of as cast Y3 Co-free (0.3Nb) after annealing at 1200°C 3h are presented in Figure 5.20. The dendritic form after casting is still distinguishable, however it is mostly due to presence of precipitates at the borders of dendrites. Primary precipitation of Nb-rich phase is still visible, although the shape of particles has changed, approaching a spherical form. Moreover, their size somewhat decreased. Both those observations allow to think that dissolution indeed takes place, however the kinetics of this process is extremely slow. Despite quite significant distances an Nb atom could diffuse to during such heat treatment it is still blocked in the precipitates. It would appear that the dissolution itself is difficult. In addition, no signs of liquefaction are present, which reinforces the NbC dissolutions hypothesis.

Overall chemical composition was unified thanks to the annealing and elements other than niobium are equally distributed in the alloy. However, the equilibrium single phased area predicted by thermodynamic simulation was not reached, and full dissolution of NbC precipitates in the matrix was not successful.

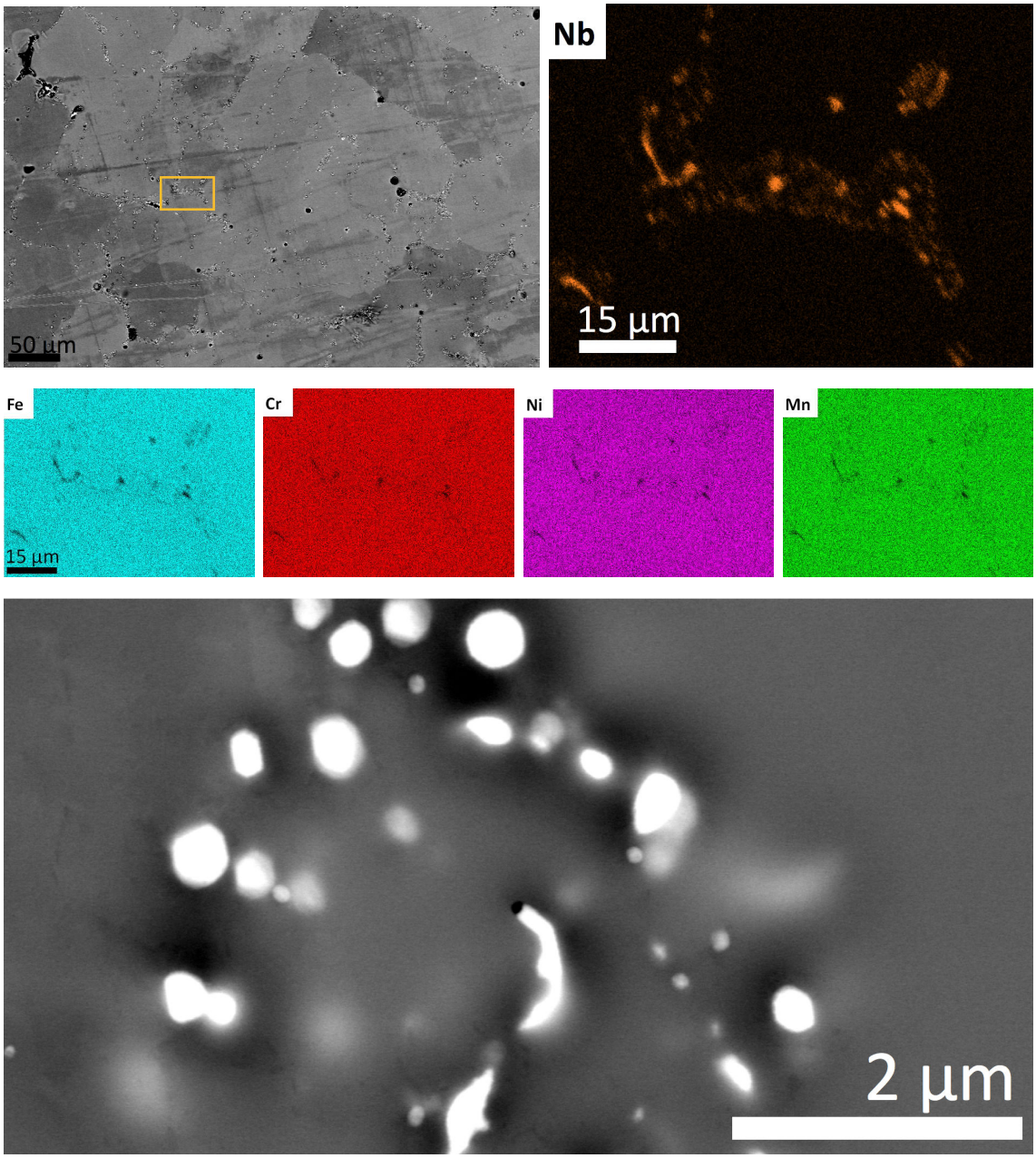

Figure 5.20: *As cast Y3 Co-free (0.3Nb) alloy after annealing at 1200°C 3h, SEM BSE micrographs together with zoom on the NbC precipitates and the local distribution of chemical elements in the restricted zone marked by the orange box.*

Yet, two selected grades, Y3 Co-free (0.1Nb) and Y3 Co-free (0.3Nb) were hot forged. Standard conditions were applied, with annealing at 1000°C for 3h and forging close to 1060°C. This is the limit temperature for Nb-doped composition as the hot cracking tests confirmed. No problems were detected during forging; in particular, no cracks or any other signs of brittleness were found. Presence of primary precipitation has no negative influence on the forging process and in selected thermal conditions of forging, no liquefaction was observed. SEM BSE micrographs of *as forged* niobium doped alloys, 0.1 at.% Nb and 0.3 at.% Nb, are presented in Figure 5.21. Microstructure similar to that previously reported for Y3 Co-free alloy can be observed. High complexity of the structure with frequent changes of orientation

inside the grains makes distinction of individual grains close to impossible with this observation technique. Inside the perturbed matrix, occasional precipitates are visible as white particles. The precipitates rich in heavy Nb are clearly distinguishable. The precipitates after forging are evenly distributed through the whole material without preferential positioning in the microstructure. They present themselves as sub-micrometric spherical particles. Compared to *as cast* state, they have been refined and partially dissolved during forging process.

In general, lower fraction of primary NbC is observed for Y3 0.1Nb than the composition richer in niobium. This outcome is expected, but undermines the necessity for higher Nb content. Presence of niobium in the form of primary precipitates is not interesting from the precipitation hardening point of view. On the contrary, they can be even harmful leading to embrittlement. It is expected for the totality of precipitating element to be fully dissolved in the matrix before precipitation annealing is performed. Optimisation of this process is necessary.

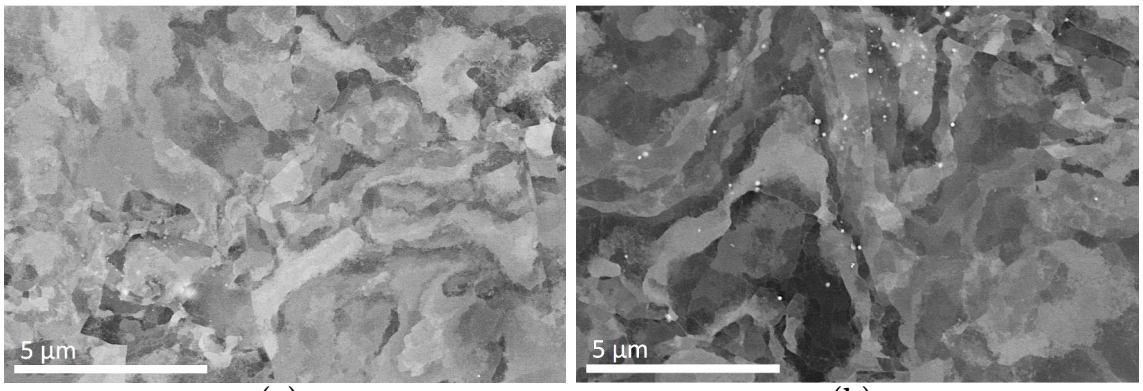

Figure 5.21: *As forged alloys containing niobium: a) Y3 Co-free (0.1Nb), b) Y3 Co-free (0.3Nb); SEM BSE images, Nb-rich particles are distinguishably white.*

Again an attempt of solution annealing was performed, this time on *as forged* samples. Applied conditions were as follow: 1200°C 24h, to assure highest chance of reaching the single phased zone predicted at equilibrium for both selected grades. Obtained microstructures are presented in Figure 5.22. It can be immediately seen that the precipitates dissolution was not achieved, presence of primary NbC is still detected. Significant grain growth and presence of twin boundaries can be noted. The very high temperature and long annealing did not result in the expected single phased alloy, so there is no reason to maintain it. A more moderate annealing will be set as standard, more comparable with the annealing done on Y3 Co-free alloy: 1080°C 2h. This temperature was chosen based on the equilibrium phase diagram, as the one to bring a compromise between sufficiently high temperature above the line of NbC formation, at least 50°C for both grades, and minimisation of this temperature as much as possible avoiding excessive grain growth. Such *annealed* state will be used as the initial one for precipitation heat treatments.

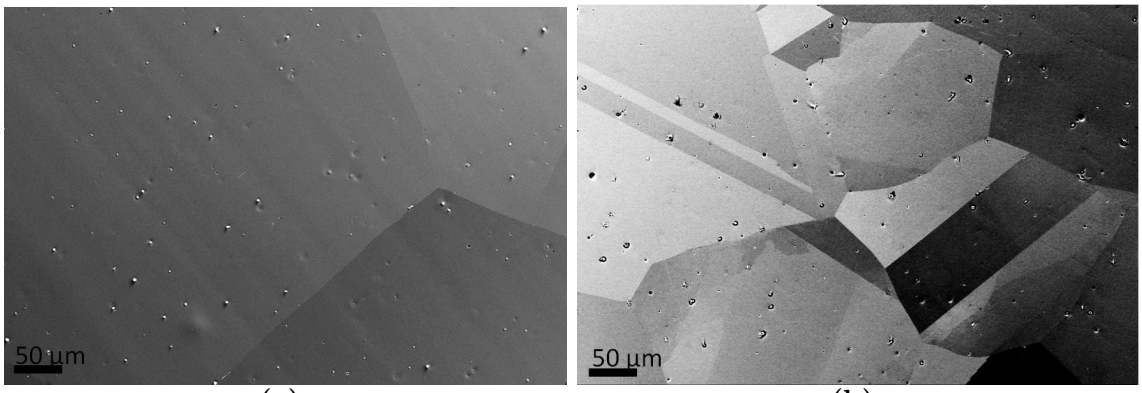

(a) (b)

Figure 5.22: *SEM BSE images of forged alloys containing niobium after annealing at 1200° C for 24h: a) Y3 Co-free (0.1Nb), b) Y3 Co-free (0.3Nb).*

First however, the influence of primary precipitates upon annealing at 1080°C 2h on mechanical behaviour of Y3 0.3Nb was checked. Tensile tests were done both at room temperature and in cryogenic conditions. The results are presented in Figure 5.23, in Table 5.3 and are compared with the *annealed* Y3 Co-free composition. Little difference was found between two alloys. Similar shapes of curves are visible, with slightly higher work hardening for Nb doped composition. Increased work hardening in the Y3 Co-free (0.3Nb) alloy could partially explain the somewhat raised elongation to fracture. Same tendency for simultaneous strength and elongation increase at -150 °C was found in the Nb doped alloy, analogously to pure Y3 alloy. Increase in yield strength and ultimate tensile strength for Y3 (0.3Nb) compared to the Y3 Co-free alloy were observed. Raise in YS and UTS values is of 60 - 100 MPa for tests at both temperatures. It is a sign that additional hardening already takes place. However, it is most probably due to solution hardening of Nb atoms in the matrix rather than influence of second phase precipitation, the size of observable NbC being to high. At the same time, no signs of brittleness due to those primary precipitates were found. This is a very promising result, as the difficulty to eradicate primary NbC does not have significant influence on the material's behaviour, their presence can be disregarded in the first approach. Attempts to obtain fine hardening precipitation can be done on the annealed Y3 Nb doped alloys.

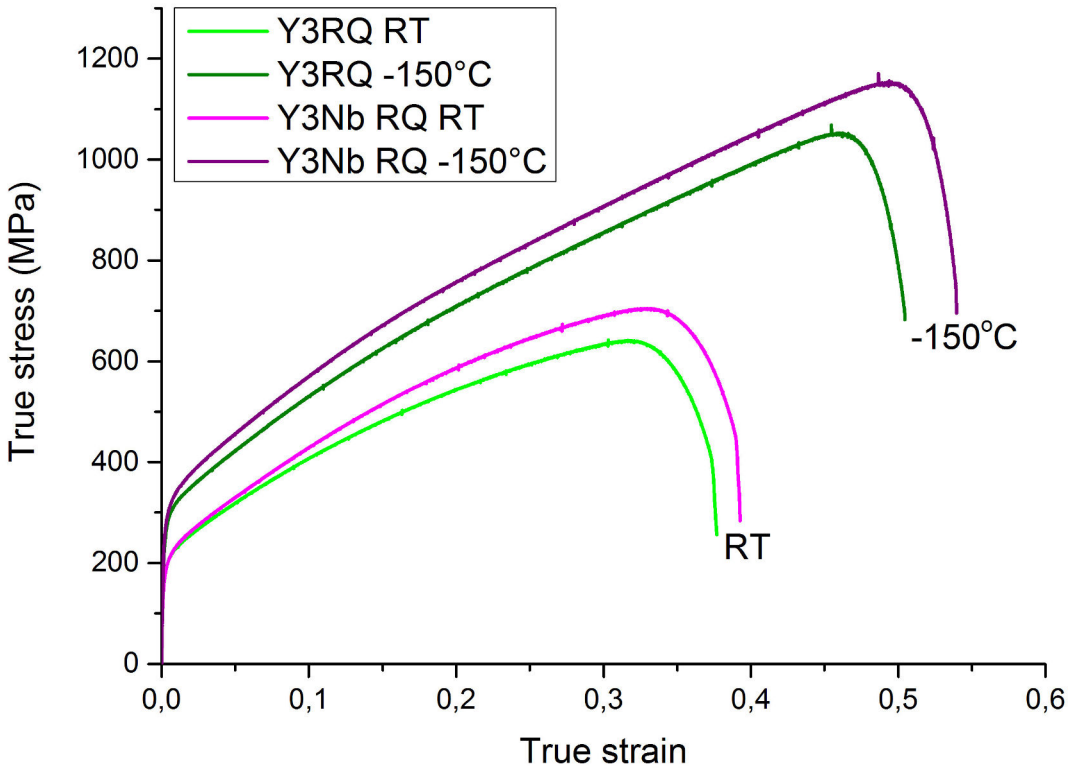

Figure 5.23: *Tensile true stress vs true strain curves for annealed Y3 Co-free alloy, in green, and Y3 Co-free (0.3Nb), in purple. Tests performed at room temperature (RT), brighter curves, and at -150° C, darker curves.*

Table 5.3: *Yield strength (YS), ultimate engineering tensile stress (UTS) and elongation to fracture (El) for annealed Y3 Co-free alloy and annealed Y3 Co-free alloy doped with 0.3 Nb. Tests performed at room temperature and at -150° C.*

Alloy	**Test T** [°C]	**YS** [MPa]	**UTS** [MPa]	**El** [%]
Y3 Co-free	25	207	640	46
	-150	287	1051	66
Y3 Co-free (NbC)	25	272	704	48
	-150	387	1152	72

Beforehand, another encountered difficulty needs to be addressed. Upon observations of samples coming from various places in the forged and annealed rod, a significant difference in grain size was found. Figure 5.24 shows the grain size distribution as a function of position in the rod: closer to the rod extremities, approximately 1/4 from each side of total rod length equal to 45 cm, the grain size was two times larger than in the central part. The average grain size was determined by intercept method based on the SEM BSE images. Representative images for each region are shown in the graph. Such a difference in grain size distribution was not observed in any case of previously described pure Y3 Co-free alloy. It would mean that the

addition of Nb + C promotes this abnormal grain growth. However, the distribution of Nb and C by chemical analyses (infrared absorption) were verified along the ingot prior to forging and after the thermomechanical transformation. No significant discrepancies were found in the macroscopic distribution of those elements. Since chemical analyses did not show any particular segregation of Nb or C, it could be suspected that the elements are present under two distinct forms; on one hand in the solid solution, on the other as precipitates. This in consequence could lead to differences in precipitation fraction between centre and tip of the rod resulting in uneven grain growth.

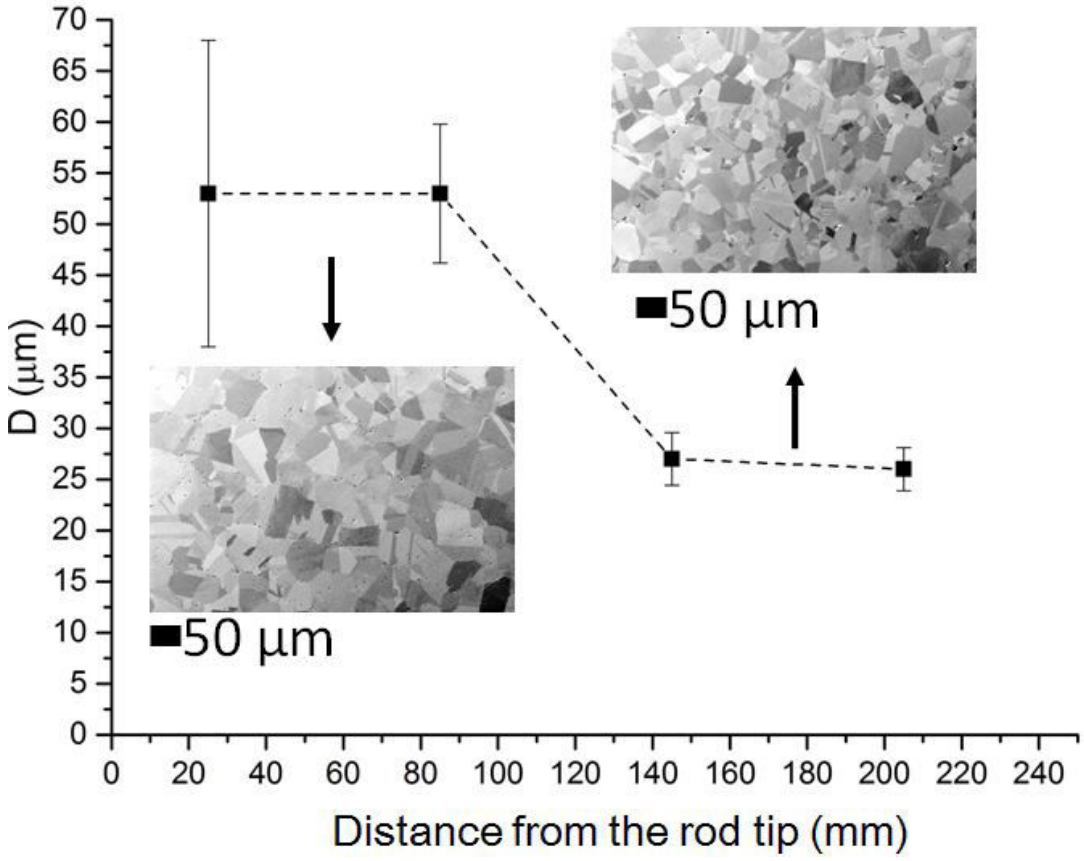

Figure 5.24: *Evolution of grain size as a function of position in the rod of Y3 Co-free (0.3Nb) alloy. SEM BSE representative images of microstructure in each area.*

When analogous cast in APERAM laboratory was prepared, somewhat similar problem was encountered. Upon annealing (1200°C 2h) of a hot rolled sheet of Y3 0.3Nb alloy, an abnormal grain growth was found, as presented in Figure 5.25. In the centre of the sheet the grain size was several times bigger than close to the surface of the sample. Again, content of Nb, C and even N were verified through the sheet thickness to find that no variation is present, just like in the case of forged alloy. A common cause for such abnormal grain growth between forged and rolled samples should be looked for.

Forging and rolling are different processes, yet they have two parameters in com-

mon: first, heterogeneity of temperature through the rod/sheet during deformation, and second, heterogeneity of applied stress. Along hot forging, the rod is held by the extremities, forged on one side than returned and forged on the other side. One can notice that such procedure leads to more stress applied to the centre of the rod as it is hit by the sledgehammer twice as often: once with the first side of the rod than with the second one. It could lead to uneven stress distribution along the rod. At the same time, uneven stress distribution during hot rolling can be observed as well. At the surface, in direct contact with the cylinders, applied stress exceeds the one in the centre of the sheet. Curiously, smaller grain size upon annealing is found in both cases in the areas that were more severely deformed (centre of the rod and surface of the sheet). It could be hypothesized that the distribution of precipitates in the material depends on the total applied stress in those areas. It is a question that would need to be answered for further study of this material. Additionally, variation of temperature during both deformation processes most probably plays an important role as well. However it's influence was not directly correlated with observed microstructures. Understanding the influence of stress and temperature during thermomechanical transformation is necessary if influence of precipitation on microstructural evolution and mechanical properties are to be studied. Unfortunately, due to late coming into sight of this question, it could not have been answered within the time period of this thesis.

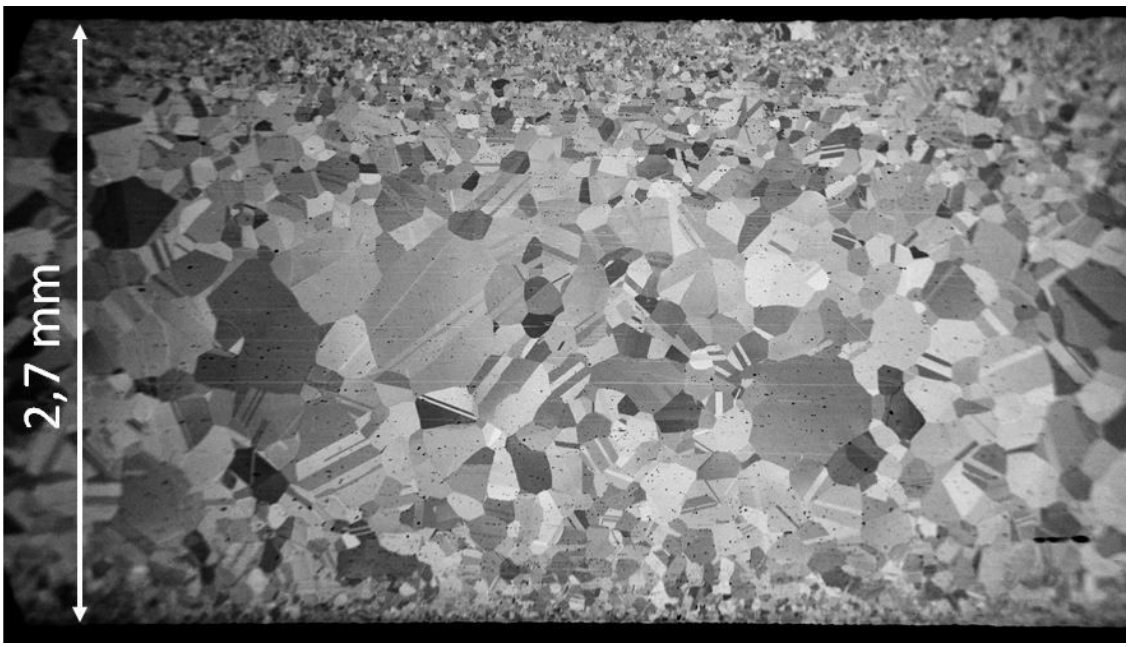

Figure 5.25: *Grain size distribution through a hot rolled and annealed sheet from industrial laboratory cast of Y3 Co-free (0.3Nb), SEM BSE image.*

Nonetheless, the possibility of hardening precipitation on Nb doped alloys was verified, for both 0.1 % and 0.3 % of Nb. Series of heat treatments was done on annealed samples, at temperatures where precipitation should occur according to

equilibrium phase diagram in Figure 5.16. For Y3 0.3Nb composition, two annealing temperatures have been chosen: 930°C and 810°C. Temperatures selected for Y3 0.1Nb were 810°C and 720°C. Various times of heat treatments were applied to the samples, however only few examples of microstructures will be presented here.

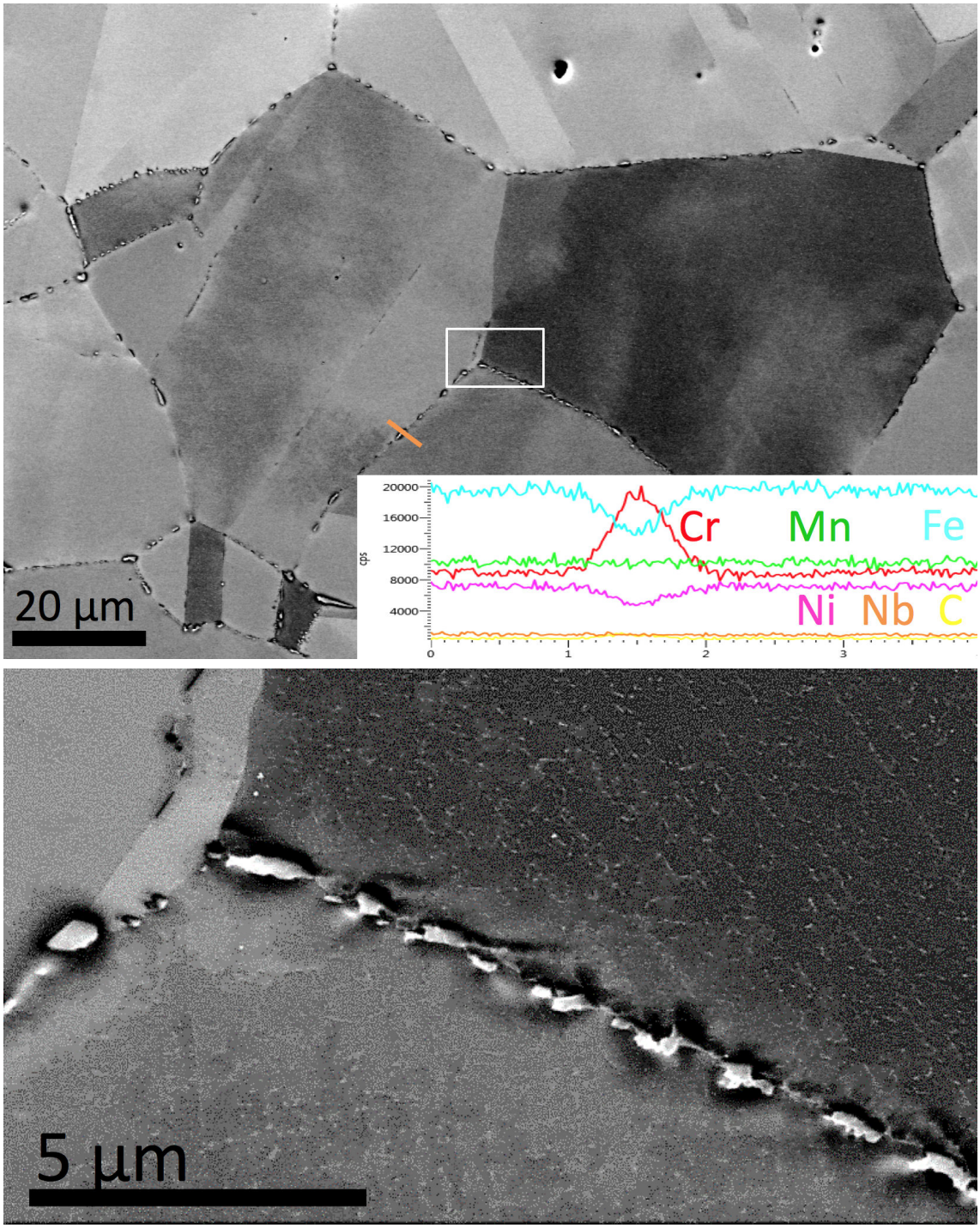

Figure 5.26: *Y3 0.1 Nb after 1 week annealing at 720° C. Visible Cr-rich precipitation at grain boundaries; results of the chemical analysis along the orange line are shown in the bottom right corner. Zoom on the triple point where fine precipitation inside the grains is distinguishable is shown in the bottom picture.*

Firstly, the alloy with lower Nb content annealed at 720°C for 1 week is presented in Figure 5.26a. For this low content of niobium, precipitation of Cr-rich carbides at the grain boundaries is favoured, as the EDX local chemical analyses through such a precipitate, along the orange line, shows a clear increase of Cr content: it is accompanied by a depletion in Fe and Ni. These are most probably the Cr-rich $M_{23}C_6$ type carbides. Yet, their that presence of Cr-rich precipitates is in disagreement with Thermo-Calc predictions. However, with presence of primary NbC precipitates, the matrix composition might be shifted to lower Nb contents, where $Cr_{23}C_6$ carbides are stable. Fortunately, no such precipitation was found in the Nb-rich Y3 Co-free (0.3Nb) alloy. Up to now, the interest in increased Nb content seamed moderate, however this observation of Y3 0.1Nb after precipitation annealing proves the necessity for more niobium in the alloy.

At the same time, even for the Y3 0.1Nb alloy, the possibility of hardening precipitation was seen. A zoom on a triple point in the bottom picture in Figure 5.26a is shown. Apart from big precipitation at the grain boundaries, a fine precipitation inside the grains is distinguishable. Second phase particles of size lesser than 100 nm are visibly aligned along one type of planes. Most probably, as it was shown previously for the *annealed* Y3 Co-free alloy, those are selected {111}-type planes where dislocations density is increased.

Similar behaviour was observed in the Y3 0.3Nb alloy after 2 weeks at 820°C as shown in Figure 5.27a. Again, fine precipitation is observed inside the grains. Here a twin boundary is present and surprisingly NbC particles are present also on this boundary line. Those are still precipitates of quite big size from the precipitation hardening point of view: they have probably little influence on mechanical resistance of the material. However, it has to be reminded that the applied heat treatment was not yet optimised. Observation on the scale of TEM revealed the presence of fine precipitates that can already have the intended impact on materials resistance, as shown in Figure 5.27b on a sample annealed at 920°C 24h. Those observations allowed to confirm that indeed we are dealing with NbC precipitates, as it could have been identified through diffraction pattern analysis shown in Figure 5.27c. Again, those precipitates are far from being of the optimal size, but their presence is a very promising result. It can be expected that with properly adapted heat treatment finer and more efficient precipitation could be obtained. Since niobium atoms are big, it can be suspected that the very fine particles, with size of the order of few tens of nanometres, will form on dislocations lines leading to their immobilisation and consequently enhancement of mechanical properties, as it can be found in austenitic steels [164].

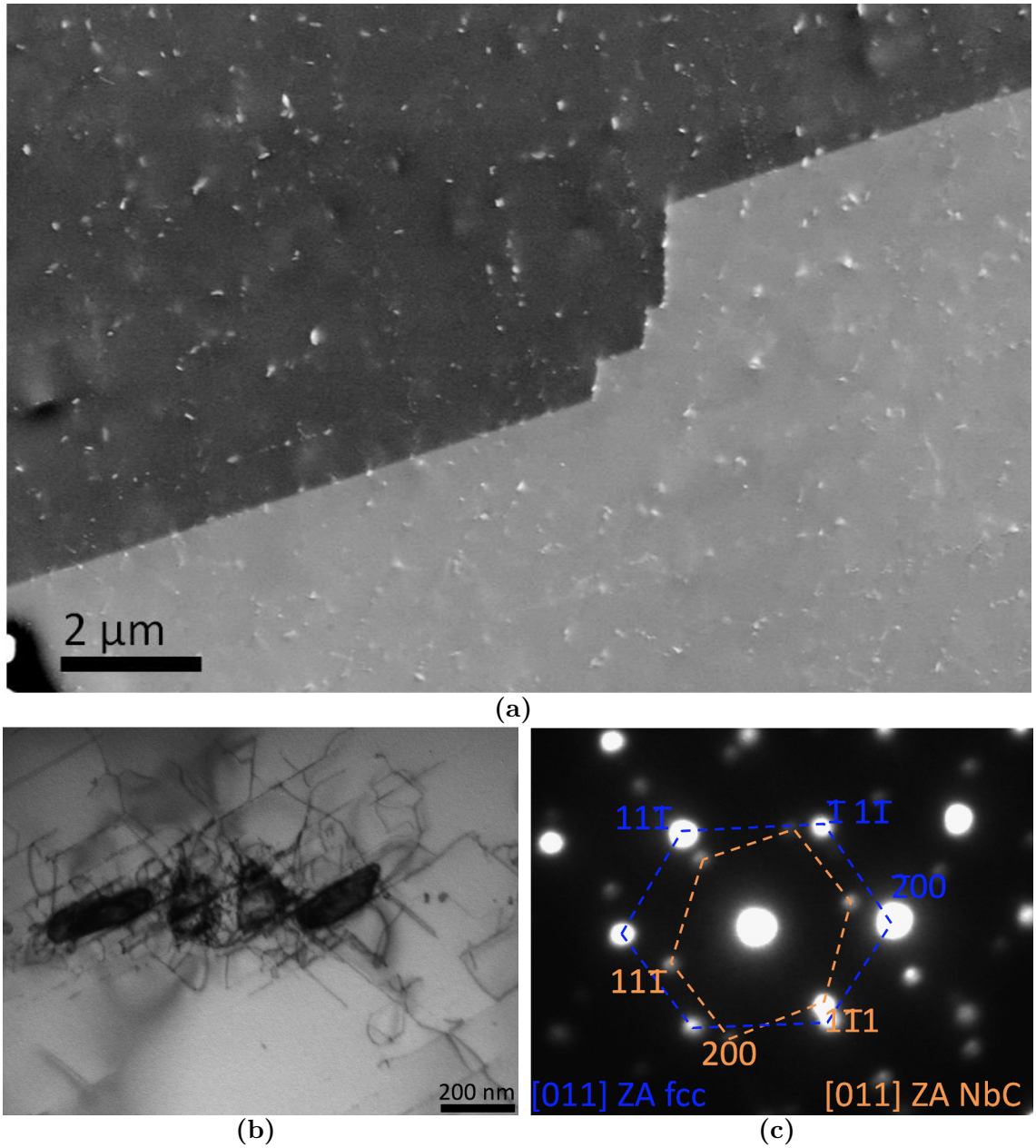

Figure 5.27: *a) Fine precipitation inside a grain and along the twin boundary of Y3 0.3Nb alloy annealed at 810°C for 2 weeks, SEM BSE image; b) precipitates and immobilised dislocations around them in Y3 0.3Nb alloy annealed at 920°C for 24 h, TEM micrograph; c) diffraction diagram of observed area with distinguishable two patterns, one from the fcc matrix (in blue) and one form the NbC precipitates (in orange).*

Even if the heat treatments were not really optimised and no real information is available as to the Nb content in solid solution, an attempt of estimation of efficiency of the hardening effect by NbC has been performed through hardness measurements. However, due to observed variation in grain size through rod length after forging and annealing, the results can not be directly correlated with temperature and time of annealing. Instead, all hardness measurement results are shown as a function of grain size, in a representation similar to classical Hall-Petch analysis, in Figure 5.28. This presentation allows to take into account the variation of grain size that might play a

role in the overall material hardening. All the presented results come from samples after precipitation heat treatments and create a cloud of data points. In general a somewhat higher hardening is found for the same grain size in the 0.1Nb grade than in the 0.3Nb. Anyhow, all cases show increased hardness values as compared to the pure Y3 alloy. The Nb doping allows to add at least 15 HV going up to 50 HV in some cases. Such increase in hardness should correspond to 30 MPa up to 100 MPa gain on the yield strength. It is reasonable to assume that even farther gain is possible without loss of other characteristics like ductility: supplementary presence of fine precipitation will not result in any brittleness knowing that the coarse NbC particles present upon annealing did not lead to any loss of ductility. These promising observations suggest that with proper optimisation of the whole melting process, solution annealing and precipitation heat treatment, significant gain in mechanical resistance can be reached.

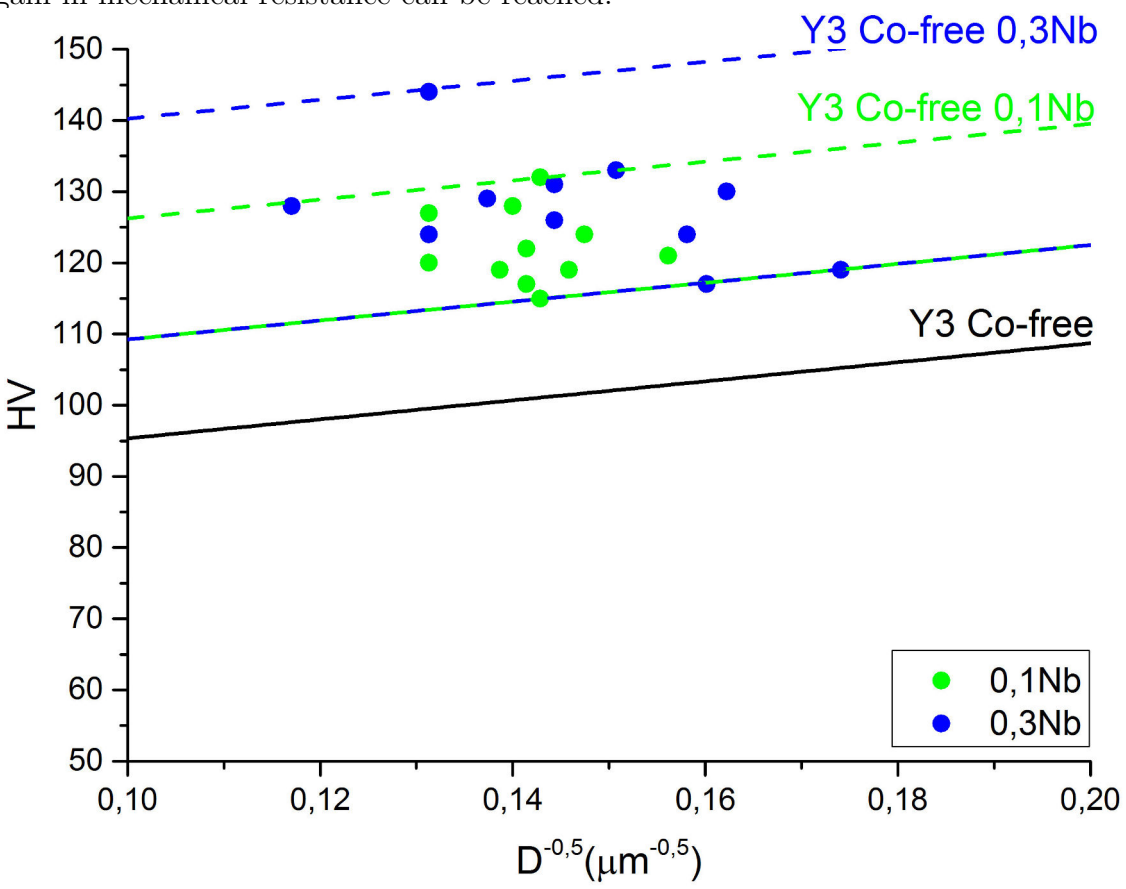

Figure 5.28: *Influence of NbC precipitates on hardness values. Comparison of Y3 Co-free 0.3Nb, Y3 Co-free 0.1Nb with basic Y3 Co-free alloy. All data represented under the form of Hall-Petch relation.*

Despite the difficulties with primary precipitation in the selected Nb doped grades, the possibility of precipitation hardening was shown. Presence of primary NbC was found even though the equilibrium phase diagram predicts solidification into single fcc domain. However, one have to bare in mind that solidification process is far from equilibrium and discrepancies between phase diagram and cast material are to be ex-

pected. Local composition of liquid changes during solidification and consequently, the local equilibrium is altered. Presence of those primary precipitates does not induce any brittleness and does not hinder further thermal or mechanical transformations. Still, sensibility to stress and/or temperature during hot deformation was observed to influence the grain growth upon solution annealing. Nonetheless, fine precipitation could have been obtained and its positive influence of hardness was found with values up to 1,5 times higher than for pure Y3 alloy. Precipitation as a hardening solution of Y3 Co-free composition shows high potential upon further optimisation of technological aspects.

5.5 Partial conclusion

Hardening mechanisms at various scales were analysed in the Y3 Co-free alloy. It was shown via activation volume measurements that forest hardening by dislocations plays a major role in mechanical resistance of the alloy. Influence of solution strengthening was also observed, although it appears as less efficient than in Cantor's alloy. Yet, no new deformation mechanisms were found in the HEAs, as the classical strengthening theory applies.

It was shown that plastic deformation of Y3 alloy follows the Voce law, hence the Kocks-Mecking model of strain hardening can be applied. The analysis of parameters describing both dislocations creation and annihilation allowed to position the Y3 alloy, in terms of strain hardening, among other known fcc materials. As a consequence the stacking fault energy of selected HEA was found to be close to that of Cantor's alloy, 304L steel and pure Ag, which is of the order of 20-30 mJ/m^2.

Efficiency of grain boundaries hardening could have been estimated through Hall-Petch relation. It was found that grain boundaries play lesser role in hardening of Y3 alloy as compared to other HEAs from Cantor's family or the 316L stainless steel. However, with this approach, the efficiency of forest hardening by dislocations could have been proved. Comparison of intrinsic hardness of *as forged* and *annealed* states confirmed that the enhanced mechanical resistance of the material is in agreement with the increase of dislocation density.

An attempt of material strengthening through secondary precipitation was done. Two compositions containing niobium and doped with 200 ppm carbon were designed based on thermodynamic calculations and later produced. Despite technological difficulties, namely: presence of primary precipitation even upon solution annealing both with abnormal grain growth, the efficiency of hardening was shown. A number of promising results obtained through hardness measurements indicate potential improvement of mechanical resistance of Y3 alloy thanks to NbC precipitation, once the technological route is optimised.

Conclusions and Perspectives

Presented thesis study focused on design and optimisation of new high entropy alloys (HEAs) from Cantor's CoCrFeMnNi family, with decreased content of cobalt. The aim was to propose new grades with high mechanical resistance lowering or eliminating presence of this strategic element. To achieve this goal, an in-depth analysis of microstructure correlated with mechanical properties and strengthening mechanisms was performed.

A successful design of three new alloys was accomplished through thermodynamic calculations (Thermo-Calc). Based on the so obtained phase diagrams, promising compositions, showing large fcc domain and suppressed secondary phase formation, were selected. Their feasibility in both academic and industrial conditions was verified with a favourable outcome. Thermo-Calc simulations proved to be accurate at high temperatures, however at lower temperatures (500°C) prolonged heat treatments of few hundred days showed formation of unpredicted phases. Presence of MnNi-rich phase and FeCr-rich phase next to the matrix was observed as opposed to predicted σ phase. Nonetheless, Thermo-Calc stays a good tool as a first approach to material design.

So designed alloys showed single fcc phased structure and good mechanical properties in the *as forged* state with yield strength in the range of 480 - 640 MPa at room temperature. None of the materials showed signs of martensitic transformation upon deformation at low temperatures, keeping the amagnetic, single phased character. First evaluation of mechanical properties allowed to choose the most promising grade among so-designed HEAs and to narrow down the study to the Co-free alloy, the so called Y3 grade. Despite the lowest mechanical resistance of Y3 alloy as compared to other preselected grades, the absence of cobalt in its composition ruled in its favour. Let us note that the behaviour typical for alloys from Cantor's family, in explicit simultaneous increase of yield strength and elongation to fracture, was also maintained in the selected Y3 Co-free alloy.

Microstructural description at various scales was performed and correlated with mechanical properties. Two mechanical regimes were distinguished: first, the regime with high yield strength and low work hardening coefficient; second, the regime with low yield strength and high work hardening coefficient. Those observations are in

agreement with what was reported in the A3S composition, previously developed in EMSE. It was found that a nano-sized substructure, obtained upon forging, is at the origin of elevated mechanical resistance in the first regime. Annealing at temperatures above 600°C lead to reorganisation of dislocation structure and change in mechanical behaviour's regime.

Dislocations density was found to be unusually elevated in all observed states. Their values are as high as 10^{14} m^{-2} after forging and only one order of magnitude lower, 10^{13} m^{-2}, after casting or after annealing at high temperature (1000°C). Such elevated dislocations density even after annealing is surprising, specially that proofs of grain growth were found. The phenomenon of recrystallisation in the selected material was hence undermined. However a study focusing on evidence of nucleation upon annealing, allowed to confirm that indeed, the recrystallisation does take place after heat treatments at high temperatures. First signs of recrystallisation were found at 0.57 melting temperature; however, the time necessary for the microstructural evolution was very long (48 hours for partial recrystallisation). Such long annealing time, together with high purity of the material, lead us to estimate that standard recrystallisation conditions (one hour for fully recrystallised microstructure) will correspond to temperatures much higher than that. Even though the temperature of recrystallisation is somewhat increased as compared to those of classical materials, the kinetics are very low and in the end the dislocations density is not decreased. The dislocations seam to be easily formed and stable in the Y3 alloy. The question concerning the reasons of their high density and stability, still needs to be answered.

Analysis of hardening mechanisms showed that the same strengthening processes as in classical fcc materials are present: forest hardening through dislocations and solid solution strengthening were shown to be active in the analysed composition. Those phenomena do not change even at low temperatures. Successful application of Kock-Mecking model of strain hardening theory, shows that the Y3 alloy does not deviate from other known fcc materials. The same laws abide and no new phenomena specific to HEAs are found. That is why positioning of Y3 alloy among other fcc metals allowed to estimate its stacking fault energy at the same level as Cantor's alloy or 304L stainless steel with low SFE. Contrarily to A3S, Cantor's alloy or 316L steel, little efficiency of grain boundaries hardening was found. However, the comparison was made here between materials with different levels of purity. Surely absence of interstitial atoms in the Y3 alloys matrix, decreases its resistance as well as the efficiency of hardening through grain boundaries in the material. At the same time, dislocations hardening was shown to be highly efficient, dislocations are easily formed and their presence does not decrease the ductility of the material. Consequently, use of Y3 alloy in the *as forged*, work hardened, state could be considered in the future.

Hardening through secondary precipitation of NbC was proposed and verified. Two compositions based on Y3 Co-free grade, alloyed with niobium and doped with carbon were designed through thermodynamic simulations. Unfortunately, out of equilibrium solidification conditions lead to the presence of primary precipitates upon casting. Attempts of dissolution of those precipitates have been conducted with minor efficiency. Yet, since presence of these primary precipitates have little impact from the mechanical point of view (no loss of ductility), an attempt to obtain fine precipitation was done. It could have been shown that obtained second phase lead to material hardening, with a gain of the order of 15-50 HV corresponding to a possible gain of 30-100 MPa on yield strength, even if the precipitation conditions could not be optimised. This promising route needs to be further explored: once the technological process improved the material strengthening though secondary phases shows high potential.

This work brings some new insights to the HEAs design, still several questions remain open.

One of the most surprising aspects found in the alloys developed recently, the A3S and Y3 alloys, is the elevated dislocations density. The origin of their presence is still unknown. Yet, dislocations play a significant role in defining the mechanical properties. The need to understand their stability could be satisfied through atomistic calculations. Simulations of energetically favourable conditions for dislocations formation through atomic neighbourhood of the dislocations, should bring some insight as to their favourable presence in the material

Strengthening mechanisms in the Y3 alloy have been found to be classical ones allowing us to assume their additive character. Optimisation of mechanical properties can be thus done on various levels involving them all. In particular, strain hardening, could be a highly efficient source of material strengthening.

Hardening through second phase was shown to be a promising route to follow; it can influence the properties not only at the level of dislocations motion but also through grain size control. Encountered difficulties like segregation and primary precipitation should be addressed. To avoid this type of precipitation, modification of chemical composition could be considered. Further optimisation through thermodynamic simulations, so alloys design, is necessary.

Finally, the results obtained within this PhD thesis, even though interesting and with potential, are only the first step in development of Y series of alloys. Numerous other characteristics should be verified and optimised to aim genuine applications.

Appendix 1: Relaxation curves analysis

Definition of activation volume was done based on relaxation tests, according to the method developed by Spatig et al. [91]. In this approach a series of five repeated stress relaxations during tensile test is done. The time span, Δt, of each relaxation is constant, as presented in Figure 2.4. The apparent activation volume is considered to be constant during the load relaxation test that must be analysed over "short duration". In the case of this study the Δt was set at 30s.

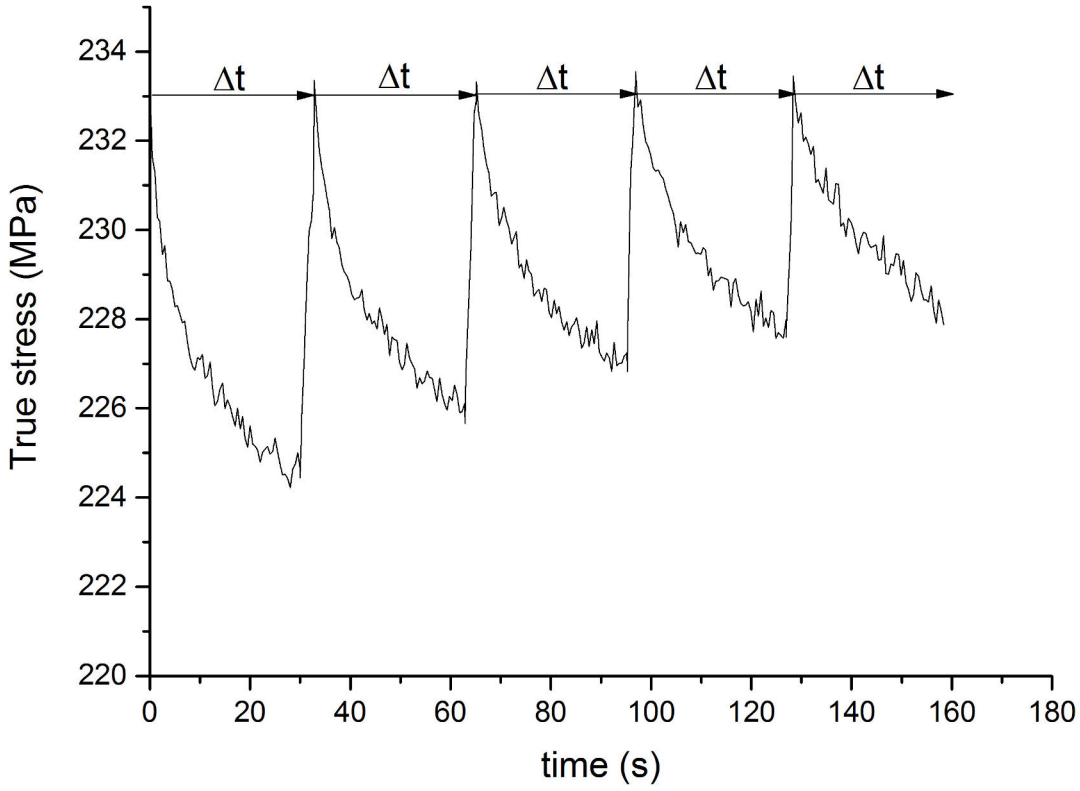

Figure 1: *An example of a series of five repeated stress relaxations during tensile test for a given stress value (233 MPa in this case), time span Δt = 30s.*

Drop of true stress, $\Delta\sigma$, during all relaxations is determined and can be represented as in Figure 2. It can be easily noted that for each consecutive relaxation the drop is lesser, which is due to lesser impact of strain hardening.

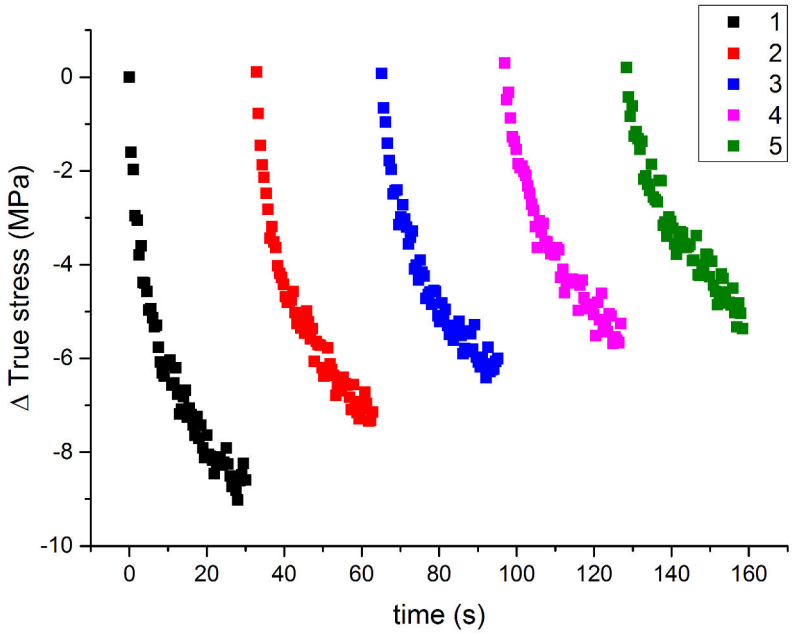

Figure 2: *Example of stress drops measured during one set of repeated relaxations.*

To define the apparent activation volume, V_{app}, first relaxation curve is taken into consideration. It is fitted according to equation 1, where M is the Taylor factor ($\sim$ 3), k is the Boltzman constant, T is the test temperature, t is the time of relaxation (30s) and c is an integration constant (dependant on the elastic modulus of the machine–specimen assembly and the plastic strain rate at the start of the load relaxation test). The value of V_{app} is then calculated for the parameter $A = MkT/V_{app}$.

$$\Delta\sigma = -\frac{MkT}{V_{app}} ln\left(1 + \frac{t}{c}\right) \Rightarrow V_{app} = \frac{A}{MkT} \tag{1}$$

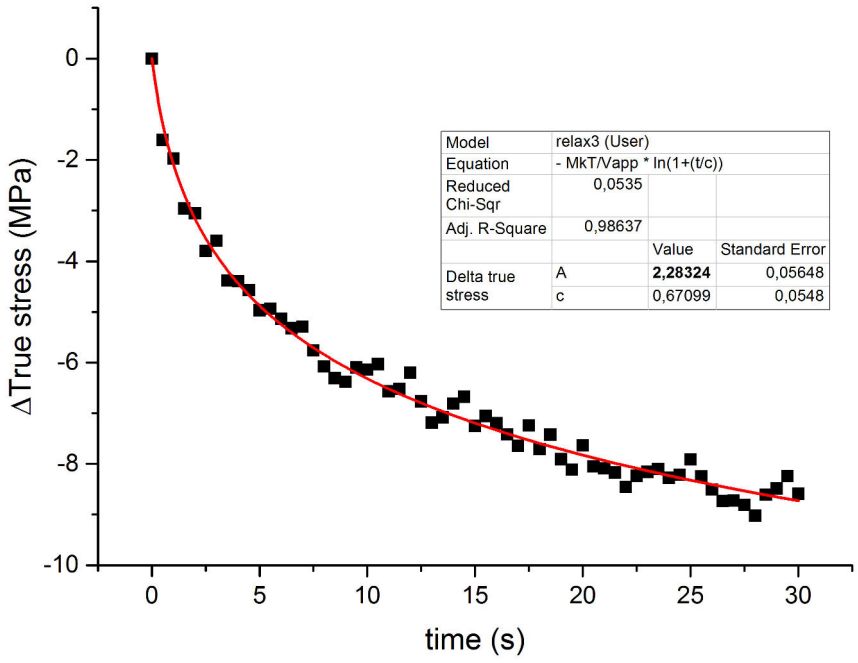

Figure 3: *Fit performed on the first relaxation curve of the series allowing to define the apparent activation volume V_{app} according to equation 1.*

The apparent activation volume is burdened with the error of strain hardening occurring during tensile test. Relationship between physical and apparent activation volumes can be described by equation 2, where where Θ is, the work-hardening rate ($d\sigma/d\varepsilon$) and S is the elastic modulus of the machine–specimen assembly.

$$V_{app} = V\left(1 + \frac{\Theta}{S}\right) = V + V_h \tag{2}$$

To access the physical activation volume V, the work-hardening term V_h needs to be determined. It is the subsequent four relaxations that allow it. Spatig et al. [91] showed that V_h is related to successive stress drops following the equation 3, where n is the number of load relaxations, σ_1 and σ_n are the stress drops in the first and n^{th} load relaxation, respectively, and the average stress drop $\bar{\Delta\sigma}$ is given by equation 4.

$$(n-1)\,V_h = \frac{MkT}{\bar{\Delta\sigma}} ln\left(\frac{exp\left(-\frac{\Delta\sigma_n V_{app}}{MkT}\right) - 1}{exp\left(-\frac{\Delta\sigma_1 V_{app}}{MkT}\right) - 1}\right) \tag{3}$$

$$\bar{\Delta\sigma} = \frac{1}{n}\sum_n \Delta\sigma_n \tag{4}$$

If the right hand side of the equation 3 is plotted as a function of number of relaxation, n, a linear regression is obtained as shown in Figure 4. The slope of this line represents the work-hardening term V_h, that can be further introduced into equation 2. Hence the efficient activation volume can be obtained.

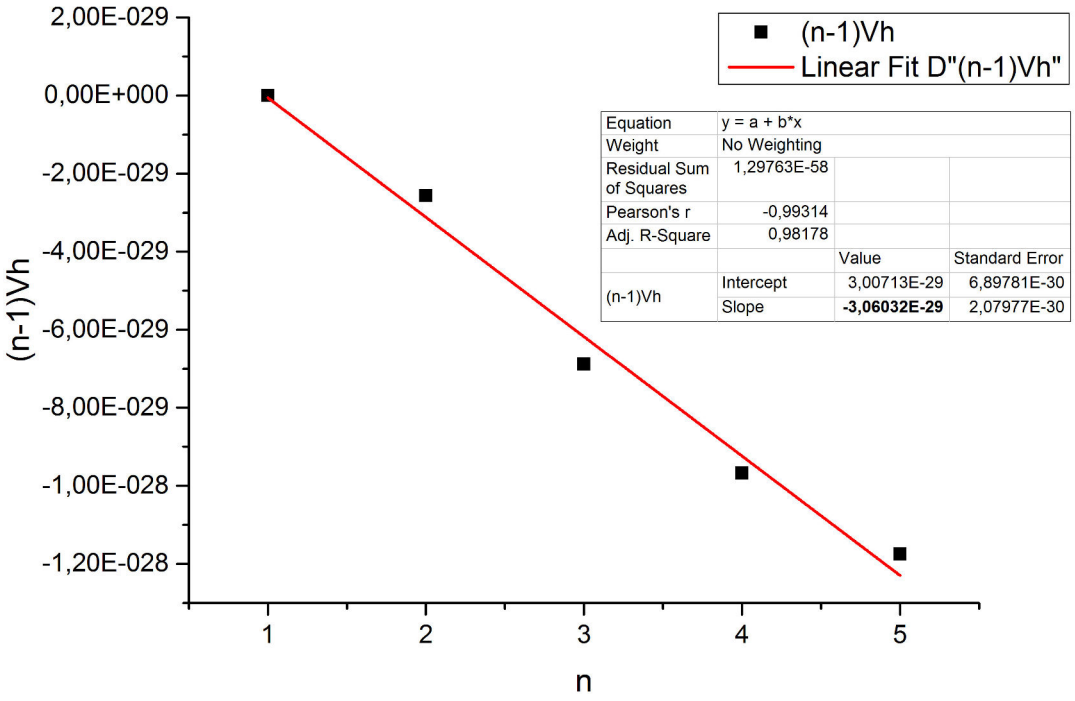

Figure 4: *Linear fit of (n-1)V_h, right side of the equation 3, for a series of five relaxations in one set.*

Such study was performed by Laplanche et al. [22] on the Cantor's alloy. Results obtained on the same composition, the equiatomic CoCrFeMnNi, coming from this publication and this thesis are compared in Figure 5. Similar values for both experimental sets are obtained. It validates the experimental setup put together at EMSE, allowing further sturdy on Y3 alloy and comparison of all results.

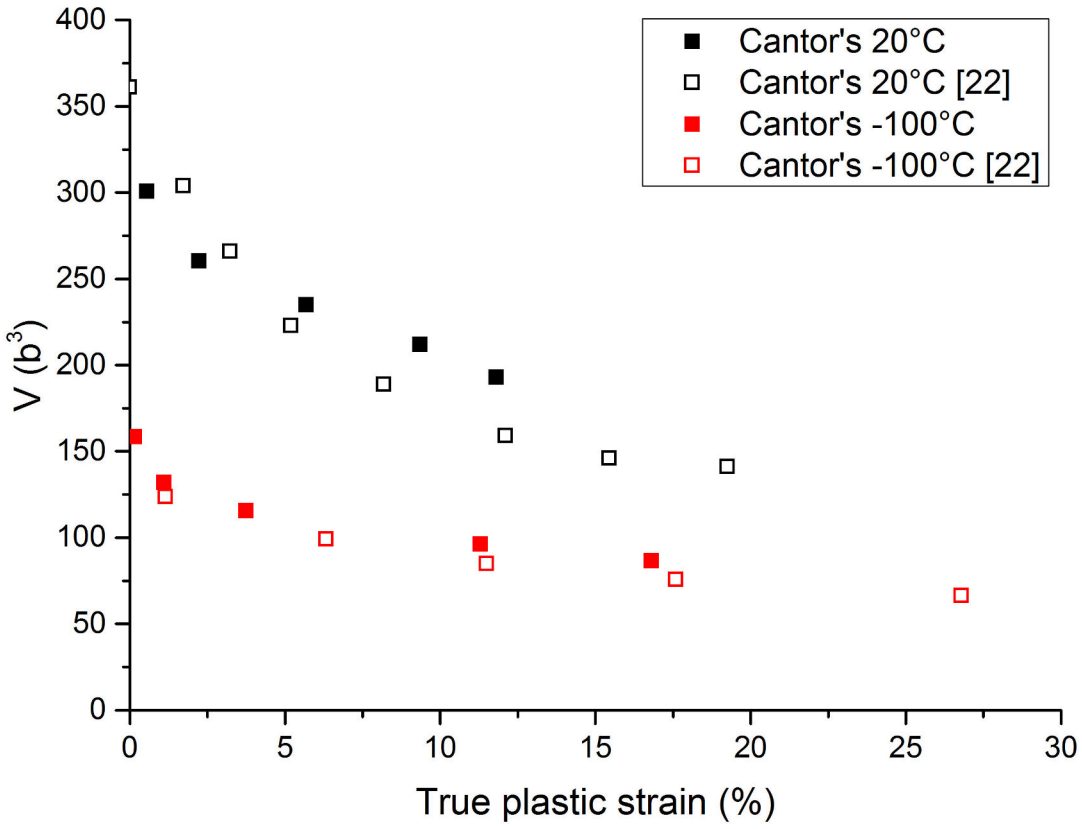

Figure 5: *Comparison between activation volumes for Cantor's alloy obtained at EMSE (full symbols) and by Laplanche et al. [22] (empty symbols).*

Appendix 2: Data analysis for Kocks-Mecking model

All data implemented in the Kock-Mecking model was treated according to the following procedure. Strain and stress were defined as shown in Chapter 2.4.2. Afterwards the Young modulus E was defines from the linear fit in the elastic part, as shown in Figure 1. The slope of this fit gives us the value of E. It is further used to define the plastic part of the curve according to equation 1, where elastic part is deducted from the totality.

$$\varepsilon_p = \varepsilon - \frac{\sigma}{E} \tag{1}$$

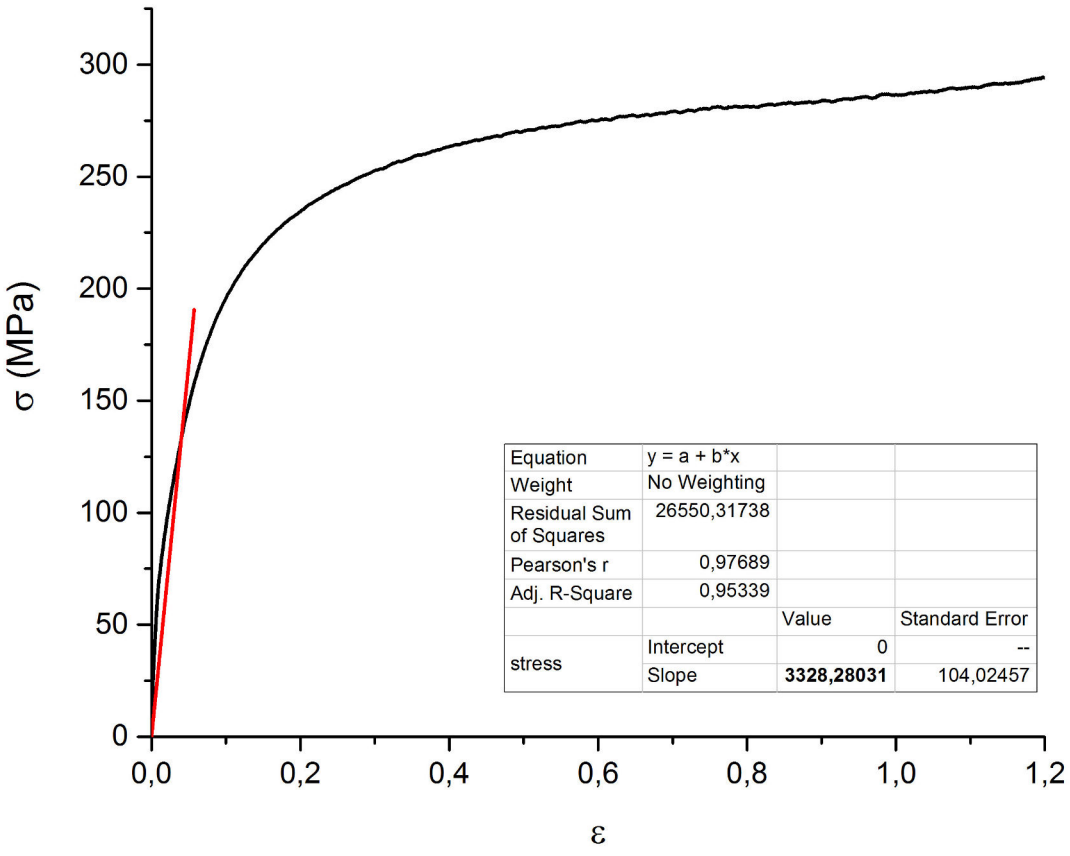

Figure 1: *Definition of Young modulus on a stress - strain curve of a compression test, example based on a test at 850° C.*

Next steps are performed only on the plastic part of the curve that is presented in Figure 2. This part is next smoothed to eliminate excessive noise from to high number of points. The smooth is made by normalising the step between strain points, in explicit, instead of taking all measurements points only those every 0.01 are kept. Comparison of measured and smoothed curves is shown in the same figure. Good correlation is found, showing that no information is lost upon smoothing process.

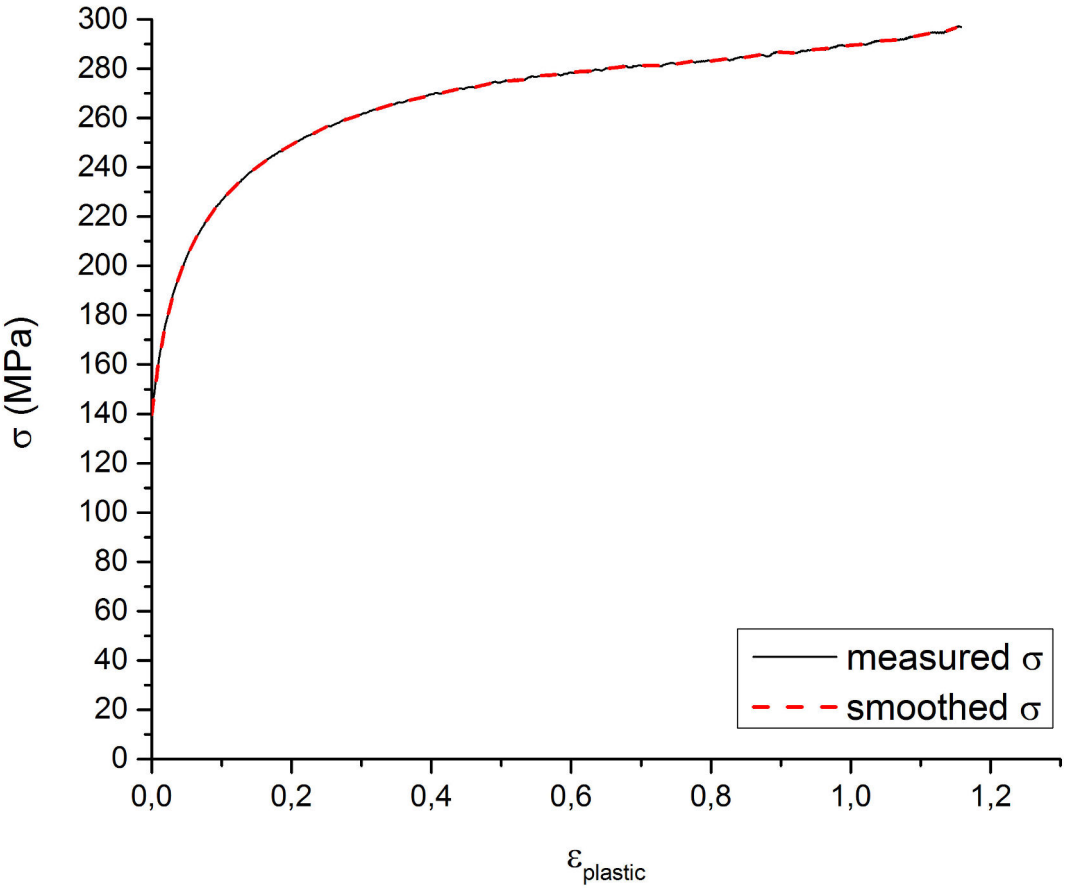

Figure 2: *Plastic part of a compression curve. Comparison between measured stress and smoothed one.*

First derivative of stress is calculated in respect to strain and is called theta, $\theta = d\sigma/d\varepsilon$. The obtained values are plotted firstly as a function of strain as shown in Figure 3. Such plot can give information about activation of additional deformation mechanisms during mechanical test, it is a common way to look for significant twinning in TWIP alloys. The presented curve shows still presence of some noise. Such form was found for all analysed curves and can be treated as a representative one.

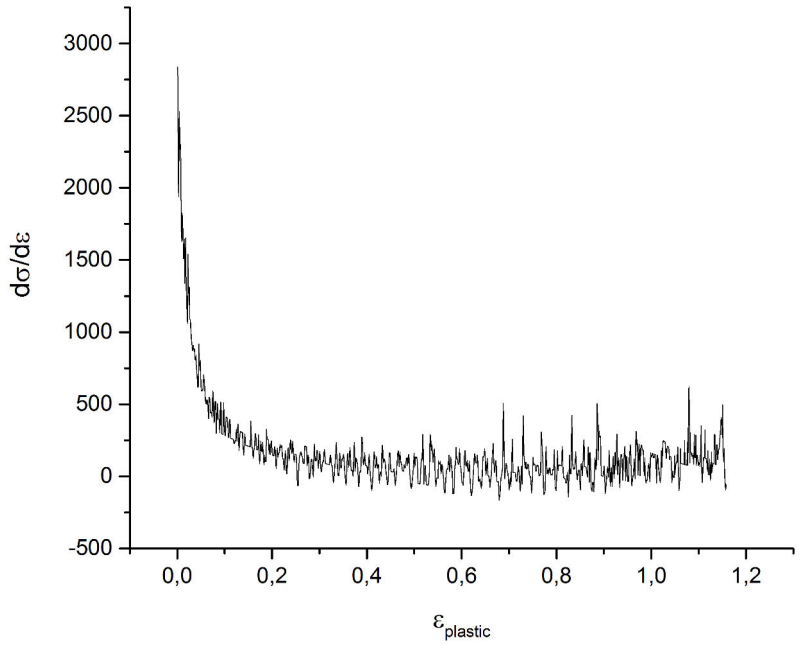

Figure 3: *Theta as a function of strain.*

Secondly, θ was plotted as a function of stress, which is presented in Figure 4. This graph allows to obtain the $theta_0$ and σ_V parameters necessary for Kocks-Mecking model. Those two parameters can be found by fitting and extrapolating the linear region, as marked by red line in the figure. Firstly, θ_0 corresponds to the θ value for $\sigma = 0$. Secondly, the Voce stress σ_V is the value at the intercept of the linear fit with the abscissa, for $\theta = 0$.

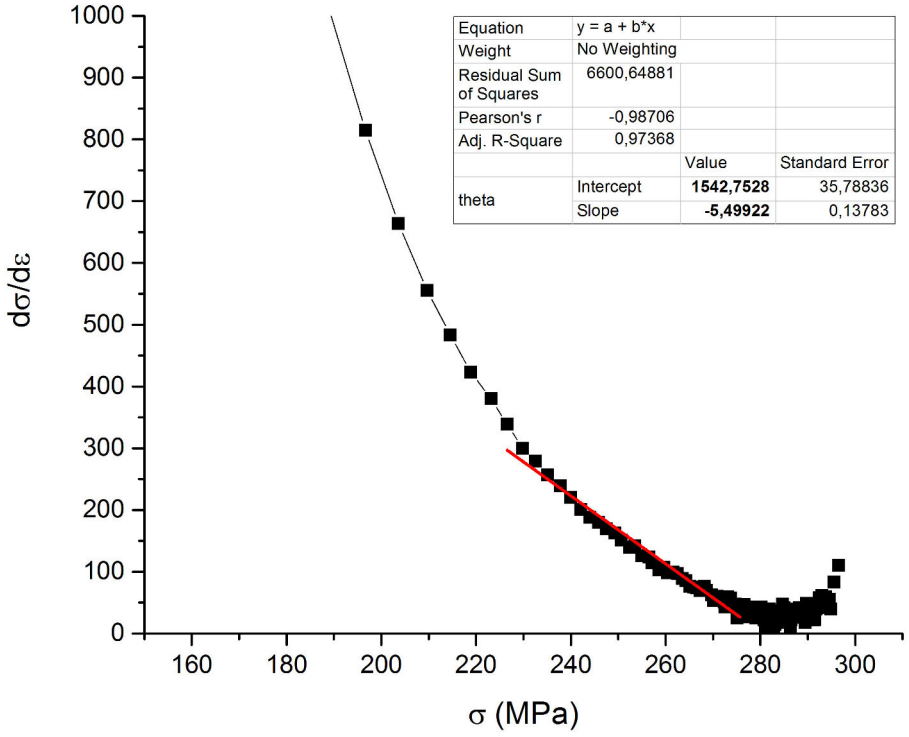

Figure 4: *Theta as a function of stress, with a fit in the linear part (red line).*

Parameters obtained this way were further analysed according to Kocks-Mecking model, as shown in Chapter 5.2.

Appendix 3: Summaries in French

Chapitre 1: Nouvelle génération d'alliages métalliques: les alliages à forte entropie

Le concept d'alliage à haute entropie, *high entropy alloys HEA*, a été introduit en 2004 par Yeh [1] et Cantor [4]. Yeh formule l'hypothèse que l'entropie de mélange est maximale lorsque les éléments d'alliage sont introduits en proportions atomiques similaires. L'existence d'un alliage équiatomique à cinq éléments monophasé CoCrFeMnNi est attribuée à cette haute entropie de mélange. La famille des alliages à haute entropie est créée, regroupant par définition les alliages multi-éléments en haute concentration, formant une solution solide unique. Toutefois, au cours du développement des HEA, certains alliages multi-phasés à haut intérêt scientifique ont été découvert. Ces alliages sont regroupés sous l'appellation d'alliages complexes concentrés, *complex concentrated alloys, CCA*. Les définitions des HEA et CCA sont aujourd'hui couramment employées pour distinguer les alliages à haute entropie de mélange monophasés et multi-phasés [6].

Yeh [7] attribue les propriétés physiques des HEA aux quatre *"core effects"*. Tout d'abord, l'effet d'entropie de mélange conduit à un abaissement de l'énergie de Gibbs de l'alliage, et donc à la stabilisation de la solution solide. Cet effet est relié aux concentrations importantes en éléments d'alliage [8]. Cependant, l'effet d'entropie de mélange s'est révélée non prédominant au regard d'autres effets d'entropie mais aussi d'enthalpie [6]. Ensuite, un ralentissement de la diffusion atomique dans les HEA est suspecté, à l'issue d'observations d'évolutions microstructurales plus lentes dans ces alliages que dans les alliages classiques [17]. Cette hypothèse, bien que non-validée à l'heure actuelle, pourrait être à l'origine de certaines propriétés physiques exacerbées des HEA, tel qu'une meilleure stabilité de phases, ou une résistance améliorée au fluage et à l'irradiation. Comme troisième effet, l'hypothèse de distorsion de la maille cristalline est aussi envisagée. Ce phénomène pourrait en effet être à l'origine de certaines observations inattendues sur ces matériaux, tel qu'un durcissement par les joints de grain plus efficace [18], ou une perte d'intensité des pics de diffraction aux rayons X [21]. Enfin, l'effet cocktail, dû à la présence d'éléments de natures différentes au sein de l'alliage, conduit à un écart à la loi des mélanges [27]. Cet

effet, bien qu'exacerbé dans le cas des HEA, est aussi observable dans les alliages classiques.

Le nombre très élevé de compositions possibles pour l'obtention de HEA rend nécessaire la mise en place de critères pour la formation d'une phase solide. Ces critères, couramment utilisés en métallurgie, ont été appliqués aux alliages à forte entropie sur la base des HEA connus. Les critères thermodynamiques définissent des valeurs limites d'entropie et d'enthalpie de mélange pour l'obtention d'une phase solide [31,32,35]. Les critères relatifs à la physique de la matière, tel que les valeurs du rayon atomique, éléctronegativité, configuration électronique, sont basés sur les règles de Hume-Rothery [30]. Ces critères, purement empiriques, suggèrent un intervalle de confiance et non des limites strictes [30, 31, 35, 36]. Ces critères sont appliqués au design d'alliages à haute entropie, avec deux approches possibles. Une approche purement thermodynamique est employée dans la méthode CALPHAD, qui permet de simuler les diagrammes de phases. Il s'agit de la méthode la plus couramment utilisée pour les alliages classiques [8,45,46,50]. Une approche probabiliste de l'obtention d'une phase solide a été mise en place par Tancret [51]. Cette méthode prend en compte l'ensemble des paramètres thermodynamiques et des paramètres relevant de la physique des atomes. Elle attribue à ces paramètres un poids statistique, basé sur leur fiabilité dans l'obtention des HEA connus.

Les HEA déjà identifiés ont été repartis en familles, en fonction de leurs éléments constituants [6]. Les deux familles les plus étudiées et les plus prometteuses à l'heure actuelle sont la famille des HEA élaborés à partir des métaux de transition 3d [18, 22, 23, 72–85], et la famille des HEA réfractaires [6, 29, 52–60]. Les HEA de transition 3d sont proches des aciers austénitiques en termes de structure et de propriétés mécaniques. Les HEA réfractaires sont surtout développés en vue de remplacement des superalliages base nickel, par leur microstructure et leur propriétés mécaniques à haute température. Bien que moins étudiées, les autres familles des HEA peuvent offrir une réponse à des demandes ciblées. Cependant, malgré l'intérêt indéniable et grandissant de ce groupe des matériaux, l'ensemble des HEA nécessite encore de grands efforts d'optimisation et de développement afin de concurrencer les alliages classiques.

Les alliages à haute entropie les plus étudiés sont les alliages de la famille CoCrFeMnNi. L'alliage $Co_{20}Cr_{20}Fe_{20}Mn_{20}Ni_{20}$ équiatomique est nommé *alliage de Cantor*, du nom de Brian Cantor qui l'a découvert en 1981 [4]. Cet alliage est monophasé austénitique et son comportement mécanique ne se conforme pas aux lois de la métallurgie classique [18, 22, 23, 72–85]. Notamment, la résistance mécanique et la ductilité de l'alliage de Cantor augmentent simultanément lorsque la température est abaissée dans le domaine cryogénique [72]. Malgré une structure similaire aux aciers austénitiques, cet alliage leur présente des propriétés mécaniques supérieures.

Il a notamment été observé dans cet alliage une facilitation de la formation des nanostructures [115], une meilleure efficacité du durcissement par les joints de grains [18], ou encore une résistance à l'irradiation améliorée [126] par rapport aux aciers austénitiques couramment employés, tels que le 304L et le 316L.

Les "*core effects*" présents dans l'alliage de Cantor, en particulier la diffusion ralentie et la distorsion de la maille cristalline, sont probablement à l'origine de certaines de ces différences de comportement mécanique. Des études réalisées à l'échelle nano-scopique ont révélé une facilité de création et d'annihilation des fautes d'empilement, ainsi qu'une aptitude au nano-maclage. Ces observations ont été reliées, par mesures et par simulations, à une énergie de faute d'empilement basse, entre 20 et 30 mJ/m^2 [77, 88, 89]. Par ailleurs, la densité de dislocation élevée dans ce matériau, de l'ordre de 10^{13} à 10^{14} m^{-2} [22, 115], a été attribuée à la stabilité des dislocations. Un ordre atomique à courte distance dans l'environnement proche des dislocations est suspecté, ce qui pourrait avoir un effet stabilisant. Toutefois, les mécanismes de déformation observés dans l'alliage de Cantor, par glissement de dislocations et maclage, ne présentent pas de singularité par rapport aux mécanismes observés dans les phases cfc classiques [10, 22, 82, 92, 97]. De même, la structure de recristallisation est proche de celle des autres alliages cfc, notamment par la présence de macles de recristallisation [18, 103, 106, 150].

Certains essais de recristallisation ont conduit à la formation d'une ou plusieurs phases secondaires [17, 111–115]. La formation de ces phases est accélérée par la déformation sévère à froid préalable à la recristallisation. Les phases secondaires observées sont une phase σ, une phase cc riche en Cr, une phase $L1_0$ riche en MnNi, et une phase B2 riche en FeCo. La présence d'une ou plusieurs de ces phases dépend de la température de recuit. Toutefois, la cinétique de décomposition de ces phases est faible, leur formation n'étant possible que pour des températures de recuit inférieures à 800°C [115].

Sur la base de l'alliage de Cantor, d'autres nuances on été développées, en faisant varier les proportions du mélange [87, 115], ou en y ajoutant des éléments [34, 44, 70, 95, 116–123, 123, 127–131]. Des nuances multiphasées ont été obtenues par ajout d'éléments permettant un renforcement par précipitation d'une phase secondaire. L'élément le plus fréquemment ajouté est l'aluminium, qui en plus de précipiter sous la forme d'une phase durcissante, permet aussi d'alléger le matériau [44, 70, 116–118, 120, 121]. Des précipités durcissants ont aussi été obtenus suite à l'ajout de V, Nb, Mo, Cu, Ta ou encore W. A l'image des aciers TRIP [132–134], une augmentation de la teneur en manganèse rend l'alliage susceptible à une transformation martensitique sous contrainte [124]. Une diminution de la teneur en chrome et en manganèse dans l'alliage de Cantor a conduit au design de nuances monophasées dont la résistance mécanique est augmentée par formation d'une sous-structure nanométrique [115].

Ces différentes nuances ouvrent aux HEA la possibilité de concurrencer les aciers austénitiques à haute valeur ajoutée. Dans cette optique, le domaine nucléaire peut être un marché propice à l'emploi des HEAs. Cependant, la présence de cobalt dans les alliages de la famille Cantor est rédhibitoire à son utilisation en milieu radioactif [125]. À l'heure actuelle, l'élimination du Co dans les HEAs est encore peu étudiée [126]. Affin de conserver une structure monophasée en l'absence de Co, il est nécessaire de diminuer la teneur en Cr, ce qui résulte en un écart à l'équi-atomicité du mélange. Un exemple d'une telle nuance, exempt de Co, affiche une bonne résistance à l'irradiation, rendant envisageable le développement de ces matériaux.

Le travail de la thèse ici présentée s'inscrit dans cette démarche, au travers de développement de nuances à teneur en Co faible ou nulle. Affin de garantir et d'améliorer les propriétés mécaniques de ces alliages, une compréhension approfondie des mécanismes régissant la stabilité de phase, la recristallisation et le comportement des dislocations a été nécessaire.

Chapitres 2: Méthodes et procédures

Les méthodes expérimentales utilisées sont décrites en précisant les conditions de travail. Les détailles d'utilisation de logiciel de calculs thermodynamique, Thermo-Calc, sont précisés. Pour l'analyse microstructurale, les paramètres des techniques comme microscopie optique, microscopie électronique en balayage, EBSD ou encore microscopie électronique en transmission sont présentés. Les moyens d'essais mécaniques sont décrits: testes de dureté, de compression ou traction.

Chapitre 3: Sélection et première évaluation de nouvelles nuances HEA

Une nouvelle nuance HEA, exempte de Co, a été recherchée. Sa composition a été établie au travers de calculs thermodynamiques permettant la simulation de diagrammes de phases. Le logiciel Thermo-Calc et les bases de données associées ont été employés; pour la majorité des calculs la base fer TCFE5 a été choisie. L'analyse de ces diagrammes de phases a permis de sélectionner trois compositions, au travers de critères définis au préalable. Nous avons tout d'abord recherché un large domaine de stabilité de la phase cfc monophasée, ce domaine devrait s'étendre aux températures les plus basses possibles ($< 600°C$). Une absence de phases secondaires, en particulier la phase σ, est souhaitée. À minima, la formation des phases secondaires doit être limité à de températures basses, afin de diminuer la force motrice pour la

précipitation basée sur des phénomènes diffusifs. Enfin, une teneur en chrome suffisamment importante ($> 15\%$) pour garantir la résistance à l'oxydation est requise.

La composition de départ est la nuance CrFeMnNi équiatomique. Par la suite, les proportions du mélange ont été modifiées pour répondre aux critères précédemment mentionnés. Le diagramme de phases le plus proche des exigences a été obtenu sur la base de la composition de l'alliage A3S, contenant du Co. Ce composant indésirable a été progressivement substitué par d'autres éléments présents dans la nuance. Le choix de substituer le Co entièrement par Fe, en conservant les proportions de CrMnNi, s'est finalement avéré le plus concluant. Cette procédure a mené aux trois compositions sélectionnées: Y1 bas-Co(V), Y2 bas-Co, Y3 sans-Co.

Au cours de cette étude une base de données HEA pour Thermo-Calc, TCHEA1, a été publiée. Les trois compositions ont été simulées sur cette base. Les diagrammes de phases obtenus sont plus complexes que ceux obtenus avec la base de données Fe, avec une présence plus marquée des phases secondaires, et notamment de la phase σ. Toutefois, les domaines d'intérêt recherchés sont conservés. Quelques artefacts présents dans les simulations avec TCHEA1 révèlent cependant les limites de cette base de données.

La simulation de l'évolution de composition du liquide en cours de solidification prédit une ségrégation de Mn et Ni dans les régions inter-dendritiques, et de Fe et Cr dans les dendrites. Ce phénomène a été confirmé via des analyses chimiques par EDX sur l'état coulé, ce qui valide les calculs Tehrmo-Calc sur ces compositions.

En même temps, Thermo-Calc prédit une présence de la phase σ à l'équilibre aux alentours de 500°C pour ces compositions. En suivant une étude de Otto et al. [17] sur la décomposition de l'alliage de Cantor, un maintien des alliages étudiés à 500°C pendant plusieurs centaines de jours a été réalisé affin de vérifier la prédiction Thermo-Calc. Une précipitation préférentielle aux joints de grains a bien été observée en microscopie électronique. Toutefois, les fractions de phases secondaires présentes se sont avérées trop faibles pour permettre leur détection par la technique de diffusion X. Des analyses chimiques et de diffraction au MET, sur une zone précisément choisie, ont permis de déterminer la nature de ces phases secondaires. Deux types de précipités ont été identifiés: une phase tétragonale MnNi et une phase de structure cubique centrée $Fe_{30}Cr_{70}$. Ces phases, également observées lors de la décomposition de l'alliage de Cantor, ne correspondent pas aux prédictions de Thermo-Calc. Finalement, ces observations ont révélé que la matrice de l'alliage Y3 est plus stable que celle de l'alliage de Cantor, malgré l'absence de Co. Cependant elle, présente une légère baisse de stabilité par rapport à la nuance A3S.

Tous les critères de formation de solution solide ont été vérifiés pour les nuances sélectionnées. La composition Y3 ne possédant que quatre éléments, elle ne remplit pas les conditions de la définition HEA. L'alliage Y3 devrait donc être considéré

comme un alliage à moyenne entropie. Cependant, cette nuance étant monophasée, il sera tout de même considéré comme un HEA.

L'influence du procédé de préparation du matériau sur sa microstructure a été étudiée.

Des coulées en laboratoire académique (EMSE) et industriel ont été réalisées. Les compositions obtenues sont proches des nominales, et les taux d'impuretés obtenus correspondent aux attentes, avec toutefois une teneur en soufre un peu trop importante. Cette teneur en soufre est associée à la présence de Mn, qui est typiquement contaminé en soufre. De plus, Mn s'oxydant facilement, son introduction dans une coulée pose parfois des difficultés. Malgré ces difficultés, la plupart des coulées ont donné les résultats attendus.

Pour assurer l'homogénéité chimique et une microstructure adéquate, tous les lingots ont été traités thermomécaniquement. Les coulées réalisées en laboratoire industriel ont été laminées à chaud. La première coulée réalisée à APERAM a fourni de bons résultats, cependant la seconde coulée a présenté un défaut à l'issue du laminage à chaud. En effet, le cœur de la tôle laminée de la seconde coulée présentait une couche d'oxyde de Mn, rendant la matière inexploitable. La transformation thermomécanique à l'EMSE consiste en un forgeage à chaud en plusieurs étapes, qui a été étudié en détail au cours de cette thèse. Des forgeages à différentes températures (entre 950°C et 1100°C) ont été conduits pour évaluer l'influence de ce paramètre sur la microstructure et les propriétés mécaniques de la nuance Y3. La température de forgeage ne semble pas impacter la microstructure, avec toutefois quelques exceptions constatées. De même l'évolution de propriétés mécaniques reste faible dans le large intervalle de températures de forgeage testées.

Les premières études des compositions sélectionnées ont été réalisées sur des échantillons à l'état forgé, produits à l'EMSE. Conformément aux attentes, les trois compositions présentent une unique phase cfc de paramètres de mailles proche de 3.6Å, confirmé par des mesures DRX, des observations microscopiques et des analyses chimiques. Les analyses EDX ont révélé une répartition homogène des éléments à l'issue du forgeage. La structure fortement déformée à l'issue du forgeage ne permet pas l'observation des grains par électrons rétrodiffusés, des analyses EBSD ont donc été menées. Les microstructures observées sont très proches entre les trois nuances étudiées. Ces nuances ont été comparées au travers d'essais de dureté et de compression, ce qui a permis leur classification en termes de propriétés mécaniques. Y2 s'est révélé l'alliage le plus résistant et présentant la plus haute limite d'élasticité en compression (YS = 640 MPa), suivi de Y1 (YS = 573 MPa) puis de Y3 (YS = 483 MPa). L'étude s'est par la suite recentrée sur la nuance Y2, de par ses propriétés mécaniques importantes, et sur la nuance Y3, car exempt de Co et présentant tout de même des propriétés mécaniques élevées. La nuance Y1 a quant

à elle été écartée.

Chapitre 4: Microstructure: source de propriétés mécaniques optimisées de Y3 sans-Co

La microstructure est un élément clef dans l'optimisation des propriétés mécaniques. Dans ce chapitre, la microstructure de l'alliage Y3 et son influence sur les propriétés mécaniques ont été étudiées.

En premier lieu, trois états de l'alliage Y3 ont été étudiés : l'état coulé, forgé, et recuit. À l'état coulé, le matériau présente une densité de dislocations anormalement élevée. Une présence préférentielle des dislocations sur certains plans {111} a été constatée. Une distance régulière de 200 nm a été trouvée entre ces plans.

Après forgeage, une microstructure complexe est observée à différentes échelles. À l'échelle de la microscopie optique, une structure austénitique classique est observée, avec une forte présence de macles. À l'échelle du MEB, une forte désorientation à l'intérieur des grains est observée, rendant les joints de grain difficilement distinguables. Les analyses EBSD ont permis de caractériser la microstructure. La distribution de taille de grain suit une loi Log normale. La valeur moyenne de taille de grain a pu être définie, et vaut 3 μm. Cette valeur moyenne est fortement influencée par un grand nombre de grains de taille inférieure à 1 μm, et n'est donc pas représentative des observations optiques. Une moyenne pondérée par la surface des grains a donc été calculée, donnant une valeur de 19 μm. Les observations en microscopie électronique à transmission ont révélé une sous-structure nanométrique à l'intérieur des grains. Si ce type de structures est habituellement observé dans des matériaux fortement déformés, elles restent surprenantes pour des alliages issus d'un forgeage à chaud.

Les propriétés mécaniques de cet alliage sont fortement influencées par cette nanostructuration, résultant en une limite d'élasticité plus importante que celle d'un acier austénitique recristallisé standard (500 MPa pour le Y3 contre 300 MPa pour le 304L à température ambiante). Dans cet état, l'alliage Y3 possède par ailleurs un coefficient d'écrouissage plus faible que le 304L. Une autre particularité de l'Y3, et d'autres HEA de la famille Cantor, est l'augmentation simultanée de la résistance mécanique et de l'allongement à rupture dans le domaine des températures cryogéniques. L'alliage Y3 possède par ailleurs une importante stabilité de phase, le rendant insensible à la transformation martensitique sous contrainte à froid (-150°C), contrairement aux aciers austénitiques tel que le 304L.

Après recuit, la limite d'élasticité du Y3 est divisée par deux par rapport à l'état forgé, la résistance mécanique est cependant moins impactée (diminution d'environ 20%), puisque le coefficient d'écrouissage augmente fortement. Ces variations de

propriétés mécaniques à l'issue du recuit sont le résultat d'évolutions microstructurales. Les grains présentent une apparence de grains recristallisés, avec une faible densité de sous-joints, une forte présence de macles et des orientations cristallographiques uniformes à l'intérieur des grains. La taille de grain, plus importante après traitement thermique, a aussi un impact sur les propriétés mécaniques. A l'échelle du MET, la structure des dislocations est similaire à celle observée à l'état coulé, avec une présence préférentielle des dislocations sur certains plans {111}.

Les densités de dislocations des trois états ont été mesurées. Ces valeurs ne pouvant pas être obtenues avec confiance sur la base d'une seule méthode de mesure, trois techniques ont été utilisées : méthode des interceptes sur des clichés MET, mesures de diffraction de rayons-X et application de la loi de Taylor aux essais de compression. Les états coulé et recuit présentent des densités de dislocations proches, de l'ordre de 10^{13} m^{-2}, tandis que l'état forgé est caractérisé par une densité de dislocations légèrement supérieure, de l'ordre de 10^{14} m^{-2}. Bien que le Y3 possède des densités de dislocations similaires à l'état coulé et recuit, les valeurs mesurées sont largement supérieures à celles attendues pour un alliage classique à l'équilibre (de l'ordre de 10^{9} m^{-2}). Des densités de dislocations de l'ordre de 10^{13}-10^{14} m^{-2} étant habituellement trouvées dans des matériaux fortement écrouis, l'existence du phénomène de la recristallisation a dû être remise en question et étudiée.

Afin de déterminer une température de recristallisation, des recuits ont été réalisés sur le matériau à l'état forgé, entre 600°C et 1000°C, pour des durées de quelques heures à plusieurs centaines d'heures. Consécutivement aux traitements thermiques, des essais de compression ont été conduits pour observer un éventuel changement de comportement mécanique. A l'issue des recuits à 600°C, un régime à haute limite d'élasticité et faible coefficient d'écrouissage est conservé, peu importe la durée du traitement thermique. Après un recuit au-delà de 700°C, un régime à faible limite d'élasticité et fort coefficient d'écrouissage est obtenu, y compris pour des traitements de courte durée. Le comportement mécanique après recuit à 650°C dépend fortement de la durée du traitement. Pour des temps de traitement courts, un comportement proche du régime à haute limite d'élasticité et faible coefficient d'écrouissage est observé. Pour des temps de traitement longs, un comportement proche du régime à basse limite d'élasticité et fort coefficient d'écrouissage est constaté.

Des analyses EBSD et des observations MET ont révélé un changement de microstructure des alliages traités thermiquement à partir de 650°C. Les analyses EBSD ont permis d'identifier un passage d'une structure fortement désorientée par des sous-joints à une structure orientée uniformément et contenant beaucoup de macles. Les observations MET montrent un passage d'une sous-structure nanométrique des dislocations vers un arrangement des dislocations sur certains plans {111} à l'issue

de recuit.

Un lien entre évolutions microstructurales et propriétés mécaniques a donc été établi lorsque la température de recuit excède 650°C. De plus, cette température correspond à 0.57 T_M, qui est le domaine de températures de recristallisation des alliages classiques. Cependant, les durées nécessaires pour obtenir une réorganisation de la microstructure, jusqu'à plusieurs centaines d'heures à 650°C, ne correspondent pas aux durées classiques de recristallisation, de l'ordre de quelques minutes à une heure. Des analyses complémentaires sont donc nécessaires pour vérifier l'hypothèse de recristallisation.

Le phénomène de recristallisation implique une étape de germination de nouveaux grains. Une diminution de la taille de grain en cours de recuit serait une conséquence directe de cette étape de germination. Une analyse d'évolution de la taille de grains lors de recuits de courtes durées à températures élevées (800°C et 1000°C) a donc été conduite, à partir de l'état forgé. Les mesures de taille de grains « recristallisés », à l'issue de recuits avec une durée de maintien en température allant de 0 sec à 300 sec, n'ont pas été cependant concluants. En effet, les valeurs obtenues sont supérieures aux attentes, et se positionnent entre les deux valeurs de taille de grains initiales correspondant aux deux définitions de ce paramètre dans l'état forgé. Cette étude ne permet donc pas de statuer sur la validité de l'hypothèse de recristallisation.

Le traitement thermomécanique par forgeage à chaud induit une texturation du matériau, qui a été constatée par analyse de diffraction de rayons-X. Une conséquence de l'éventuelle recristallisation en cours de recuit serait un changement de texture de l'alliage, consécutif à la germination de nouveaux grains ayant une orientation différente par rapport à celle d'origine. Une analyse de diffraction de rayons-X après un recuit de 2h à 1000°C a mis en évidence une perte de texture du matériau par rapport à l'état forgé. Ce résultat est une preuve directe de la recristallisation de l'alliage Y3 en cours de recuit. Cet alliage présente donc bien une structure recristallisée après recuit au-delà de 650°C, contenant cependant une densité de dislocations anormalement élevée qui n'est pas expliquée à l'heure actuelle.

Chapitre 5: Mécanismes de durcissement de l'Y3 sans-Co

Les mécanismes durcissants présents dans l'alliage Y3 à différentes échelles ont été étudiés. Des modèles de durcissement classiques ont été employés, afin de positionner cet alliage par rapport aux autres matériaux cfc.

Le volume d'activation a été mesuré afin de déterminer à quelle échelle les mécanismes de durcissement prédominants opèrent. Des essais de relaxation de contraintes ont été réalisés afin de mesurer l'évolution du volume d'activation avec la température et la déformation plastique imposée. Ces essais ont été réalisés aussi sur l'alliage de Cantor, et complétés par des valeurs de la littérature. Les volumes d'activation mesurés pour l'alliage de Cantor correspondent aux données issues mesurées par Laplanche et al. [22] . Les volumes d'activation mesurées sur l'alliage Y3 sont plus élevés que ceux de l'alliage de Cantor, pour toutes les conditions de température et de déformation plastique. Cette grandeur étant directement liée à la densité de dislocations, ces résultats sont en accord avec la densité de dislocations plus faible dans le Y3 que dans l'alliage de Cantor mise en évidence précédemment. Ces essais ont aussi permis de déduire l'influence du durcissement par solution solide dans ces deux alliages. Le durcissement par solution solide s'avère être plus efficace dans l'alliage de Cantor que dans l'alliage Y3, ce qui s'explique par une complexité de système plus faible dans ce dernier. Ces deux mécanismes sont prédominants pour le durcissement des deux alliages, et sont actifs à l'échelle des dislocations. Par ailleurs, les résultats obtenus sont conformes aux théories classiques de la métallurgie physique, et n'indiquent donc pas la présence d'un autre mécanisme de durcissement propre aux HEA.

L'écrouissage en cours de déformation plastique repose sur la création et l'annihilation des dislocations. Ces phénomènes dépendent de la température et de la vitesse de déformation. Un modèle développé par Kocks et Mecking [147] propose d'extraire, à partir d'une courbe d'écrouissage, deux paramètres gouvernés par la création et l'annihilation des dislocations. L'analyse de l'évolution de ces deux paramètres permet de distinguer des domaines de température et de vitesse de déformation dans lesquels l'écrouissage du matériau est régi principalement par la création de dislocations, et des domaines dans lesquels il est gouverné majoritairement par l'annihilation des dislocations. Kocks et Mecking ont démontré une relation linéaire entre ces phénomènes à l'origine de l'écrouissage et les conditions d'essai, pour un matériau donné. Il est donc par la suite possible de représenter cette relation sur un même graphique pour plusieurs matériaux, et ainsi de les classer. De plus, l'énergie de faute d'empilement influençant fortement les structures de dislocations, il s'agit en réalité d'un classement des matériaux en fonction de l'énergie de ce défaut. Ainsi,

par application de la méthode de Kocks et Mecking, il est possible de positionner l'énergie de faute d'empilement de l'alliage Y3 comme étant proche de celle de l'alliage de Cantor, de l'acier 304L et de métaux purs cfc comme argent.

Une étude de l'efficacité du durcissement par les joints de grain a été menée, sur des échantillons laminés à froid puis recuits avec différentes durées afin d'obtenir une variation de taille de grain. Des mesures de duretés ont ensuite été effectuées sur ces échantillons. Le coefficient de Hall-Petch ainsi que la valeur de résistance intrinsèque de la matrice ont ainsi été déterminés. La résistance intrinsèque de l'alliage Y3 s'avère plus importante que celle de l'alliage de Cantor et de l'alliage A3S, mais un peu plus faible que celle du 316L. L'efficacité du durcissement par les joints de grains est cependant moins importante dans l'alliage Y3 que dans les autres alliages. Les résistances intrinsèques de l'alliage Y3 à l'état forgé et recristallisé ont aussi été comparées, révélant une valeur trois fois plus importante après forgeage. Une densité de dislocations dix fois supérieure dans l'état forgé par rapport à l'état recuit avait été trouvée précédemment. Ces deux valeurs, limite d'élasticité et densité de dislocations, sont en accord avec la loi de Taylor. L'efficacité du durcissement par les dislocations dans l'alliage Y3 est une fois de plus mise en évidence. Cependant, comme durcissement par dislocations ne résulte pas en perte de ductilité, ce matériau peut donc probablement être utilisé à l'état écrouit.

Affin d'augmenter la résistance mécanique de l'alliage, les possibilités de son durcissement pa précipitation fine a été analysé. L'obtention de précipités durcissant par ajout d'éléments a été envisagée. Deux nouvelles compositions ont été déterminées, sur la base de la composition de l'alliage Y3. Différents éléments susceptibles de former des précipités durcissant ont été testés via des simulations Thermo-Calc. Les éléments W, Nb, V, Ti ont été envisagés pour la précipitation conjointe avec C, N, ou C + N. Les diagrammes les plus prometteurs ont été obtenus pour des teneurs en Nb de 0.1 at.% et 0.3 at.%, avec 200ppm de C.

Les deux nouvelles nuances ainsi définies ont été coulées en laboratoire. Malheureusement, dans ces alliages, la ségrégation à la coulée conduit à la précipitation primaire de carbures de niobium. Cette observation confirme en fait la simulation des conditions de solidification en suivant le modèle de Scheil-Guliver (Thermo-Calc): une ségrégation des éléments entre les dendrites et les zones inter-dendritiques se produit; elle est suivie, aux alentours de 1150°C, d'une précipitation primaire de NbC en fin de solidification. Ces précipités primaires sont trop volumineux pour apporter un effet durcissant, et sont susceptibles de fragiliser le matériau. De plus, la captation d'une partie du Nb par ces précipités primaires diminue l'efficacité potentielle de la précipitation secondaire. Des recuits à haute température (1200°C) pendant 3h ont été réalisés, afin de dissoudre les précipités primaires: si une homogénéisation de la composition chimique de la matrice a pu être obtenue, les précipités

n'ont pas été dissouts. Cependant, pendant le recuit, les précipités ont été montrés d'évoluer vers des formes plus sphériques tout en diminuant leur diamètre. Ceci permet d'envisager leur dissolution qui se produit cependant avec des cinétiques extrêmement lentes.

Les nuances avec niobium ont tout de même été forgées à chaud, ce qui a permis une uniformisation de la distribution des précipités primaires, sans toutefois les faire disparaître. Un recuit de mise en solution après forgeage, à 1200°C pendant 24h, a été conduit. Aucun effet notable sur les précipités primaires n'a été observé. Des essais de traction à température ambiante et à -150°C après recuit ont cependant révélé une légère augmentation de la dureté et de la ductilité par rapport au Y3 pur. Ainsi, la présence des précipités primaires ne semble pas être détrimentaire pour les propriétés mécaniques des deux nuances sélectionnées. Un traitement thermique permettant une précipitation secondaire fine peut donc être envisagé.

A l'issue de la mise en solution de ces deux nuances, une croissance non homogène des grains sur la longueur du barreau a été constatée en présence de Nb et C. La taille de grain est plus importante aux extrémités du barreau et plus fine dans la partie centrale. Un phénomène similaire a été constaté dans les tôles laminées provenant de l'industrie, avec des grains fins proche de la peau et des grains grossiers au cœur de la tôle. Un tel phénomène n'a jamais pas été observé dans l'alliage Y3 pur. La distribution de Nb et C dans l'épaisseur d'une tôle ou la longueur d'un barreau est homogène, ce qui ne permet donc pas d'expliquer cette évolution de taille de grain. Il semble probable que la distribution des contraintes en cours de traitement thermomécanique conduit à une précipitation préférentielle de NbC dans certaines zones, ce qui influencerait la croissance des grains dans ces zones.

Les difficultés technologiques précédemment évoquées (précipitation primaire, inhomogénéité de taille de grain) n'ont pas permis d'optimiser les traitements thermiques de précipitation fine. Cependant, les traitements de précipitation secondaire réalisés ont amené à un durcissement de 15 à 50 HV par rapport à l'Y3 pur. Bien que nécessitant une optimisation du procédé de fabrication, les nuances Y3 durcies par précipitation de NbC sont donc prometteuses.

Bibliography

[1] J.-W. Yeh, S.-K. Chen, S.-J. Lin, J.-Y. Gan, T.-s. Chin, T.-T. Shun, C.-h. Tsau and S.-Y. Chang : Nanostructured High-Entropy Alloys with Multiple Principal Elements: Novel Alloy Design Concepts and Outcomes. *Advanced Engineering Materials*, 6(5):299–303, 2004.

[2] J.-W. Yeh : Alloy Design Strategies and Future Trends in High-Entropy Alloys. *JOM*, 65(12):1759–1771, 2013.

[3] M. C. Gao, J.-W. Yeh, P. K. Liaw and Y. Zhang, editors. *High-Entropy Alloys*. Springer International Publishing, Cham, 2016.

[4] B. Cantor, I. Chang, P. Knight and A. Vincent : Microstructural development in equiatomic multicomponent alloys. *Materials Science and Engineering: A*, 375-377(1-2 SPEC. ISS.):213–218, 2004.

[5] Y. Zhang, T. T. Zuo, Z. Tang, M. C. Gao, K. A. Dahmen, P. K. Liaw and Z. P. Lu : Microstructures and properties of high-entropy alloys. *Progress in Materials Science*, 61(October 2013):1–93, 2014.

[6] D. Miracle and O. Senkov : A critical review of high entropy alloys and related concepts. *Acta Materialia*, 122:448–511, 2017.

[7] J.-W. Yeh : Recent progress in high-entropy alloys. *Annales de Chimie Science des Matériaux*, 31(6):633–648, 2006.

[8] F. Zhang, C. Zhang, S. Chen, J. Zhu, W. Cao and U. Kattner : An understanding of high entropy alloys from phase diagram calculations. *Calphad*, 45:1–10, 2014.

[9] A. Takeuchi and A. Inoue : Mixing enthalpy of liquid phase calculated by miedema's scheme and approximated with sub-regular solution model for assessing forming ability of amorphous and glassy alloys. *Intermetallics*, 18(9): 1779–1789, 2010.

[10] F. Otto, Y. Yang, H. Bei and E. George : Relative effects of enthalpy and entropy on the phase stability of equiatomic high-entropy alloys. *Acta Materialia*, 61(7):2628–2638, 2013.

[11] L. A. Domínguez, R. Goodall and I. Todd : Prediction and validation of quaternary high entropy alloys using statistical approaches. *Materials Science and Technology*, 31(10):1201–1206, 2015.

[12] A. Takeuchi, K. Amiya, T. Wada, K. Yubuta and W. Zhang : High-Entropy Alloys with a Hexagonal Close-Packed Structure Designed by Equi-Atomic Alloy Strategy and Binary Phase Diagrams. *JOM*, 66(10):1984–1992, 2014.

[13] B. Murty, J. Yeh and S. Ranganathan : A Brief History of Alloys and the Birth of High-Entropy Alloys. In *High Entropy Alloys*, pp. 1–12. Elsevier, 2014.

[14] M. S. Lucas, G. B. Wilks, L. Mauger, J. A. Muñoz, O. N. Senkov, E. Michel, J. Horwath, S. L. Semiatin, M. B. Stone, D. L. Abernathy and E. Karapetrova : Absence of long-range chemical ordering in equimolar FeCoCrNi. *Applied Physics Letters*, 100(25):251907, 2012.

[15] K.-Y. Tsai, M.-H. Tsai and J.-W. Yeh : Sluggish diffusion in Co–Cr–Fe–Mn–Ni high-entropy alloys. *Acta Materialia*, 61(13):4887–4897, 2013.

[16] C.-J. Tong, Y.-L. Chen, J.-W. Yeh, S.-J. Lin, S.-K. Chen, T.-T. Shun, C.-H. Tsau and S.-Y. Chang : Microstructure characterization of Al x CoCrCuFeNi high-entropy alloy system with multiprincipal elements. *Metallurgical and Materials Transactions A*, 36(4):881–893, 2005.

[17] F. Otto, A. Dlouhý, K. Pradeep, M. Kuběnová, D. Raabe, G. Eggeler and E. George : Decomposition of the single-phase high-entropy alloy CrMnFeCoNi after prolonged anneals at intermediate temperatures. *Acta Materialia*, 112:40–52, 2016.

[18] W. H. Liu, Y. Wu, J. Y. He, T. G. Nieh and Z. P. Lu : Grain growth and the Hall-Petch relationship in a high-entropy FeCrNiCoMn alloy. *Scripta Materialia*, 68(7):526–529, 2013.

[19] P. Aloke : Comments on "Sluggish diffusion in Co–Cr–Fe–Mn–Ni high-entropy alloys" by K.Y. Tsai, M.H. Tsai and J.W. Yeh, Acta Materialia 61 (2013) 4887–4897. *Scripta Materialia*, 135:153–157, 2017.

[20] Z. Wu, H. Bei, F. Otto, G. Pharr and E. George : Recovery, recrystallization, grain growth and phase stability of a family of FCC-structured multi-component equiatomic solid solution alloys. *Intermetallics*, 46:131–140, 2014.

[21] J.-w. Yeh, S.-y. Chang, Y.-d. Hong, S.-k. Chen and S.-j. Lin : Anomalous decrease in X-ray diffraction intensities of Cu – Ni – Al – Co – Cr – Fe – Si alloy systems with multi-principal elements. 103:41–46, 2007.

[22] G. Laplanche, J. Bonneville, C. Varvenne, W. Curtin and E. George : Thermal activation parameters of plastic flow reveal deformation mechanisms in the CrMnFeCoNi high-entropy alloy. *Acta Materialia*, 143:257–264, 2018.

[23] C. Varvenne, A. Luque and W. A. Curtin : Theory of strengthening in fcc high entropy alloys. *Acta Materialia*, 118:164–176, 2016.

[24] M. Laurent-Brocq, L. Perrière, R. Pirès, F. Prima, P. Vermaut and Y. Champion : From diluted solid solutions to high entropy alloys: On the evolution of properties with composition of multi-components alloys. *Materials Science and Engineering: A*, 696:228–235, 2017.

[25] I. Toda-Caraballo and P. E. Rivera-Díaz-del Castillo : Modelling solid solution hardening in high entropy alloys. *Acta Materialia*, 85:14–23, 2015.

[26] I. Toda-Caraballo, J. S. Wróbel, S. L. Dudarev, D. Nguyen-Manh and P. E. J. Rivera-Díaz-Del-Castillo : Interatomic spacing distribution in multicomponent alloys. *Acta Materialia*, 97:156–169, 2015.

[27] S. Ranganathan : Alloyed pleasures: Multimetallic cocktails. 85:1404–1406, 2003.

[28] O. Senkov, G. Wilks, D. Miracle, C. Chuang and P. Liaw : Refractory high-entropy alloys. *Intermetallics*, 18(9):1758–1765, 2010.

[29] O. Senkov, G. Wilks, J. Scott and D. Miracle : Mechanical properties of Nb25Mo25Ta25W25 and V20Nb20Mo20Ta20W20 refractory high entropy alloys. *Intermetallics*, 19(5):698–706, 2011.

[30] M. G. Poletti and L. Battezzati : Electronic and thermodynamic criteria for the occurrence of high entropy alloys in metallic systems. *Acta Materialia*, 75:297–306, 2014.

[31] Y. Zhang, Y. J. Zhou, J. P. Lin, G. L. Chen and P. K. Liaw : Solid-Solution Phase Formation Rules for Multi-component Alloys. *Advanced Engineering Materials*, 10(6):534–538, 2008.

[32] S. GUO and C. LIU : Phase stability in high entropy alloys: Formation of solid-solution phase or amorphous phase. *Progress in Natural Science: Materials International*, 21(6):433–446, 2011.

[33] O. Senkov and D. Miracle : A new thermodynamic parameter to predict formation of solid solution or intermetallic phases in high entropy alloys. *Journal of Alloys and Compounds*, 658:603–607, 2016.

[34] J. He, W. Liu, H. Wang, Y. Wu, X. Liu, T. Nieh and Z. Lu : Effects of Al addition on structural evolution and tensile properties of the FeCoNiCrMn high-entropy alloy system. *Acta Materialia*, 62:105–113, 2014.

[35] X. Yang and Y. Zhang : Prediction of high-entropy stabilized solid-solution in multi-component alloys. *Materials Chemistry and Physics*, 132(2-3):233–238, 2012.

[36] S. Guo, C. Ng, J. Lu and C. T. Liu : Effect of valence electron concentration on stability of fcc or bcc phase in high entropy alloys. *Journal of Applied Physics*, 109(10):103505, 2011.

[37] S. Guo, Q. Hu, C. Ng and C. Liu : More than entropy in high-entropy alloys: Forming solid solutions or amorphous phase. *Intermetallics*, 41:96–103, 2013.

[38] G. Bracq, M. Laurent-Brocq, L. Perrière, R. Pirès, J.-M. Joubert and I. Guillot : The fcc solid solution stability in the Co-Cr-Fe-Mn-Ni multi-component system. *Acta Materialia*, 128:327–336, 2017.

[39] M. H. Tsai, J. H. Li, A. C. Fan and P. H. Tsai : Incorrect predictions of simple solid solution high entropy alloys: Cause and possible solution. *Scripta Materialia*, 127:6–9, 2017.

[40] M.-H. Tsai, A.-C. Fan and H.-A. Wang : Effect of atomic size difference on the type of major intermetallic phase in arc-melted CoCrFeNiX high-entropy alloys. *Journal of Alloys and Compounds*, 695:1479–1487, 2017.

[41] Wikipedia : *Electronegativity; https://en.wikipedia.org/wiki/Electronegativity #Allen_electronegativity*, btitle.

[42] J. B. Mann, T. L. Meek, E. T. Knight, J. F. Capitani and L. C. Allen : Configuration energies of the d-block elements. *Journal of the American Chemical Society*, 122(21):5132–5137, 2000.

[43] U. Mizutani : *Hume-Rothery rules for structurally complex alloy phases*. CRC Press, Boca Raton, 2011.

[44] S. Singh, N. Wanderka, B. Murty, U. Glatzel and J. Banhart : Decomposition in multi-component AlCoCrCuFeNi high-entropy alloy. *Acta Materialia*, 59(1):182–190, 2011.

[45] M. Gao and D. Alman : Searching for Next Single-Phase High-Entropy Alloy Compositions. *Entropy*, 15(12):4504–4519, 2013.

[46] C. Zhang, F. Zhang, S. Chen and W. Cao : Computational Thermodynamics Aided High-Entropy Alloy Design. *JOM*, 64(7):839–845, 2012.

[47] N. Saunders and A. Miodownik : *CALPHAD: A Comprehensive Guide*. Pergamon Materials Series, 1998.

[48] Thermo-Calc Software, Stockholm, Sweden : *Thermo-Calc thermodynamic equilibrium calculations*, btitle.

[49] J.-O. Andersson, T. Helander, L. Höglund, P. Shi and B. Sundman : Thermo-Calc & DICTRA, computational tools for materials science. *Calphad*, 26(2):273–312, 2002.

[50] O. Senkov, J. Miller, D. Miracle and C. Woodward : Accelerated exploration of multi-principal element alloys with solid solution phases. *Nature Communications*, 6(1):6529, 2015.

[51] F. Tancret, I. Toda-Caraballo, E. Menou and P. E. J. Rivera Díaz-Del-Castillo : Designing high entropy alloys employing thermodynamics and Gaussian process statistical analysis. *Materials & Design*, 115:486–497, 2017.

[52] O. Senkov and C. Woodward : Microstructure and properties of a refractory NbCrMo0.5Ta0.5TiZr alloy. *Materials Science and Engineering: A*, 529:311–320, 2011.

[53] O. Senkov, S. Senkova, C. Woodward and D. Miracle : Low-density, refractory multi-principal element alloys of the Cr–Nb–Ti–V–Zr system: Microstructure and phase analysis. *Acta Materialia*, 61(5):1545–1557, 2013.

[54] O. N. Senkov, S. V. Senkova, D. B. Miracle and C. Woodward : Materials Science & Engineering A Mechanical properties of low-density , refractory multi-principal element alloys of the Cr – Nb – Ti – V – Zr system. *Materials Science & Engineering A*, 565:51–62, 2013.

[55] O. Senkov, S. Senkova and C. Woodward : Effect of aluminum on the microstructure and properties of two refractory high-entropy alloys. *Acta Materialia*, 68:214–228, 2014.

[56] O. N. Senkov and S. L. Semiatin : Microstructure and properties of a refractory high-entropy alloy after cold working. *Journal of Alloys and Compounds*, 649:1110–1123, 2015.

[57] N. D. Stepanov, D. G. Shaysultanov, G. A. Salishchev and M. A. Tikhonovsky : Structure and mechanical properties of a light-weight AlNbTiV high entropy alloy. *Materials Letters*, 142:153–155, 2015.

[58] Y. Zou, S. Maiti, W. Steurer and R. Spolenak : Size-dependent plasticity in an Nb25Mo25Ta25W25 refractory high-entropy alloy. *Acta Materialia*, 65: 85–97, 2014.

[59] J. P. Couzinié, G. Dirras, L. Perrière, T. Chauveau, E. Leroy, Y. Champion and I. Guillot : Microstructure of a near-equimolar refractory high-entropy alloy. *Materials Letters*, 126:285–287, 2014.

[60] L. Lilensten, J. P. Couzinié, L. Perrière, J. Bourgon, N. Emery and I. Guillot : New structure in refractory high-entropy alloys. *Materials Letters*, 132:123–125, 2014.

[61] J. K. Jensen, B. A. Welk, R. E. Williams, J. M. Sosa, D. E. Huber, O. N. Senkov, G. B. Viswanathan and H. L. Fraser : Characterization of the microstructure of the compositionally complex alloy Al1Mo0.5Nb1Ta0.5Ti1Zr1. *Scripta Materialia*, 121:1–4, 2016.

[62] O. N. Senkov, D. Isheim, D. N. Seidman and A. L. Pilchak : Development of a refractory high entropy superalloy. *Entropy*, 18(3):1–13, 2016.

[63] V. H. Hammond, M. A. Atwater, K. A. Darling, H. Q. Nguyen and L. J. Kecskes : Equal-Channel Angular Extrusion of a Low-Density High-Entropy Alloy Produced by High-Energy Cryogenic Mechanical Alloying. *JOM*, 66(10): 2021–2029, 2014.

[64] K. M. Youssef, A. J. Zaddach, C. Niu, D. L. Irving and C. C. Koch : A novel low-density, high-hardness, high-entropy alloy with close-packed single-phase nanocrystalline structures. *Materials Research Letters*, 3(2):95–99, 2014.

[65] X. Yang, S. Y. Chen, J. D. Cotton and Y. Zhang : Phase Stability of Low-Density, Multiprincipal Component Alloys Containing Aluminum, Magnesium, and Lithium. *Jom*, 66(10):2009–2020, 2014.

[66] K. J. Laws, C. Crosby, A. Sridhar, P. Conway, L. S. Koloadin, M. Zhao, S. Aron-Dine and L. C. Bassman : High entropy brasses and bronzes - Microstructure, phase evolution and properties. *Journal of Alloys and Compounds*, 650:949–961, 2015.

[67] T. K. Chen, M. S. Wong, T. T. Shun and J. W. Yeh : Nanostructured nitride films of multi-element high-entropy alloys by reactive DC sputtering. *Surface and Coatings Technology*, 200(5-6):1361–1365, 2005.

[68] M.-H. Tsai, C.-H. Lai, J.-W. Yeh and J.-Y. Gan : Effects of nitrogen flow ratio on the structure and properties of reactively sputtered (AlMoNbSiTaTiVZr) N x coatings. *Journal of Physics D: Applied Physics*, 41(23):235402, 2008.

[69] V. Braic, A. Vladescu, M. Balaceanu, C. R. Luculescu and M. Braic : Nanostructured multi-element (TiZrNbHfTa)N and (TiZrNbHfTa)C hard coatings. *Surface and Coatings Technology*, 211:117–121, 2012.

[70] Q. S. Chen, Y. P. Lu, Y. Dong, T. M. Wang and T. J. Li : Effect of minor B addition on microstructure and properties of AlCoCrFeNi multi-compenent alloy. *Transactions of Nonferrous Metals Society of China (English Edition)*, 25(9):2958–2964, 2015.

[71] B. Cantor : Multicomponent and High Entropy Alloys. *Entropy*, 16(9):4749–4768, 2014.

[72] F. Otto, A. Dlouhý, C. Somsen, H. Bei, G. Eggeler and E. George : The influences of temperature and microstructure on the tensile properties of a CoCrFeMnNi high-entropy alloy. *Acta Materialia*, 61(15):5743–5755, 2013.

[73] A. Gali and E. George : Tensile properties of high- and medium-entropy alloys. *Intermetallics*, 39:74–78, 2013.

[74] B. Gludovatz, A. Hohenwarter, D. Catoor, E. H. Chang, E. P. George and R. O. Ritchie : A fracture-resistant high-entropy alloy for cryogenic applications. *Science*, 345(6201):1153–1158, 2014.

[75] M. J. Jang, S. Praveen, H. J. Sung, J. W. Bae, J. Moon and H. S. Kim : High-temperature tensile deformation behavior of hot rolled CrMnFeCoNi high-entropy alloy. *Journal of Alloys and Compounds*, 730:242–248, 2018.

[76] G. Laplanche, A. Kostka, C. Reinhart, J. Hunfeld, G. Eggeler and E. George : Reasons for the superior mechanical properties of medium-entropy CrCoNi compared to high-entropy CrMnFeCoNi. *Acta Materialia*, 128:292–303, 2017.

[77] N. L. Okamoto, S. Fujimoto, Y. Kambara, M. Kawamura, Z. M. T. Chen, H. Matsunoshita, K. Tanaka, H. Inui and E. P. George : Size effect, critical resolved shear stress, stacking fault energy, and solid solution

strengthening in the CrMnFeCoNi high-entropy alloy. *Scientific Reports*, 6(1): 35863, 2016.

[78] Z. Zhang, M. M. Mao, J. Wang, B. Gludovatz, Z. Zhang, S. X. Mao, E. P. George, Q. Yu and R. O. Ritchie : Nanoscale origins of the damage tolerance of the high-entropy alloy CrMnFeCoNi. *Nature Communications*, 6(1):10143, 2015.

[79] J. He, C. Zhu, D. Zhou, W. Liu, T. Nieh and Z. Lu : Steady state flow of the FeCoNiCrMn high entropy alloy at elevated temperatures. *Intermetallics*, 55:9–14, 2014.

[80] Z. Wu, Y. Gao and H. Bei : Thermal activation mechanisms and Labusch-type strengthening analysis for a family of high-entropy and equiatomic solid-solution alloys. *Acta Materialia*, 120:108–119, 2016.

[81] R. R. Eleti, T. Bhattacharjee, L. Zhao, P. P. Bhattacharjee and N. Tsuji : Hot deformation behavior of CoCrFeMnNi FCC high entropy alloy. *Materials Chemistry and Physics*, 210:176–186, 2018.

[82] L. Patriarca, A. Ojha, H. Sehitoglu and Y. Chumlyakov : Slip nucleation in single crystal FeNiCoCrMn high entropy alloy. *Scripta Materialia*, 112:54–57, 2016.

[83] N. Stepanov, D. Shaysultanov, M. Tikhonovsky and G. Salishchev : Tensile properties of the Cr–Fe–Ni–Mn non-equiatomic multicomponent alloys with different Cr contents. *Materials & Design*, 87:60–65, 2015.

[84] M. Yao, K. Pradeep, C. Tasan and D. Raabe : A novel, single phase, non-equiatomic FeMnNiCoCr high-entropy alloy with exceptional phase stability and tensile ductility. *Scripta Materialia*, 72-73:5–8, 2014.

[85] M. Laurent-Brocq, A. Akhatova, L. Perrière, S. Chebini, X. Sauvage, E. Leroy and Y. Champion : Insights into the phase diagram of the CrMnFeCoNi high entropy alloy. *Acta Materialia*, 88:355–365, 2015.

[86] T. Mitchell : Dislocations and Plasticity in Single Crystals of Face-Centered Cubic Metals and Alloys. In *Progress in Applied Materials Research, vol. 6*, pp. 119–237. Heywood and co edition, 1964.

[87] A. J. Zaddach, C. Niu, C. C. Koch and D. L. Irving : Mechanical Properties and Stacking Fault Energies of NiFeCrCoMn High-Entropy Alloy. *JOM*, 65(12):1780–1789, 2013.

[88] A. Haglund, M. Koehler, D. Catoor, E. George and V. Keppens : Polycrystalline elastic moduli of a high-entropy alloy at cryogenic temperatures. *Intermetallics*, 58:62–64, 2015.

[89] G. Laplanche, P. Gadaud, O. Horst, F. Otto, G. Eggeler and E. George : Temperature dependencies of the elastic moduli and thermal expansion coefficient of an equiatomic, single-phase CoCrFeMnNi high-entropy alloy. *Journal of Alloys and Compounds*, 623:348–353, 2015.

[90] S. I. Hong, J. Moon, S. K. Hong and H. S. Kim : Materials Science & Engineering A Thermally activated deformation and the rate controlling mechanism in CoCrFeMnNi high entropy alloy. *Materials Science & Engineering A*, 682:569–576, 2017.

[91] P. Spätig, J. Bonneville and J.-L. Martin : A new method for activation volume measurements: application to Ni3(Al,Hf). *Materials Science and Engineering: A*, 167(1-2):73–79, 1993.

[92] G. Laplanche, A. Kostka, O. Horst, G. Eggeler and E. George : Microstructure evolution and critical stress for twinning in the CrMnFeCoNi high-entropy alloy. *Acta Materialia*, 118:152–163, 2016.

[93] J. He, Q. Wang, H. Zhang, L. Dai, T. Mukai, Y. Wu, X. Liu, H. Wang, T.-G. Nieh and Z. Lu : Dynamic deformation behavior of a face-centered cubic FeCoNiCrMn high-entropy alloy. *Science Bulletin*, 63(6):362–368, 2018.

[94] Z. Wu, C. M. Parish and H. Bei : Nano-twin mediated plasticity in carbon-containing FeNiCoCrMn high entropy alloys *. 647:815–822, 2015.

[95] Y. H. Jo, S. Jung, W. M. Choi, S. S. Sohn, H. S. Kim, B. J. Lee, N. J. Kim and S. Lee : Cryogenic strength improvement by utilizing room-temperature deformation twinning in a partially recrystallized VCrMnFeCoNi high-entropy alloy. *Nature Communications*, 8:15719, 2017.

[96] N. Stepanov, M. Tikhonovsky, N. Yurchenko, D. Zyabkin, M. Klimova, S. Zherebtsov, A. Efimov and G. Salishchev : Effect of cryo-deformation on structure and properties of CoCrFeNiMn high-entropy alloy. *Intermetallics*, 59:8–17, 2015.

[97] Y. Deng, C. Tasan, K. Pradeep, H. Springer, A. Kostka and D. Raabe : Design of a twinning-induced plasticity high entropy alloy. *Acta Materialia*, 94:124–133, 2015.

[98] B. Jaoul : *Etude de la plasticite e application aux metaux*. Mines ParisTech Les Presses, 1965.

[99] A. Hedayati, A. Najafizadeh, A. Kermanpur and F. Forouzan : The effect of cold rolling regime on microstructure and mechanical properties of AISI 304L stainless steel. *Journal of Materials Processing Technology*, 210(8): 1017–1022, 2010.

[100] M. Beyramali Kivy and M. Asle Zaeem : Generalized stacking fault energies, ductilities, and twinnabilities of CoCrFeNi-based face-centered cubic high entropy alloys. *Scripta Materialia*, 139:83–86, 2017.

[101] T. Smith, M. Hooshmand, B. Esser, F. Otto, D. McComb, E. George, M. Ghazisaeidi and M. Mills : Atomic-scale characterization and modeling of 60° dislocations in a high-entropy alloy. *Acta Materialia*, 110:352–363, 2016.

[102] H. Idrissi, K. Renard, L. Ryelandt, D. Schryvers and P. J. Jacques : On the mechanism of twin formation in Fe-Mn-C TWIP steels. *Acta Materialia*, 58(7):2464–2476, 2010.

[103] F. Otto, N. Hanold and E. George : Microstructural evolution after thermomechanical processing in an equiatomic, single-phase CoCrFeMnNi high-entropy alloy with special focus on twin boundaries. *Intermetallics*, 54:39–48, 2014.

[104] C. Haase and L. A. Barrales-Mora : Influence of deformation and annealing twinning on the microstructure and texture evolution of face-centered cubic high-entropy alloys. *Acta Materialia*, 150:88–103, 2018.

[105] P. Bhattacharjee, G. Sathiaraj, M. Zaid, J. Gatti, C. Lee, C.-W. Tsai and J.-W. Yeh : Microstructure and texture evolution during annealing of equiatomic CoCrFeMnNi high-entropy alloy. *Journal of Alloys and Compounds*, 587:544–552, 2014.

[106] G. D. Sathiaraj and P. Bhattacharjee : Analysis of microstructure and microtexture during grain growth in low stacking fault energy equiatomic CoCrFeMnNi high entropy and Ni–60wt.%Co alloys. *Journal of Alloys and Compounds*, 637:267–276, 2015.

[107] H. Hu and C. S. Smith : The formation of low-energy interfaces during grain growth in alpha and alpha-beta brasses. *Acta Metallurgica*, 4(6):638–646, 1956.

[108] R. L. Fullman and J. C. Fisher : Formation of Annealing Twins During Grain Growth. *Journal of Applied Physics*, 22(11):1350–1355, 1951.

[109] R. K. Ray : Rolling textures of pure nickel, nickel-iron and nickel-cobalt alloys. *Acta Metallurgica Et Materialia*, 43(10):3861–3872, 1995.

[110] T. Leffers and R. K. Ray : The brass-type texture and its deviation from the copper-type texture. *Progress in Materials Science*, 54(3):351–396, 2009.

[111] N. Stepanov, D. Shaysultanov, M. Ozerov, S. Zherebtsov and G. Salishchev : Second phase formation in the CoCrFeNiMn high entropy alloy after recrystallization annealing. *Materials Letters*, 185:1–4, 2016.

[112] N. Park, B. J. Lee and N. Tsuji : The phase stability of equiatomic CoCrFeMnNi high-entropy alloy: Comparison between experiment and calculation results. *Journal of Alloys and Compounds*, 719:189–193, 2017.

[113] E. Pickering, R. Muñoz-Moreno, H. Stone and N. Jones : Precipitation in the equiatomic high-entropy alloy CrMnFeCoNi. *Scripta Materialia*, 113: 106–109, 2016.

[114] B. Schuh, F. Mendez-Martin, B. Völker, E. P. George, H. Clemens, R. Pippan and A. Hohenwarter : Mechanical properties, microstructure and thermal stability of a nanocrystalline CoCrFeMnNi high-entropy alloy after severe plastic deformation. *Acta Materialia*, 96:258–268, 2015.

[115] M. Mroz : *Design and structural optimization of a high entropy alloy (HEA) of the CoCrFeMnNi family with high mechanical resistance*. PhD thesis, Ecole des Mines de Saint Etienne, 2018.

[116] A. Manzoni, H. Daoud, R. Völkl, U. Glatzel and N. Wanderka : Phase separation in equiatomic AlCoCrFeNi high-entropy alloy. *Ultramicroscopy*, 132:212–215, 2013.

[117] J. Olszewska, M. Mroz, M. Mondon, G. He and A. Fraczkiewicz : Evaluation of anoriginal grade of HEA alloys from AlCrFeMnNi family. *To be published*, 2016.

[118] S. T. Chen, W. Y. Tang, Y. F. Kuo, S. Y. Chen, C. H. Tsau, T. T. Shun and J. W. Yeh : Microstructure and properties of age-hardenable AlxCrFe1.5MnNi0.5 alloys. *Materials Science and Engineering A*, 527(21-22):5818–5825, 2010.

[119] C. Lee, C. Chang, Y. Chen, J. Yeh and H. Shih : Effect of the aluminium content of AlxCrFe1.5MnNi0.5 high-entropy alloys on the corrosion behaviour in aqueous environments. *Corrosion Science*, 50(7):2053–2060, 2008.

[120] M. Komarasamy, N. Kumar, Z. Tang, R. S. Mishra and P. K. Liaw : Effect of microstructure on the deformation mechanism of friction stir-processed Al0.1CoCrFeNi high entropy alloy. *Materials Research Letters*, 3(1): 30–34, 2014.

[121] M. Komarasamy, N. Kumar, R. S. Mishra and P. K. Liaw : Anomalies in the deformation mechanism and kinetics of coarse-grained high entropy alloy. *Materials Science and Engineering: A*, 654:256–263, 2016.

[122] N. Stepanov, D. Shaysultanov, G. Salishchev, M. Tikhonovsky, E. Oleynik, A. Tortika and O. Senkov : Effect of V content on microstructure and mechanical properties of the CoCrFeMnNiVx high entropy alloys. *Journal of Alloys and Compounds*, 628:170–185, 2015.

[123] Y. Zhao, T. Yang, J. Zhu, D. Chen, Y. Yang, A. Hu, C. Liu and J.-J. Kai : Development of high-strength Co-free high-entropy alloys hardened by nanosized precipitates. *Scripta Materialia*, 148:51–55, 2018.

[124] Z. Li, K. G. Pradeep, Y. Deng, D. Raabe and C. C. Tasan : Metastable high-entropy dual-phase alloys overcome the strength–ductility trade-off. *Nature*, 534(7606):227–230, 2016.

[125] Z. Wu and H. Bei : Microstructures and mechanical properties of compositionally complex Co-free FeNiMnCr 18 FCC solid solution alloy. *Materials Science and Engineering: A*, 640:217–224, 2015.

[126] N. K. Kumar, C. Li, K. Leonard, H. Bei and S. Zinkle : Microstructural stability and mechanical behavior of FeNiMnCr high entropy alloy under ion irradiation. *Acta Materialia*, 113:230–244, 2016.

[127] J. He, H. Wang, H. Huang, X. Xu, M. Chen, Y. Wu, X. Liu, T. Nieh, K. An and Z. Lu : A precipitation-hardened high-entropy alloy with outstanding tensile properties. *Acta Materialia*, 102:187–196, 2016.

[128] J. He, H. Wang, Y. Wu, X. Liu, H. Mao, T. Nieh and Z. Lu : Precipitation behavior and its effects on tensile properties of FeCoNiCr high-entropy alloys. *Intermetallics*, 79:41–52, 2016.

[129] F. He, Z. Wang, S. Niu, Q. Wu, J. Li, J. Wang, C. Liu and Y. Dang : Strengthening the CoCrFeNiNb0.25 high entropy alloy by FCC precipitate. *Journal of Alloys and Compounds*, 667:53–57, 2016.

[130] W. Liu, J. He, H. Huang, H. Wang, Z. Lu and C. Liu : Effects of Nb additions on the microstructure and mechanical property of CoCrFeNi high-entropy alloys. *Intermetallics*, 60:1–8, 2015.

[131] W. Liu, Z. Lu, J. He, J. Luan, Z. Wang, B. Liu, Y. Liu, M. Chen and C. Liu : Ductile CoCrFeNiMox high entropy alloys strengthened by hard intermetallic phases. *Acta Materialia*, 116:332–342, 2016.

[132] D. Kaoumi and J. Liu : Deformation induced martensitic transformation in 304 austenitic stainless steel: In-situ vs. ex-situ transmission electron microscopy characterization. *Materials Science and Engineering A*, 715(May 2017):73–82, 2018.

[133] Y. Tian, A. Borgenstam and P. Hedström : Comparing the deformation-induced martensitic transformation with the athermal martensitic transformation in Fe-Cr-Ni alloys. *Journal of Alloys and Compounds*, 766:131–139, 2018.

[134] M. Moallemi, A. Kermanpur, A. Najafizadeh, A. Rezaee, H. S. Baghbadorani and P. D. Nezhadfar : Deformation-induced martensitic transformation in a 201 austenitic steel: The synergy of stacking fault energy and chemical driving force. *Materials Science and Engineering A*, 653:147–152, 2016.

[135] F. He, Z. Wang, X. Shang, C. Leng, J. Li and J. Wang : Stability of lamellar structures in CoCrFeNiNbxeutectic high entropy alloys at elevated temperatures. *Materials and Design*, 104:259–264, 2016.

[136] A. Abbasi, A. Dick, T. Hickel and J. Neugebauer : First-principles investigation of the effect of carbon on the stacking fault energy of Fe-C alloys. *Acta Materialia*, 59(8):3041–3048, 2011.

[137] Ecorys : Mapping resource prices : the past and the future. *Ecorys*, (October 2012):13–25, 2012.

[138] P. E. A. Turchi : Ab Initio and Calphad Thermodynamics of Materials. *computational Modeling and Simulation of Materials*, 2004.

[139] Thermo-calc : Thermo-Calc Version 2018b. *Thermo-Calc Documentation Set*, 2018.

[140] A. Borbély and I. Groma : Variance method for the evaluation of particle size and dislocation density from x-ray Bragg peaks. *Applied Physics Letters*, 79(12):1772–1774, 2001.

[141] E. Rauch and M. Véron : Automated crystal orientation and phase mapping in TEM. *Materials Characterization*, 98:1–9, 2014.

[142] A. Fraczkiewicz : Patent FR-1459567. October, 2014.

[143] G. V. Samsonov : *Handbook of the Physicochemical Properties of the Elements*. Springer US, Boston, MA, 1968.

[144] D. Kopeliovich : http://www.substech.com/dokuwiki/doku.php?id=deoxidation_of_steel. 2012.

[145] Z. J. Zheng, Y. Gao, J. W. Liu and M. Zhu : A hybrid refining mechanism of microstructure of 304 stainless steel subjected to ECAP at 500°C. *Materials Science and Engineering A*, 639:615–625, 2015.

[146] R. Z. Valiev, E. V. Kozlov, Y. F. Ivanov, J. Lian, A. A. Nazarov and B. Baudelet : Deformation behaviour of ultra-fine-grained copper. *Acta Metallurgica Et Materialia*, 42(7):2467–2475, 1994.

[147] U. F. Kocks and H. Mecking : Physics and phenomenology of strain hardening: The FCC case. *Progress in Materials Science*, 48(3):171–273, 2003.

[148] J. Favre : *Recrystallization of L-605 cobalt superalloy during hot-working process Julien Favre*. PhD thesis, INSA Lyon, 2013.

[149] J. Bernard, A. Miche, J. Philibert and J. Talbot : *Metallurgie generale*. Masson edition, 1984.

[150] G. Laplanche, O. Horst, F. Otto, G. Eggeler and E. George : Microstructural evolution of a CoCrFeMnNi high-entropy alloy after swaging and annealing. *Journal of Alloys and Compounds*, 647:548–557, 2015.

[151] M. Hillert : On the theory of normal and abnormal grain growth. *Acta Metallurgica*, 13(3):227–238, 1965.

[152] Z. Basinski, R. Foxall and R. Pascual : Stress equivalence of solution hardening. *Scripta Metallurgica*, 6(9):807–814, 1972.

[153] J. Bonneville : *Etude des parametres d'activaition du glissement devie dans le cuivre*. PhD thesis, Ecole Polytechnique Federale de Lausanne, 1985.

[154] P. L. P. Kubin : Description de la préplasticité par la théorie des phénomènes thermiquement activés. *Philosophical Magazine*, 30(4):705–718, 1974.

[155] G. I. Taylor : The Mechanism of Plastic Deformation of Crystals. Part II. Comparison with Observations. *Proceedings of the Royal Society A: Mathematical, Physical and Engineering Sciences*, 145(855):388–404, 1934.

[156] Y. Estrin and H. Mecking : A unified phenomenological description of work hardening and creep based on one-parameter models. *Acta Metallurgica*, 32(1):57–70, 1984.

[157] B. Bawab : Modelling mechanical properties of High Entropy Alloys. Technical report, Ecole des Mines de Saint Etienne, Saint-Etienne, 2018.

[158] G. Laplanche, P. Gadaud, C. Bärsch, K. Demtröder, C. Reinhart, J. Schreuer and E. George : Elastic moduli and thermal expansion coefficients of medium-entropy subsystems of the CrMnFeCoNi high-entropy alloy. *Journal of Alloys and Compounds*, 746:244–255, 2018.

[159] ASTM : *E1876-01, Standard Test Method for Dynamic Young's Modulus, Shear Modulus, and Poisson's Ratio by Impulse Excitation of Vibration, American Society for Testing and Materials, 2001.*
https://www.astm.org/Standards/ E1876.htm., btitle.

[160] D. R. Steinmetz, T. Ja, B. Wietbrock and P. Eisenlohr : Author ' s personal copy Revealing the strain-hardening behavior of twinning-induced plasticity steels : Theory , simulations , experiments. 61:494–510, 2013.

[161] G. Smagghe : Modélisation de la recristallisation lors du forgeage à chaud de l ' acier 304L – une approche semi-topologique pour les modèles en champs moyens To cite this version : HAL Id : tel-01665156 THÈSE DE DOCTORAT DE L ' UNIVERSITÉ DE LYON l ' École des Mines . 2017.

[162] K. K. Singh, S. Sangal and G. S. Murty : Hall–Petch behaviour of 316L austenitic stainless steel at room temperature. *Materials Science and Technology*, 18(2):165–172, 2002.

[163] B. Sparke, D. James and G. Leak : Lattice diffusion in gamma-iron. *Journal of the Iron and Steel Institute*, 203:152, 1965.

[164] K. Maminska : *Optimisation microstructurale d'un acier HP pour des applications a haute temperature.* PhD thesis, Ecole des Mines de Saint Etienne, 2013.

École Nationale Supérieure des Mines de Saint-Étienne

NNT : 2019LYSEM007

Julia OLSZEWSKA

Dissertation title: **Conception and development of a novel grade of high resistance High Entropy Alloy from the CrFeMnNi family**

Speciality: Material Science and Engineering

Keywords: high entropy alloys (HEA), CrFeMnNi, deformation mechanisms, activation volume, nanostructure, dislocations, thermodynamic modelling, alloys design

Abstract:

The concept of High Entropy Alloys, HEAs, is based on the exploration of centres of phase diagrams for compositions composed of 5 elements or more, in similar proportions. It was found among others in Cantor's alloy, the equiatomic CoCrFeMnNi, that solid solution formation is favoured, even if the high entropy of mixing is not the predominant element assuring such outcome. Some of HEAs present unique properties such as simultaneous increase of yield strength and elongation to fracture down to cryogenic temperatures, eased formation of nanostructures or decreased phase transformation kinetics.

This PhD dissertation presents the design and evaluation of new compositions from the CoCrFeMnNi family focusing on low-Co or Co-free compositions. Three grades characterised by a large single phased domain were selected based on thermodynamic simulations (Thermo-Calc). Those alloys were prepared both in the academic laboratory of EMSE and in the industrial laboratory of APERAM. First analysis allowed to focus the study on one composition, the so called Y3 CrFeMnNi, a cobalt free grade.

Microstructural optimisation of Y3-CrFeMnNi grade was based on mechanical testing combined with principal techniques of microscopic observations (SEM, EBSD, TEM), to be able to describe the finest microstructures at the origin of mechanical properties. Multiple strengthening mechanisms were identified and analysed. Secondary precipitation, as a possible source of additional hardening, was proposed. High efficiency of strain hardening, already found in similar HEAs, was confirmed in the selected material. Hot transformation of the alloy leads to creation of high density of dislocations that are surprisingly stable as for a metallic alloy. Their presence leads to eased formation of nanostructures as well as slows down the recrystallization process. Furthermore, the recrystallisation results in only slightly decreased dislocations density in the matrix. Through relaxation tests dislocations forest hardening together with solid solution hardening where shown to be major contributors to materials hardening and plastic deformation behaviour. Those mechanisms stay predominant even at cryogenic temperature. Finally, it was shown that the studied HEA obeys the macroscopic deformation laws as proposed by the Kocks-Mecking model. Y3 grade is characterised by a behaviour close to other fcc materials with a low stacking fault energy value.

École Nationale Supérieure des Mines de Saint-Étienne

NNT : 2019LYSEM007

Julia OLSZEWSKA

Titre de la thèse : **Conception et développement d'une nuance d'alliage de type HEA (High Entropy Alloys) de la famille CrFeMnNi à résistance mécanique élevée.**

Spécialité : Science et Génie des Matériaux

Mots clefs : alliages à haute entropie (HEA), CrFeMnNi, mécanismes de déformation, volume d'activation, nanostructure, dislocations, modélisation thermodynamique, conception d'alliages

Résumé :

Le concept d'alliages à forte entropie (High Entropy Alloys, HEAs) consiste à explorer les centres des diagrammes de phases pour des compositions contenant au moins 5 éléments en proportion proche d'équiatomiques. La formation des solutions solides a été confirmée entre autres dans l'alliage de Cantor, le CoCrFeMnNi, même si l'entropie de mélange élevée n'y est pas le paramètre déterminant. Certains des HEAs présentent des propriétés uniques et prometteuses telles qu'une augmentation simultanée de la limite d'élasticité et de l'allongement à la rupture même à de températures cryogéniques, la formation facile de nanostructures, et enfin un ralentissement de la cinétique de transformations de phases.

Ce travail de thèse porte sur la conception et l'évaluation de nouvelles compositions de la famille CoCrFeMnNi, avec une concentration de cobalt faible voire nulle. Trois compositions présentant une large plage cfc ont été sélectionnées sur la base des simulations thermodynamiques (Thermo-Calc). Les alliages ont été fabriqués au sein du laboratoire EMSE et dans le laboratoire industriel d'APERAM. Après une analyse préliminaire, notre choix s'est porté sur la nuance Y3 CrFeMnNi, sans cobalt.

L'optimisation microstructurale de la nuance Y3-CrFeMnNi comporte une caractérisation mécanique et utilise les principales techniques de microscopie électronique (MEB, EBSD, MET) pour une analyse fine des microstructures en vue de compréhension des phénomènes à l'origine des propriétés mécaniques. Plusieurs mécanismes de durcissement de l'alliage sont analysés. La voie de durcissement par précipitation fine de seconde phase, malgré l'intérêt indéniable, a dû être abandonnée à cause des difficultés liées au procédé de coulée. L'efficacité de durcissement par écrouissage a été confirmée dans ce matériau, comme déjà observé dans d'autres HEA de la même famille. Les dislocations, issues du procédé de transformation, présentent une stabilité surprenante pour un matériau métallique, ce qui conduit à la formation facile de nanostructures, mais aussi à une recristallisation lente. De plus, cette dernière ne diminue que faiblement la densité de défauts dans la matrice. Le durcissement par dislocations ainsi que durcissement en solution solide comme mécanismes principaux de déformation de cet alliage ont été confirmés à partir des essais de relaxation; ces mécanismes restent actifs même à des températures cryogéniques. Enfin, nous avons pu montrer que l'alliage étudié obéit la loi de comportement macroscopique proposée par Kocks-Mecking; ses caractéristiques sont proches de celles d'un matériau de structure cfc et d'une énergie de faute d'empilement basse.